N^o d'ordre 171-2002 Année 2002

Thèse

présentée devant

l'UNIVERSITE LYON I - CLAUDE BERNARD

pour l'obtention

du DIPLOME DE DOCTORAT
(arrêté du 30 mars 1992)

présentée et soutenue publiquement le

8 novembre 2002

par

Ketel TURZÓ

Study of the $^{12}C+^{197}Au$ Reaction at Relativistic Energies with the INDRA 4π Multidetector

Directeur de thèse et tuteur:
MM. Daniel Guinet et Wolfgang Trautmann

Jury:	M. Joseph Rémillieux	Président
	M. Philippe Chomaz	
	M. Daniel Guinet	
	M. Herbert Orth	Rapporteur
	M. Giovanni Raciti	Rapporteur
	M. Wolfgang Trautmann	

Merci! Danke! Thanks!

an Prof. Dr. Uli Lynen für die freundliche Aufnahme in seine Arbeitsgruppe und die damit verbundenen grosszügigen Arbeitsmöglichkeiten an der Gesellschaft für Schwerionenforschung in Darmstadt.

an Dr. habil. Wolfgang Trautmann für die intensiven Diskussionen, die zahlzeichen Anregungen bei der Auswertung der Daten und die Unterstützung bei der Diskussion der Resultate, die viel zum Gelingen der Arbeit beigetragen haben.

à mon directeur de thèse Dr. Daniel Guinet pour toute l'attention et l'aide apportées au bon déroulement de ce travail à Darmstadt comme à Lyon.

to my PhD referees Prof. Dr. Herbert Orth and Prof. Dr. Giovanni Raciti for their careful reading and helpful comments during the writing of this work, and to Prof. Dr. Joseph Remillieux and Dr. Philippe Chomaz for their perspicacious participation in the PhD committee.

to Carsten Schwarz and David Gourio to have guide my first steps in research, to Walter Müller, Jerzy Łukasik, Andrea Saija, and Arnaud Le Fèvre for their intense collaboration in the analysis of the INDRA@GSI data and to my colleagues of the ALADIN group: Titti Sfienti, Khalid Kezzar, Nepomuk Otte, Alexander Botvina, Jost Lühning, Andrej Sokolov, Andriy Mykulyak, Ralf Bittiger and Isia Busch.

to all coworkers in the INDRA@GSI experiment: G. Auger, Ch.O. Bacri, M.L. Begemann-Blaich, N. Bellaize, F. Bocage, B. Borderie, R. Bougault, B. Bouriquet, Ph. Buchet, J.L. Charvet, A. Chbihi, R. Dayras, D. Doré, D. Durand, J.D. Frankland, E. Galichet, S. Hudan and F. Lavaud who were also involved as PhD students in the data analysis, B. Hurst, G. Immé, Ph. Lautesse, J.L. Laville, Ch. Leduc, R. Legrain, O. Lopez, L. Nalpas, E. Plagnol who was the spokesperson and project leader of the INDRA@GSI experiment, E. Rosato, W. Seidel, J.C. Steckmeyer, G. Tabacaru, B. Tamain, A. Trczinski, E. Vient, M. Vigilante, C. Volant for his collaboration in pion and proton studies, B. Zwieglinski and L. Tassan-Got for his help in the data reduction.

à mon ami, à mes amis et à ma famille en France, en Allemagne et ailleurs.

Contents

List of Figures

Introduction

Multifragmentation is the emission of several intermediate mass fragments ($3 \leq Z \leq 30$) from a hot nucleus, a phenomenon observed in nuclear reactions, using light and heavy projectiles over a wide range of incident energies. The goal of these studies is to learn more about the tendency of fermionic nuclear matter to appear in clusters and, perhaps eventually, about the topology of the nuclear phase diagram (see Fig. 1), in particular the evasive liquid-to-gas transition. Additionnally, the explosive features of some of the reactions allow us to study the compressibility of nuclear matter. In fact, the multifragmentation process is believed to appear in the instable region, also called spinodal region, of the nuclear phase diagram where liquid and gas phases coexist. Such information can be important for astrophysical applications as, for instance, during the neutron star formation and the explosion of a supernova of type II. During these processes, the prevailing thermodynamic conditions are expected to be similar to those obtained in the multifragmentation of finite nuclei [Vio98, Bay71, Bet90].

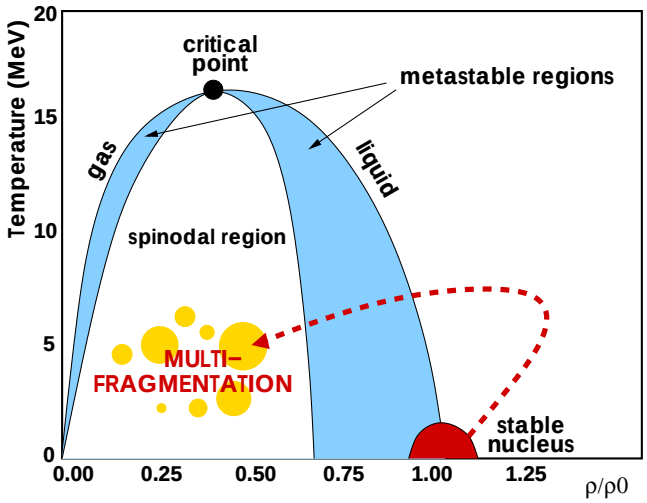

Figure 1: *Phase diagram of nuclear matter. The temperature is plotted as a function of the relative density, ρ_0 is the stable nucleus density. During the collision, the highly excited compound nucleus is believed to follow the trajectory indicated by the dashed arrow, from the liquid phase to the spinodal region, where the multifragmentation occurs. This region is a mixture of liquid and gas phases and is unstable.*

In 1995, the study of the liquid-gas phase transition led to the publication of the first caloric curve, the relation between temperature T and energy E, of nuclear matter by the ALADIN group [Poc95] shown in the left panel of Fig. 2. This caloric curve, obtained from data for the system Au+Au at the incident energy of 600 AMeV, presents a plateau-like behaviour from liquid to gas phases in agreement with the thermodynamical view of multifragmentation. This plateau may be interpreted as a sign of a liquid-gas phase transition.

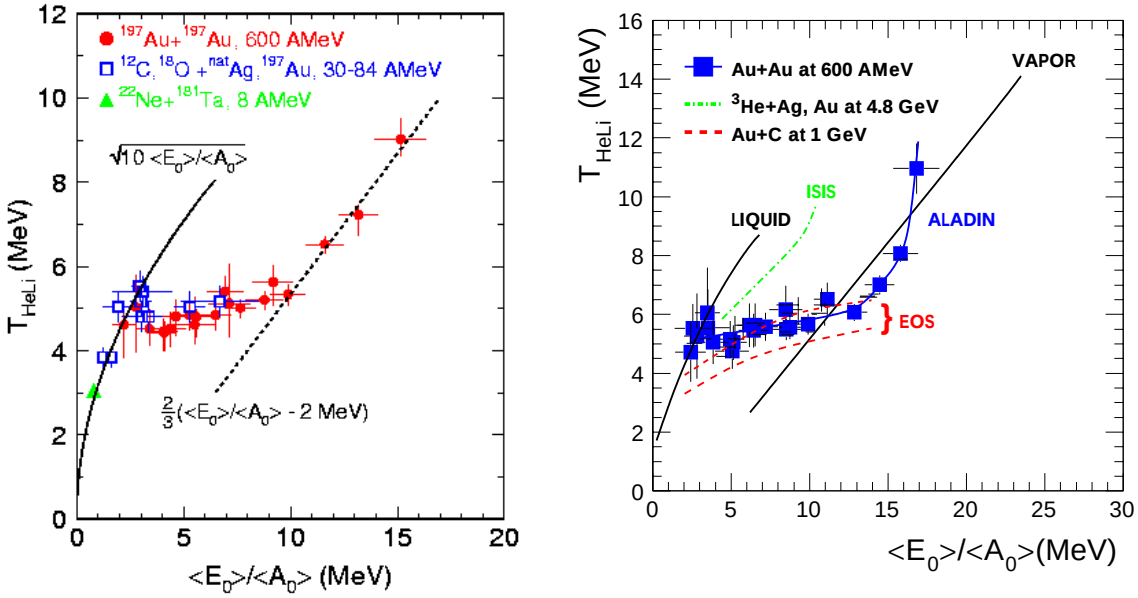

Figure 2: *Left panel: Caloric curve for the system Au+Au at the incident energy of 600 AMeV in 1995 [Poc95]. The full line corresponds to the liquid curve and the dashed line to the vapor one. Right panel: Caloric curves in 2001. ALADIN (squares), EOS (dashed lines) and ISIS (dashed-dotted line) data are compared [Ode99, Kwi98, Hau98].*

In recent years, several caloric curves for various reaction systems and beam energies were published which show discrepancies between them as exposed in the right panel of Fig. 2 [Ode99, Kwi98, Hau98]. One, if not the main difficulty when comparing caloric curves obtained from different reactions at different incident energies is the determination of the excitation energy. It is obtained by summing up kinetic energies of all particles *after* equilibration has been achieved. Since a non-negligible amount of light particles is emitted prior to equilibration, the number of these preequilibrium particles and also their energies have to be known. This requires a detailed knowledge of their energy spectra.

Some theoretical models also highlight the importance of the kinetic energies. The statistical multifragmentation model (SMM) points out the contradiction between kinetic and microscopic temperatures [Ode99] (see chapter A.1). The negative heat capacity, considered as a signal of a phase transition, is determined partly from particle kinetic energies [Dag00]. The classical molecular dynamics model (CMD) predicts from fragment kinetic energies that the expansion of the source is a non-equilibrium phenomenon [Cam02].

Fig. 2 also shows that the study of liquid-gas phase transition may imply very different reactions from light hadron to heavy ion projectiles. In this work we focus on spectator reactions in asymmetric systems. Historically, multifragmentation was observed in asymmetric systems [Mey80, Jak82]. Nowadays, the interest comes from the supposed equilibrated source created in this kind of reactions from the largest nucleus, the target in normal kinematics or the projectile in inverse kinematics. Asymmetric collisions in normal kinematics were studied by the ISIS and FASA collaborations, also with ^{12}C projectiles in the FASA case [Kwi98, Avd98]. ALADIN and EOS performed experiments in inverse kinematics, in particular ^{197}Au+^{12}C [Sch96, Hau98]. The latter type of experiments permits the detection of the heavy fragments without threshold, a certain advantage for the study of multifragmentation. However, the hydrogen isotopes are difficult to detect in the ALADIN spectrometer because of their wide distribution in rapidity and their charge-to-mass ratio which is twice that of the fragments. In EOS, a Time Projection Chamber at the target was used for the study of these light particles. In general, the kinetic energies in the source frame are more difficult to determine in inverse kinematics because of the need of a transformation into the moving system.

Because of these limitations of inverse kinematics and the interest in kinetic energies, it was decided to use the INDRA[1] 4π multidetector (see Fig. 3) to study various systems and incident energy ranges, amoung them ^{12}C+^{197}Au reactions at relativistic beam energies. This detector, designed for installation at GANIL[2], was relocated to GSI[3] from 1998 to 1999.

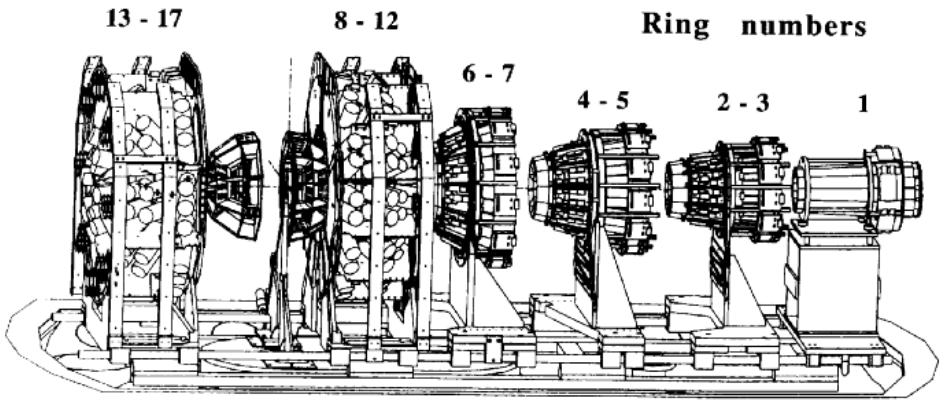

Figure 3: *INDRA: exploded view of the detector assembly consisting of 96 ionization chambers, 192 silicon detectors and 336 crystals of cesium iodide organised in 17 rings centered on the beam axis.*

Its large angular coverage, 90% of 4π in solid angle, and its very good resolution for light particles make INDRA a good device to study the reaction stages. Of course, this detector also has some disadvantages including thesholds which forbid the detection of the heaviest fragments and upper limits in kinetic energy given by the detector lengths for the light particles.

[1]Identification de Noyaux et Détection avec Résolution Accrue
[2]Grand Accélérateur d'Ions Lourds (Caen, France)
[3]Gesellschaft für SchwerIonenforschung (Darmstadt, Germany)

The choice of the $^{12}C+^{197}Au$ system [Aug96] at the incident energies from 95 AMeV to 1800 AMeV was determined by the weight of the projectile, heavy enough to produce a maximum number of fragments in central collisions and light enough to avoid δ-electron problems. The use of INDRA with relativistic beams provided an experimental challenge. The beam halo, although negligible in relative intensity, generated considerable amounts of light particles with low multiplicities at the highest incident energies.

The present thesis is an overview of the new results obtained in the $^{12}C+^{197}Au$ experiments of the INDRA@GSI campaign. This campaign was the occasion of the study of several systems over a wide range of energies: Au+Au from 40 to 150 AMeV, Xe+Sn from 20 to 200 AMeV, and C+Au,Sn from 95 to 1800 AMeV. This work gives as an introduction into multifragmentation studies a general presentation of the equation of state applied to nuclear matter, the nuclear temperature and the relativistic heavy ion collisions. The INDRA@GSI experiment is presented in its particularities as are the data reduction methods for particle identification and calibration. The event centrality selection is described with a comparison of different global variables used for the determination of the impact parameter. The main physics topic studied in this work is the eventual determination of the reaction stages, i.e. of the early and target sources, by analysing proton and fragment kinetic energy spectra. The proton spectra are compared to combinations of theoretical models including early and multifragmentation emissions. The characteristics of the fragment target source are compared to previous ALADIN results and to a combination of models supporting the concept of the equilibrated source. The pions, identified for the first time in INDRA, and the fast protons are exploited to study possible correlations between them and intermediate mass fragments. The status of these results is given as a summary and accompanied by a description of future prospects on $^{12}C+^{197}Au$ reactions and multifragmentation study.

Chapter 1

Nuclear Matter and Relativistic Heavy Ion Collisions

1.1 Properties of nuclear matter

Nuclear matter is very different from ordinary matter in many aspects. Its density is considerably higher than the one of the bulk matter, its interaction is governed by the strong and weak forces in addition to the electromagnetic forces. Nevertheless, this matter can sometimes be described with macroscopic variables like pressure or temperature in the frame of specific limitations. The evolution of the system consequently to the changes of the macroscopic variables is described by a relation between these variables: the equation of state.

Phase diagram

By analogy to four states of the ordinary matter (gas, liquid, solid, plasma), it is possible to define also such four states to describe the features of the nuclear matter, as sketched by the Fig. 1.1.

The *liquid phase*, for the low temperatures and densities, corresponds to the nuclear matter in its ground state.
The *condensed phase* is supposed to be cold matter at high density where nucleons are organised like into a crystal. The protons and neutrons alternate in the net, with neighbouring spins that are oriented in opposite directions.
The *gaseous phase* appears at fairly high temperatures and low densities at which the nuclei evaporate into a hadron gas. This phase is explored by the high energy physics experiments at CERN, GSI, Fermilab, RHIC, etc...
The *plasma phase* is predicted for densities of five to ten times the normal density of nuclear matter and for temperatures above around 150 MeV. One should observe then the dissociation of hadrons into their elementary constituents and the appearance of a deconfined mixture of quarks and gluons.

Today most of this diagram still remains unexplored. Only very recent experiments may have permitted to reach the quark-gluon plasma or the condensed phase.

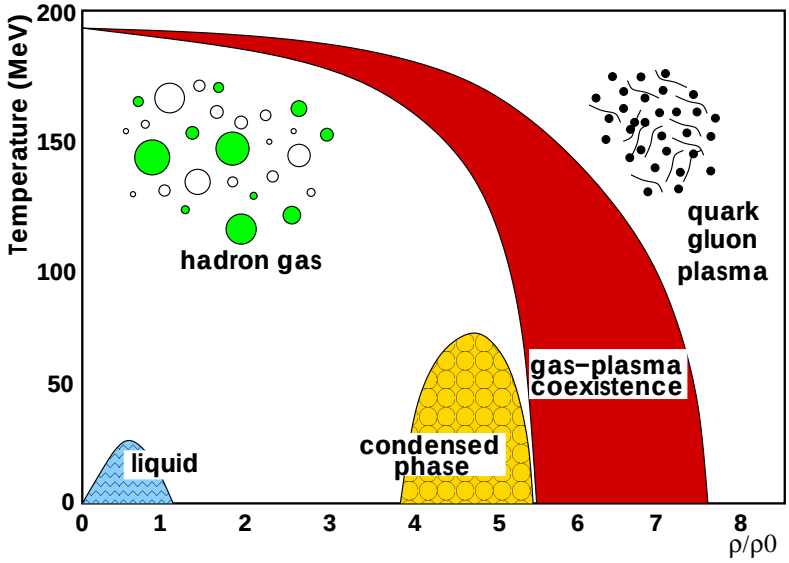

Figure 1.1: *Phase diagram of nuclear matter. The temperature is plotted as a function of the relative density, ρ_0 is the stable nucleus density. The four states of nuclear matter are represented : liquid, hadron gas, condensed matter, and quark-gluon plasma.*

The equation of state of nuclear matter

Generally, the equation of state of a system is a relation between three thermodynamical variables. Expressed in the most usual form, the nuclear equation of state relates the internal energy E to the density ρ and the temperature T, distinguishing a thermal component and a compression component:

$$E(\rho, T) = E_C(\rho, T = 0) + E_{TH}(\rho, T) + E_0 \tag{1.1}$$

with $E_C(\rho, T = 0)$: compression energy at T=0, E_{TH}: thermal energy, and E_0: binding energy of the infinite nuclear matter in its ground state.

Fig. 1.2 displays an example of the corresponding shape of the equation of state at temperature zero. The top dashed line corresponds to the energy of an excited system, divided in a thermal component E_{TH} and a compression component E_C. The notion of saturation means that, for a sufficiently heavy nucleus, increasing its number of constituents does not modify the density of nucleons in its central part. Reaching a limit value, this density, so-called saturation density ρ_0, becomes independent of the nuclear size. This property is fundamental since one can then assimilate the core of heavy nuclei to infinite nuclear matter. For a system symmetric in numbers of protons and neutrons, the saturation density was theoretically estimated to be $\rho_0 = 0.17 \pm 0.02 \quad nucleon.fm^{-3}$. The universality of this value has been confirmed by experiments of nuclear radius measurements. They demonstrated for almost all ground state nuclei the validity of a nuclear radius formula $R = r_0 A^{1/3}$ ($r_0 = 1.2fm$) indicating that each nucleon occupies the same elementary volume $\frac{4}{3}\pi r_0^3 \simeq 7fm^3$ inside any nucleus.

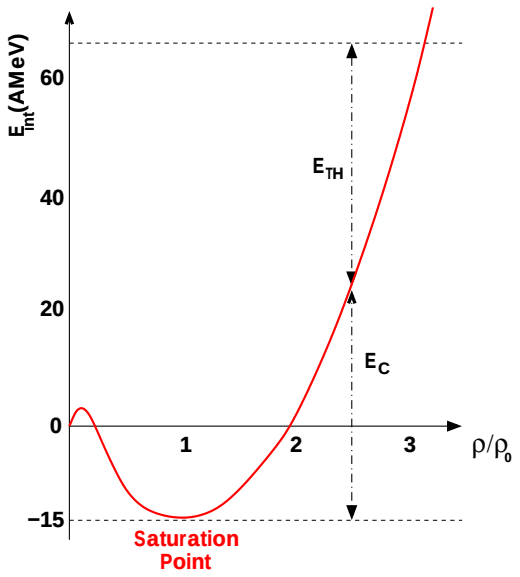

Figure 1.2: *Predicted equation of state for nuclear matter. The internal energy per nucleon is sketched as a function of the density ρ normalised to the saturation density ρ_0. The total energy at temperature zero (top dashed line) is composed of the thermal component E_{TH} and the compression component E_C.*

Different theoretical descriptions have been developped on the basis of the nuclear matter such as the liquid drop model [Eva55]. These approaches authorise, on the basis of the Bethe-Weizsäcker formulae, the extension of the properties of the infinite nuclear matter to the finite nuclei. Their principle is to introduce parametrised correction terms that take into account the specificity of nuclei due to the effects of surface, Coulombian repulsion, and isospin asymmetry. For a symmetric system of infinite nuclear matter, the term of volume effects gives the binding energy per nucleon E_0 estimated to E_0=-16 AMeV.

An important parameter of nuclear matter is the compressibility which is determined by the curvature of the internal energy per nucleon as a function of the density. In the vicinity of the saturation point, this function has a minimum and one parametrises the compression energy by a parabolic function like:

$$E_c(\rho) = \frac{K_\infty}{18}\frac{(\rho-\rho_0)^2}{\rho_0^2} \tag{1.2}$$

whose quadrature coefficient is fixed by the compressibility module K_∞:

$$K_\infty = 9\rho_0^2\left[\frac{d^2E_c}{d\rho^2}\right]_{\rho=\rho_0} \tag{1.3}$$

The experimental determination of K_∞ can be done from giant monopol resonances, or through studies related to astrophysics [Gle88] and to the collective phenomena in heavy ion collisions. The results as obtained until now estimate K_∞ to be between 200 and 400 MeV. If K_∞ is low ($\simeq$ 200 MeV), the equation of state is called *soft* because one has to give relatively little compression energy to reach high densities. If K_∞ is high ($\simeq$ 400 MeV), one speaks about a *hard* equation of state because, one must give a comparatively higher compression energy to reach the same densities.

From recent results of the FOPI collaboration [And99, And02], experimental data in comparison to IQMD simulations, for Au+Au at 400 and 600 AMeV, seem to be closer to a soft equation of state. A similar report emerges from studies of kaons and pions production in Au+Au and C+C collisions between 600 and 1500 AMeV with the KAOS detector [Stu01, Fuc01].

The difficulties of theoretical approaches

The equation of state permits the macroscopic description of a system through thermodynamical variables. These variables explicitly depend on microscopic properties. So any equation of state is based on the knowledge of the elementary interactions between the constituents.

The nucleon-nucleon interaction potential is known as having a dominant term that is repulsive at short range ($\leq$ 0.5 fm) and attractive at longer range ($\geq$ 0.8 fm) [Eva55]. In order to roughly characterise the equation of state of nuclear matter, one can compare the potential to the one of a molecule. This formal correspondence suggests that the equation of state of an infinite system of nucleons is comparable to the one of a Van der Waals gas. It allows to predict the shape of the isotherms and the existence of a liquid-gas phase transition.

Using a more rigorous approach, in particular the fermionic nature of nucleons brings serious problems. In contrary to the simple real fluids, it becomes more difficult to link the nucleon-nucleon interaction to the equation of state. Consequently, the actual models describe only approximatively the saturation point, a basic property of the nuclear matter, from the nucleon-nucleon interaction. Theoretically, the saturation mechanism is defined in a simple way as being the balance between the attractive part of the nuclear interaction potential and the repulsion between nucleons, due to their fermionic nature, and the repulsive part of the potential. But in their attempt to reproduce the saturation point, the calculations technically fail because of n-body forces (from three-body forces to in-medium effects). Concerning this latter point, it means that it is necessary to take into account the contribution of all the other nucleons in the elementary processes of scattering. The Brückner theory is used in this aim in calculating an effective interaction from the free nucleon-nucleon interaction [Eva55]. However, this theory does not describe the saturation point. Another method is to build classes of phenomenologic forces as the Skyrme forces [Vau72]. This approach allows to describe the saturation but this description is obtained by tuning a certain number of free parameters which do not originate from the nucleon-nucleon interaction.

Predictions at finite temperatures

Although the formulation of an equation of state at zero temperature still remains a challenge from the theoretical point of view, it is interesting to attempt an estimate of its shape for finite temperatures. By extending different calculations realised to non-zero temperature, it has been demonstrated that the purely thermal effect on the structure of the nucleon-nucleon interaction is relatively modest [Fri81]. This is the reason why on can use these forces at finite temperature, once parametrized at zero temperature. Such studies [Sau76] predict the behaviour displayed in Fig. 1.3 in the pressure-density plane. We can observe a coexistence region of liquid-gas phases (full line cutting isotherms), defined for temperatures lower than a critical temperature (T_C = 17.9 MeV). We note also a so-called spinodal region (area with circles) at low density, which

is characterised by a mecanically unstable regime for which the fluctuations of density are amplified, whereas they are attenuated outside these special conditions of ρ and T. This spinodal region corresponds also to a negative compressibility $K = -\frac{1}{V}\frac{dP}{dV}$ causing this instability. Nuclei reaching this region blow up into several fragments. This phenomenon is supposed to be multifragmentation [Gua96, Gua97]. As this occurrence is believed to take place in a region of coexistence of the liquid and gas phases, multifragmentation is a way to study the transition between these two phases.

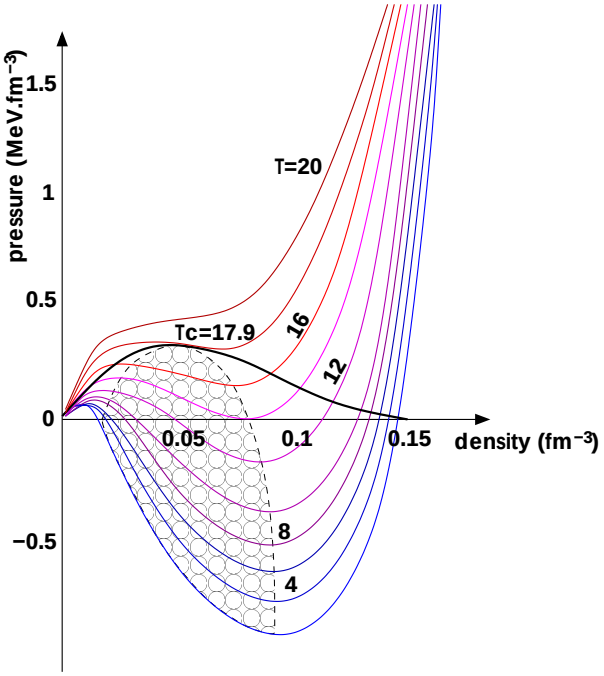

Figure 1.3: *Predicted equation of state for nuclear matter for different temperatures indicated in MeV (adapted from [Sau76]). The pressure is sketched as a function of the density. The full line cutting the isotherms delimits the coexistence region of liquid-gas phases. The spinodal region is represented by the area with circles.*

Nuclear temperature

The concept of temperature is well defined in classical statistical mechanics. We attempt to apply this definition to nuclear systems although some shortcomings are present: the short time range of the reaction, the finite size of the system, the complex dynamics, and the various interactions which occur in a collision.

One of the fundamental quantities used in classical statistical mechanics is the number of states $\Gamma(E, N)$ of a given system with a particle number N which lies in the vicinity ΔE of the energy E. This function is directly proportional to the density of states $\rho(E, N)$ at energy E, such that:

$$\Gamma(E, N) = \rho(E, N).\Delta E \tag{1.4}$$

It is also convenient to introduce the entropy of the system $S(E, N)$:

$$S(E, N) = ln(\Gamma(E, N)) = ln(\rho(E, N)) + ln(\Delta E) \tag{1.5}$$

With these quantities, the definition of the temperature provided by statistical mechanics is:

$$\frac{1}{T} = \frac{\partial S}{\partial E} = \frac{\partial ln(\rho(E,N))}{\partial E} \tag{1.6}$$

where ΔE is considered independent of E. This definition is applicable to any isolated system, like a nuclear system if one regards the very short range of the nuclear force.

While the formal definition of temperature is simple, the relevance of the concept and its measurability depend on further requirements which, in more realistic nuclear cases, one may only approximately meet. The excitation of an isolated system can be characterised by an energy but, in order to determine its temperature, two additional major features must be known: the degree of equilibration and the specific density of states. The most critical of these requirements is that the ensemble must be in full statistical equilibrium. This means that each of the states included in $\rho(E,N)$ is populated with equal probability. For highly excited nuclear systems, the requirement of full equilibrium may be difficult to achieve in practice. With the increase of the excitation energy, a reduction of the lifetime of the system is observed and a homogeneous population of the states becomes less probable.

It is difficult to know, a priori, the degree of equilibrium of a nuclear system because the dynamics are complex and only partly known. Nevertheless, previous works on relativistic heavy-ion collisions present results indicating an independence of fragment emission to incident energy that may be interpreted as a signal of an equilibration [Sch96, Ode99]. To continue the exploration of equilibrium, it is instructive to assume that the population of states is sufficiently complete to allow the utilisation of the concept of temperature for nuclear systems.

1.2 Relativistic heavy ion collisions.

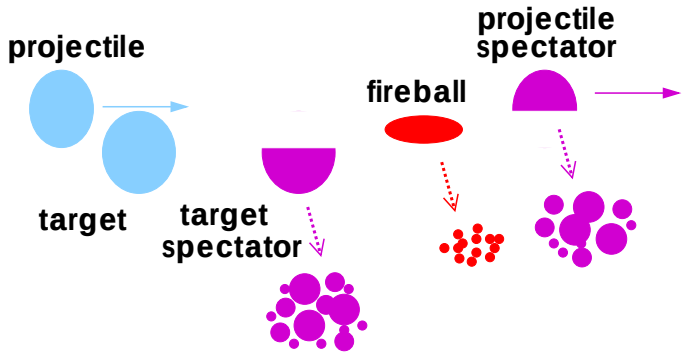

Figure 1.4: *After collision, there exists three sources of light particles and fragments: the projectile and target spectators and the participant region, so-called 'fireball'.*

The heavy ion collisions at relativistic energies (100 AMeV $\leq E_{lab} \leq$ 2 AGeV) are the unique tool to study in the laboratory nucleonic systems under extreme conditions of temperature and pressure. It is hoped to access to the properties of nuclear matter by exploring wide regions of

its phase diagram and to reach thromodynamical conditions that are similar to the inner part of supernovae, of the neutron stars and in the early universe. At relativistic energies, the collision can be described within the geometrical participant-spectator picture. In this scheme, that is shown in Fig. 1.4, a geometrical overlap region between the target and the projectile is associated to each impact parameter. When this region is sufficiently large, a so-called 'fireball' is created, which is the seat of high densities and temperatures. The fireball contains the 'participant' nucleons wich are supposed to be free during its explosion. The residues of the target and the projectile, outside the overlapping region, are excited by the collision. They constitute the 'spectator' matter that deexcites by evaporation or multifragmentation.

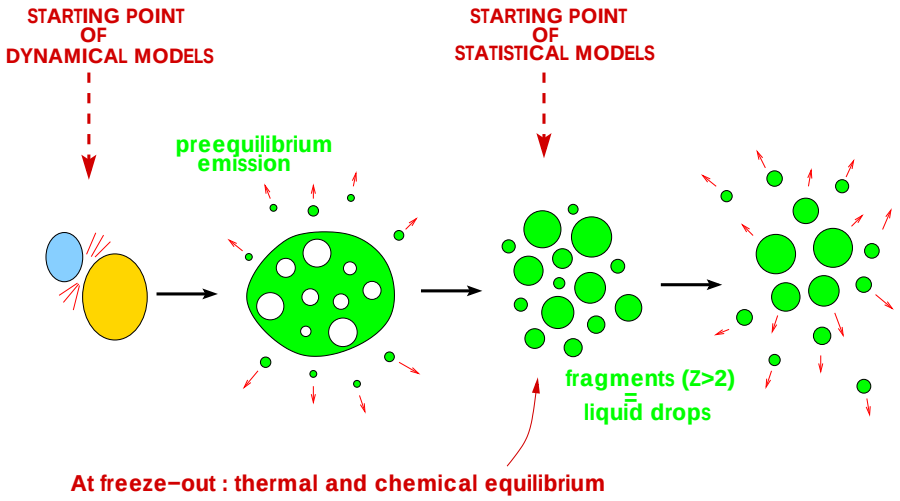

Figure 1.5: *Possible multifragmentation scenario.*

The mechanisms taking place in a heavy-ion reaction have dynamical and statistical aspects. A deep knowledge of these mechanisms is needed in order to extract the equation of state. The heavy ion collisions at relativistic energies may lead to different processes, from the formation of a compound system that deexcites by evaporation to the total disintegration of the system into a hadron gas. The intermediate regime is characterised by the breakup of the nuclear system into fragments ($Z \geq 2$) of various masses and several nucleons (see Fig. 1.5). This is accompanied, at sufficient incident energy, by the production of additional hadrons such as pions, kaons, etc... The usually believed scenario of collisions can be schematically decomposed into three stages. First, the penetration of the two nuclei causes a phase of heating and compression during which the temperature reaches some tens of MeV and the density two to five times the normal density. When the maximal density is reached, at about 15 fm/c (5.10^{-23} s) after the contact of the nuclei, an expansion stage begins until the reaction products do not interact any more with each other, the so-called 'freeze-out' stage. At this point, the system dissociates into

aggregates and various components. A first emission of light particles (n, p, d, t, ^3He, ^4He) and elementary particles like pions is observed before and during the expansion stage. At the breakup of the composite system, there is emission of light particles, intermediate mass fragments ($3 \leq Z \leq 30$), and heavy fragments ($Z \geq 30$). Finally, subsequently 'secondary' light particles are produced from the de-excitation of the emitted fragments. the total length of the collision varies with the system and the incident energy but it is roughly around 150 to 200 fm/c.

The formation mechanism of the fragments, whether they are the remnants of an incomplete destruction or the products of a condensation out of the disordered matter, is still the topic of very active research [Bon95b, Mor93, Fel99]. In order to investigate this question, recent experiments with the ISiS detector at Brookhaven studied reactions of energetic hadrons including pions and antiprotons with gold targets in a momentum range from 5 GeV/c to 14.6 GeV/c [Lef99b, Bea99, Bea00]. The aim of these experiments was to determine the role of the excitation energy in the fragment production. It is based on the expectation, tested with intranuclear cascade calculations (see appendix B), that light energetic projectiles will generate a statistical (thermal) disorder without exciting collective modes such as compression, rotation, or shape deformations. These are known to break nuclei very efficiently and would mask the nuclear response to the thermal excitation [Col97]. The ISiS experiments show that the antiproton projectiles at high momentum may generate a very high excitation energy. However, the corresponding fragment multiplicities are significantly smaller for the less energetic antiproton beam for the same range of excitation energy. It is therefore an open question whether the excitation energy by itself is the only parameter that governs the decay properties and fragment production. While this may be partly connected to the difficulties inherent with experimentally determining the excitation energy [Sch96], it is nevertheless obvious that the solution of this problem will help to better understand how fragments are formed [Ode00].

The limits of generating excitation energy can be overcome with composite projectiles. Systematic sets of data with projectiles of various mass and energy have been collected by different collaborations as ALADIN, EOS, or FASA [Sch96, Hau00, Avd98]. The ALADIN results exhibit a contimuing rise of the cross-section for high excitations with increasing mass of the target for the fragmentation of gold projectiles while the isotopic temperatures T_{HeLi} remain independent. These isotopic temperatures are determined from the double ratio of the yields of two pairs of nuclides with the same differences in neutron and proton numbers, ^{3}He/^{4}He and ^{6}Li/^{7}Li, according to the method suggested by Albergo and coworkers [Alb85]. However these temperatures present a dependence on the variable Z_{bound}, representing the sum of the atomic numbers Z_i of all projectile fragments with $Z_i \geq 2$, which is inversely correlated with the excitation energy. The isotopic temperatures tend to their highest values ($T_{HeLi} \sim 11$ MeV) at low Z_{bound}, i.e. at the highest excitation energies reached in these reactions. Large systems at even higher excitations can be produced in central collisions. In this case, the idea of excitation as a simple heating process has to be abandoned. Collective modes, compression as well as the directed outward motion of particles and clusters from primary collisions generate an explosive pattern, quantified as collective radial flow [Rei97]. The production of large clusters is rare and inversely correlated with the observed amount of flow. Some features of these energetic reactions have been reproduced with molecular dynamics calculations [Chi00] but to fully understand the clusterization mechanism in the dynamical environment still remains an interesting problem of future research.

Chapter 2

INDRA@GSI Experiment

In 1998 and 1999, a series of experiments was conducted at GSI with the INDRA multidetector. Several projectile-target systems over a wide range of energies were studied, Au+Au from 40 to 150 AMeV, Xe+Sn from 20 to 200 AMeV, and C+Au and C+Sn from 95 to 1800 AMeV. Enriched targets of ^{112,124}Sn were used in order to study isotopic effects.

The 4π-multidetector INDRA was developed at GANIL by a collaboration of French laboratories : GANIL, IPNO [1], DAPNIA [2], and LPC [3]. The INDRA detector is also used by the IPNL [4], Italian, Canadian, and Romanian groups. Three experimental campains have been performed at GANIL in 1993, 1994, and 1997 at intermediate energies (energies limited at 29 AMeV for Au).

These three campaigns of INDRA at GANIL have been devoted to the study of the production and decay modes of excited nuclei produced with intermediate-energy heavy-ion beams. The continuation of these measurements and their extension to higher beam energies, accessible with the heavy-ion synchrotron SIS, hase been one of the motivations for the INDRA@GSI campaign.

The present chapter describes briefly the accelerator devices of GSI and the INDRA detector and focus on technical particularities of the experiment, especially the relativistic energy part.

2.1 GSI accelerator facility

GSI operates a heavy ion accelerator facility consisting of the linear accelerator UNILAC (energy of 2 - 20 AMeV), the synchrotron SIS[5] 18 (1 - 2 GeV/u), and the experimental storage ring ESR[6] (E $<$ 1 AGeV) (Fig. 2.1). Ions from a Penning source are injected by the North and South injectors and then pass through the adjoining Wideröe structure. Alternatively, they originate in the high-charge injector before being into the Alvarez structure of the UNILAC at about 5% of the speed of light. In the UNILAC, the ion beam reaches 16% of the speed of light. Part of the

[1] Institut de Physique Nucléaire d'Orsay, Paris (France)

[2] Département d'Astrophysique, de physique des Particules, de physique Nucléaire et de l'Instrumentation Associée

[3] Laboratoire de Physique des Corpuscules, Caen (France)

[4] Institut de Physique Nucléaire de Lyon, Lyon (France)

[5] SchwerIonenSynchrotron

[6] Energy Storage Ring

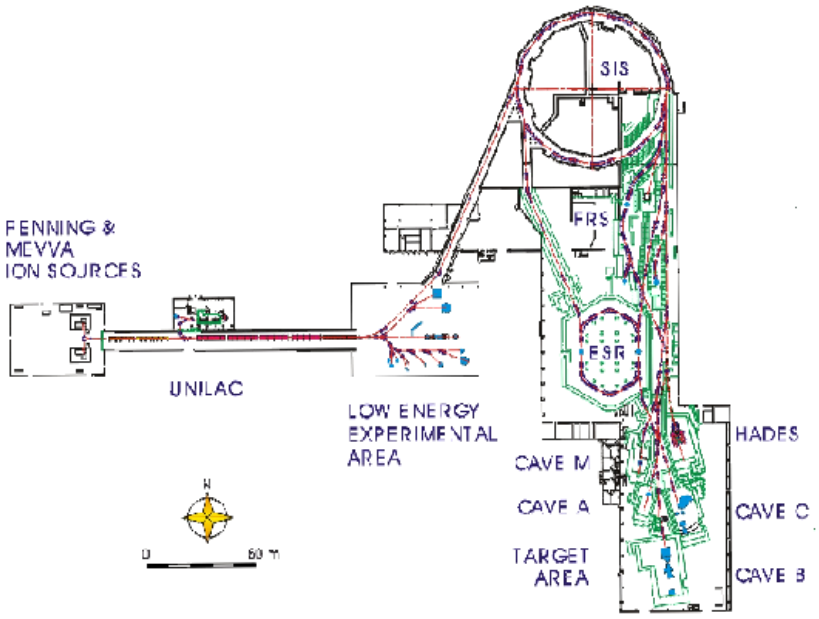

Figure 2.1: *GSI acceleration facility: UNILAC (Linac), SIS (Synchrotron), ESR (Storage Ring)*

beam is then diverted to the adjoining experimental hall for experiments, while the remainder is transferred to the heavy ion synchrotron SIS for further acceleration. There, the ions reach up to 90% of the speed of light, before being directed to experiments at the fragment separator FRS, the ESR, or the target hall.

During this experimental campaign, the INDRA detector was installed in the cave B, in the target hall.

2.2 INDRA multidetector

The 4π-multidetector INDRA offers high capabilities for the simultaneous detection of the numerous light charged particles and nuclear fragments that are emitted during heavy ion collisions. A total of 640 individual detectors (ionisation chambers, silicon detectors and cesium iodide crystals) covers 90% of the 4π solid angle (see Fig. 2.2) [Pou95].

These 640 detectors are organised in 336 modules. Each module consists of two or three detectors according to the angle: 96 ionisation chambers, 192 silicon diodes (Si), 336 thallium activated Cesium Iodide scintillators (CsI). The telescopes are grouped in 17 rings around the beam axis. Each ring consists of 8, 12, 16 or 24 detection modules.

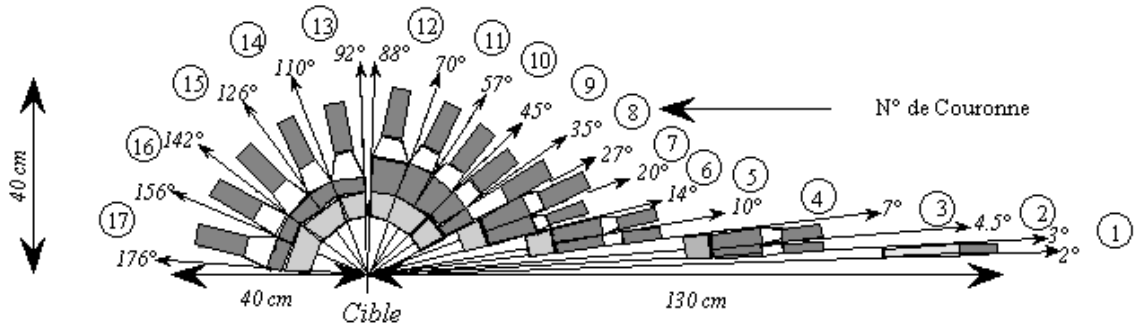

Figure 2.2: *INDRA: a detector assembly consisting of 17 rings ('Couronnes') of telescopes covering 90% of 4π around the target ('Cible') [Pou95].*

These rings have the following types of modules:
- ring 1 ($2^o \leq \theta_{lab} \leq 3^o$) : 12 telescopes of Si's and CsI's with photomultipliers, newly developped for INDRA@GSI.
- rings 2 to 9 ($3^o \leq \theta_{lab} \leq 45^o$) : 12 or 24 telescopes of ionisation chambers, Si's and CsI's with photomultipliers (Fig. 2.3, left panel).
- rings 10 to 17 ($45^o \leq \theta_{lab} \leq 178^o$) : 8, 16 or 24 modules of ionisation chambers and CsI's with photomultipliers.

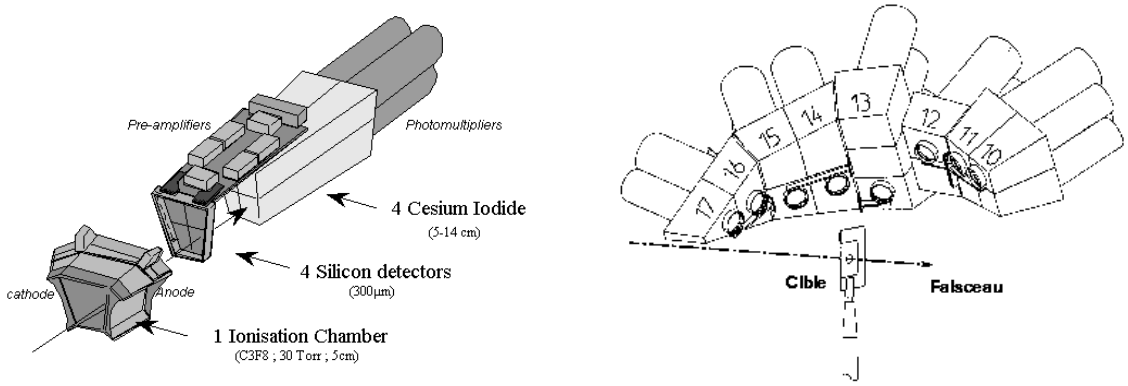

Figure 2.3: *Left-hand side: a typical INDRA module (between 7^o and 45^o). The detectable particle (longest arrow) punches trough the ionisation chamber, the silicon detector, and ends up in the CsI(Tl) crystal. Right-hand side:: mechanical assembly of the 8 Si-Si-CsI(Tl) telescopes in rings 10 to 17 of the INDRA detector ($\theta_{lab} > 45°$). The silicon detectors are represented by the disks in front of the CsI crystals which are facing the target (cible). The dashed line corresponds to the beam (faisceau) axis [Pou95].*

The INDRA geometry was optimised for the observation of multiple fragment emission. The most forward ring has to withstand a high rate due to elastic scattering. Rings 2 to 9 have to cover a large energy range and to avoid the double counts, the backward rings complete the angular coverage.

A part of the INDRA@GSI campaign has been dedicated to asymmetric systems like ^{12}C+^{197}Au and ^{12}C+^{112,124}Sn at beam energies ranging from 95 to 1800 AMeV. The ^{12}C+^{197}Au system is the purpose of the present work. The velocity of the target spectators is small also at relativistic energies, and their emission nearly isotropic in the laboratory frame while light particles from the initial reaction stages are forward peaked. Consequently, the study of spectator fragmentation is better achieved at backward angles where, however, a good isotopic resolution with low threshold is only provided by the Si-Si-CsI(Tl) calibration telescopes of INDRA (Fig. 2.3, right panel). These eight telescopes are distributed in the angular range from 45° to 180°, one module per ring, and consist of two circular silicon detectors of 2cm of diameter, a 80-μm detector followed by a Si(Li) detector with thickness 2000 μm, mounted between the ionisation chamber and the CsI(Tl) crystal of a telescope module.

2.3 The experimental setup: INDRA at GSI

The move of INDRA to GSI presents some setup particularities because of the very narrow entrance of the detector: 12 mm of diameter. As the beam emittance of a synchrotron (GSI) is larger than that of a cyclotron (GANIL), it is essential to control very carefully the beam focalisation all along the beam axis before and during the experiment[Tur98].

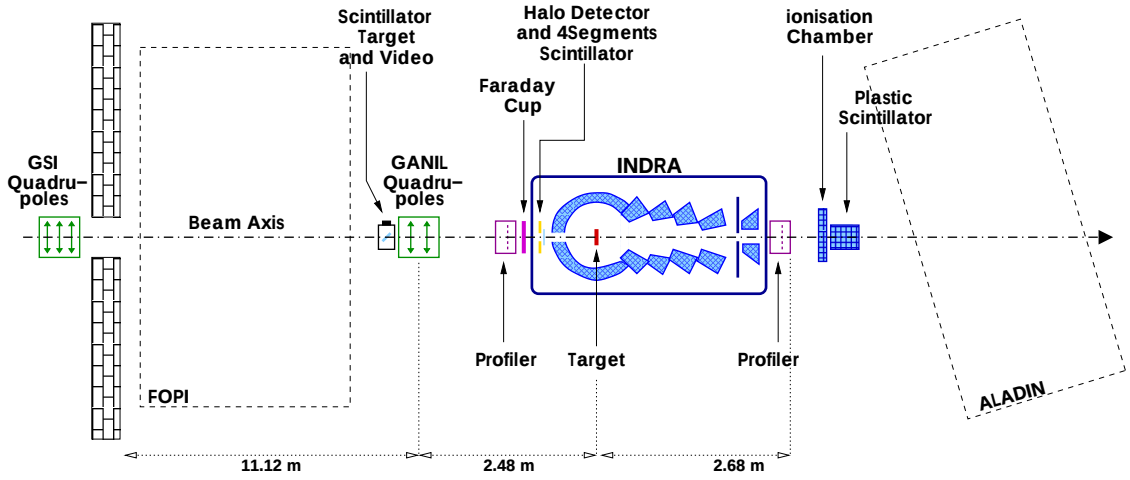

Figure 2.4: *Experimental setup of INDRA@GSI experiment in cave B at GSI.*

Along the beam line (from the last GSI quadrupole towards INDRA), as it is drawn in Fig. 2.4, one finds successively a scintillator target with video, the two GANIL quadrupoles, a first profiler in front of a Faraday cup, a halo detector, the INDRA reaction chamber, and a second profiler back. The first ring of INDRA ($2^o - 3^o$) is shielded with a removable brass plate, 2cm thickness, in order to avoid hard damages during the focalisation.

The scintillator target with its video is used to control the position of the beam just before the GANIL quadrupoles. These quadrupoles play a major role in the beam focalisation. They

permit the focalisation on the target by focusing first on the front profiler and afterwards and the back profiler. The focalisation on the target is determined knowing the quadrupole current densities corresponding to this two tunings and the distances between the profilers and the target. For the non-relativistic beams of the INDRA@GSI campaign, the Faraday cup may protect INDRA during the first beam settings while the beam intensity is lowered from 10^7 to 10^4 particles per spill.

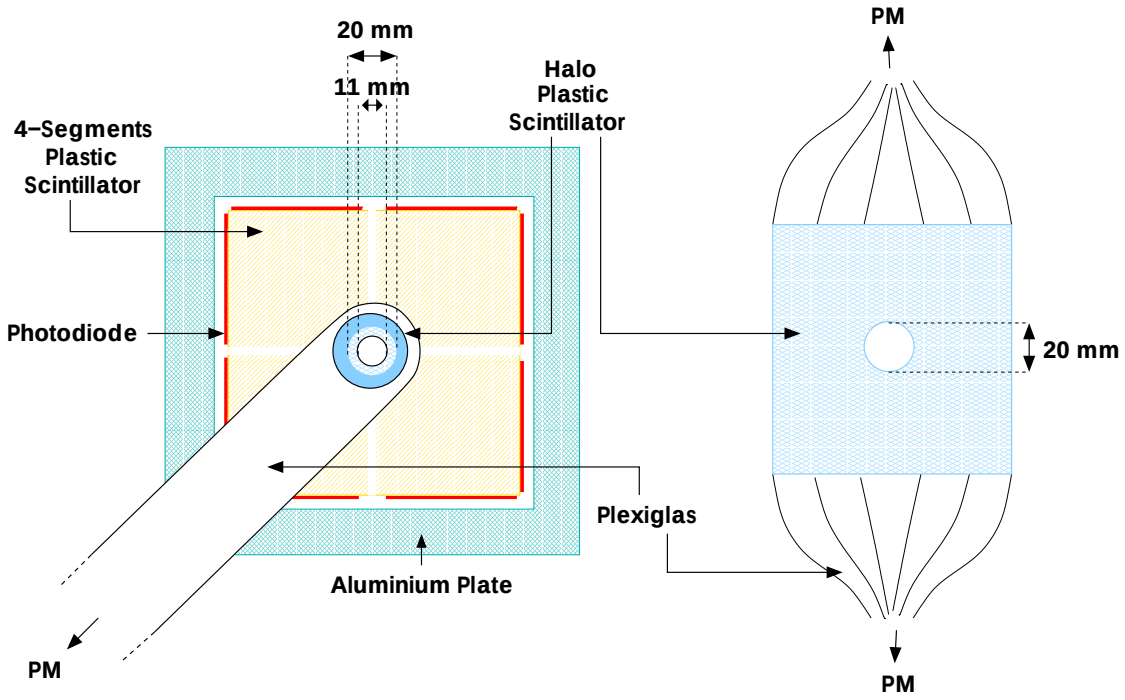

Figure 2.5: *Left-hand side: the halo detector is a ring of plastic scintillator connected to a photomultiplier (PM) by a light guide in plexiglas. The 4-segments scintillator is an ensemble of four squared layers of orange plastic scintillator of 2mm thickness connected to photodiodes with a central hole of 20 mm diameter. The whole setup is held by a thick aluminium plate. Right-hand side: the 'big' halo detector is a plate of blue plastic scintillator of 80 mm side, 4 mm thickness, with a central hole of 20 mm of diameter.*

After the focalisation period, during the experiment, the control on line is performed by the halo detector, the '4-segments' scintillator, and the first ring scalers. The halo detector is a ring of blue plastic scintillator of 200 μm thickness for the Au and Xe beams and 2mm thickness for the C beams, connected with a light guide to a photomultiplier and held by a thick aluminium plate (see Fig. 2.5) just in front of the entrance of the detector. The diameter of the hole of the halo detector is 1mm smaller than the diameter of INDRA entrance. The 4-segments scintillator is an ensemble of four squared layers of orange plastic scintillator of 2mm thickness connected to photodiodes with a central hole of 20 mm diameter. This detector is placed between the halo detector and the aluminium plate. The 4-segments detector gives the direction of the beam in case of unprecise focalisation and is only used on-line. The halo detector plays the important

role of a veto during the experiment and the data reduction. Some events may be produced by projectiles punching through this detector and may be likely to come from reactions in the technical structure of INDRA. By the use of the halo detector as a veto, these events can be rejected from the event selection.

The focalisation of carbon beams at relativistic energies was less precise than that of beams at lower energies. In order to improve the veto ability of the detectors in front of the backward rings of INDRA, a second and bigger halo detector was installed in the vacuum chamber, in front of the first halo scintillator. This second detector consists in a plate of blue plastic scintillator of 80 mm side, 4 mm thickness, with a central hole of 20 mm of diameter (see Fig. 2.5). Two sides are connected with light guides to photomultipliers. For the carbon beams, the signals of the two halo detectors are coupled as a unique 'halo' signal.

2.4 Characteristics of the C+Au experiment

This work is devoted to the asymmetric reaction C+Au at the incident energies 95, 300, 600, 1000, and 1800 AMeV. One of the main features of the C+Au system at relativistic energies is that the target emissions remain at the same rapidity in the laboratory for all the incident energies. This characteristic is visible in the invariant rapidity spectra of lithium fragments presented in Fig. 2.6. The rapidity is defined as usual,

$$y = \frac{1}{2} ln \frac{E + p_{//}}{E - p_{//}} \tag{2.1}$$

with the longitudinal momentum $p_{//}$ and the total energy E of the particle.

These spectra show for all the five energies (for 95 to 1800 AMeV, from the top to the bottom) a large circle corresponding to the target emissions and a small circle coming from the projectile, which is detected at 95 AMeV and still slightly visible at 300 AMeV. The target emissions of lithium fragments are centered around the target rapidity at y=0 and have a rapidity range approximately from y=-0.2 to y=0.3 for all incident energies.

At high incident energies as 600, 1000, and 1800 AMeV, the main beam, vetoed with the halo detectors, was accompanied during the experiment by a component of beam particles that arrived at large distance from the beam axis, as it is sketched in Fig. 2.8. Fig. 2.7 presents the 'good' (which means not detected by the halo detector) event distribution and the 'halo' event distribution as functions of the charged particle multiplicity N_c. The two main features of the 'halo' events is their low multiplicity and their increasing amount with the increasing incident energy. The 'halo' presents two components for the energies 95 to 1000 AMeV. The high energy component comes from the events produced by projectiles hiting the thin inner ring of 1mm radius of the halo detector and the target without touching the INDRA structure. These events are vetoed by the halo detectors and rejected from the event selection.

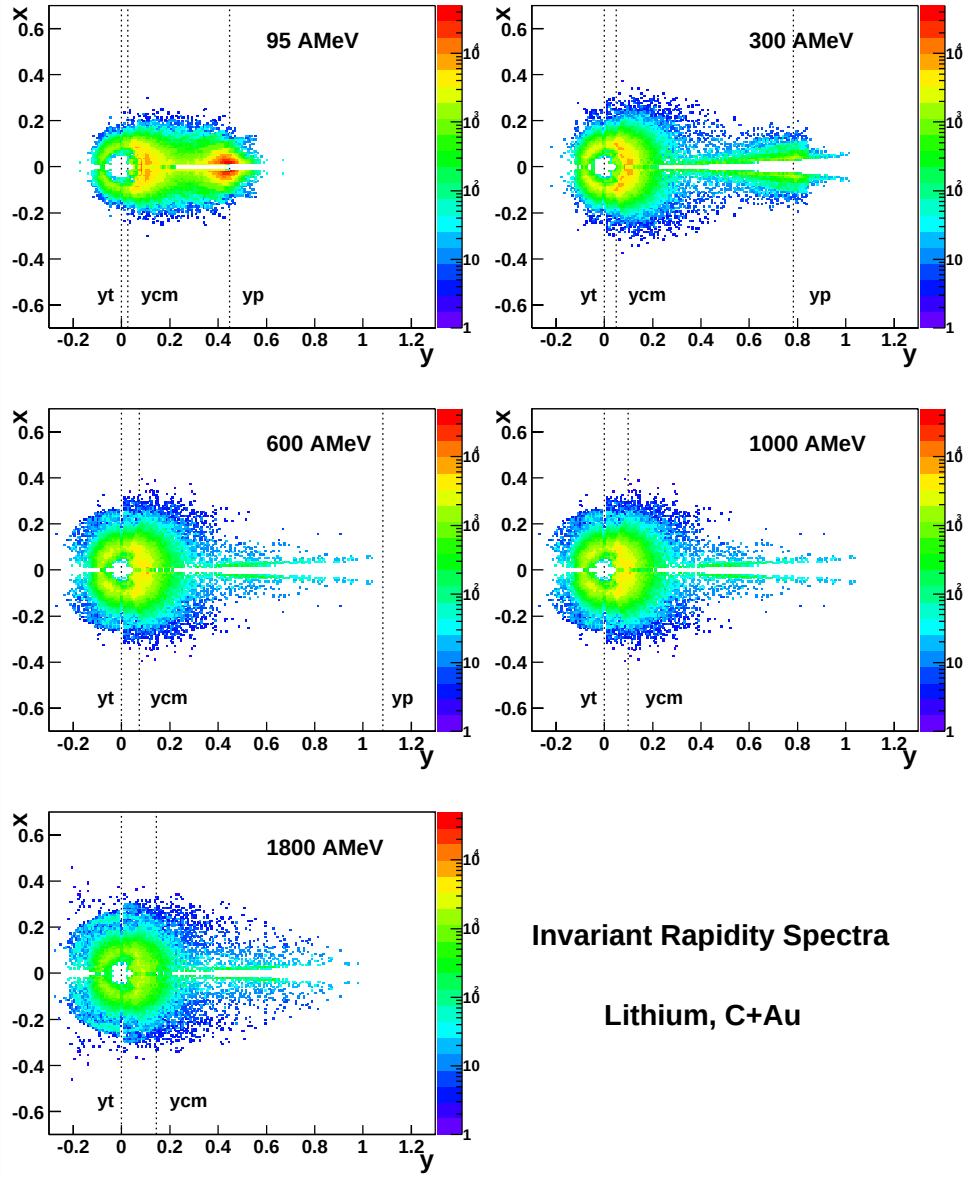

Figure 2.6: *Invariant rapidity spectra of lithium fragments for the reactions C+Au at 95, 300, 600, 1000, and 1800 AMeV (inclusive data). The X-coordinate is the rapidity defined by the equation 2.1, the Y-coordinate is* $x = p_\perp/m$. *The large circle corresponds to the target and the little circle visible for 95 and 300 AMeV is the projectile. The first vertical dotted line from the left indicates the target rapidity 'yt', the second one the rapidity of the center of mass 'ycm', and the third one the projectile rapidity 'yp'.*

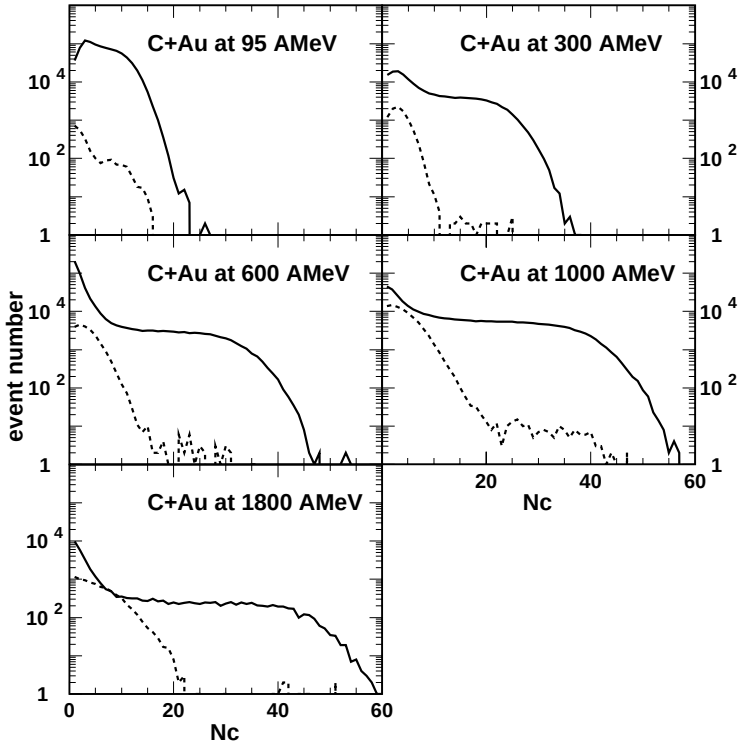

Figure 2.7: *'Good'(full line) and 'halo' (dashed line) event distributions as function of the charged particle multiplicity N_c for the systems C+Au at 95, 300, 600, 1000, and 1800 AMeV.*

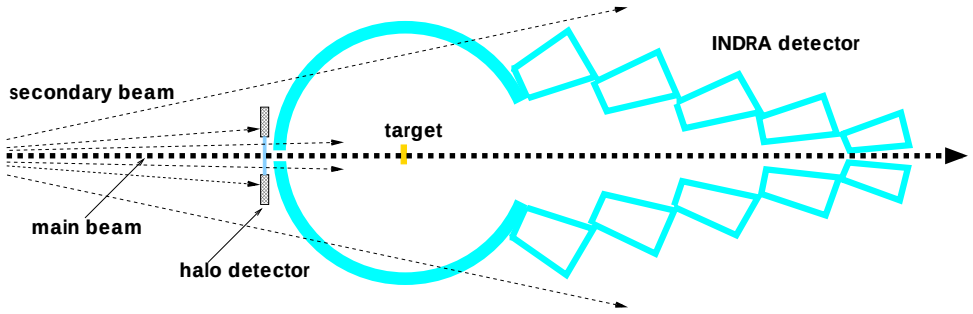

Figure 2.8: *Schematical setup of the INDRA detector with a view of the stray particles punching through the halo detector or directly the backward rings of the detector.*

The beam component coming from scatterings in the beam line is not detected by the halo detectors as it touches mainly the backward rings of INDRA beyond the aluminium structure of the halo detectors (see Fig. 2.8). These stray particles may react with the technical structure or the telescopes themselves. It leads to particle emissions with a low multiplicity and an increasing rate with the increasing beam energy. These particles are light particles and light ions as lithium fragments.

This background is visible in the rapidity spectra of lithium fragments for a carbon beam at the incident energy of 1000 AMeV, as shown in the Fig. 2.9. The left panel corresponds to reactions with a gold target and the right panel to reactions without target. The fifth plot (bottom left) of the both panels presents the peripheral collisions with the reduced impact parameter b/b0=0.8-1.0. The reduced impact parameter is here determined from the charged particle multiplicity according to the selection method explained in the next chapter 4. These plots present in both cases a large circle accompanied by a narrower one for the reactions with a gold target. The large circle corresponds to stray particle effects while the narrow circle comes from reactions in the target.

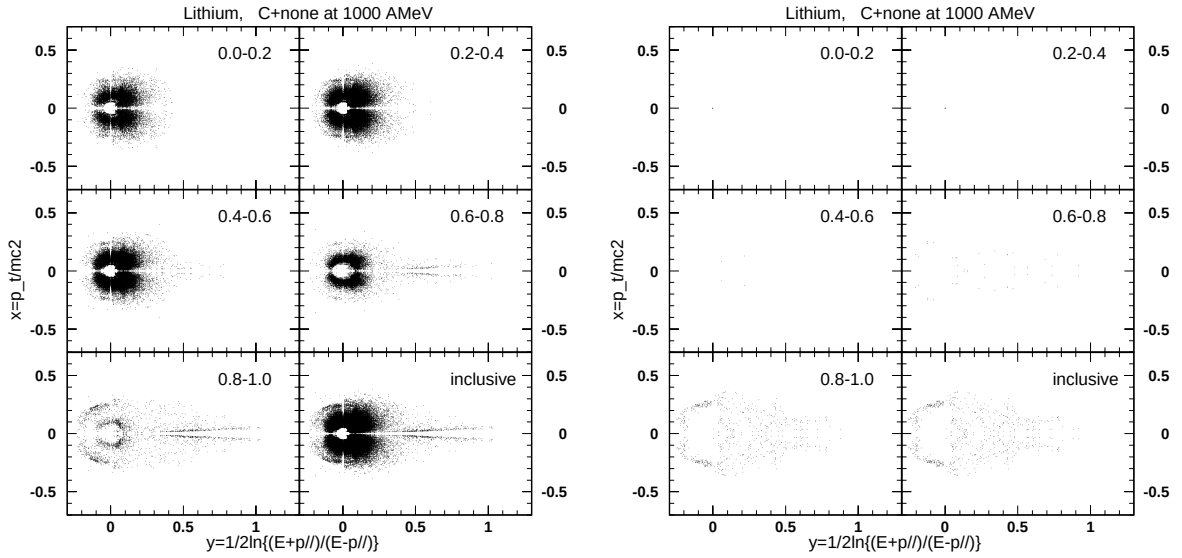

Figure 2.9: *Rapidity spectra of lithium for an incident energy of 1000 AMeV as a function of the reduced impact parameter from central collisions (0.0-0.2) to peripheral reactions (0.8-1.0). The inclusive spectra are also presented. The left panel corresponds to reactions with a Au target and the right panel to reactions without target.*

The case of the lithium fragments allows an easy analysis by cutting the higher energy part of the particles with an appropriate choice of the energy limit. This method will be used for the light ions in the analysis of fragment emission (see chapter 6). For the protons, produced in large quantities by reactions with and without target, the analysis of the most peripheral collisions needs a correction. It can be done by subtraction of the 'no target' spectra from the 'good' spectra with the application of a normalization factor, i.e. the ratio of event numbers counted in the halo detectors in both cases. This technique is usually applied in spectroscopy [Jon01, Jon02]. Fig. 2.10 presents original and corrected proton kinetic energy spectra for very peripheral collisions at $3^o \leq \theta_{lab} \leq 176^o$. The correction lowers the spectra yield by maximum a factor 5 for the backward angles for a kinetic energy close to 100 MeV. The results involving light particles and pions presented in the chapters 5 and 7 are corrected following the procedure indicated above.

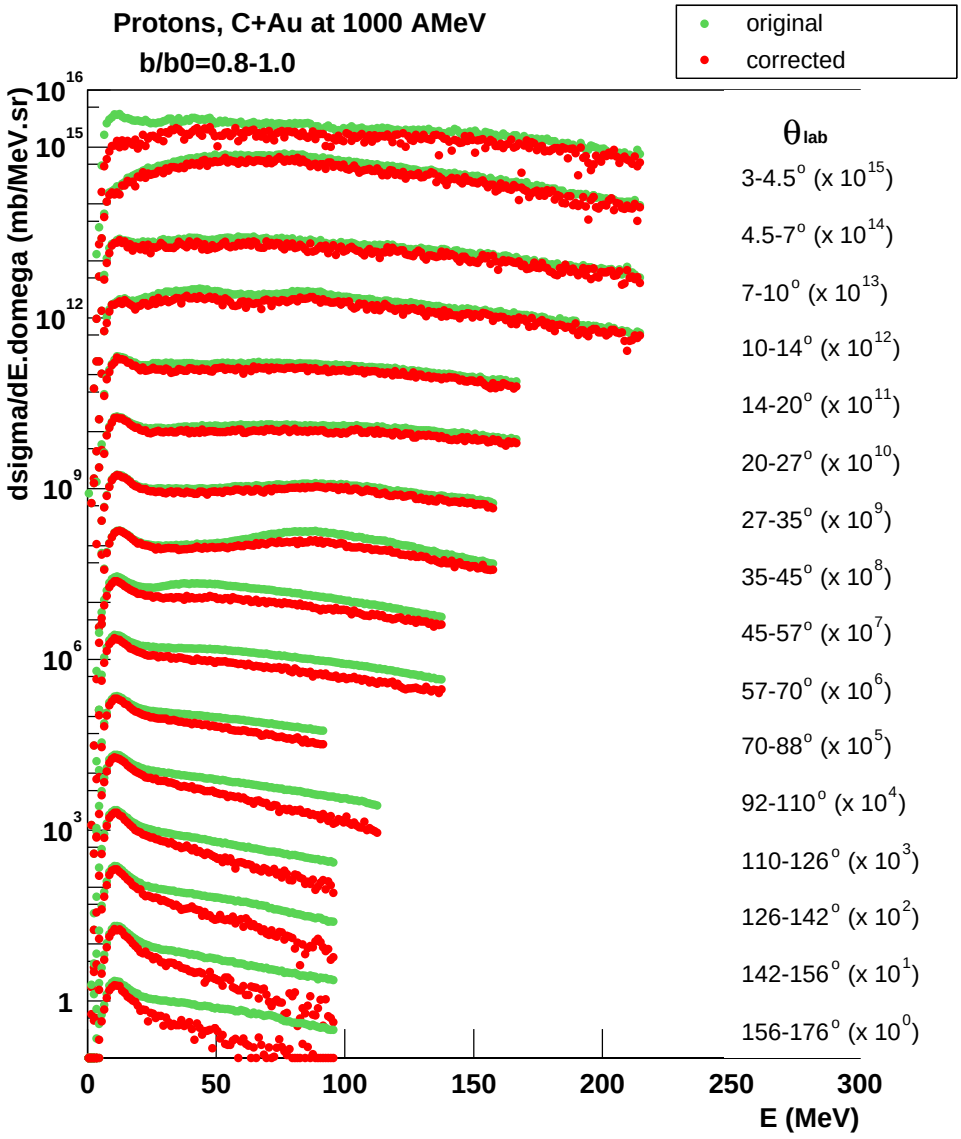

Figure 2.10: *Proton energy spectra for reactions C+Au at 1000 AMeV, original spectra (grey points) and corrected (black points) ones, for peripheral reactions (b/b0=0.8-1.0).*

Chapter 3

Identification and Calibration

This chapter is devoted to the description of the different methods utilised in the INDRA@GSI data reduction to obtain the two most important experimental informations : the particle identification and the energy calibration.

3.1 Identification

Identification in ionisation chambers and silicons

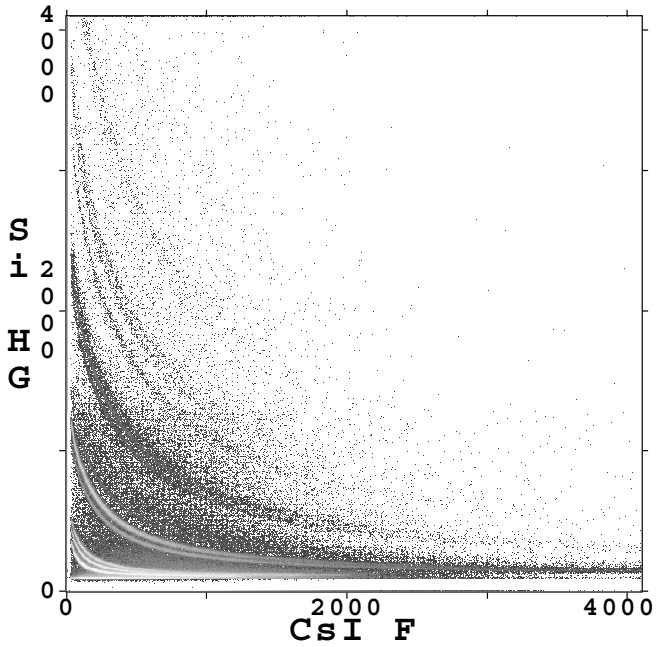

Figure 3.1: *ΔE-E matrix (in channels) obtained with a SiLi-CsI telescope at backward angles, illustrating the achieved isotopic resolution up to lithium. The label 'Si HG' corresponds to the high gain channels of the silicon and the label 'CsI F' to the fast gate of the scintillator [Sai02].*

The identification of particles losing their energy and/or stopping in the first stages of the INDRA telescopes is done following the Bethe-Bloch formula [Bet30, Leo87]:

$$\frac{\Delta E}{\Delta x} \simeq C_1 \frac{AZ^2}{E} log \frac{C_2 E}{A} \tag{3.1}$$

with the energy loss ΔE, the incident energy E, the particle charge and mass Z and A, the detector thickness Δx, and the material constants C_1, C_2.

Knowing its energy loss and incident energy, the charge and mass of a particle punching through a material can be deduced. On a bidimensional diagram $\Delta E \quad vs \quad E$ as Fig. 3.1, each curved 'line' corresponds to a mass and each line group in bands to a charge. In the case of the ionisation chambers, only a charge resolution is available. By this $\Delta E - E$ method, the fragments up to the tin (Z=50) are identified in the ionisation chambers and a part of the light particles and ions, with an isotopic resolution until the boron (Z=5), in the silicons.

Identification in Scintillators

The 336 scintillators of Cesium Iodide of the INDRA detector are devoted to the identification of the light isotopes, up to the charge Z=4.

A particle passing through a scintillator may excite its molecular levels. The deexcitation of these levels corresponds to the emission of a luminous radiation. In the case of the CsI(Tl) crystals, this radiation is separated in two different time constants (Fig. 3.2). The producted light amount $h(t)$ can be approximated by two exponential components :

$$h(t) = h_1 . exp \frac{-t}{\tau_1} + h_2 . exp \frac{-t}{\tau_2} \tag{3.2}$$

with the life time τ_i ($\tau_1 = 0.4 - 0.7 \mu s, \tau_2 = 7 \mu s$) and the intensity of the component h_i.

The total signal is the sum of these two components. The particle identification is done by discrimination of this signal: it is integrated on two time gates, the first from 0 to 390 ns (fast gate), the second from 1590 to 3090 ns (slow gate), as shown in the left panel of Fig.3.2. The combination of these two signals results in a fan-shaped matrix where each straight line corresponds to an isotope (right panel of Fig. 3.2). The identification is done by coding lines on the 'lines' formed by the particles themselves. Fig. 3.3 (left panel) presents, for instance, from the right to the left side, a first line corresponding to the neutral particles (neutrons and gammas which can not be disentangled), the three following are the three hydrogen isotopes coming before the ^3He, ^4He, ^6He, and double ^4He lines. One may remark that the identification in scintillators can become difficult due to imperfections of the crystal. In the fifth ring ($10^o \leq \theta_{lab} \leq 14^o$), for example, some modules show winding hydrogen lines. The CsI detectors provide an isotopic resolution up to the beryllium (Z=4), shown in the right panel of Fig. 3.3.

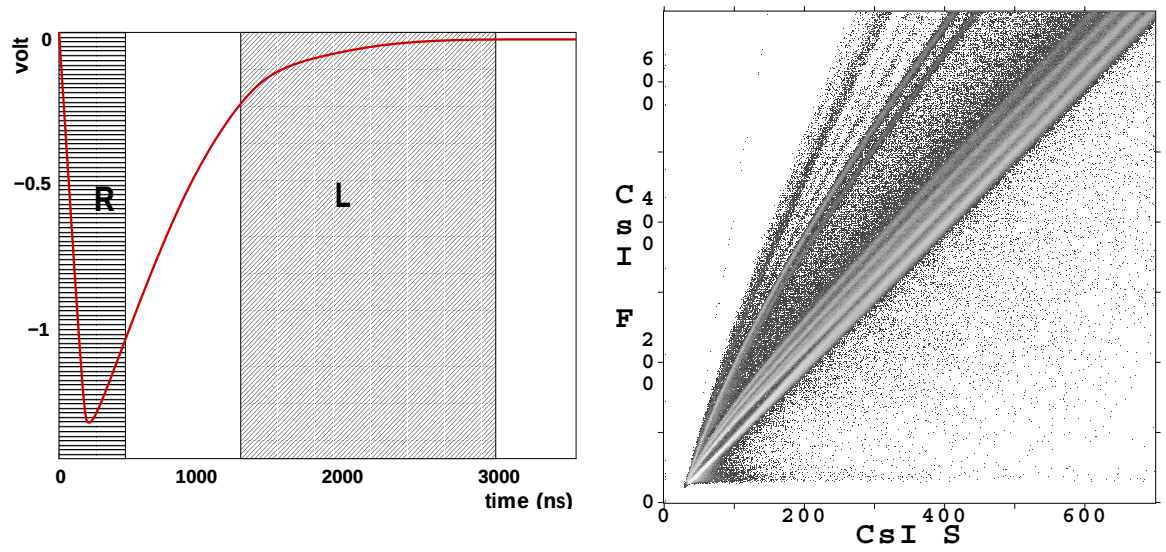

Figure 3.2: *Left panel : CsI signal in Volts as a function of time. The 'R' part corresponds to the fast gate, and the 'L' part to the slow one. Right panel : CsI(fast) versus CsI(slow) identification matrix (in channels) obtained with the two CsI signals in one telescope at* $35^o \leq \theta_{lab} \leq 45^o$ *[Sai02].*

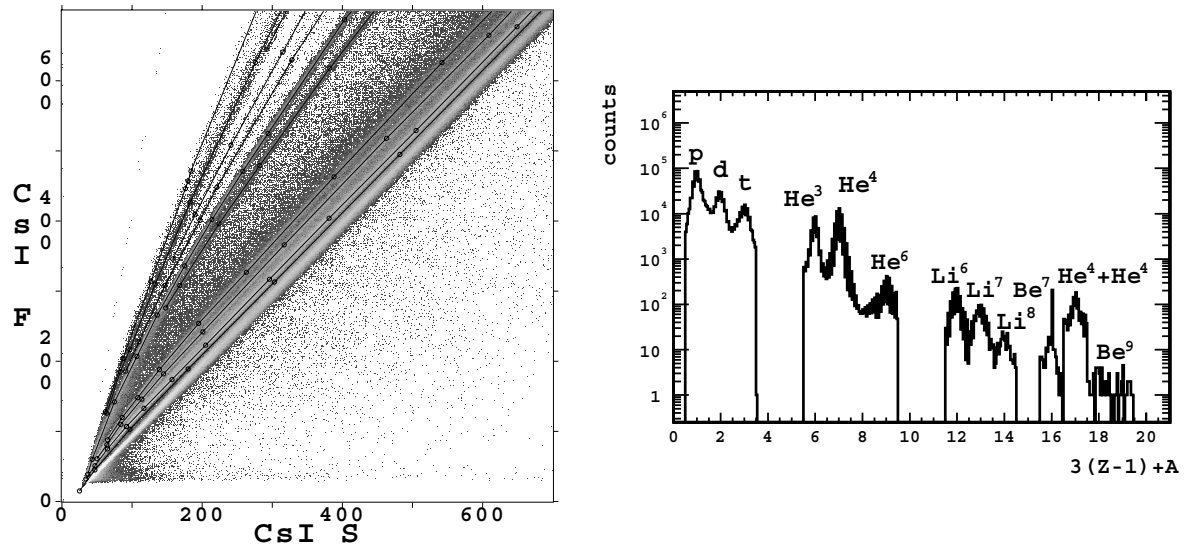

Figure 3.3: *Left panel : CsI(fast) versus CsI(slow) identification matrix (in channels) with identification lines in one telescope at* $35^o \leq \theta_{lab} \leq 45^o$*. Rightpanel : isotopic spectra obtained with CsI(Tl) for a collection of C+Au and C+Sn reactions at all studied energies in the same telescope[Sai02].*

General identification features of the C+Au experiment.

The identification in several stages due to the telescope configuration of the INDRA detector gives a good isotopic identification of the light particles and ions. As exhibited in the left panel of Fig. 3.4, the protons, deuterons, tritons, ^3He's, and ^4He's are well identified in the whole detector from $\theta_{lab} = 2^o$ to $\theta_{lab} = 176^o$. Due to the reaction dynamics, the heavier ions are identified at forward angles ($\theta_{lab} < 90^o$). The main isotope of each species is identified on a wider angular range than the other isotopes. In this picture, the ^8Be's correspond to double ^4He's. These ^4He's punching through the detectors in coincidence are about 50% from the products of ^8Be decay and 50% from accidental coincidences of ^4He's [Stu99]. The charge identification presented in the right panel of Fig. 3.4 points out as well a forward emission of the heaviest fragments. The ions are identified in the whole angular coverage until the colbalt (Z=27).

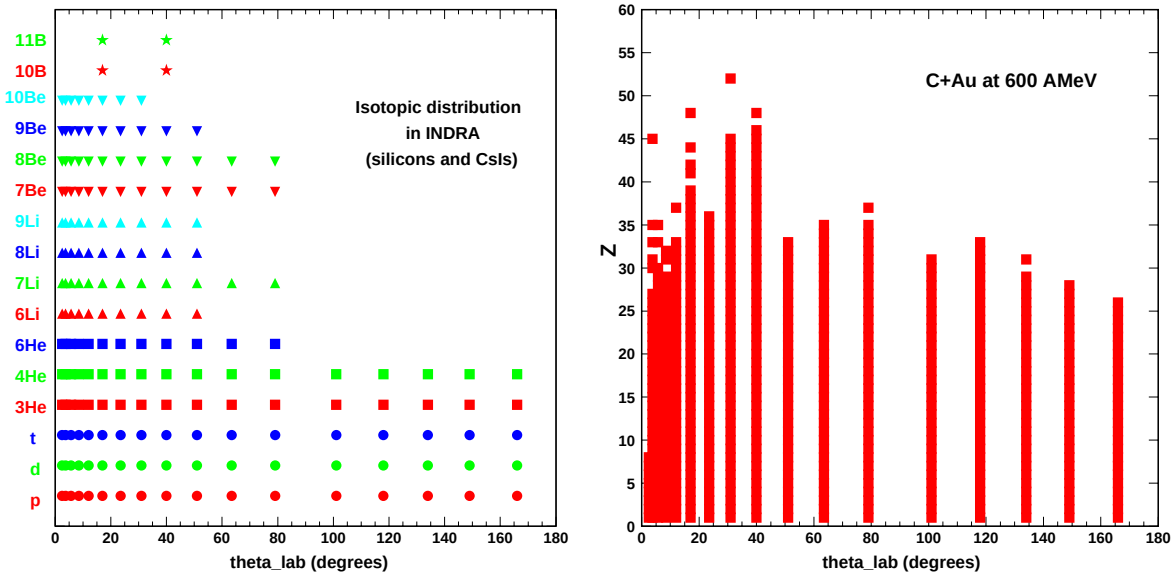

Figure 3.4: *Isotopic (left panel) and charge (right panel) distributions in the INDRA detector as function of the polar angle θ_{lab} for the reaction C+Au at 600 AMeV.*

3.2 Calibration

In this thesis, only the calibration methods for the CsI(Tl) scintillator crystals and the Si-Si-CsI(Tl) calibration telescopes are reported [Luk02].

Scintillators in forward rings ($2^o \leq \theta_{lab} \leq 45^o$)

For the INDRA@GSI campaign, the reaction Xe+Sn at 50 AMeV was measured with the intention to use the existing calibration of the same reaction from the first INDRA campaign in GANIL. In this first campaign, the energies of Z=1,2 particles measured in CsI detectors of rings 2 to 9 ($3^o \leq \theta_l ab \leq 45^o$) were calibrated using the elastically scattered secondary beams of those particles [Pou95, Mar95]. The calibration was based on the fast ('rapide') signal of the CsI detectors and a phenomenological formula relating this fast signal and the energy [Mar95].

The fragments with $Z \geq 3$ measured in CsI detectors of rings 2 to 9 were calibrated using the ΔE in $Si300\mu m$ and range-energy tables [Hub90]. The rings 10 to 17 were calibrated using the calibration telescopes, so-called 'étalons'. The calibration of these telescopes will be treated in the following of the section.

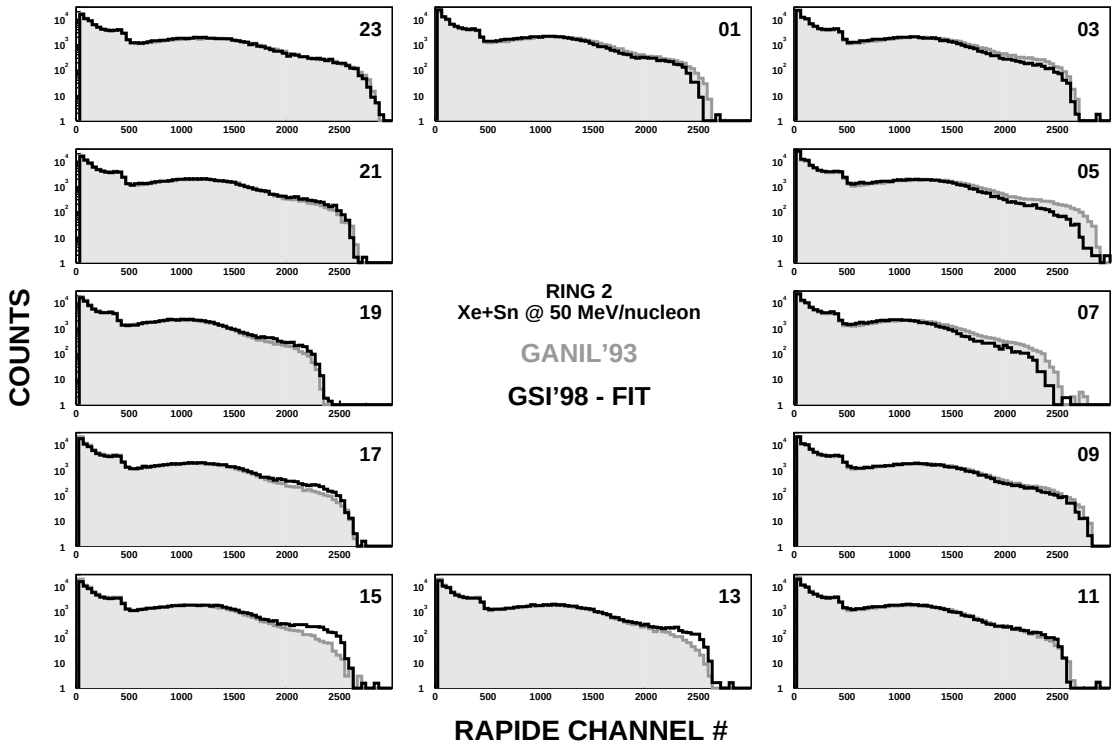

Figure 3.5: *1st and 4th campaign global CsI_r spectra for ring 2 for the system Xe+Sn at 50 AMeV. The spectra contain all the particles detected. the increase at low channels corresponds to Z=1,2. The spectrum of the module 1 are at the top middle, the spectra are organised following the clock way [Luk02].*

In order to use the first campaign calibration for Z=1,2 in the rings 2 to 9, the global fast signal spectra of the INDRA@GSI campaign are fitted to those of the first campaign as it is shown in Fig. 3.5. The gain factors obtained from the fitting procedure make possible the use of the first campaign calibration parameters directly to INDRA@GSI. This 'scaled calibration' constitutes the reference to obtain the calibration based on the relation between the total light and the energy loss [Par00]:

$$L = a_1 E_0[1 - a_2 \frac{AZ^2}{E_0} ln(1 + \frac{1}{\frac{AZ^2}{a_2 E_0}})] + a_4 a_3 AZ^2 ln(1 + \frac{E_0}{E_\delta + a_2 AZ^2})$$

with the light L, the particle energy E_0, the particle mass and charge A, Z, the inverse of the gain adjusted for each module using the first campaign data a_1, the Birks parameter, which varies from one module to an other a_2, the δ-ray production energy threshold $E_\delta = a_3 E_0$, and the fraction of deposited energy a_4.

This formula, so-called 'Pârlog-Tabacaru' formula, has a big advantage as compared to the phenomenological formula of the first campaign because, in principle, it enables to extrapolate the calibration of Z=1,2 also for IMF's ($3 \leq Z \leq 30$) and heavy fragments. The calibration of energies of fragments using total light improves considerably the energy resolution of energetic fragments as compared to the method based on the energy loss in $Si300\mu m$ and the range-energy tables.

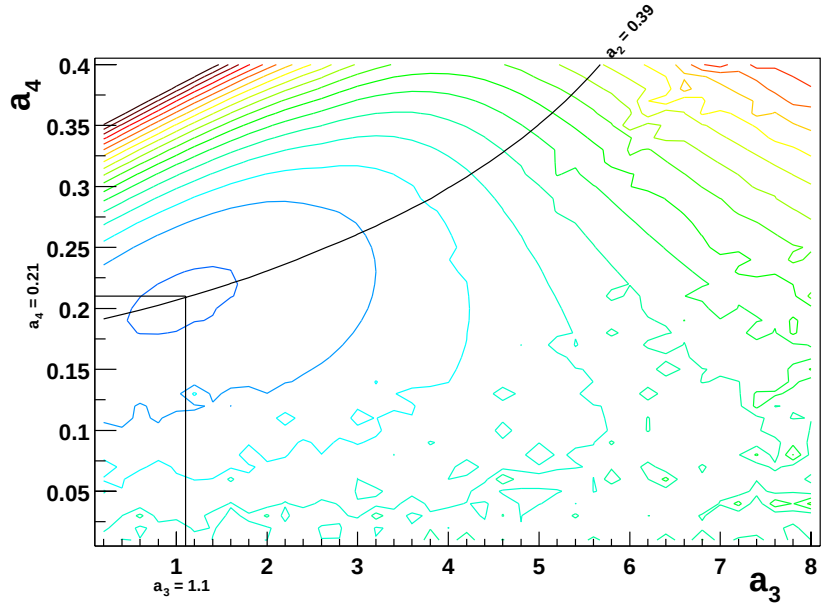

Figure 3.6: *Fit 3rd-4th campaigns: the parameters a_2, a_3, and a_4 are adjusted in order to correspond to a minimum in the distribution (on the χ^2 matrix: the intersection of the two straight lines) with the standard guess of $a_2 = 0.39$. In this case, $a_3 = 1.1$ and $a_4 = 0.21$ [Luk02].*

The parameters a_3 and a_4 of the 'Pârlog-Tabacaru' formula are found using the third INDRA campaign calibration data [Chb01]: energies of elastic peaks of isotopically resolved Z=1 to 6 species and corresponding values of the total light. Fig. 3.6 presents the result of a grid search for the parameter a_3 and a_4 for modules of the rings 2 to 6. The minimum of the mean χ^2 is used as a 'standard' one in case it was not known from the previous campaigns. The parameter a_1 is adjusted for each module of the rings 2 to 9 by fitting the energy spectra of p, d, t and ^4He particles calibrated using the 'Pârlog-Tabacaru' formula to those calibrated by the 'scaled calibration'. Five different sets of a_1 parameters are necessary for p, d, t, ^{3}He, and ^{4}He and heavier fragments even though a_2 should take care of the mass and charge dependence. The ring 1 is calibrated using the spectra of the ring 2.

In order to check the predictive power of the 'Pârlog-Tabacaru' formula for heavier fragments, the theoretical $\Delta E - E$ lines generated using the formula, the $Si300\mu m$ calibration, and the Hubert range-energy tables for consecutive atomic numbers, are compared to the experimental ones. The left panel of Fig. 3.7 shows the generated lines (dotted lines) superimposed on the identification lines (solid lines) for charges up to Z=54 in steps of $\Delta Z = 2$. The right panel presents the 'theoretical' $\Delta E - E$ lines on top of the experimental data (Xe+Sn reactions at 50

to 250 AMeV). The lines connecting the big solid circles correspond to the fragments of given Z with the beam energy per nucleon. As it can be seen, the 'Pârlog-Tabacaru' formula reproduces well the experimental data up to Z=20-25. For heavier fragments, its predictive power gets worse.

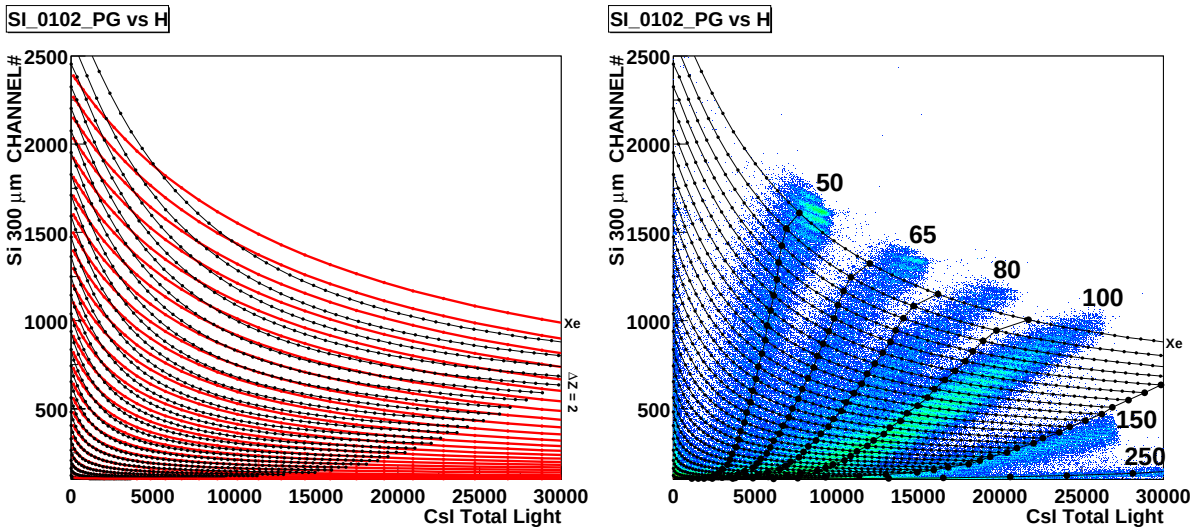

Figure 3.7: *First check of calibration with the Pârlog formula with Si(300 µm)-CsI matrices. The silicon coordinate is in channel and the CsI one in total light according to Pârlog formula. The left panel is a comparison between identification (full lines) and calibration (dotted lines). The right panel compares the calibration lines to the Xe+Sn data at 50, 65, 80, 100, 150 and 250 AMeV [Luk02].*

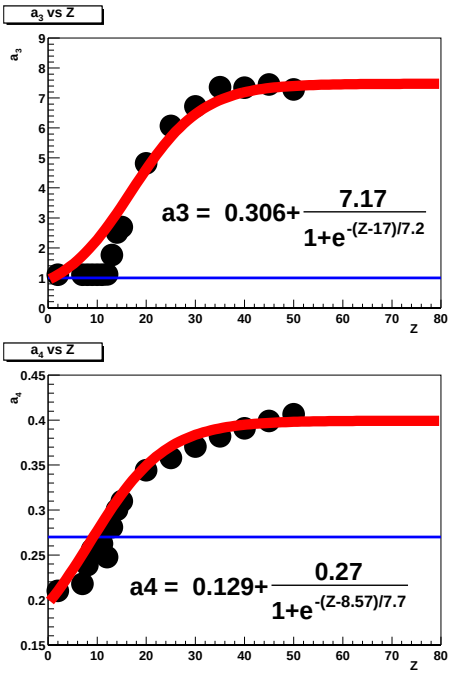

Figure 3.8: *The corrected parameters a_3 and a_4 as functions of the charge Z. The points correspond to data (Xe+Sn at 50 AMeV) and the full line to the parametrization of a_3 and a_4. The formulae of this parametrization are given in the respective panel [Luk02].*

In order to improve the energy calibration of heavier fragments, it is proposed to make the parameters a_3 and a_4 dependent of Z (Fig. 3.8), using the following phenomenological formulae:

$$a_3 = 1.1 - \frac{p_{30}}{1 + exp(\frac{-(2-p_{31})}{p_{32}})} + \frac{p_{30}}{1 + exp(\frac{-(Z-p_{31})}{p_{32}})}$$

$$a_4 = 1.1 - \frac{p_{40}}{1 + exp(\frac{-(2-p_{41})}{p_{42}})} + \frac{p_{40}}{1 + exp(\frac{-(Z-p_{41})}{p_{42}})}$$

with $p_{30} = 7.17$, $p_{31} = 17$, $p_{32} = 7.2$, $p_{40} = 0.27$, $p_{41} = 8.57$, and $p_{42} = 7.7$.

The final fit, with a_3 and a_4 as functions of Z, is presented in the figure 3.9, also for the Xe+Sn from 50 to 250 AMeV beam energy. The calibration and identification lines show a much better agreement at high Z. As the reference system was Xe+Sn at 50 AMeV, the other systems and energies were calibrated by scaling to the reference spectra. This scaling was performed separately for each ring from ring 2 to 9. The other systems and energies studied during the INDRA@GSI campaign are calibrated using the homothetie scaling of the fast-low CsI spectra and laser corrections.

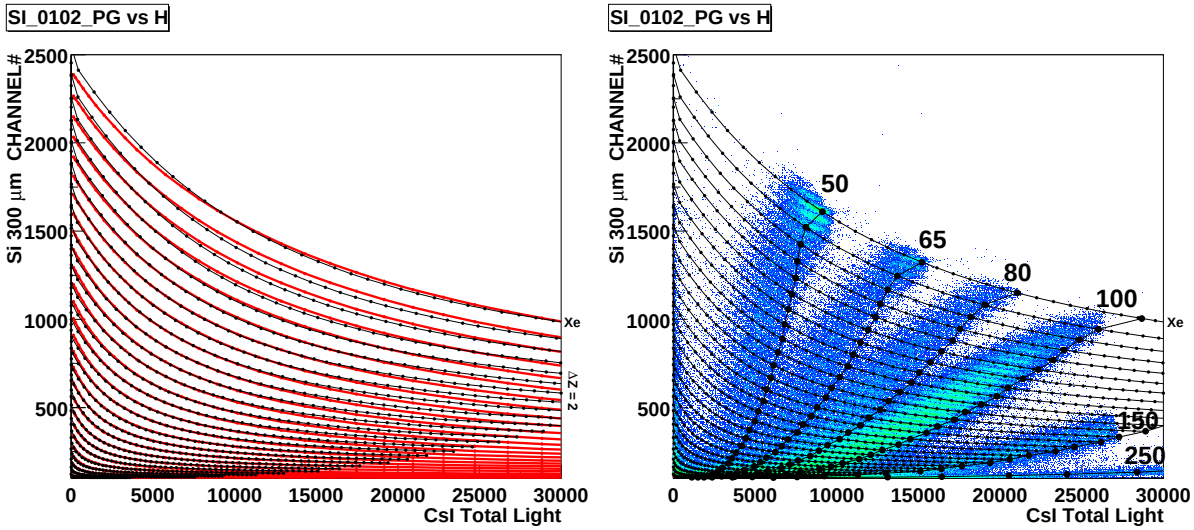

Figure 3.9: *Final check of the calibration with the Pârlog formula, after parametrization of a_3 and a_4 as functions of Z. The left panel is a comparison between identification (full lines) and calibration (dotted lines). The right panel compares the calibration lines to the Xe+Sn data at 50, 65, 80, 100, 150 and 250 AMeV [Luk02].*

Scintillators and calibration silicons in backward rings ($45^o \leq \theta_{lab} \leq 176^o$)

For the rings 10 to 17 ($45^o \leq \theta_{lab} \leq 176^o$), the calibration was done using the Si-Si-CsI(Tl) calibration telescopes.

Calibration of Si75 and Si(Li) detectors

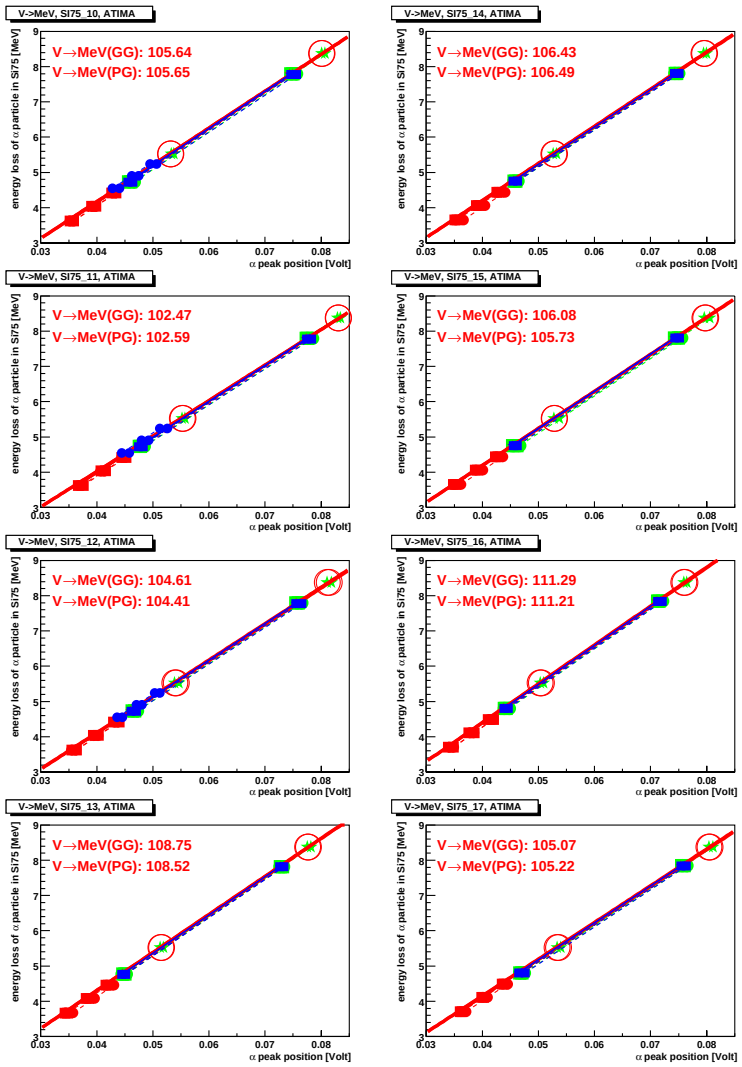

Figure 3.10: *Volt→MeV factors determined from the α and 'Thoron' sources (see text for legend). Each panel corresponds to one ring, from ring 10 (top left) to ring 17 (bottom right). The factors for high (GG) and low (PG) gains are indicated in each panel [Luk02].*

The energy calibration of Si75 detectors was carried out with two different sources: a 'Thoron' source with two peaks given by the decay products of ^{212}Pb (^{212}Bi 6.06 MeV, ^{212}Po 8.78 MeV) and a alpha source with three peaks (^{239}Pu 5.15 MeV, ^{241}Am 5.48 MeV, ^{244}Cm 5.79 MeV). Fig. 3.10 shows the factors Volt→MeV determined with the two α sources for the eight Si75 detectors.

The factors channel→Volt were found out with the so-called automate runs. During these special runs, the amplitude of the pulser was modified by steps in order to check the linearity of the silicon detectors and the associated electronics. The calibration runs were performed with and without gas, that is why there are different energy losses and positions of peaks for the same source. There are also superimposed results of high (GG) and low (PG) gains. The first three groups of symbols at lowest energies correspond to three peak source measurements made with gas. The circles at low energies for rings 10-12 correspond to measurements with 3 peak source without gas. The pairs of symbols at high energies correspond to measurements done with the 'thoron' source with or without gas. Only the measurements without gas made with the use of the 'thoron' source were taken to calibrate the SI75 (big circles and stars) to avoid additional uncertainties due to energy loss and straggling in the gas and to avoid non-linearities at low energies. The thick lines are the results of the fit to the measurements with the 'thoron' source with and without gas. The energy losses in the mylar foils of the chambers were taken into account.

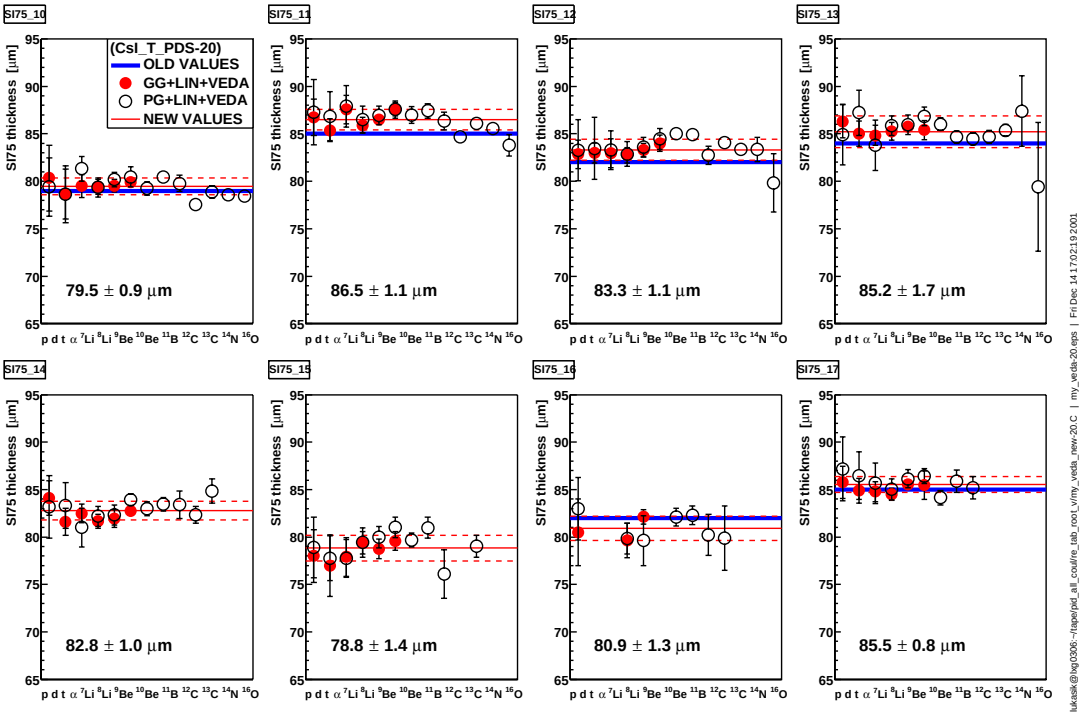

Figure 3.11: *Thickness of the silicon Si75 for each ring, determined from α source runs. One compares in these panels the thickness values measured in previous campaigns when they exist (thick full lines), the new values (thin full lines), and the values used to calculate the new values coming from low (PG, empty circles) and high (GG, full circles) gain with the use of VEDA energy loss tables. The thickness values are indicated in each panel [Luk02].*

The Si75 thickness values were resolved from the α source runs. The punch-through energies for species from the protons to the oxygens were determined from their channel position and the α source calibration. These energies were used to resolve the particle range using the VEDA energy loss tables. The thicknesses deduced from these ranges were compared to values from

previous campaigns, as it is shown in Fig. 3.11, for low and high gain ('petit' gain (PG) and 'grand' gain (GG)). The Si75 thickness values for the INDRA@GSI campaign are slightly higher than for previous experiments, except at $142^o \leq \theta_{lab} \leq 176^o$. This may be due to the evolution of the silicons with the time. The following step of the calibration process was the SiLi calibration. The SiLi thickness was taken from previous INDRA campaign values [Gen99].

CsI Calibration

The first stage of CsI calibration was the construction of 'residual' reference spectra for Z=1,2 particles punching through Si(Li), knowing their residual energies. The fits used also the Pârlog formula (see section 3.2). A double check with Si(Li) versus CsI(light) matrices was needed to verify the quality of the calibration. This last point permitted the production of 'full' reference spectra of particles that do not hit the silicons. The calibration of the other modules of each ring was realized by scaling to "full" reference spectra. For the other energies for the same system of Xe+Sn, the calibration was achieved with laser correction. For the other systems, Au+Au and C+Au, it was necessary to apply homothetie factors coming from a scale of identification maps.

A control of the calibration for the INDRA@GSI campaign is performed with the energy scale calibration of the CsI crystals for $14^o \leq \theta_l ab \leq 88^o$ using elastic and inelastic C+$(CH_2)_n$ scattering at E_{beam}= 30 AMeV. The gain parameter of the calibrationis then obtained by fitting the proton total charge spectra to the spectra predicted with Monte-Carlo simulations. At this angular range, for the protons, this second method of calibration is in agreement with the 'Xe+Sn' calibration within 4% [Trz02].

The data reduction operated via the identification and the calibration was the first step of the analysis. It will allow us in the next chapter to study the question of the centrality selection.

More informations about the identification methods in the different detectors of INDRA can be found, concerning ionisation chambers-silicons in the rings 2 to 9, in the PhD thesis of L. Nalpas, J.D. Frankland, and S. Hudan [Nal97, Fra98, Hud01]; for the ionisation chambers-cesium iodides, in the PhD thesis of L. Nalpas and N. Bellaize [Nal97, Bel00]; for the CsI detectors, forward rings, in the PhD thesis of A. Le Fèvre [Lef97], and the backward rings, in the PhD thesis of E. Genouin-Duhamel, N. Le Neindre, A. Saija [Gen99, Len99, Sai02].

Complementary presentations of calibration methods are given, for the ionisation chambers-silicons, in the PhD thesis of L. Nalpas [Nal97]; for the ionisation chambers-CsI detectors, in the PhD thesis of L. Nalpas and N. Bellaize [Nal97, Bel00]; for the CsI detectors, forward rings, in the PhD thesis of F. Lavaud [Lav01], and backward rings, in the PhD thesis of N. Marie and E. Genouin-Duhamel [Mar95, Gen99].

Chapter 4

Centrality Selection

In most experiments, the information about the centrality of the collision is extracted from quantities which relate to the collision geometry via simple intuitive pictures. Many impact parameter filters represent some measure of the 'violence' of the reaction which, in turn, is assumed to be related to the collision geometry. Common impact parameter filters are based upon the measured multiplicity of charged particles, the transverse energy, or the summed charge of particles emitted at intermediate rapidity [Sch78, Rit88, Ogi89, Cav90]. For collisions with incident energies of a few hundred MeV per nucleon (until 1 AGeV), the summed charged, Z_{bound}, of particles with atomic number $Z \geq 2$ [Hub91] has also been used. This quantity is the complement of the combined p, d, and t multiplicity.

Various more sophisticated methods have been developed in the last years and applied to data from different INDRA experiments like the Principal Component Analysis [Bel00, Lav01], the neuronal network [Bou01] or the discrimination of single-source events [Mas99, Des00].

A priori, it is unclear whether these various techniques select similar or equivalent impact parameters or one technique provides superior resolution as compared to another. At low and intermediate energies, cross-calibrations have been performed between the different impact parameter filters [Gal86, Tsa89, Pha92].

In this chapter, we will continue this study at relativistic energies. In this aim, we will follow a similar analysis than the one of L. Phair and coworkers [Pha92] and explore first the relation between impact parameters based on the charged particle multiplicity N_C, the multiplicity of hydrogen isotopes N_1, the total transverse kinetic energy of detected charged particles E_t, and the mid-rapidity summed charge Z_y. In a such experiment as the INDRA@GSI, in which as well symmetric and asymmetric systems were studied on a wide range of beam energy, a second question emerges: the sensitivity of these four quantities to system symmetry and incident energy.

4.1 Definition of impact parameter filters

In the following, we define some quantities:

1) *The charged particle multiplicity* N_C. This quantity includes all charged particles detected by the INDRA detector. Multihits in a single detector module are counted as single hits. The number N_C is therefore equal to the number of detectors in which at least one charged particle is detected in a given event.

2) *The identified hydrogen multiplicity* N_1. This quantity is defined as the number of detectors in which a Z=1 particle is identified for a given event.

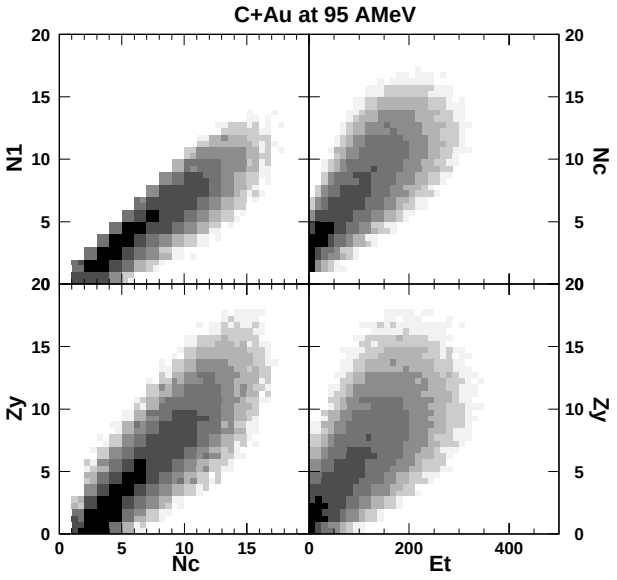

Figure 4.1: *Correlations between charged particle multiplicity* N_C*, identified hydrogen multiplicity* N_1*, transverse energy* E_t*, and intermediate rapidity charge* Z_y *observed for C+Au collisions at 95 AMeV.*

3) *The total transverse kinetic energy of identified particles* E_t. This quantity is defined as [Tsa91]:

$$E_t = \sum_i \{m_i * \sqrt{1 + (p_i sin\theta_i)^2/m_i^2} - 1\} \tag{4.1}$$

with the kinetic energy E_i, the momentum p_i, the mass m_i, and the emission angle θ_i of the particle i with respect to the beam axis.

In the following chapter, the total transverse kinetic energy of all identified particles is used in order to perform a study in the same way as L. Phair and coworkers [Pha92]. In previous studies of the INDRA collaboration, the total transverse kinetic energy of hydrogen and helium isotopes, E_{t12}, is prefered due to the energy thresholds of the detector for heavier fragments [Luk97, Boc00, Met00, Pla00].

4) *The mid-rapidity summed charge* Z_y. This quantity is defined [Ogi89] as the summed charge of all identified particles of rapidity y with:

$$0.25y_{cm} \leq y \leq 0.75y_{proj} + 0.25y_{cm}$$

Here, quantities are defined in the laboratory frame of reference. y_{cm} and y_{proj} denote the rapidities of the total center-of-mass system and of the projectile, respectively. These limits in rapidity are used in this way by L. Phair and coworkers in order to select the mid-rapidity emissions. The rapidity y of a particle is defined [Gol78] as:

$$y = \frac{1}{2} ln \frac{E_{tot} + p_{//}}{E_{tot} - p_{//}} = tanh^{-1}(\beta_{//}) \tag{4.2}$$

with the total energy of the particle E_{tot}, the longitudinal impulsion $p_{//}$, and the longitudinal velocity $\beta_{//}$.

Fig. 4.1 shows the measured correlations between the quantities N_C, N_1, E_t, and Z_y. The four quantities are strongly correlated as an increase in the value of one observable is accompanied by an increase in the value of the other three observables. From this observation, one may already conclude that all four quantities are suitable for impact parameter selection, or none: as it is sketched in Fig. 4.2, the global variables can be correlated through the impact parameter or directly. If they are correlated directly, the comparison of the different methods will just let appear the so-called autocorrelation between variables and not their correlation to the impact parameter.

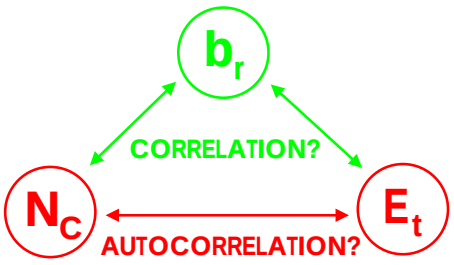

Figure 4.2: *Possible correlations between global variables and reduced impact parameter.*

In order to provide an approximate scale for the impact parameter, we adopt the geometrical prescription of C. Cavata and coworkers [Cav90]. For each of the quantities N_C, N_1, E_t, and Z_y, we assume a monotonic relationship to the impact parameter and define the reduced impact parameter scale by:

$$b(X)/b_{max} = b_r(X) = \left\{ \int_X^{\infty} \frac{dP(X')}{dX'} dX' \right\}^{1/2} \tag{4.3}$$

with the normalized probability distribution dP(X)/dX for the measured quantity X = N_C, N_1, E_t, Z_y, and the maximum impact parameter b_{max} for which particles are detected in INDRA.

In the following, we will use the reduced impact parameter scale b_r which ranges from b_r=1 for peripheral collisions to b_r=0 for central collisions.

4.2 Model predictions

The predictions of the transport model BQMD (Bohnet Quantum Molecular Dynamics, see Appendix A.3) are processed through a simple geometrical INDRA filter (constant θ bin for each ring and constant ϕ bin for each module), taking into account the energy threshold $E > 5$MeV.

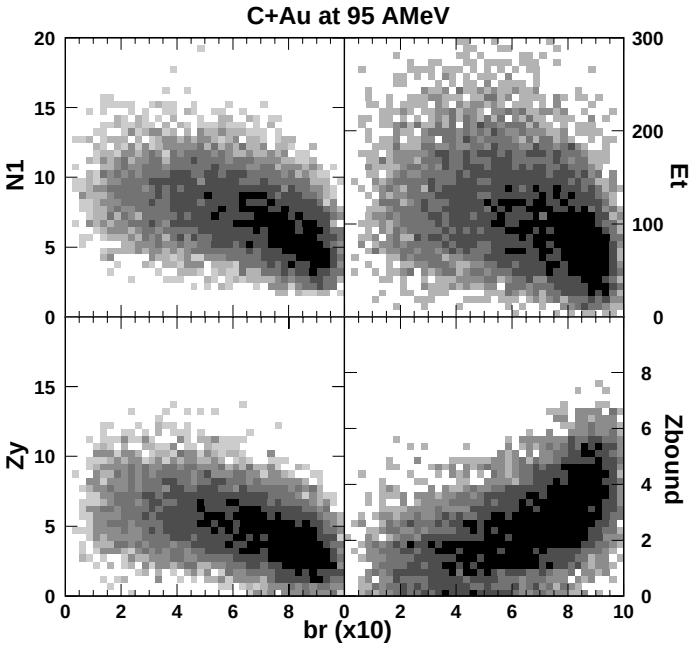

Figure 4.3: *BQMD predictions for C+Au reactions at 95 AMeV for the global variables N_1, E_t, Z_y, and Z_{bound} as functions of the reduced impact parameter br. Selection of the carbon projectile by a cut in rapidity y ≥ 0.75.*

As demonstrated in Fig. 4.3, 4.4, and 4.5, the sensitivity of the global variables N_1, E_t, Z_y, and Z_{bound} ($\sum Z$ with $Z \geq 2$) to the reduced impact parameter b_r is increasing with the symmetry of the system and the incident energy. The distributions of these four variables are narrower for Xe+Sn collisions at 50 AMeV than for C+Au at 95 AMeV. The correlation is stronger for the most symmetric system even if the beam energy for Xe+Sn is smaller. Similarly, the correlation is more pronounced for the C+Au reactions at 600 AMeV than at 95 AMeV. The strength of the correlation between global variables and impact parameter depends on the produced number of particles: a large number of particles allows a finer determination of b_r since the role of particle number fluctuations is reduced. As a consequence, the large multiplicity range leads also to relatively broad distributions in energy or charge. In Xe+Sn collisions at 50 AMeV, due to the number of nucleons in each nucleus, a lot of particles are emitted, also in C+Au reactions at 600 AMeV, this time because of the higher incident energy. The produced number of particles depends also on the geometry of the collision. This number will increase with the centrality of the collision as more and more nucleons are involved in the participating region.

In the next sections, we will expand the study of global variables to experimental data. As the model predicts a broad distribution for C+Au collisions at 95 AMeV, the choice of the best global variable for this asymmetric system at quite low beam energy seems a bit difficult.

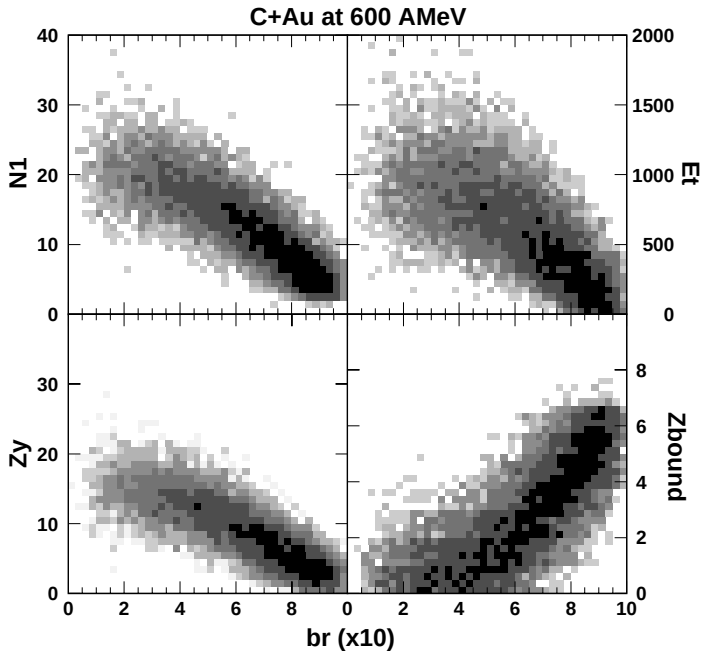

Figure 4.4: *BQMD predictions for C+Au reactions at 600 AMeV for the global variables N_1, E_t, Z_y, and Z_{bound} as functions of the reduced impact parameter br. Selection of the carbon projectile by a cut in rapidity $y \geq 0.75$.*

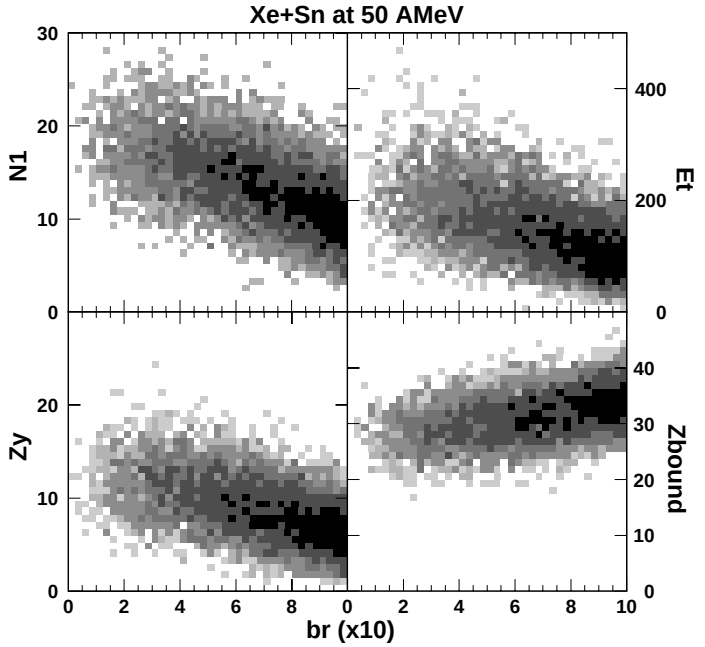

Figure 4.5: *BQMD predictions for Xe+Sn reactions at 50 AMeV for the global variables N_1, E_t, Z_y, and Z_{bound} as functions of the reduced impact parameter br. Selection of the xenon projectile by a cut in rapidity $y \geq 0.75$. At 50 AMeV, the Xe+Sn system does not reach the vaporisation regime and produces many fragments in central collisions.*

4.3 Impact parameter sensitivity

In order to investigate the relation between impact parameter scales extracted via the equation 4.3 from the various measured observables, we have set narrow gates on parameters $b_r(X)$, defined by means of an observable X, and determined the conditional distributions of impact parameters $b_r(Y)$, constructed from different observables Y ($X, Y = N_C, N_1, E_t, Z_y \quad Y \neq X$).

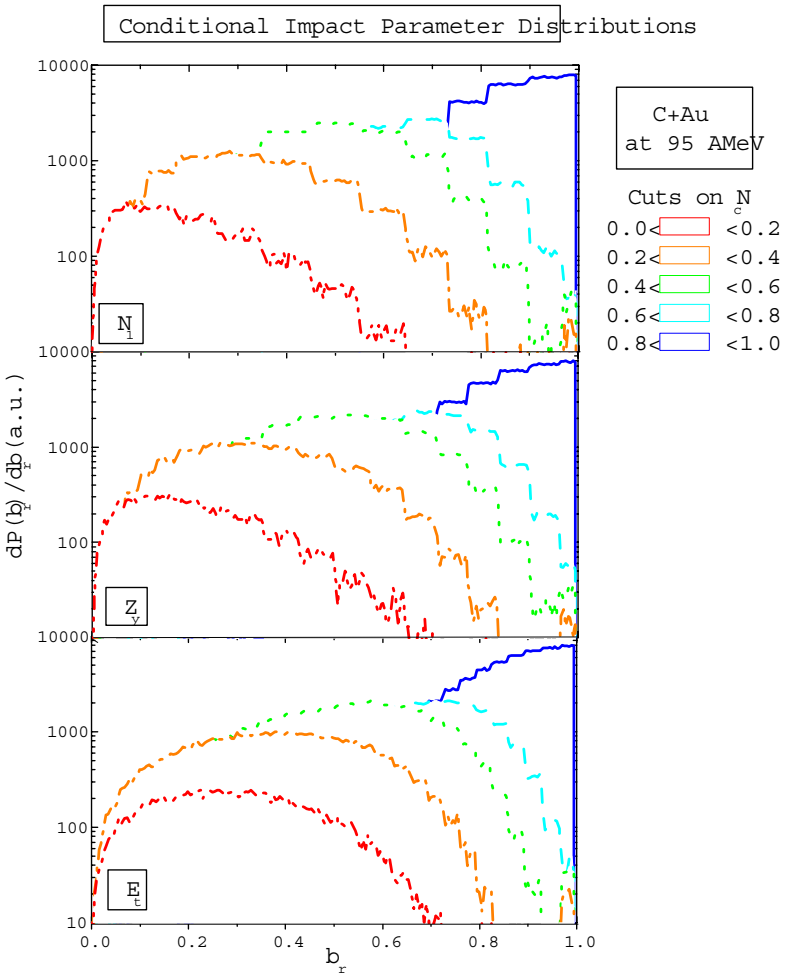

Figure 4.6: *Conditional impact parameter distributions for C+Au collisions at 95 AMeV for the global variables N_1, Z_y, and E_t. The distributions going from the left to the right and from the front to the back of the pictures correspond to five bins of the reduced impact parameter determined with N_c, from the most central (0.0-0.2) to the most peripheral (0.8-1.0).*

Fig. 4.6 presents the conditional impact parameter distributions of N_1, Z_y, and E_t for C+Au reactions at 95 AMeV for five gates on $b_r(N_C)$. These five gates were chosen to be from b_r=0.0 to b_r=1.0. These conditions on N_C give wide distributions as for $b_r(N_1) \simeq 0.0 - 0.6$ for $b_r(N_C) = 0.0 - 0.2$. Moreover the distributions are not well separated, suggesting, as predicted by BQMD calculations, a weak correlation between the four global variables for C+Au at 95 AMeV.

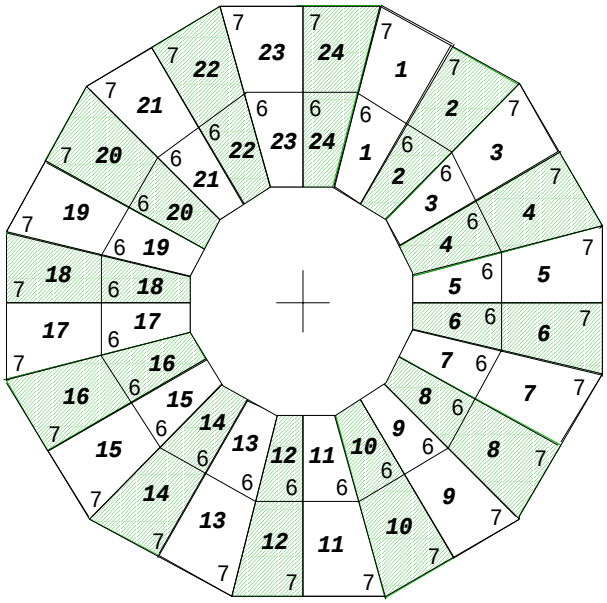

Figure 4.7: *Schematic view of the rings 6 and 7 with module arrangement. The module numbers are indicated in bold face, the even number modules are dashed, the odd number modules white.*

Conditional impact-parameter distributions for very central collisions ($b_r(X) = 0.0 - 0.1$) are presented in Fig. 4.8, 4.9, and 4.10 for the three studied systems : C+Au at 95 and 600 AMeV, and Xe+Sn at 50 AMeV. Left- and right-hand panels show distributions extracted from all the data and for even-odd separated data, respectively. In order to avoid autocorrelations (like between N_1 and N_C), we separate the data in two groups in the following way: all the modules of INDRA with an even number are in a first group denoted 'even' and, in a second one denoted 'odd', all the modules with an odd number (see Fig. 4.7). In this way, the data are cut in two equal parts with the same angular distribution and the possible autocorrelations between the global variables are destroyed. The gates are applied on one group (odd) and the distribution of the other group of data (even) is observed.

For the C+Au reactions at 95 AMeV, as the number of hydrogens N_1 is part of the sum over the charged particles N_C, there is a strong autocorrelation between both variables for the full data (first and second left panels, from the top of the Fig. 4.8). Z_y presents also a correlation with N_C (first and third left panels, from the top), but E_t is not correlated with any of the three other variables as demonstrated by the broad distributions of the fourth left panel. Moreover, the even-odd method gives very broad distributions with a mean value of $b_r \simeq 0.6$ for gates at $b_r < 0.1$. This result confirms the previous observation with gates on N_C only but from central to peripheral collisions (see Fig. 4.6).

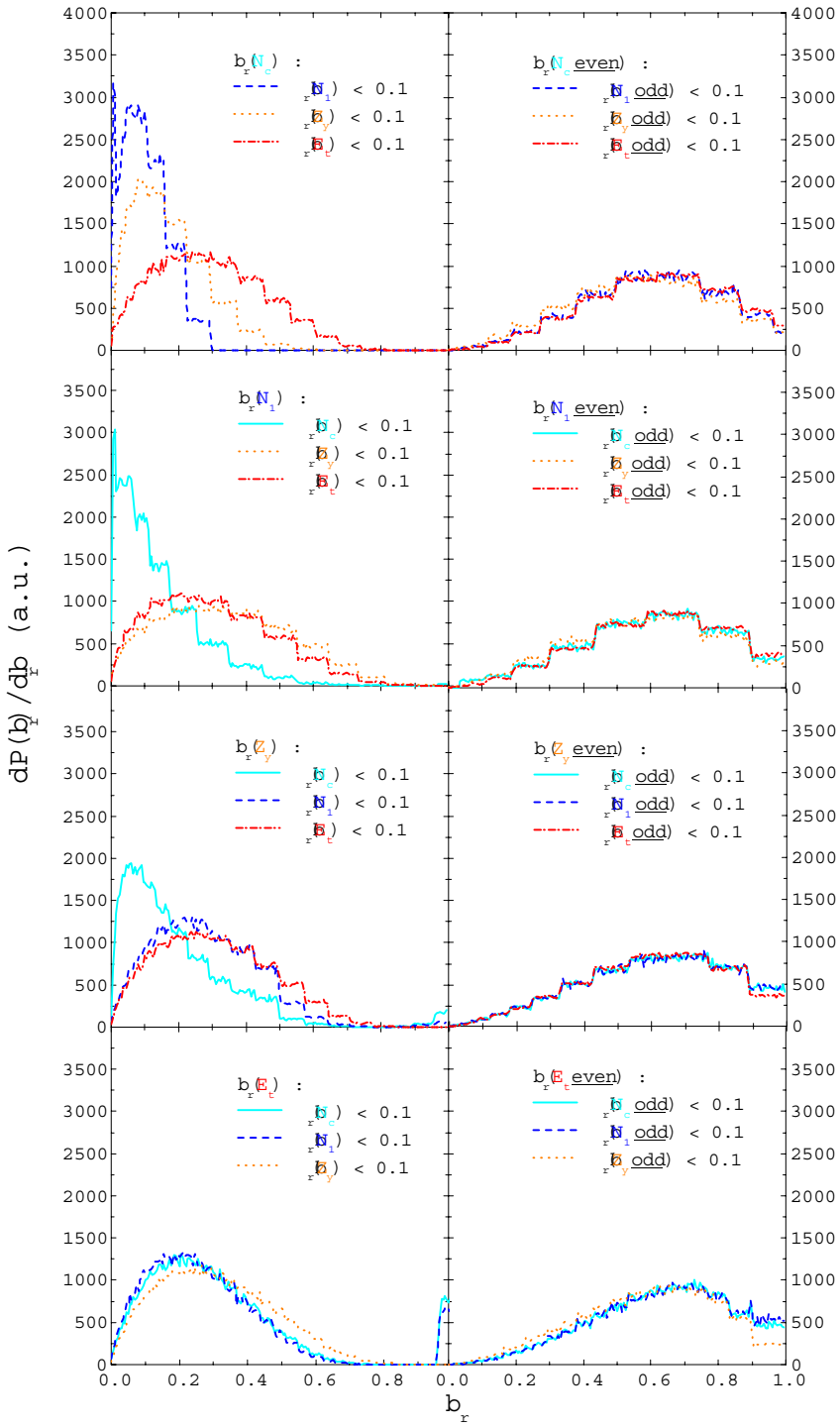

Figure 4.8: *Conditional impact parameter distributions $b_r(X)$, with $X = N_C, N_1, Z_y, E_t$, for central C+Au collisions at 95 AMeV. Full lines correspond to $b_r(N_C) < 0.1$, dashed lines to $b_r(N_1) < 0.1$, dotted lines to $b_r(Z_y) < 0.1$, and dashed-dotted lines to $b_r(E_t) < 0.1$.*

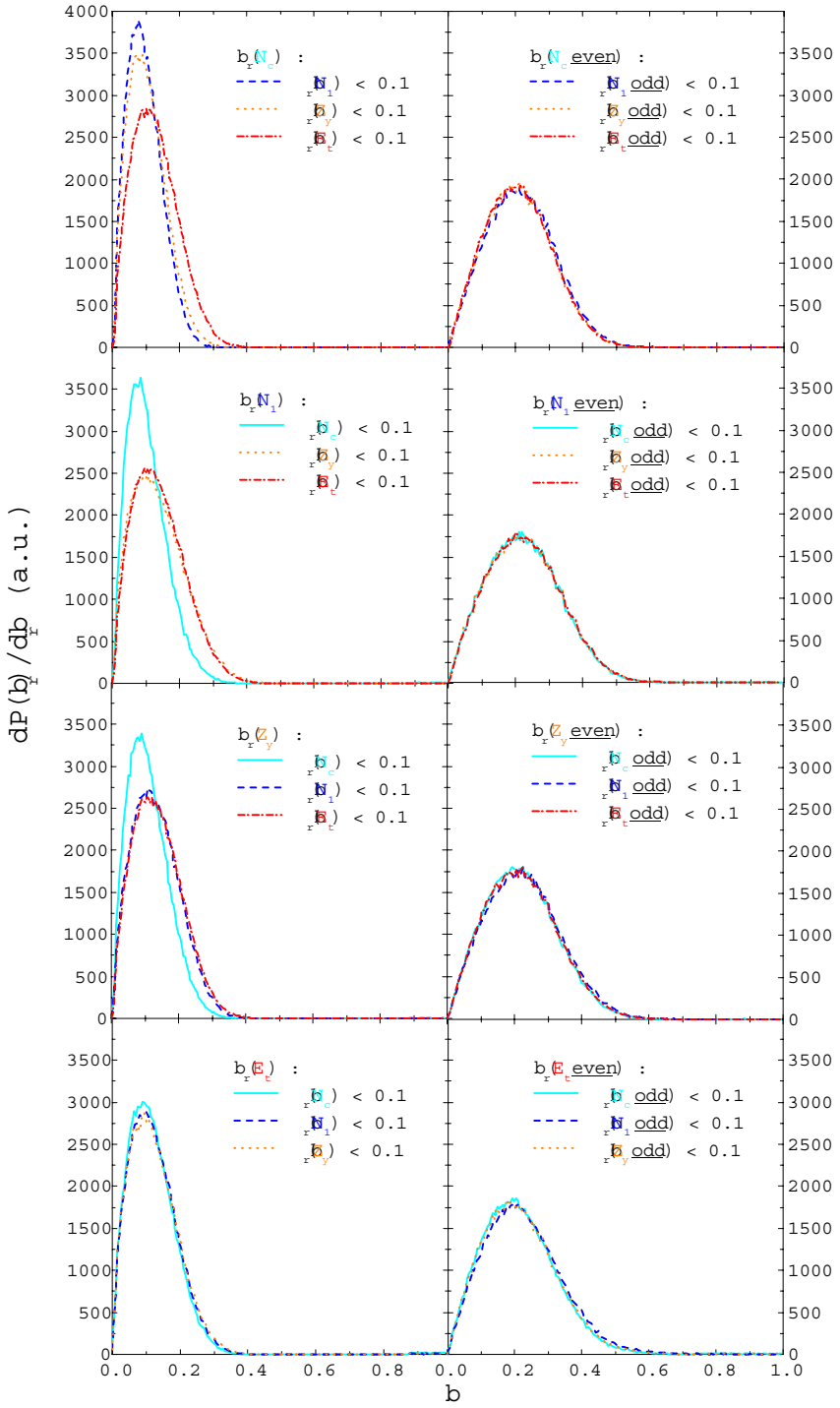

Figure 4.9: *Conditional impact parameter distributions* $b_r(X)$, *with* $X = N_C, N_1, Z_y, E_t$, *for central C+Au collisions at 600 AMeV. Full lines correspond to* $b_r(N_C) < 0.1$, *dashed lines to* $b_r(N_1) < 0.1$, *dotted lines to* $b_r(Z_y) < 0.1$, *and dashed-dotted lines to* $b_r(E_t) < 0.1$.

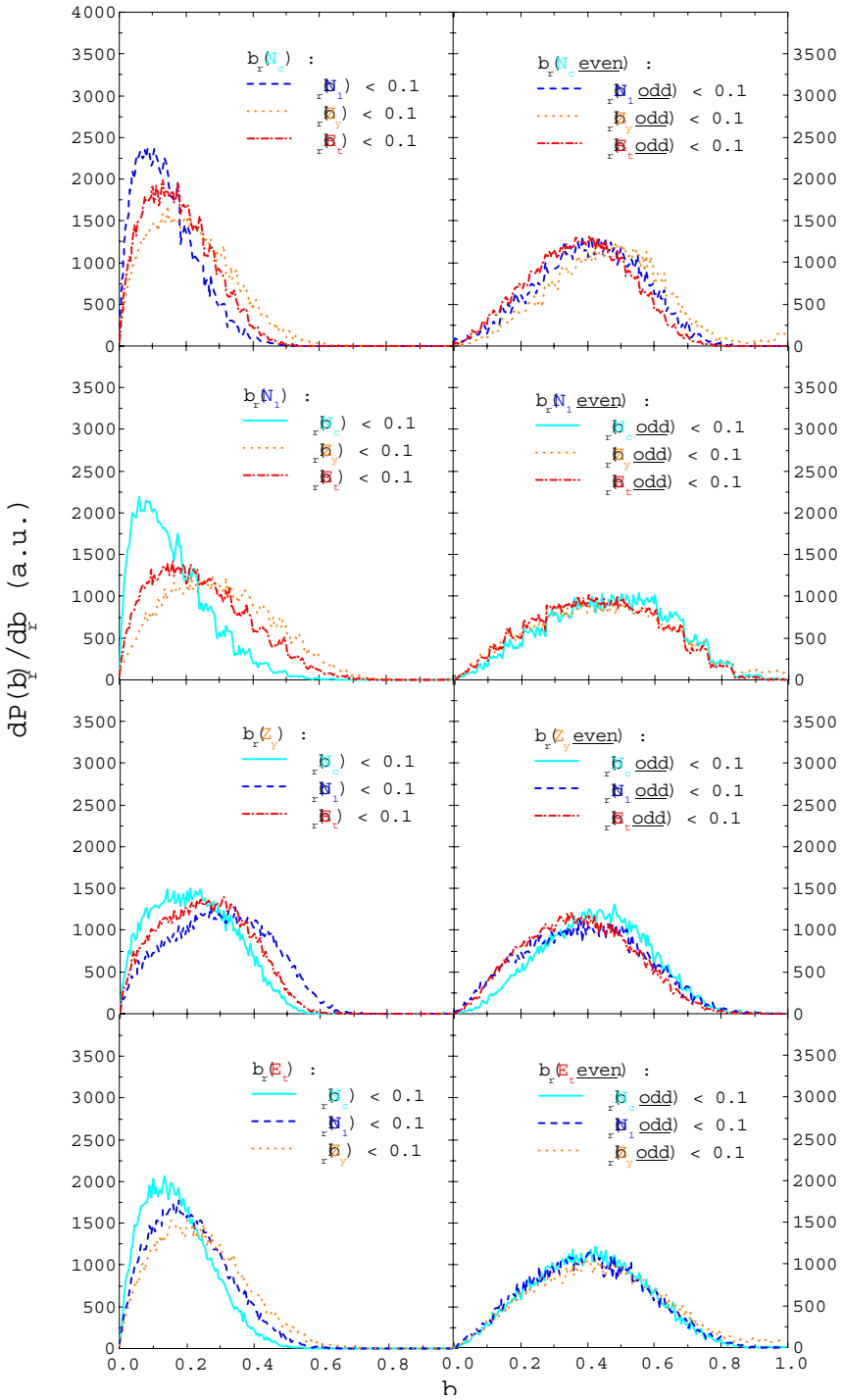

Figure 4.10: *Conditional impact parameter distributions* $b_r(X)$, *with* $X = N_C, N_1, Z_y, E_t$, *for central Xe+Sn collisions at 50 AMeV. Full lines correspond to* $b_r(N_C) < 0.1$, *dashed lines to* $b_r(N_1) < 0.1$, *dotted lines to* $b_r(Z_y) < 0.1$, *and dashed-dotted lines to* $b_r(E_t) < 0.1$.

In the case of C+Au at 95 AMeV, one has to consider that the low multiplicity introduces large fluctuations when one divides up the event in two subevents with even and odd detector numbers. The weak correlations could only be partly explained by this effect. Another effect are correlations introduced by dividing the events. The two sets of data giving N_{Ceven} and N_{Codd} present a correlation shown in Fig. 4.11 (left panel) for the reaction C+Au at 600 AMeV. In this case, one particle contributing to N_{Ceven} can not contribute to N_{Codd}. This correlation, cut on $N_{Ceven} + N_{Codd} = 16$ has a binomial distribution (Fig. 4.11, right panel) with 16 tries and equal probabilities with to have a particle in an 'even' module or an 'odd' module. The distribution has double width because the difference $N_{Ceven} - N_{Codd}$ is displayed, $\sigma = \sqrt{N_{Ceven} + N_{Codd}}$, and is well approximated by a Gaussian.

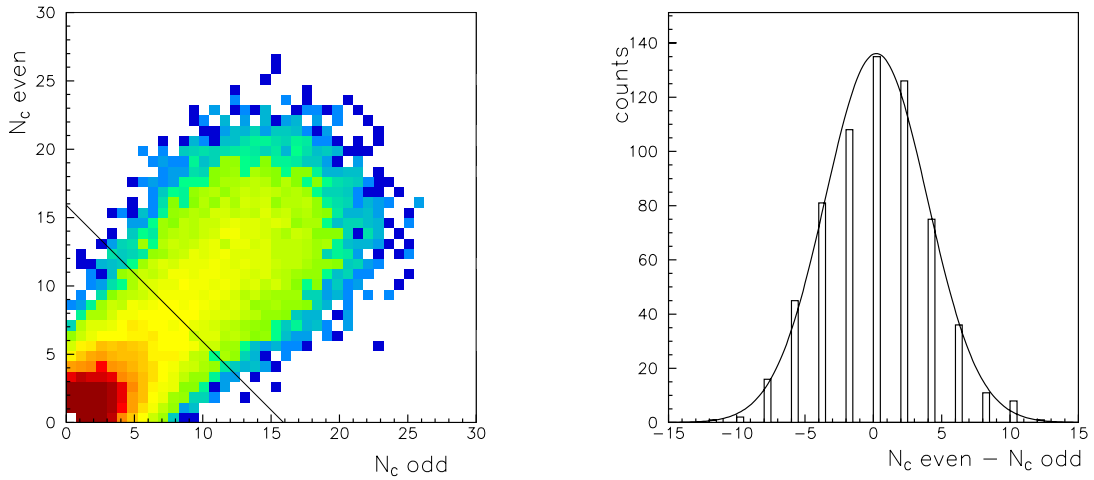

Figure 4.11: *Left panel: correlation between N_{Ceven} and N_{Codd} for C+Au reactions at 600 AMeV. Right panel: a cut at $N_{Ceven} + N_{Codd} = 16$ in the correlation gives a gaussian distribution with $\sigma = \sqrt{N_{Ceven} + N_{Codd}}$.*

The conditional impact parameter distributions are much narrower for the system C+Au at 600 AMeV (see Fig. 4.9). All the variables are well correlated for full data (observed $b_r \simeq 0.0{-}0.3$, left panels) and also for even-odd data (observed $b_r \simeq 0.0 - 0.5$, right panels). For the Xe+Sn reactions at 50 AMeV, the correlations are not so strong as for C+Au at 600 AMeV. Fig. 4.10 presents these distributions for full data (left panels), where the autocorrelation $N_1 - N_C$ and the correlation between N_C and E_t (first and fourth left panels, from the top) are visible. The odd-even test gives broad distributions with a mean value of $b_r \simeq 0.45$ which indicate a strong correlation with central collisions as in the case of the system C+Au at 95 AMeV.

The test on even and odd modules is extended from central to peripheral collisions and the mean values of the observed conditional impact parameter distributions with gates on $< b_r(N_C) >$ are presented in Fig. 4.12, for the three studied systems, for all modules in the right panels and for even and odd modules in the left panels. The distributions for all modules are very close to the perfect correclation for the three systems. However, the C+Au at 95 AMeV and Xe+Sn at 50 AMeV reduced impact parameters are slightly higher for central collisions than the

ones of C+Au at 600 AMeV. The weak correlations of the global variables for C+Au at 95 AMeV (top panels) is confirmed for all the impact parameter gates: the distribution of $< b_r(X) >$, with $X = N_1, Z_y, E_t$, as a function of $< b_r(N_C) >$ is almost flat. The same fluctuation effects observed at very central collisions are visible for almost all impact parameters. To divide up the event into subevents modify essentially the central and peripheral bins and keeps semi-peripheral reduced impact parameters very close to teh perfect correlation. The mean values of $b_r(N_C)$ for C+Au collisions at 600 AMeV are very close to the perfect correlation symbolised by the diagonal line. In the case of the reaction Xe+Sn at 50 AMeV, this holds only for the peripheral collisions ($b_r(N_C) > 0.4$).

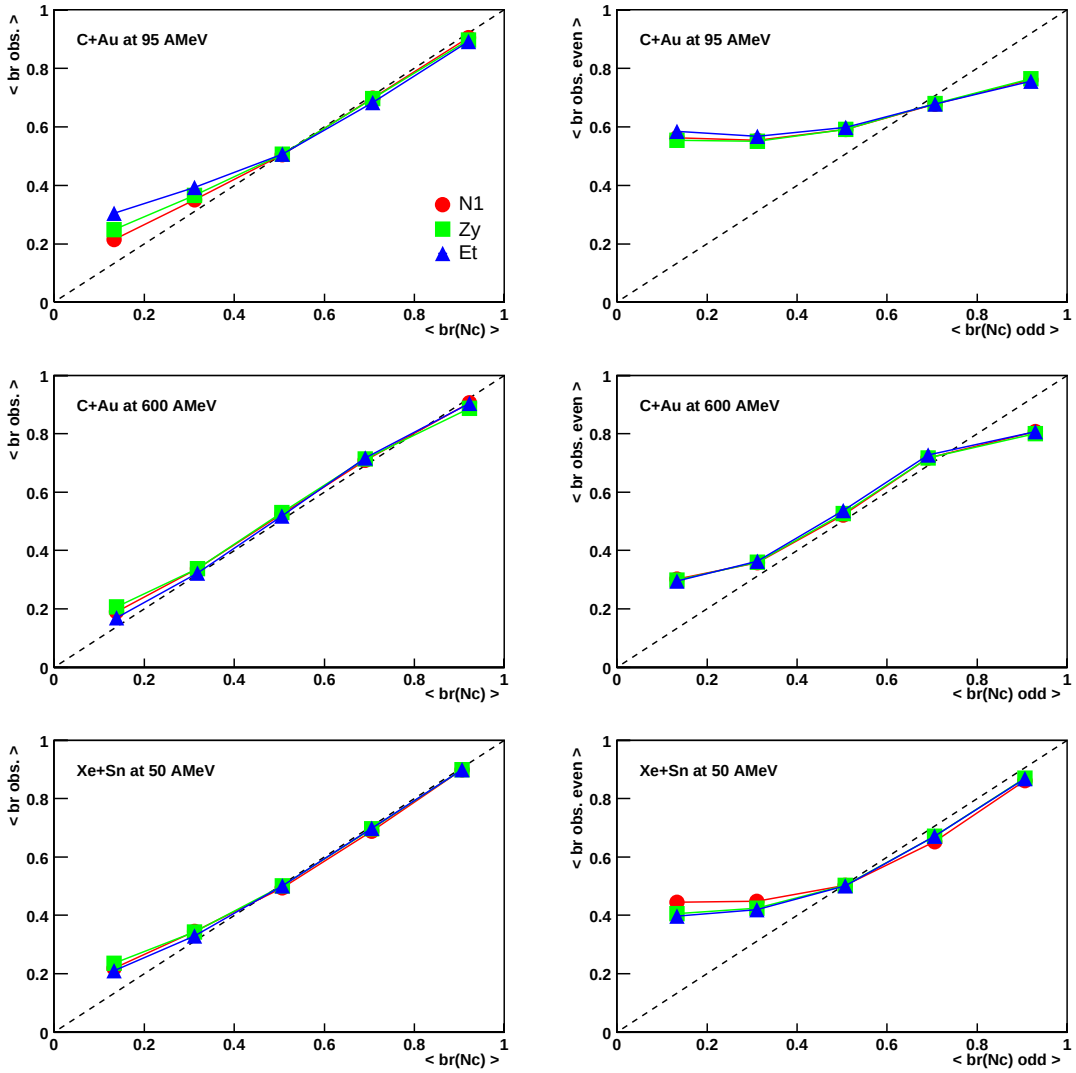

Figure 4.12: *Left panels: mean measured impact parameter for all modules* ($< b_r(obs) >$) *as a function of gates in impact parameter* $b_r(N_C)$ *for all modules* ($< b_r(cut) >$). *Right panels: mean measured impact parameter for even modules* ($< b_r(obs) >$) *as a function of gates in impact parameter* $b_r(N_C)$ *for odd modules* ($< b_r(cut) >$). *The diagonal lines correspond to the perfect correlation.*

4.4 Choice of a global variable.

In this chapter, we have studied the correlations between four global variables: the charged particle multiplicity N_C, the identified hydrogen multiplicity N_1, the mid-rapidity summed charge Z_y, and the total transverse kinetic energy of identified particles E_t. We have pointed out the increase of these correlations with the symmetry of the system and the incident energy. We tried to study autocorrelations between different variables by dividing the detector in two independent sets of detectors.

As our goal is to analyse the data coming from the reactions of C+Au at beam energies from 95 to 1800 AMeV, the system at 600 AMeV can be considered as representative of this set of data and, as the four global variables show similar behaviour and a good correlation for this system and this energy, we can choose any of these variables to select the impact parameter. In the following chapters, the impact parameter gates will be calculated from the charged particle multiplicity N_C that has the advantage to be independent of the calibration. Moreover, the BQMD calculations for C+Au at 600 AMeV predict N_C as the best variable with the narrowest width of the distribution.

Fig. 4.8 to 4.10 show that the resolution for any of these three different systems is not sufficient to make useful a large number of impact parameter. If we choose a small number of bins, we can miss evolutions with centrality that may occur inside a bin. Moreover, for the asymmetric system C+Au, there is total overlap of the nuclei of carbon and gold at a relative impact parameter $b_r = 0.4$. This leads us to the choice of five bins of impact parameter for the following of the study, as shown in Fig. 4.13.

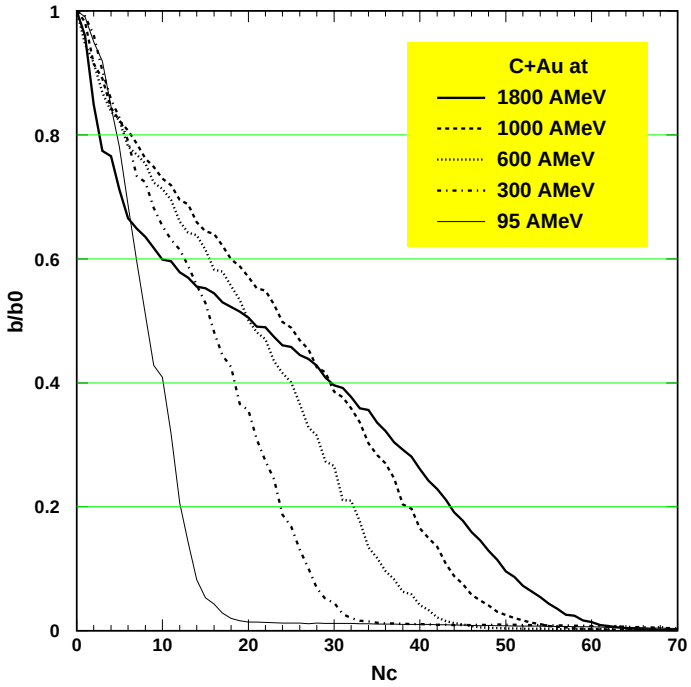

Figure 4.13: *The reduced impact parameter b/b0, also called b_r, is presented as a function of the charged particle multiplicity Nc for the system C+Au at the incident energies of 95, 300, 600, 1000, and 1800 AMeV. The horizontal lines separate the bins in reduced impact parameter that will be used in the following of the analysis.*

Chapter 5

Protons, Manifestation of the Early Source

The protons, as light particles, have the peculiarity of being emitted at each stage of a heavy-ion reaction. The initial fireball, preequilibrium, evaporation, and other secondary decay modes, all contain a strong proton component. This chapter is focused on identifying these sources and their contributions to the observed proton yields and on testing dynamical and statistical models developed for their description.

5.1 Protons in INDRA

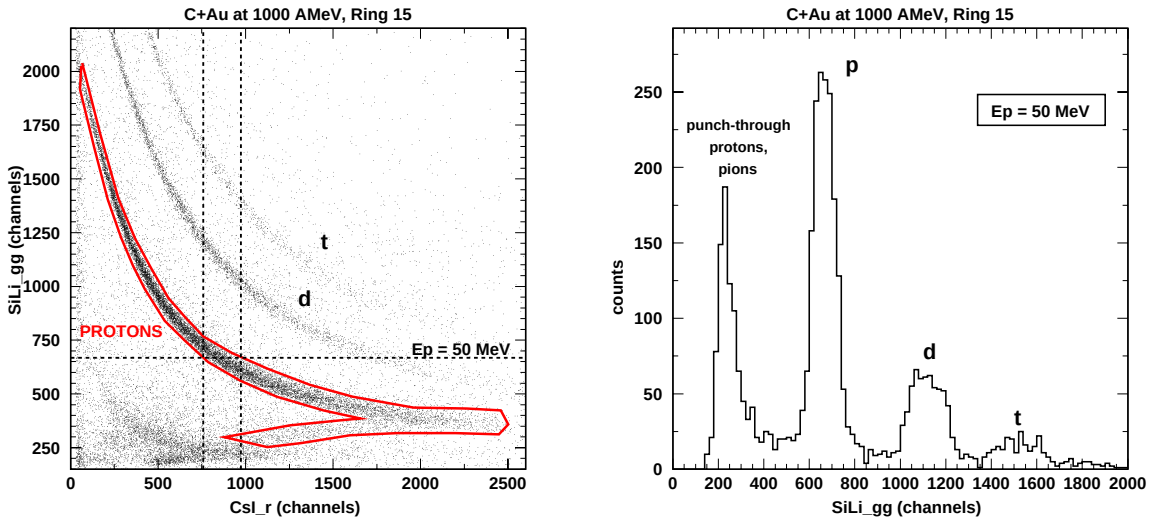

Figure 5.1: *Left panel: matrix SiLi_gg (high gain) versus CsI_r (fast component) for the ring 15* ($126^o \leq \theta_{lab} \leq 142^o$) *for the reaction C+Au at the incident energy of 1000 AMeV. One can observe, from top to bottom, curved lines corresponding to the tritons (t), the deuterons (d), and the protons. Protons are identified by a gate drawn around the stopped and punch-through proton line. Right panel: projection of the channel range in CsI_r (vertical dashed lines in the left panel) corresponding to the proton kinetic energy Ep = 50 ± 3 MeV in SiLi_gg (horizontal dashed line in the left panel).*

In the INDRA multidetector, the protons are identified in silicon-CsI ΔE-E maps and in the CsI crystals by pulse-shape analysis. In order to determine the quality of the identification, we compare in this section three methods to identify the protons: in the CsI's alone, in the SiLi-CsI telescope by a simple gate drawn around the stopped and punched-through proton line, as displayed in the left panel of Fig. 5.1 for C+Au at 1000 AMeV and $126^o \leq \theta_{lab} \leq 142^o$ (the gate is stopped before the pion line), and in the 'etalon' calibration telescopes (Si75-SiLi-CsI) at backward angles ($45^o \leq \theta_{lab} \leq 176^o$).

In the second case, the proton calibration is done using the energy loss in the SiLi detector and range-energy tables [Hub90]. The background in the SiLi detector can be estimated for a proton kinetic energy Ep = 50 ± 3 MeV in SiLi_gg by a projection of the channel range in CsI_r corresponding to this energy (see Fig. 5.1). The background between the punch-through proton and pion peak and the stopped proton peak is about 10 ± 5 %. The same channel range is applied on the fast CsI_r and the slow CsI_l component of the following CsI crystal (see Fig. 5.2). The projection in CsI_r+CsI_l give then a background estimation of about 6 ± 3 % between the proton and deuteron peaks. The background in the SiLi-CsI telescope increases for smaller angles in the laboratory.

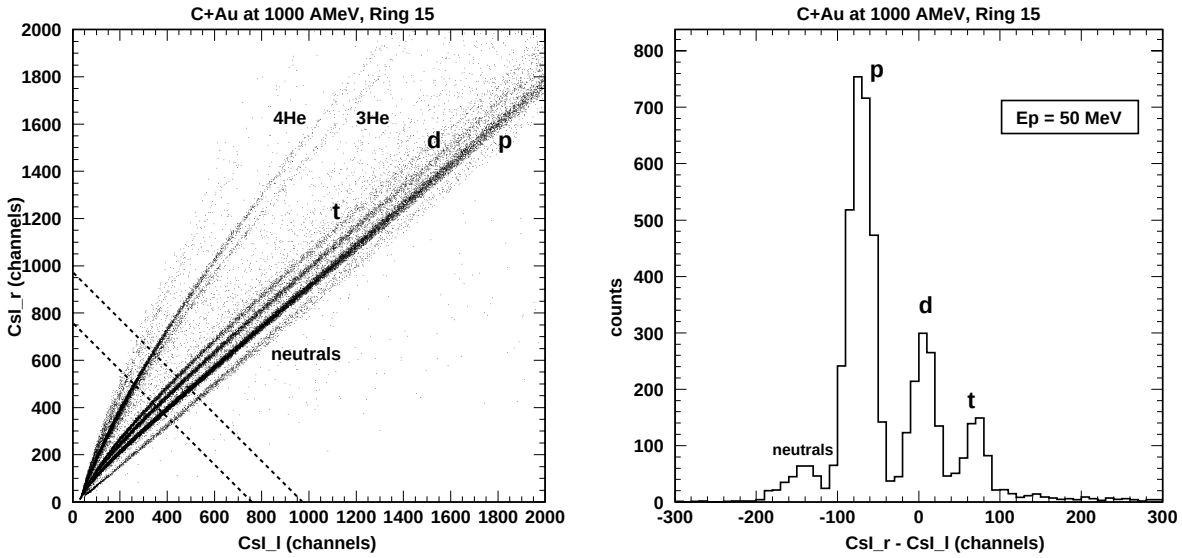

Figure 5.2: *Left panel: matrix CsI_r (fast component) versus CsI_l (slow component) in channels for the ring 15 ($126^o \leq \theta_{lab} \leq 142^o$) for the reaction C+Au at the incident energy of 1000 AMeV. On can observe, from the right side, lines corresponding to the neutral particles (γ's, neutrons), the protons (p), the deuterons (d), the tritons (t), the ^3He's, and the ^4He's. Right panel: projection of the channel range in CsI_r+CsI_l (diagonal dashed line in the left panel) corresponding to the proton kinetic energy Ep = 50 MeV in SiLi_gg.*

As we are using CsI scintillation crystals, we have to consider the reaction losses coming from elastic and inelastic nuclear interaction of charged particles passing through the crystals. An elastic scattering of a particle leads to a slight change in its initial energy detected by the scintillator. In the inelastic interactions of a particle with a nucleus, the loss of its primary energy

can be high, especially for light particles as protons. In a CsI, according to the Glauber model, the energy losses of protons can reach 25% for a kinetic energy of E = 215 MeV, maximum measured in INDRA at forward angles ($2^o \leq \theta_{lab} \leq 14^o$) [Avd99].

Fig. 5.3 presents the comparison between the proton energy spectra obtained by gates in the SiLi-CsI telescopes (symbols) and in the CsI (lines) by the usual identification and calibration (see chapter 3), for central (b/b0=0.0-0.2) C+Au reactions at 1000 AMeV for the backward angles ($45^o \leq \theta_{lab} \leq 176^o$). The energy spectra are not corrected for the reaction energy losses. As both kinds of spectra should be corrected in the same way, their comparison is not affected. The normalization of these spectra is done over the involved detector solid angle ($\Delta\Omega_{etalon}$ = 13.15 msr), the SiLi-CsI telescope in the first case, the whole CsI ring in the second case. The statistical error bars of the proton spectra presented in this chapter are included in the symbols.

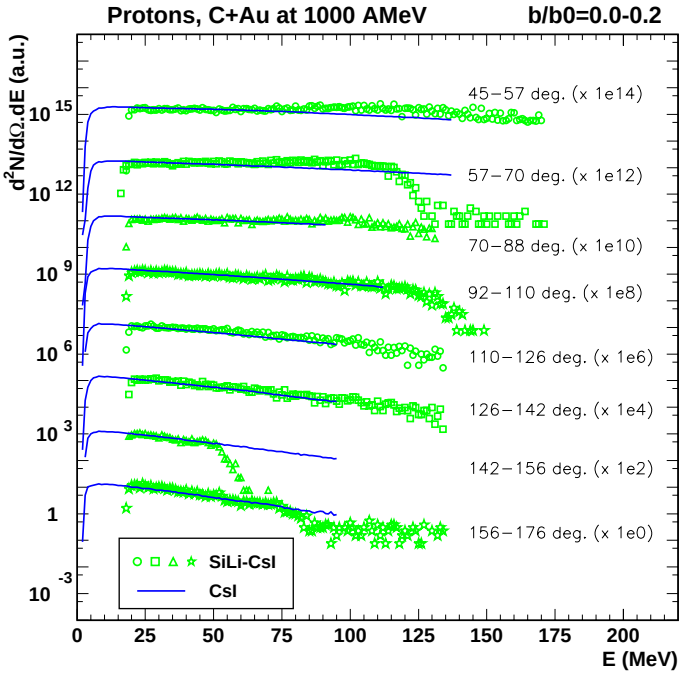

Figure 5.3: *Proton kinetic energy spectra identified by a gate in the matrix SiLi vs CsI (symbols) or in the CsI crystals (lines) for central (b/b0=0.0-0.2) C+Au reactions at 1000 AMeV for the backward angles ($45^o \leq \theta_{lab} \leq 176^o$).*

The SiLi-CsI spectra begin at a higher energy than the CsI spectra because, in the first case, the protons with a kinetic energy $E_{kin} < 15$ MeV are stopped in the SiLi detector (2 mm of silicon) after passing through the ionization chamber and the Si75 (80 μm of silicon). At $57^o \leq \theta_{lab} \leq 70^o$ and $142^o \leq \theta_{lab} \leq 146^o$, the discrimination threshold were set at a slightly higher level and cut into the high energy proton branch. At the other angles, this threshold is lower and permits in the SiLi-CsI matrix the identification and calibration of protons punching through the CsI, contrary to the usual identification and calibration in the CsI. This gives spectra extending to higher energy but with essentially the same slope parameter as the CsI spectra. The different maximum energies of the CsI spectra correspond to the different lengths of the CsI crystals (see chapter 2). The drawing of the gate may also influence the shape of the spectra. When the proton gate has a wide lower angle just before the pion line, it includes more protons with the same energy than when the gate angle is more acute. In the first case, the spectra stop then sharply, as for $45^o \leq \theta_{lab} \leq 57^o$, without the smooth decrease visible at $92^o \leq \theta_{lab} \leq 110^o$.

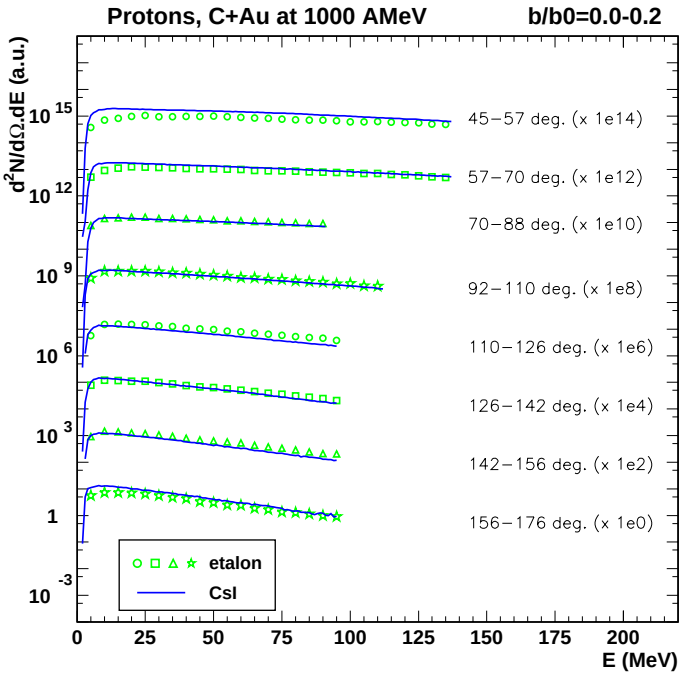

Figure 5.4: *Proton kinetic energy spectra identified in the 'etalon' calibration telescopes (symbols) or in the CsI crystals (lines) for central (b/b0=0.0-0.2) C+Au reactions at 1000 AMeV for the backward angles ($45^o \leq \theta_{lab} \leq 176^o$). The binning of the 'etalon' spectra is 5 MeV.*

Both kinds of spectra are in good agreement. Nevertheless, we note that, at $45^o \leq \theta_{lab} \leq 88^o$ and E > 80 MeV, the SiLi-CsI spectra are twice as high as the CsI spectra. This angular region corresponds to detectors with a high background, partly due to the overlap of punch-through proton and deuteron lines. Moreover, this energy range coincides in the SiLi-CsI matrix with the region where the stopped and punch-through proton lines are very close to each other. The gate is very large at this place as shown in Fig. 5.1 and may increase the spectra yields by selecting also more background. The other angles show discrepancies of maximum 10%.

Another comparison is done between proton kinetic energy spectra coming from the CsI and the calibration telescopes (Si75-SiLi-CsI) , so-called 'etalon', for central (b/b0=0.0-0.2) C+Au reactions at 1000 AMeV. Fig. 5.4 shows the general agreement within 10% between the various spectra at $45^o \leq \theta_{lab} \leq 176^o$. Nevertheless, some disagreements are visible diminished by the highly compressed logarithmic scale as at $45^o \leq \theta_{lab} \leq 57^o$ where the etalon spectrum is lower than the CsI one by 15% for E=130 MeV to 100% for E=10 MeV. The angles $47^o \leq \theta_{lab} \leq 70^o$ and $156^o \leq \theta_{lab} \leq 176^o$ present also differences of 50% and 35% for E=10 MeV. At $70^o \leq \theta_{lab} \leq 88^o$, the proton spectrum is the most likely to be correct.

The overall good agreement among three different methods to identify and calibrate protons in the INDRA multidetector leads us to the choice of using only the CsI proton spectra in the following analysis.

5.2 Characteristics of the proton sources

The sources emitting particles in heavy ion collisions can be characterised in various ways, for example by their temperatures, their cross-sections, their velocities, their Coulomb energies, and their radial flows. In this work, the nuclear temperature is prefered because it is, at the origin, a thermodynamical and macroscopical variable that we attempt to apply to a nuclear system (see chapter 1.1). The experimental procedures for temperature determination which are currently used in nuclear reactions involve the examination of three aspects of the emitted particles: their relative number [Alb85], their excited state populations [Mor94], and their kinetic energy. In a ideal situation, each of these thermometers should give the same temperature. Under realistic situations, each can be influenced in different ways by experimental and analysis conditions. In this work, we will only study the kinetic thermometer described in the following.

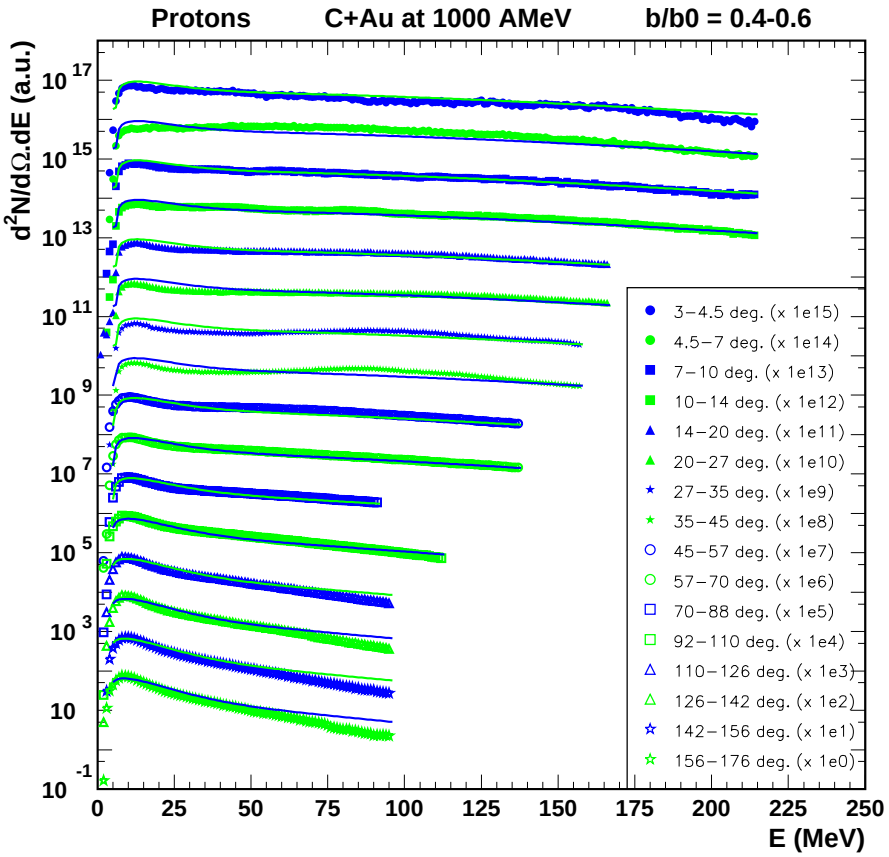

Figure 5.5: *Fits (full lines) of the proton kinetic energy spectra (symbols) for the system C+Au at 1000 AMeV for semi-peripheral collisions (b/b0=0.4-0.6) at* $3^o \leq \theta_{lab} \leq 176^o$.

In a canonical ensemble, the probability to find a particle in a defined energy is determined by the Boltzmann factor $exp(-E/T)$ which contains the temperature of the system. The kinetic energy spectra show in classical approximation a Maxwell-Boltzmann distribution:

$$N(E_{kin}) \propto \sqrt{E_{kin}}.e^{(-\frac{E_{kin}}{T})} \tag{5.1}$$

As the temperature corresponds then to the inverse of the slope of the energy spectra, the temperature obtained in this way is also called 'slope temperature'. In the statistical limit, the particle source is expected as a Boltzmann source. In this way, we hope to identify the proton sources (and the fragment sources in the next chapter) on the basis of their temperatures. To analyse the proton kinetic energy spectra, we use the Moving Source Fit code that is a combination of relativistic Maxwell-Boltzmann functions (see appendix C). We apply, in our case, the formulae corresponding to two sources moving in the laboratory with certain temperatures, cross sections, and velocities. The Coulomb repulsion, peak energy and width, is considered only for the target emission. The radial flow is fixed to zero for the two sources.

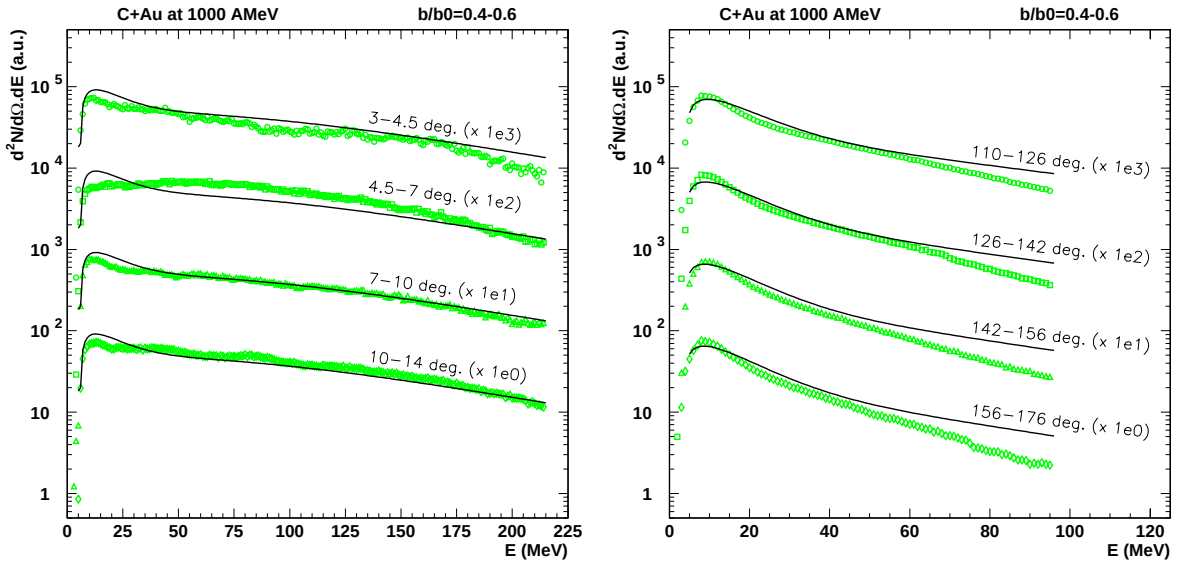

Figure 5.6: *Fits (full lines) of the proton kinetic energy spectra (symbols) for the system C+Au at 1000 AMeV for semi-peripheral collisions (b/b0=0.4-0.6) at* $3^o \leq \theta_{lab} \leq 14^o$ *(left panel) and at* $110^o \leq \theta_{lab} \leq 176^o$ *(right panel).*

The proton kinetic energy spectra are shown in Fig. 5.5 for semi-peripheral C+Au reactions at 1000 AMeV at $3^o \leq \theta_{lab} \leq 176^o$. The centrality is given by the reduced impact parameter b/b0, here b/b0=0.4-0.6 (see chapter 4). These spectra are fitted all together for two sources, the fits are represented by the full line on each spectrum. These fits converge to values very close to the experimental spectra. However, one can remark some discrepancies at low energies and at forward angles, and at high energies and at backward angles, as presented in Fig. 5.6. In both cases, the fit converges on higher values than the experimental proton spectra while the fit is in good agreement with the data at low energies at backward angles and at high energies at forward angles. As the Moving Source Fit is based on the hypothesis of isotropic sources, we notice that the sources at low and high energies may be anisotropic. Due to this feature of the proton sources, it is chosen to fit the low energy source only at backward angles ($70^o \leq \theta_{lab} \leq 176^o$) and for an energy E < 20 MeV (see left panel Fig. 5.7). In the same way, the high energy source is fitted only at forward angles $3^o \leq \theta_{lab} \leq 27^o$ and for energies E > 40 MeV (see right panel Fig. 5.7). This choice allows a good convergence of the fits to values close to the experimental spectra, with only small discrepancies at very forward angles.

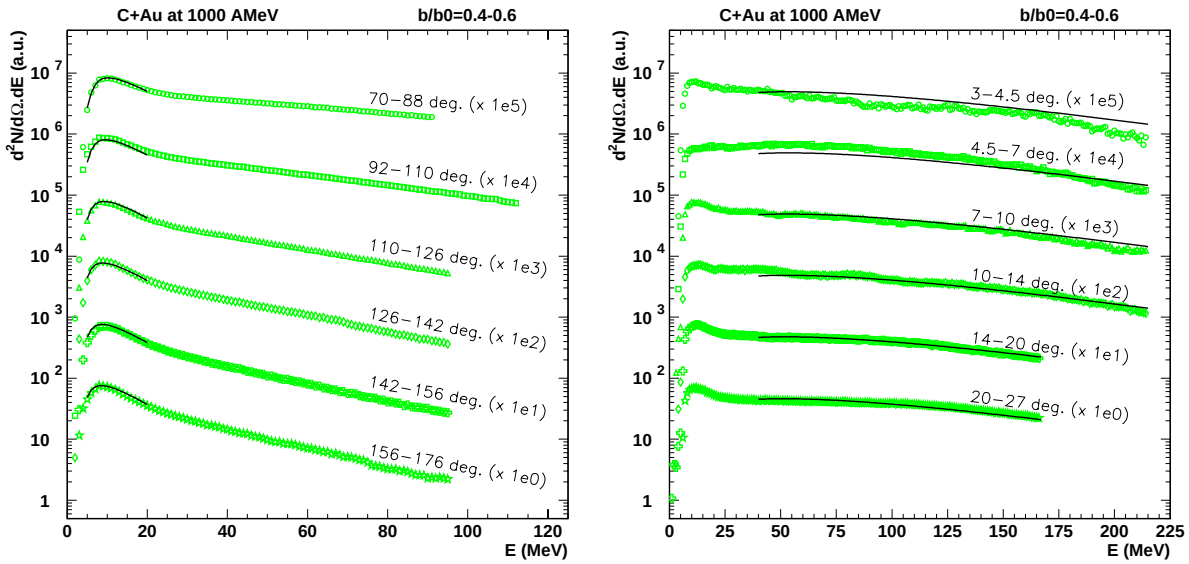

Figure 5.7: *Fits (full lines) of the proton kinetic energy spectra (symbols) for the system C+Au at 1000 AMeV for semi-peripheral collisions (b/b0=0.4-0.6) at* $70^o \leq \theta_{lab} \leq 176^o$ *for the target source (left panel) and at* $3^o \leq \theta_{lab} \leq 27^o$ *for the early source (right panel).*

b/b0	Source	T (MeV)	σ (mbarn)	β (c)	E_C (MeV)	ΔE_C (MeV)
0.0-0.2	low E	16.7 ± 0.2	910 ± 10	0.032 ± 0.003	0.2	4.5 ± 0.2
0.0-0.2	high E	66.3 ± 0.3	3770 ± 10	0.0008 ± 0.0006	0	0
0.2-0.4	low E	13.3 ± 0.1	2030 ± 10	0.026 ± 0.002	0.6 ± 0.4	4.5 ± 0.1
0.2-0.4	high E	70.8 ± 0.3	9510 ± 20	0.0021 ± 0.0007	0	0
0.4-0.6	low E	8.85 ± 0.09	2350 ± 20	0.013 ± 0.001	4.91 ± 0.06	1.5 ± 0.1
0.4-0.6	high E	53.3 ± 0.3	5080 ± 10	0.1505 ± 0.0006	0	0
0.6-0.8	low E	6.37 ± 0.09	1890 ± 10	0.000007	5.89 ± 0.05	1.7 ± 0.1
0.6-0.8	high E	28.0 ± 0.2	1220 ± 10	0.310 ± 0.001	0	0
0.8-1.0	low E	6.19 ± 0.08	136 ± 2	0.0019	6.77 ± 0.05	1.8 ± 0.1

Table 5.1: *Fit parameters for proton spectra for the reaction C+Au at 1000 AMeV as a function of the reduced impact parameter b/b0. The fits of the low and high energy sources give the temperature T, the absolute cross section* σ*, the velocity* β*, the energy* E_C *of the Coulomb peak, and the width* ΔE_C *of this peak for the two sources. The radial flow is fixed to 0 in both cases. When the value of one parameter is very small, the fit may not give any error.*

The parameters obtained by this fit method for the system C+Au at 1000 AMeV are presented in the table 5.1 for all impact parameters. Because of too low statistics after corrections of stray particle effects, the high energy source can not be fitted for very peripheral collisions (b/b0=0.8-1.0). One remarks that the slope temperature of the low energy source is decreasing with the decreasing centrality, as well as its velocity and the temperature of the high energy source. However, the velocity of this latter source increases with b/b0.

Fig. 5.8 displays the slope temperature and the velocity obtained with the Moving Source Fit code for the incident energies from 95 to 1800 AMeV for the low energy source, interpreted as the target source, for the system C+Au as a function of the reduced impact parameter b/b0. The target source presents a slope temperature increasing with the increasing incident energy and decreasing with the decreasing centrality. The low energy protons are mainly produced in central collisions at very high incident energy. One can remark that the slope temperature for the beam energy of 95 AMeV is almost constant, around 5 MeV, signal that the reaction dynamics are different at non-relativistic energies. A temperature of 5 MeV is a reasonable result for standard evaporation [Xi97] which seems to be visible at all impact parameters. The velocity of the target source also decreases with the decreasing centrality, but the dependence on incident energy seems less clear. Nevertheless, it is interesting to note that the inclusive velocity appears independent of the beam energy.

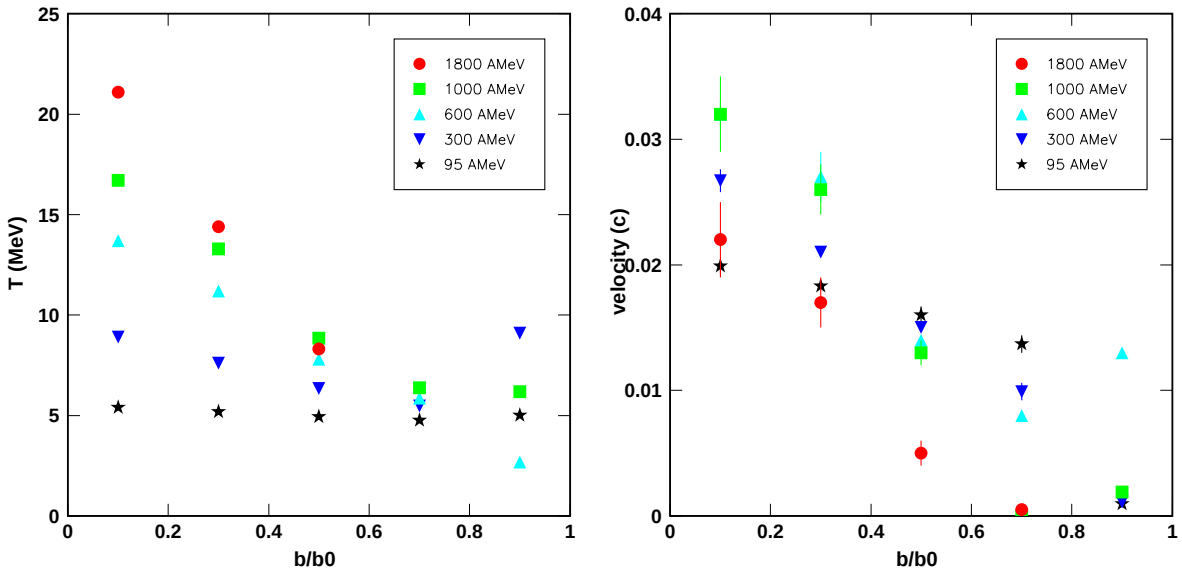

Figure 5.8: *Slope temperature and velocity of the target source for the protons as a function of the reduced impact parameter b/b0 for the incident energies 95, 300, 600, 1000, and 1800 AMeV.*

The high energy source presents in the same way an increasing temperature with an increasing incident energy for central collisions, as plotted in Fig. 5.9 as a function of the reduced impact parameter. For the other impact parameter bins, the distribution is not as systematic as for the target source. Nevertheless, the temperatures for a beam energy of 95 AMeV stay lower than at higher incident energies.

In the contrary to the low energy source, the velocity of the high energy source increases with the decreasing centrality. The proton velocity at 95 AMeV may be considered separately from the others. At this beam energy, a projectile component exists that is not present at higher incident energies (see chapter 2.4). It is arduous to well determine a source velocity by selecting only an angular coverage from 2^o to 27^o in the laboratory. At these small angles, velocity and temperature compensate each other in the calculation of the fit.

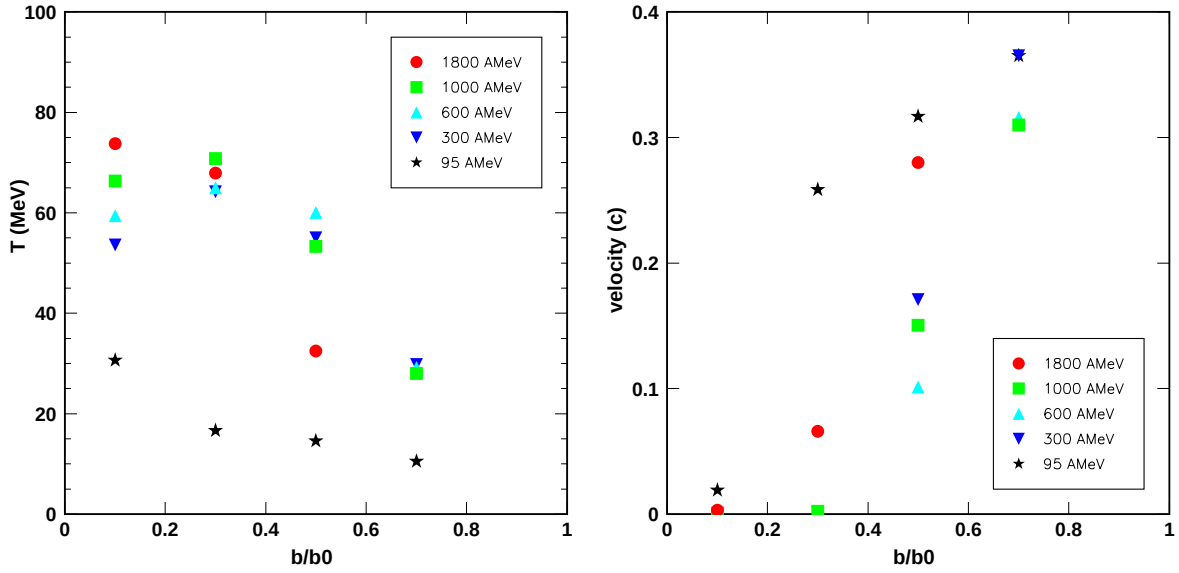

Figure 5.9: *Slope temperature and velocity of the early source for the protons as a function of the reduced impact parameter b/b0 for the incident energies 95, 300, 600, 1000, and 1800 AMeV.*

The good convergence of the fit for the high energy source poses the question of the nature of this source. The early source, also called preequilibrium or cascade source, is believed to emit light particles at the beginning of the reaction before the system reaches the multifragmentation regime. This first emission of light particles is supposed to be a dynamical process, dependent on the incident energy. Nevertheless, according to the Moving Source Fit code convergence, the observed high energy source appears thermal because of the Fermi motion and of the rescattering processes.

5.3 Discussion

Comparisons with dynamical and statistical models

To compare our experimental results with theory, the ideal tool is a model producing protons at low and high energies, in other words simulating the reaction from the early light particle emission to the multifragmentation stage and maybe secondary decays. Transport models like BUU attempt to describe the whole evolution of a heavy ion reaction. One can also employ a combination of models. This second solution is chosen here.

Fig. 5.10 presents the proton spectra for the system C+Au at 1000 AMeV for semiperipheral collisions (b/b0=0.4-0.6) at $45^o \leq \theta_{lab} \leq 57^o$ coming from the data (full circles) and from the Liège cascade coupled, in this case, to the Dresner evaporation code (full line). A percolation code provides the transition between the cascade (dashed line) and the evaporation (dotted line) codes (see Appendix B.3). The cascade code treats the colliding nuclei as clouds of nucleons, up to a certain time after which the percolation procedure is used to construct fragments. The excitation energy of these clusters is then released by means of an evaporation code. The proton

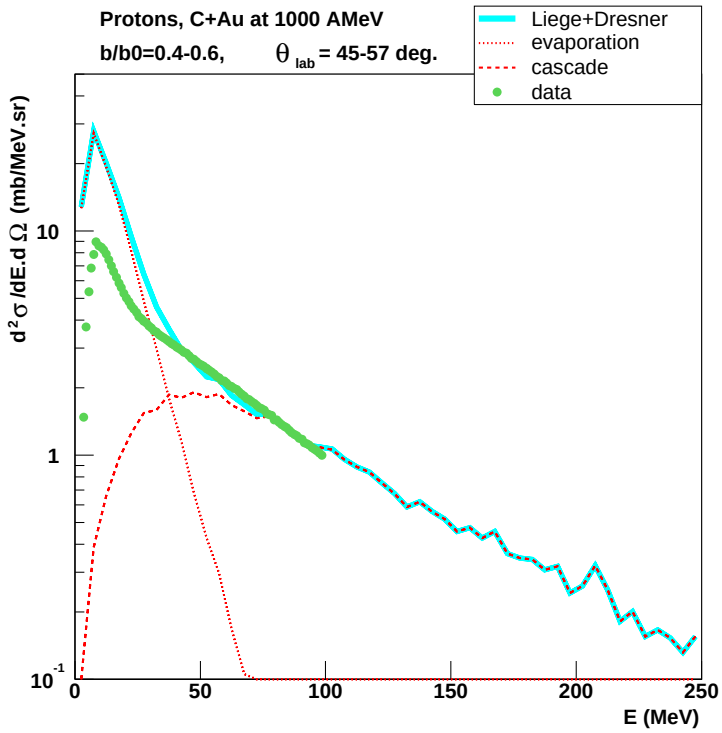

Figure 5.10: *The proton kinetic energy spectra (full circles) for C+Au at 1000 AMeV are compared to the Liège cascade model coupled to the Dresner evaporation code (full line) for b/b0=0.4-0.6 (semi-peripheral collisions) at* $45 \leq \theta_{lab} \leq 57^o$. *The dotted line corresponds to the evaporation component and the dashed line to the cascade component.*

spectra are in absolute cross-section. For this work, we choose the geometrical cross-section with a nuclear radius of $R = r_0 A^{1/3}$ with $r_0 = 1.2$ fm. This gives us a total cross-section $\sigma_{tot} = 2990$ mb. Each spectra is normalized by a factor σ/N_{evt} taking into account the geometrical cross-section σ and the number of events N_{evt} corresponding to each region of centrality. The theoretical spectra are defined in charge, mass, cross section σ, centrality b/b0, polar angle θ_{lab}, and solid angle Ω.

In Fig. 5.11 and 5.12, we show the comparison between data and the Liège cascade coupled with the Dresner evaporation code and the multifragmentation model SMM (see Appendix A.1), respectively. One may remark a good agreement between data and theory for the high energy part of the proton kinetic energy spectra corresponding to the cascade code for central C+Au reactions at 1000 AMeV at $3 \leq \theta_{lab} \leq 176^o$. However, the low energy part of these spectra is overestimated by the Dresner code but much closer to the data in the SMM case.

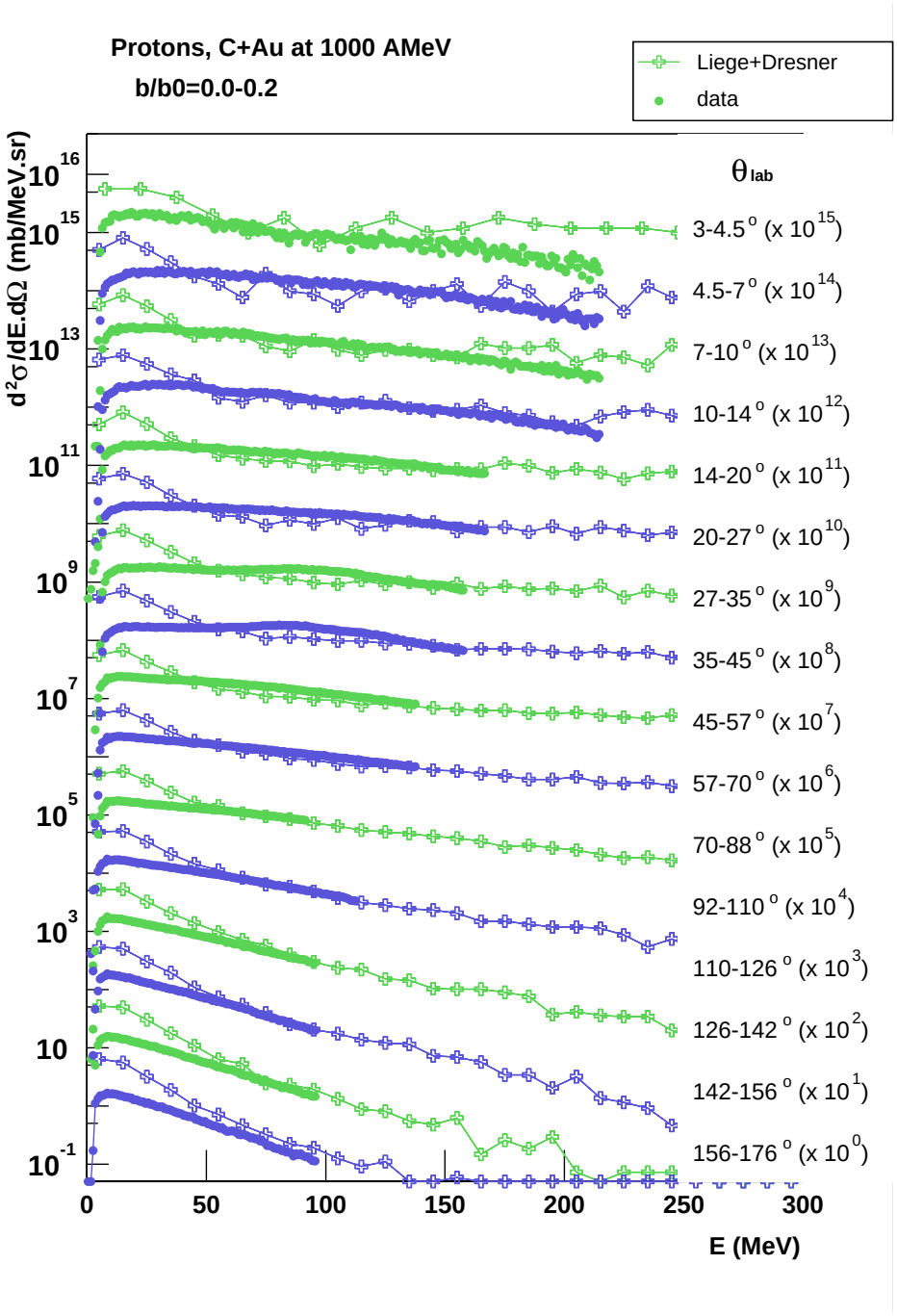

Figure 5.11: *The proton kinetic energy spectra (full circles) for C+Au at 1000 AMeV are compared to the Liège cascade model coupled to the Dresner evaporation code (open crosses) for b/b0=0.0-0.2 (central collisions) at* $3 \leq \theta_{lab} \leq 176^{o}$.

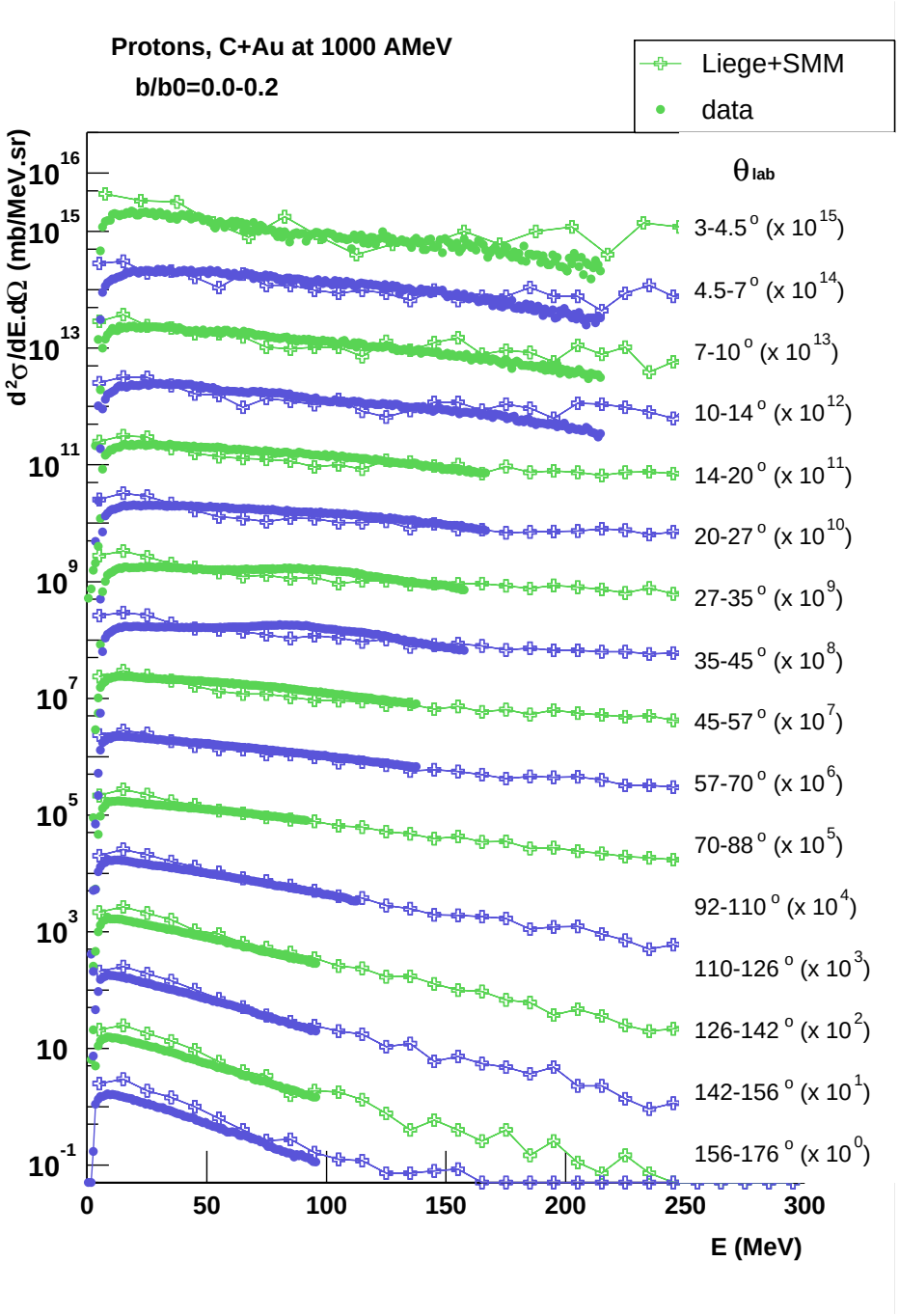

Figure 5.12: *The proton kinetic energy spectra (full circles) for C+Au at 1000 AMeV are compared to the Liège cascade model coupled to the SMM multifragmentation code (open crosses) for b/b0=0.0-0.2 (central collisions) at* $3 \leq \theta_{lab} \leq 176^o$.

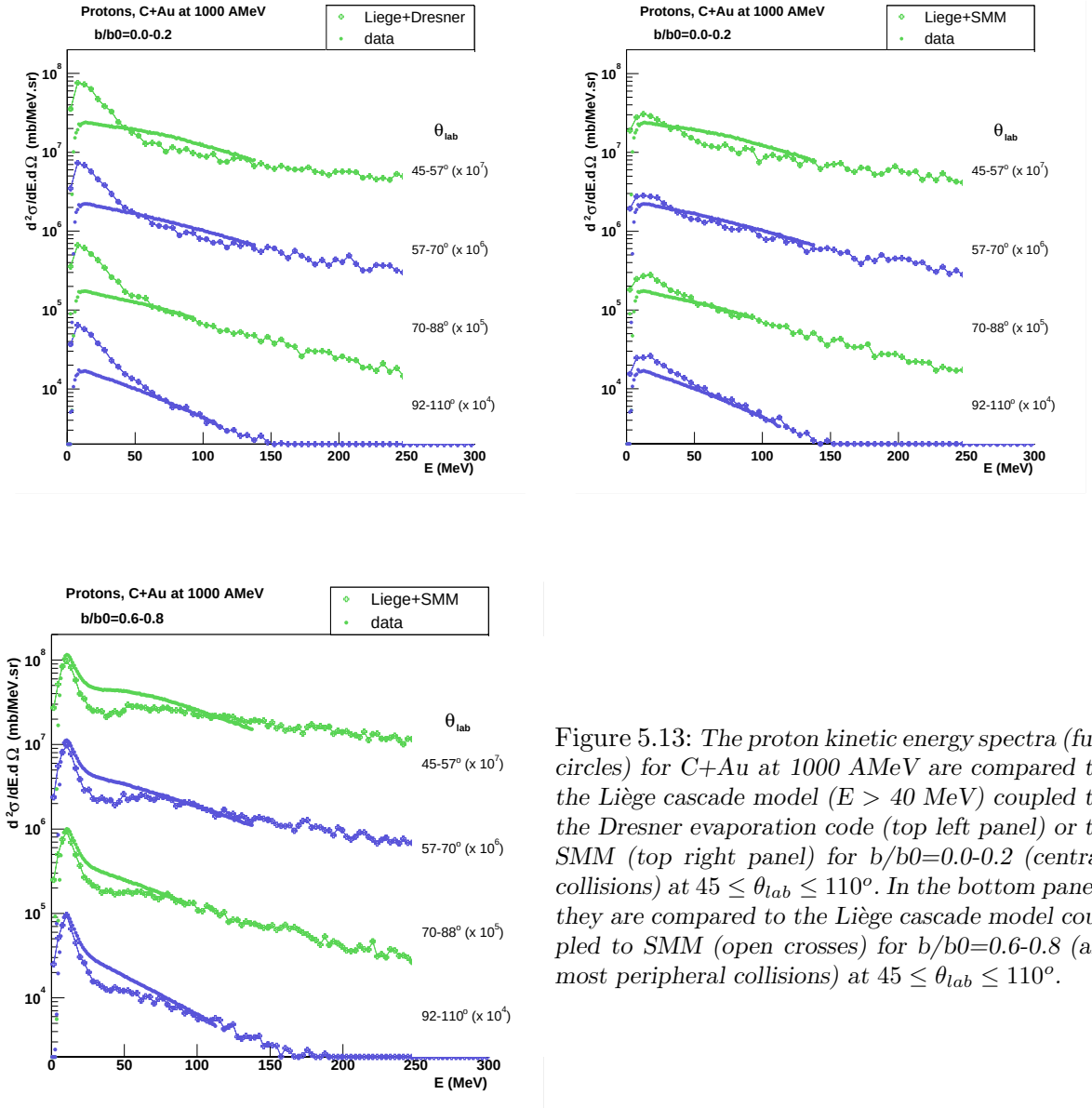

Figure 5.13: *The proton kinetic energy spectra (full circles) for C+Au at 1000 AMeV are compared to the Liège cascade model ($E > 40$ MeV) coupled to the Dresner evaporation code (top left panel) or to SMM (top right panel) for b/b0=0.0-0.2 (central collisions) at $45 \leq \theta_{lab} \leq 110^o$. In the bottom panel, they are compared to the Liège cascade model coupled to SMM (open crosses) for b/b0=0.6-0.8 (almost peripheral collisions) at $45 \leq \theta_{lab} \leq 110^o$.*

Fig. 5.13 displays the same spectra, but only for $45 \leq \theta_{lab} \leq 110^o$ (top panels). In comparison to an evaporation code, the statistical multifragmentation model SMM produces more fragments and fewer light particles. We obtain then a good agreement for the low energy part of the spectra. This model still slightly overestimates the experimental proton spectra for central collisions for $E_{kin} \leq 30$ AMeV. For peripheral reactions at b/b0=0.6-0.8, there is an underestimation of maximum a factor 2 for $30 \leq E_{kin} \leq 60$ MeV, as displayed in the bottom panel of Fig. 5.13. The comparisons between data and models are collected for these two different combinations and all the impact parameter bins, with the exception of the peripheral collisions, and at $3 \leq \theta_{lab} \leq 176^o$ in appendix D.

Other IntraNuclear Cascade models exist as the Dubna code [Ton83] (see Appendix B.1). The Dubna cascade is older but similar to the Liège cascade. Its follows each particle state as a function of time. Fig. 5.14 presents a comparison between the proton kinetic energy spectra for C+Au at 1000 AMeV and the Dubna cascade model for inclusive data at $3 \leq \theta_{lab} \leq 176^o$. This cascade model is not coupled to any percolation and evaporation codes as it is for the Liège cascade. We then compare the spectra in absolute cross-section for $E_{kin} \geq 25$ MeV. One remark,in this case, that this model reproduces well the slope of the experimental spectra but overestimates their yields by a factor 5.

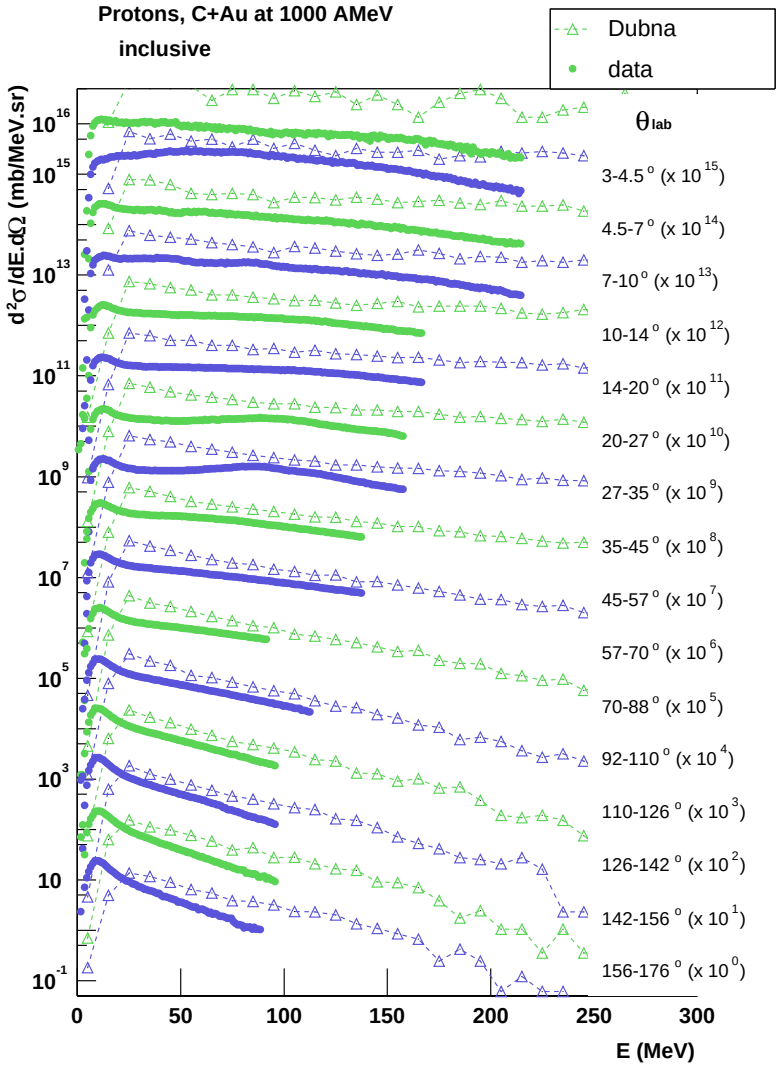

Figure 5.14: *The proton kinetic energy spectra (full circles) for C+Au at 1000 AMeV are compared to the Dubna cascade model (open stars) at* $3^o \leq \theta_{lab} \leq 176^o$ *for inclusive data.*

The Isabel cascade model differs from the Liège and Dubna cascade in the treatment of the particles. It follows not each particle but the ensemble of the particles as a function of time. We compare again inclusive proton kinetic energy spectra at $3 \leq \theta_{lab} \leq 176^o$ from the experiment and the Isabel cascade model in Fig. 5.15. As the Dubna code, the cascade is there not followed by any percolation and evaporation codes. In this case, the slope of the spectra for $E_{kin} \geq 25$ MeV is not well reproduced. Isabel overestimates the temperature of the high energy source. Nevertheless, the yields of the Isabel spectra are very close to the experimental ones for $E_{kin} \geq 90$ MeV.

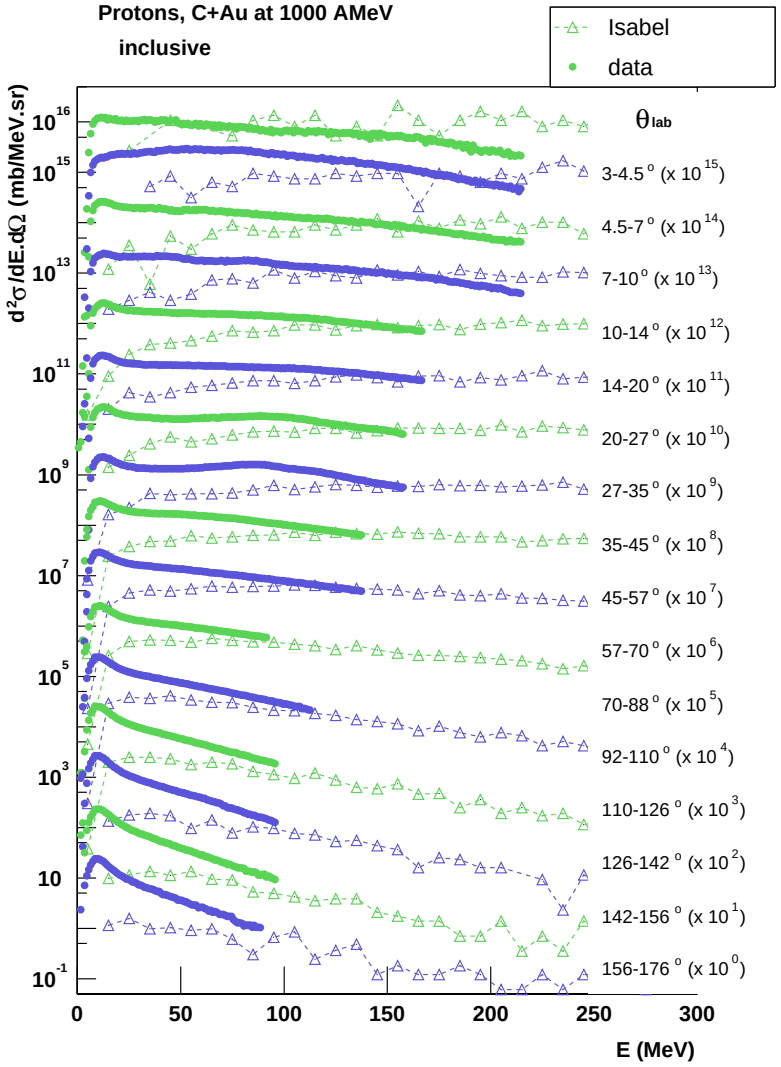

Figure 5.15: *The proton kinetic energy spectra (full circles) for C+Au at 1000 AMeV are compared to the Isabel cascade model (open triangles) at $3^o \leq \theta_{lab} \leq 176^o$ for inclusive data.*

Comparison with EOS data

The EOS collaboration performed few years ago a study of the multifragmentation of the reaction Au+C at 1000 AMeV. In order to check the quality of the INDRA analysis, we compare here the inclusive proton kinetic energy spectra coming from the two experiments. The EOS spectra are extracted from the references [Hau00] for $0 \leq E_{kin} \leq 100$ MeV and [Sri99] for $50 \leq E_{kin} \leq 300$ MeV. The spectra are there presented with their probability as Y-coordinate. These spectra are respectively normalized by the empirical factors 220 and 90, respectively, in order to overlap each other in the region $50 \leq E_{kin} \leq 100$ MeV and to be comparable to the INDRA spectrum in absolute cross-section.

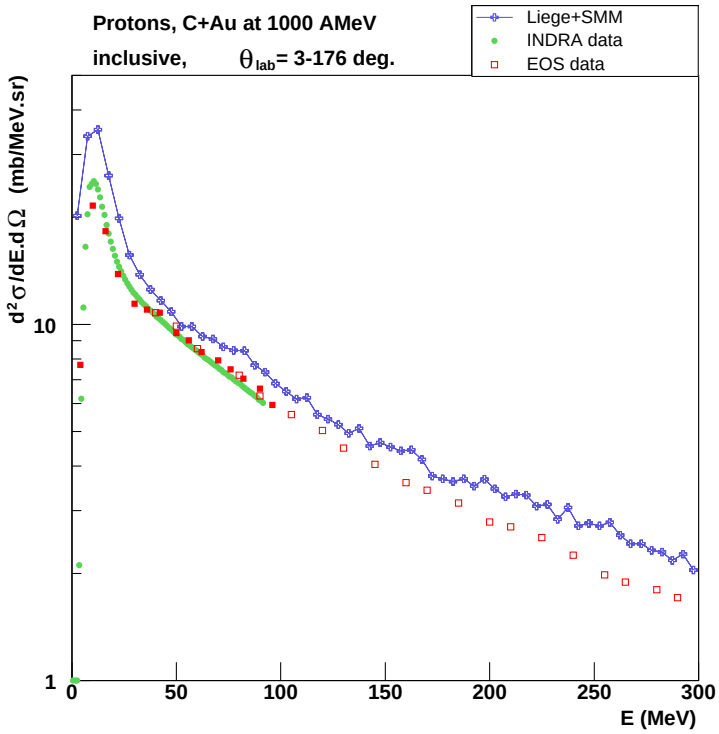

Figure 5.16: *The INDRA proton kinetic energy spectra (full circles) for C+Au at 1000 AMeV are compared to the EOS spectra (full and open squares) and to the Liège cascade model coupled to the Dresner evaporation (open crosses) for inclusive data at $3^o \leq \theta_{lab} \leq 176^o$. The full and open squares correspond to EOS data coming from the references [Hau00] and [Sri99], respectively.*

The experimental spectra are also compared to the Liège cascade model coupled with SMM. Fig. 5.16 presents the very good agreement between the two experiments. The model overestimates the inclusive experimental data by about 10% but produces a spectrum with the same slope parameter as the EOS and INDRA spectra.

Proportions of cascade and multifragmentation protons

The overall good agreement between the Liège cascade code coupled with SMM and the INDRA experimental data allows the identification of the proton sources. The proportions of protons in yield and kinetic energy emitted by these two sources are presented in Fig. 5.17 for the system C+Au at 1000 AMeV at $0^o \leq \theta_{lab} \leq 180^o$ as a function of the reduced impact parameter b/b0 for an 'ideal' detector, that means without high energy thresholds.

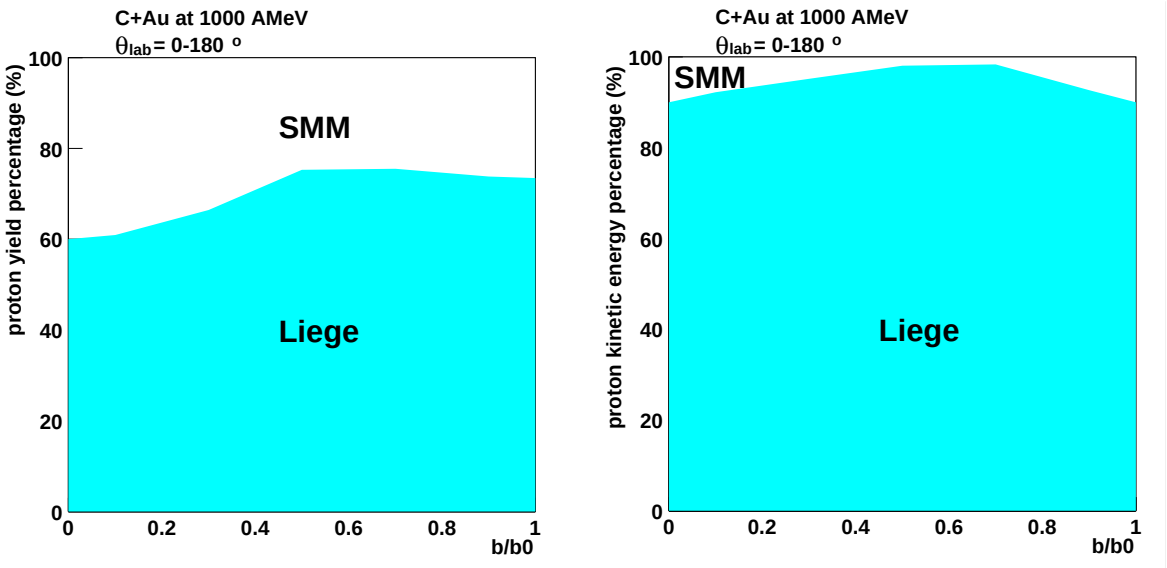

Figure 5.17: *Proportions of proton yields (left panel) and kinetic energy (right panel) between cascade (Liège) and multifragmentation (SMM) for the system C+Au at 1000 AMeV in 4π.*

The cascade proton yield increases from 60% of the total proton emission for central collisions to 75% for $0.6 \leq b/b0 \leq 0.8$ and decreases slightly for the most peripheral reactions due to the presence of the carbon projectile simulated by SMM. The cascade kinetic energy follows the same evolution from 90% for central collisions to 98% for $0.6 \leq b/b0 \leq 0.8$. because of the high energy of the projectile, the proportion of 'SMM proton' kinetic energy is higher in the peripheral collisions.

INDRA has an angular coverage of almost 4π but owns low energy thresholds in the CsI crystals depending of the telescope angle in the laboratory. Consequently, the proton proportions in yield and kinetic energy presented in Fig. 5.18 exhibit a amount of cascade protons weaker of 10 to 20% than in the case of an 'ideal' detector. However, the distributions as functions of the reduced impact parameter show about the same increase, from 40% to 55% in yield and from 70% to 88% in kinetic energy. from central to semi-peripheral collisions followed by a slight decrease. This decrease is less prononced for the kinetic energy in peripheral collisions as the particles emitted in these reactions are less energetic.

The angular distributions of the proton yield proportions presented in Fig. 5.19 show a predominance of the cascade protons at forward angles for all impact parameters, as the multifragmentation protons are emitted by the target spectators nearly isotropically in the SMM model. This predominance of the cascade protons increases from 78% to 98% with the decreasing centrality. For the most peripheral collisions (b/b0=0.8-1.0), the projectile protons enhance the SMM proportion at very small angles. Nevertheless, the proportion of cascade protons at backward angles stays around 30-40% for all impact parameters due to the asymmetry of the system.

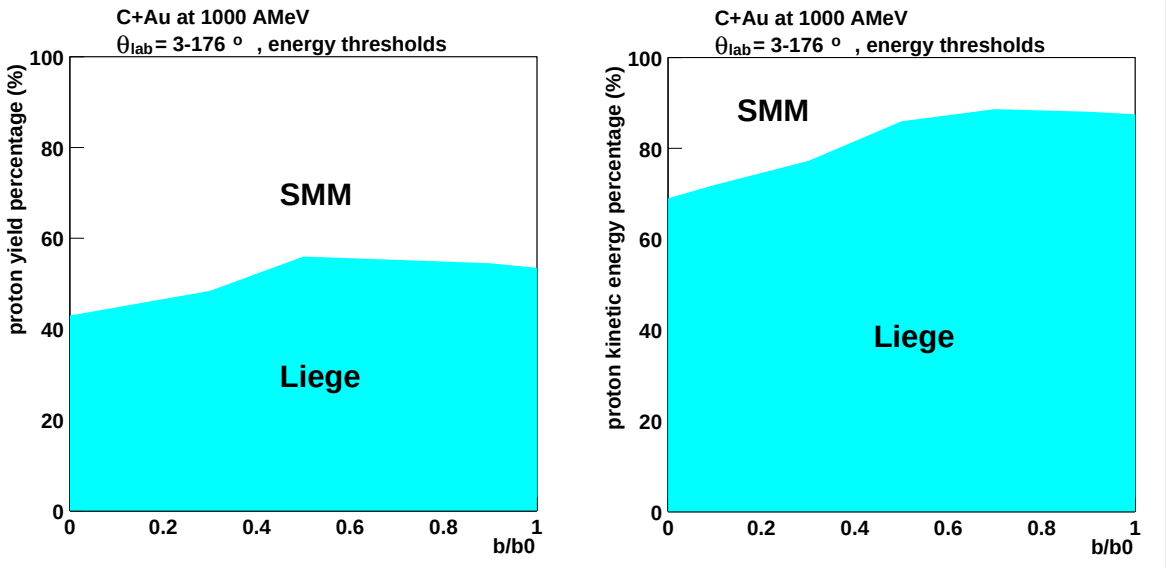

Figure 5.18: *Proportions of proton yields (left panel) and kinetic energy (right panel) between cascade (Liège) and multifragmentation (SMM) for the system C+Au at 1000 AMeV with the angular coverage ($3^o \leq \theta_{lab} \leq 176^o$) and the energy threshold conditions of the INDRA detector.*

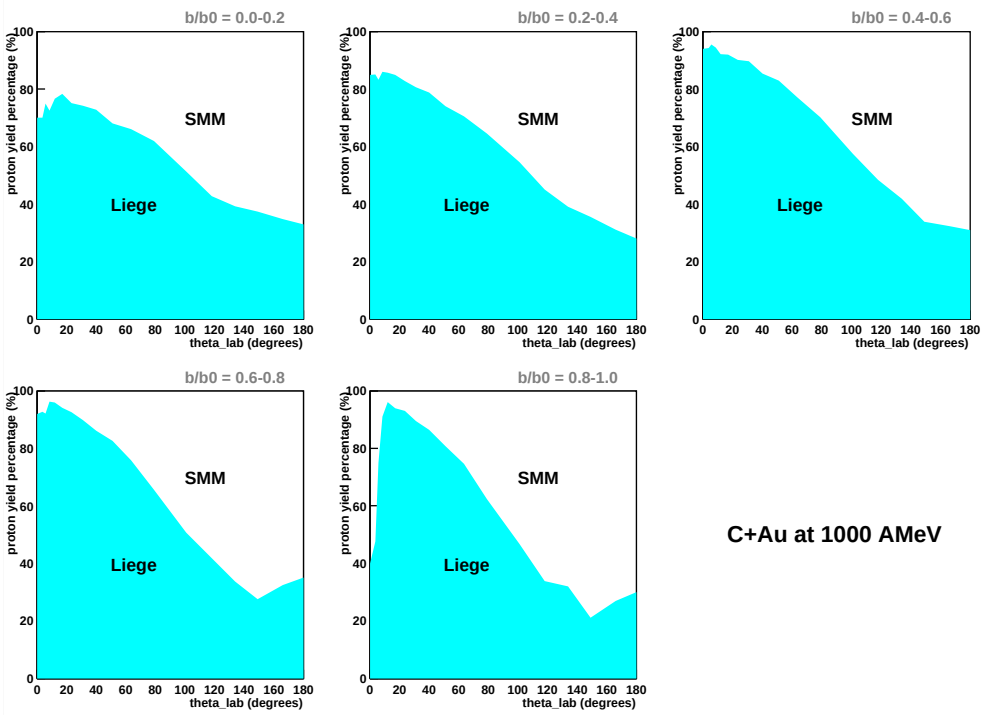

Figure 5.19: *Proportions of proton yields between cascade (Liège) and multifragmentation (SMM) as functions of θ_{lab} and the reduced impact parameter b/b0 for the system C+Au at 1000 AMeV.*

The first ALADIN caloric curve was determined from Au+Au data at 600 AMeV [Poc95] (see Introduction, Fig. 2). The features of the detector and the system led to certain analysis conditions: an angular limitation of $\theta_{lab} < 7.3^o$, i.e. $p_t < p_{beam}.sin7.3^o$, and a rapidity cut at y > 70% of the beam rapidity y_{beam}, i.e. y > 0.76. The proportions of cascade and multifragmentation proton yield and kinetic energy are presented in Fig. 5.20. In central collisions, the system is in vaporisation regime and the protons are almost all produced by the cascade model. Multifragmentation appears for mid-peripheral collisions and is revealed by a high proportion of multifragmentation protons at about 98 %. In peripheral reactions, there is evaporation of the system and still emission of fragments. This may explain the 95 % in yield and 85 % in kinetic energy of multifragmentation protons. One can remark that the proportions in yields and kinetic energy are in this case similar. This is due to the selection of the projectile source by applying the ALADIN conditions. This estimation of the proportions of protons produced by the cascade or the multifragmentation stages may allow a rough correction of the nuclear caloric curve determined in ALADIN studies.

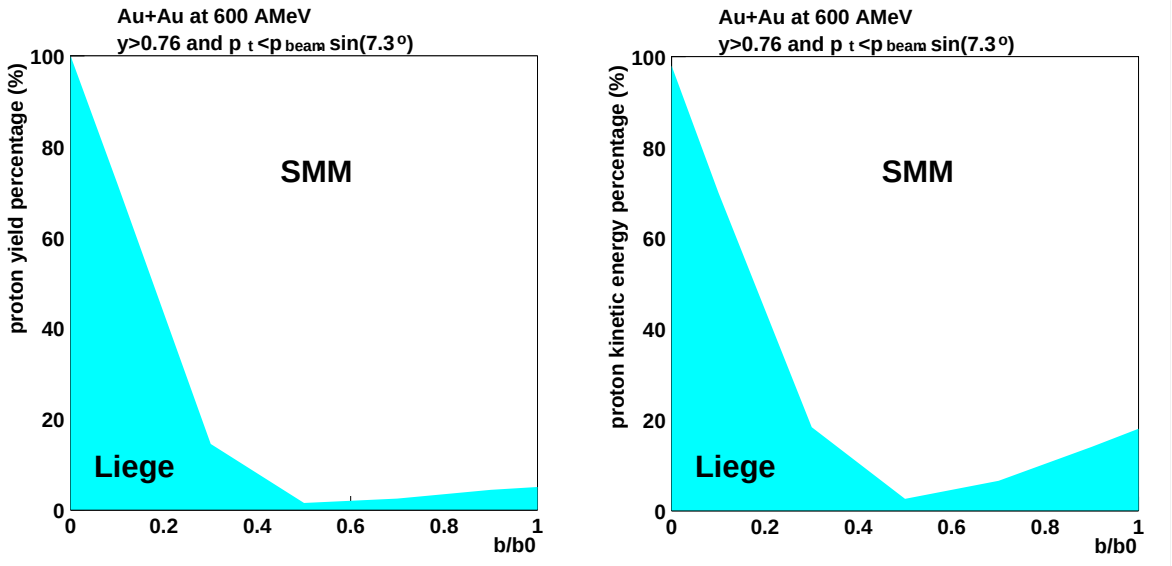

Figure 5.20: *Proportions of proton yields (left panel) and kinetic energy (right panel) between cascade (Liège) and multifragmentation (SMM) for the system Au+Au at 600 AMeV with the momentum ($p_t < p_{beam}.sin(7.3^o)$) and rapidity ($y > 0.76$) conditions applied in ALADIN analysis.*

Chapter 6

Fragments, Determination of the Target Source

According to the two-stage scenario of multifragmentation reactions, the first stage of the reaction results in the formation of a remnant, which eventually undergoes multifragmentation in the second reaction step, if sufficiently excited. This chapter is devoted to the study of fragments ($Z > 2$) coming from the breakup of this remnant.

6.1 Fragment identification

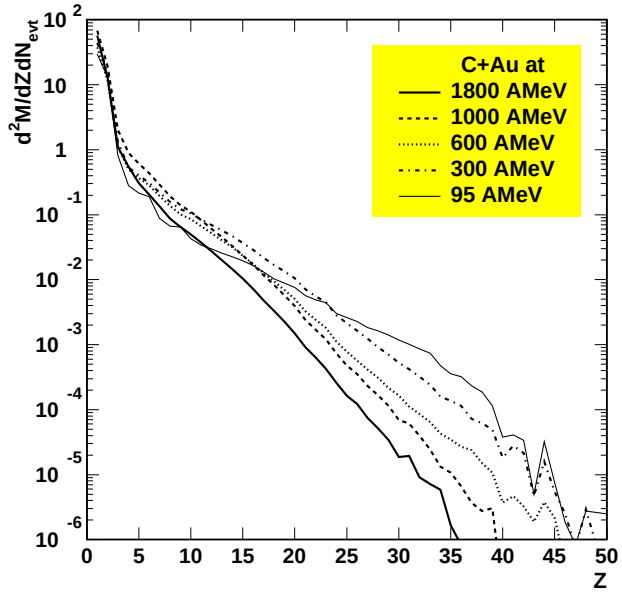

Figure 6.1: *Inclusive charge distributions for the system C+Au at the incident energies 95 (thin full line), 300 (dashed-dotted line), 600 (dotted line), 1000 (dashed line), and 1800 (thick full line) AMeV.*

In the INDRA detector, fragments are identified in the whole detector with the exception of the CsI crystals for $\theta_{lab} > 90^o$ (see chapter 3.1), the heaviest fragments being emitting at forward angles $\theta_{lab} < 45^o$. This emission decreases with the increasing incident energy, as shown in Fig. 6.1, while the amount of Intermediate Mass Fragments (IMF's) with $3 \leq Z \leq 30$

is higher for the energies 600 and 1000 AMeV. This trend is also visible in the IMF mean multiplicity as a function of the charged particle multiplicity N_c (Fig. 6.2). The IMF emission reaches a maximum around $N_c = 40$ for the incident energies 600, 1000, and 1800 AMeV. The distributions for the reactions at 1000 and 1800 AMeV decrease slightly for $N_c > 40$. This 'rise and fall' effect was already observed for symmetric and asymmetric systems for various beam energies in ALADIN experiments [Sch96, Sch96b]. The IMF distributions published by the ALADIN and EOS collaborations [Hau98] for the Au+C at 1000 AMeV reaction give a maximum IMF mean multiplicity of 4 fragments for $N_c = 40$ while the INDRA data for the same system in direct kinematics provides a mean multiplicity of 1.7 for the same value of N_c. This discrepancy is due to too high identification thresholds in the backward ionisation chambers ($\theta_{lab} > 45^o$). In direct kinematics, at relativistic energies, the target has a very low velocity and emits fragments with a low kinetic energy themselves. With high identification thresholds, about a half of the fragments is missed. Nevertheless, this inconvenience does only slightly handicap the fragment study exposed in this chapter. At backward angles, the low part of kinetic energy spectra is then not taken in account.

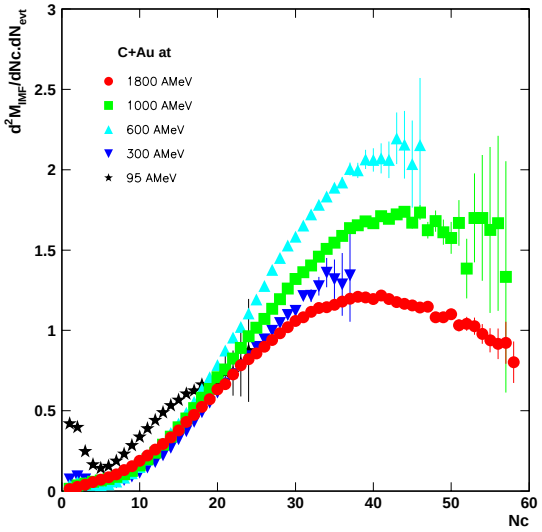

Figure 6.2: *Intermediate Mass Fragment ($3 \leq Z \leq 30$) mean multiplicities for the reaction C+Au at 95 (stars), 300 (triangles down), 600 (triangles up), 1000 (squares), and 1800 (circles) AMeV as function of the charged particle multiplicity N_c.*

6.2 Characteristic of the target source

Kinetic energy spectra

The fragments, as the protons in the previous chapter, may give indications about their emitting sources through their kinetic energy spectra. These indications can be the temperature, the cross section, the velocity, the Coulomb energy or the radial flow of the sources. In order to take into account the different sources contributing to the experimental kinetic energy spectra, we use the Moving Source Fit code, a combination of Maxwell-Boltzmann functions previously utilised in the proton case (see chapter 5 and appendix C). We apply again the formulae corresponding to two sources moving in the laboratory with certain temperatures, cross sections, and velocities. The Coulomb repulsion, peak energy and width, plays a role for the two sources, this time, and the radial flow is again fixed to zero for the two sources.

Fig. 6.4 to 6.9 present the kinetic energy spectra (symbols) of the elements lithium, beryllium, boron, carbon, nitrogen and oxygen for central collisions (reduced impact parameter b/b0=0.0-0.2) for the reaction C+Au at 1000 AMeV fitted with the Moving Source Fit code (full lines). The spectra slopes decrease with the increasing angle θ_{lab} due to the velocity of a high energy source. One can remark the non-exponential shape of the beryllium spectra at $14^o \leq \theta_{lab} \leq 45^o$ or the boron spectra at $35^o \leq \theta_{lab} \leq 45^o$. This non-exponential behaviour is due to an identification problem in the silicon detector that has not been solved up to now. Similarly, the lithium and beryllium spectra are cut at high energy at $70^o \leq \theta_{lab} \leq 176^o$ because of the non-exponential behaviour of the CsI's. The spectra are normalised according to the solid angle Ω and presented without statistical error bars for the clarity of the presentation.

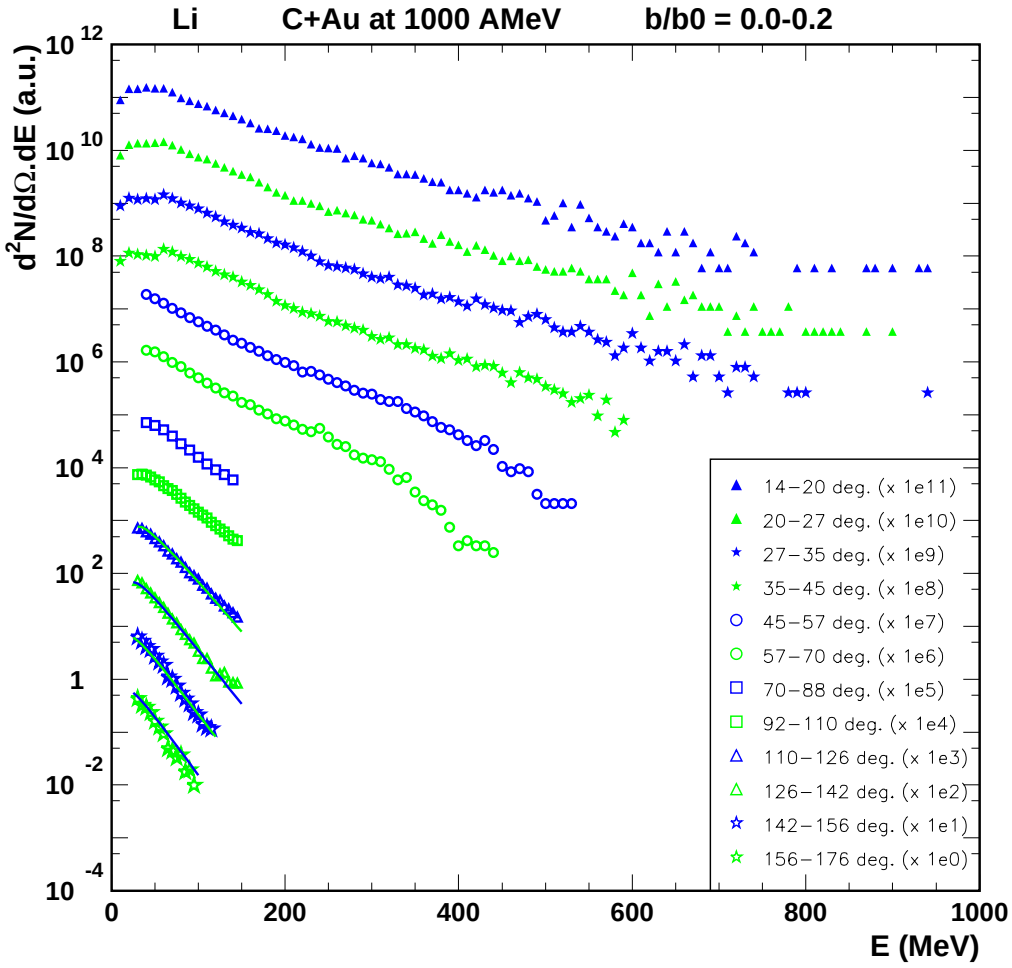

Figure 6.3: *Fit (full lines) of the target source of lithium kinetic energy spectra (symbols) for the system C+Au at 1000 AMeV for central collisions (b/b0=0.0-0.2) at* $110 \leq \theta_{lab} \leq 176^o$.

The fits are done for two sources, the target source at E $\leq$ 120 MeV and a second source at higher kinetic energies. The target source is first fitted with fit parameters for one source at backward angles ($110 \leq \theta_{lab} \leq 126^o$) as shown in Fig. 6.3. As its temperature is then determined and fixed as entrance parameter, the spectra from $\theta_{lab} = 14^o$ to $\theta_{lab} = 176^o$ are fitted together for two sources. The addition of a second source can modify the fits at backward angles as for the lithiums: the inverse slope parameters of the lithium fits at $110 \leq \theta_{lab} \leq 126^o$ are a little higher in Fig. 6.4 than in Fig. 6.3.

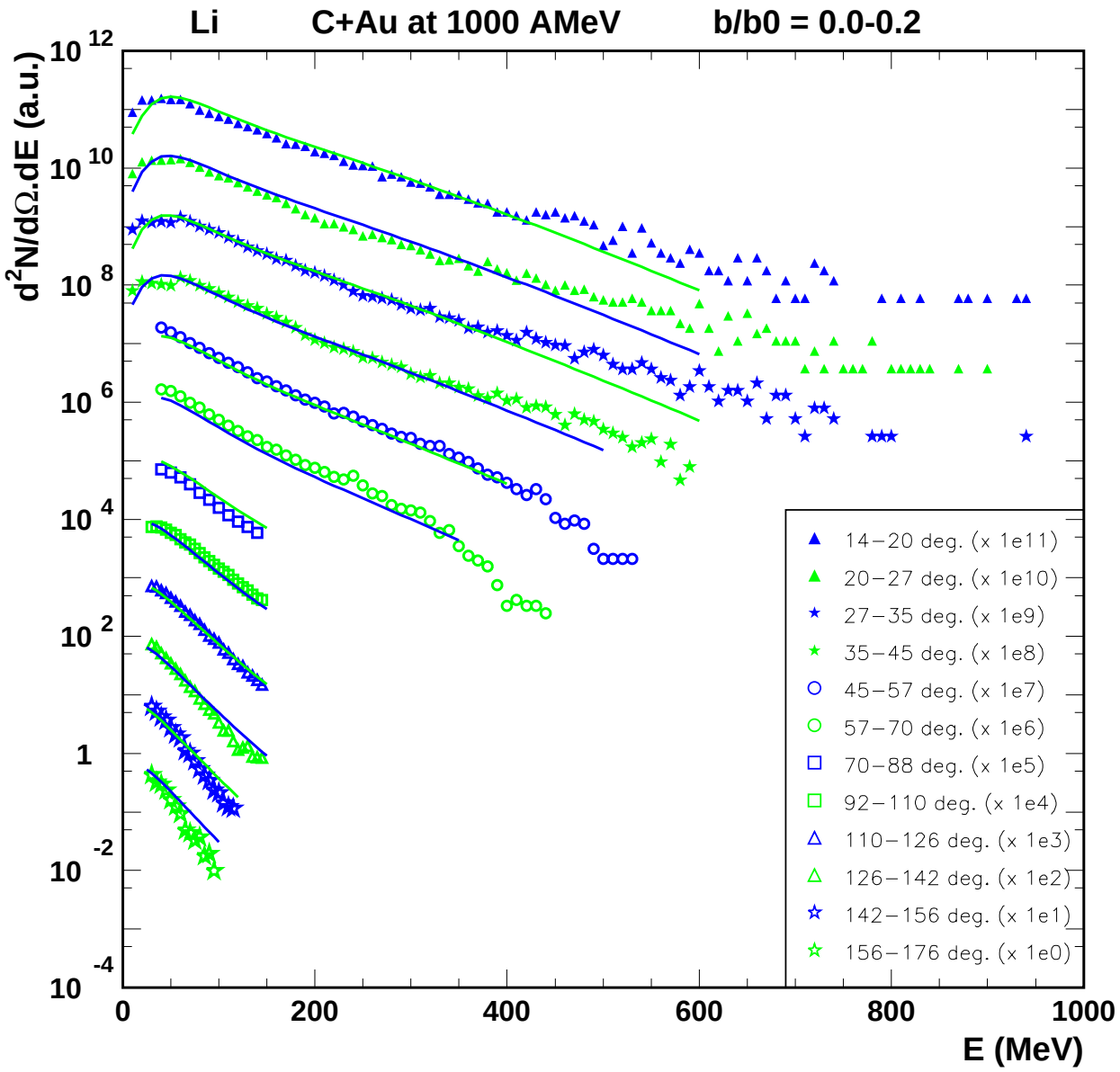

Figure 6.4: *Global fit (full lines) of lithium kinetic energy spectra (symbols) for the system C+Au at 1000 AMeV for central collisions (b/b0=0.0-0.2) at* $14 \leq \theta_{lab} \leq 176^o$.

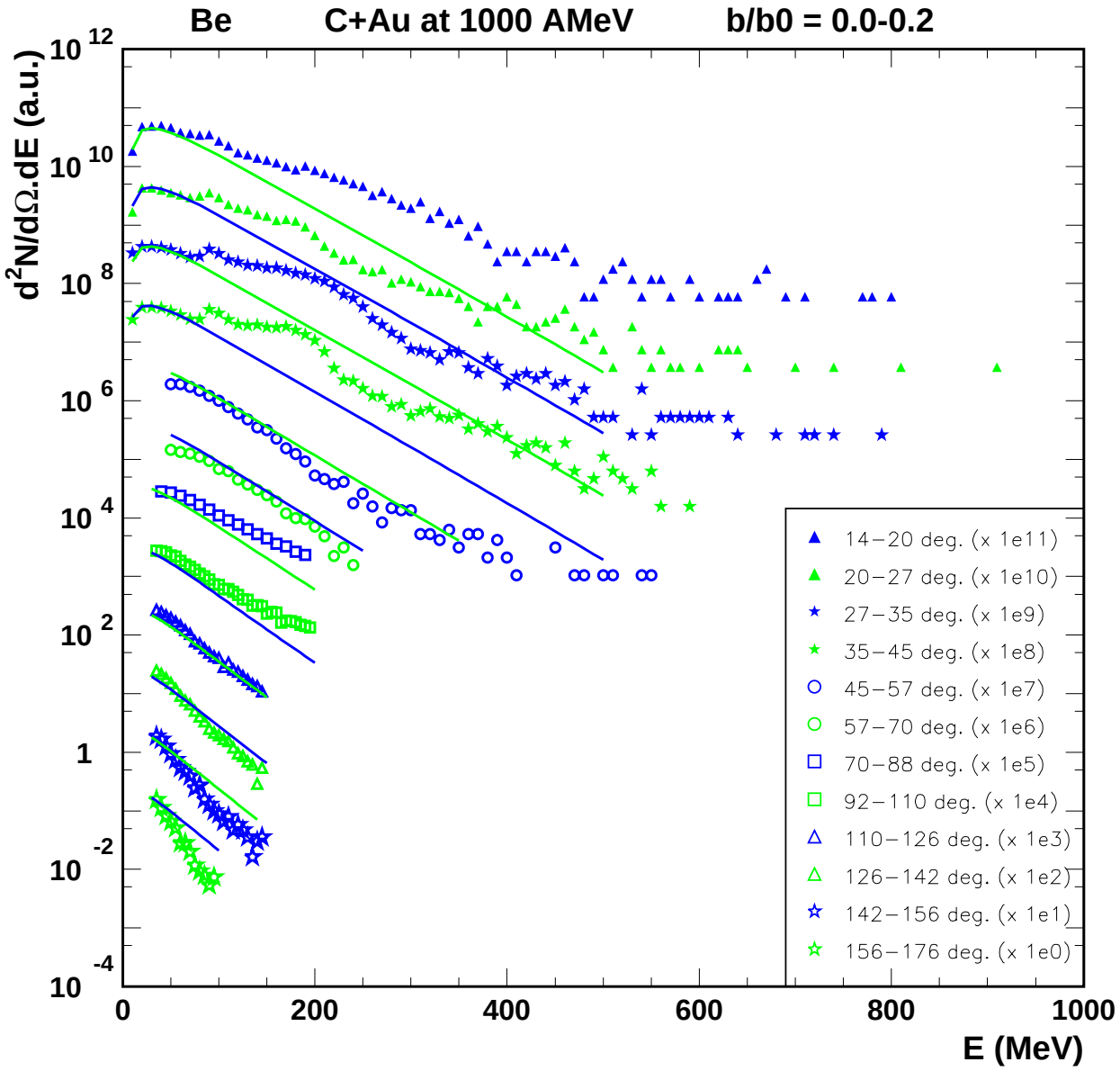

Figure 6.5: *Global fit (full lines) of beryllium kinetic energy spectra (symbols) for the system C+Au at 1000 AMeV for central collisions (b/b0=0.0-0.2) at* $14 \leq \theta_{lab} \leq 176^o$. *The non-linear shape of spectra at* $14 \leq \theta_{lab} \leq 45^o$ *is due to an identification problem in the silicon detector. The fits of these spectra take only in account the data coming from the ionisation chamber (*$E \leq 120$ *MeV) and from the CsI (*$E \geq 300$ *MeV).*

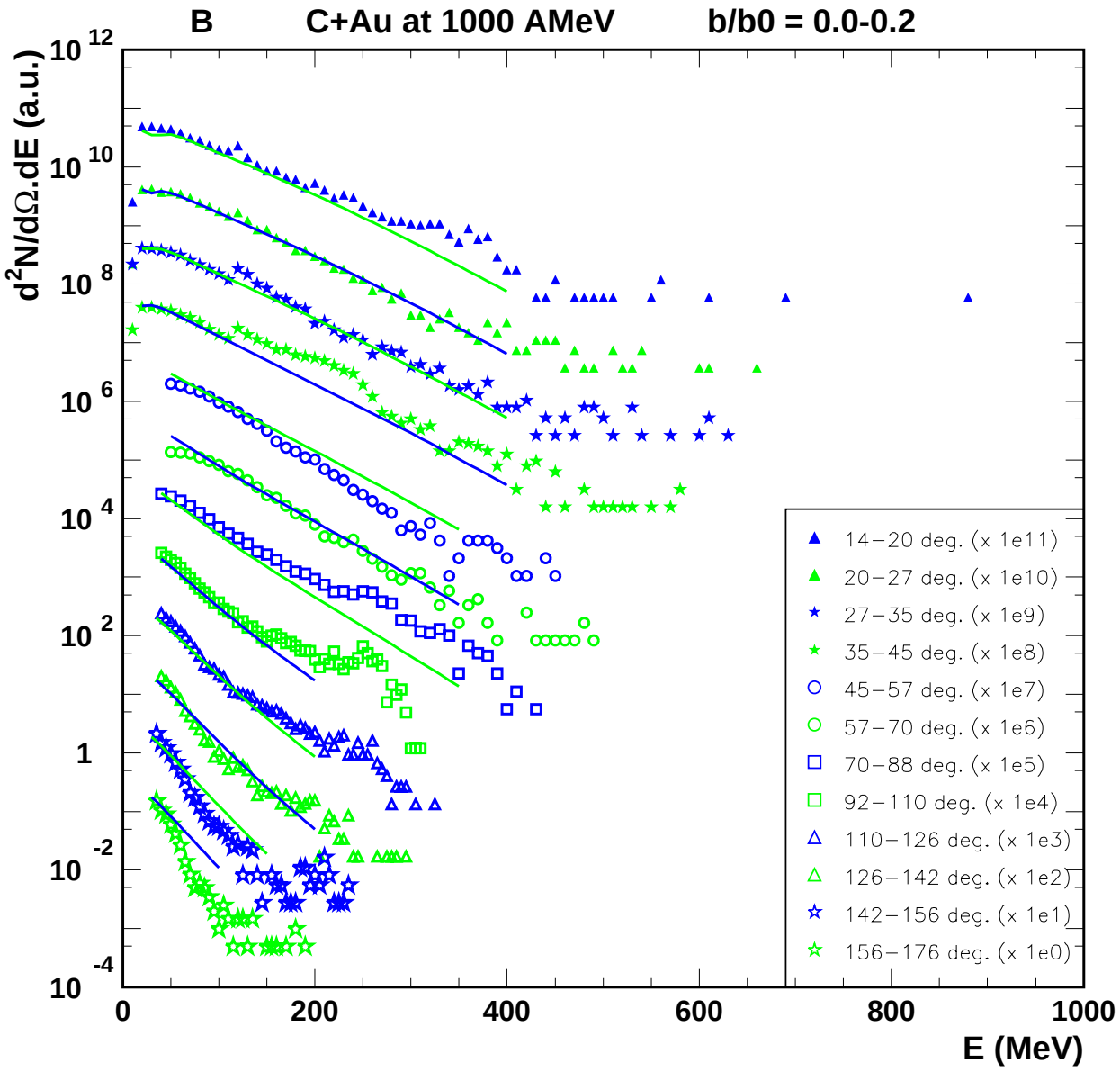

Figure 6.6: *Global fit (full lines) of boron kinetic energy spectra (symbols) for the system C+Au at 1000 AMeV for central collisions (b/b0=0.0-0.2) at* $14 \leq \theta_{lab} \leq 176^o$. *The non-linear shape of the spectrum at* $35 \leq \theta_{lab} \leq 45^o$ *is treated in the same way than in the Beryllium case.*

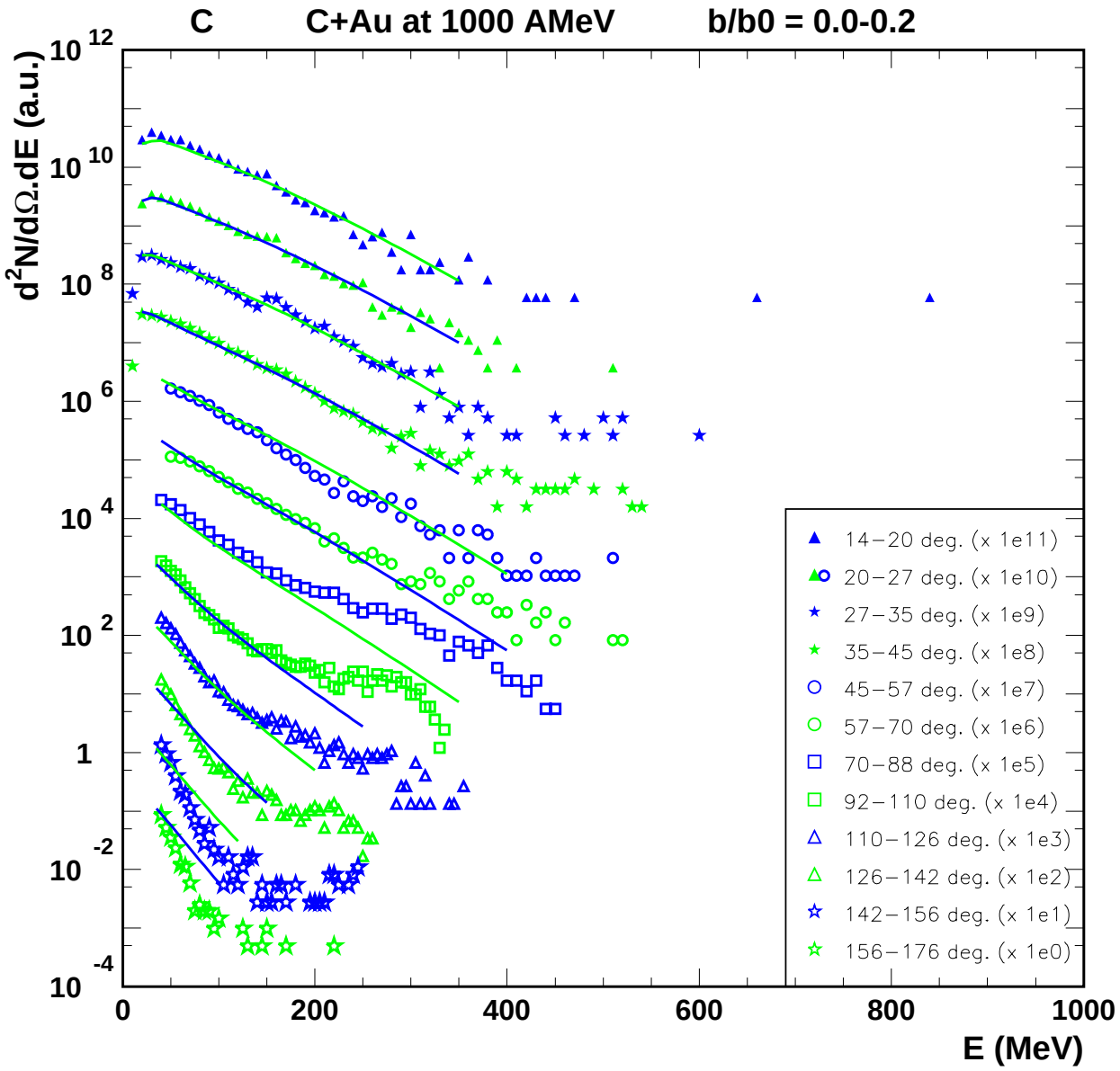

Figure 6.7: *Global fit (full lines) of carbon kinetic energy spectra (symbols) for the system C+Au at 1000 AMeV for central collisions (b/b0=0.0-0.2) at* $14 \leq \theta_{lab} \leq 176^o$.

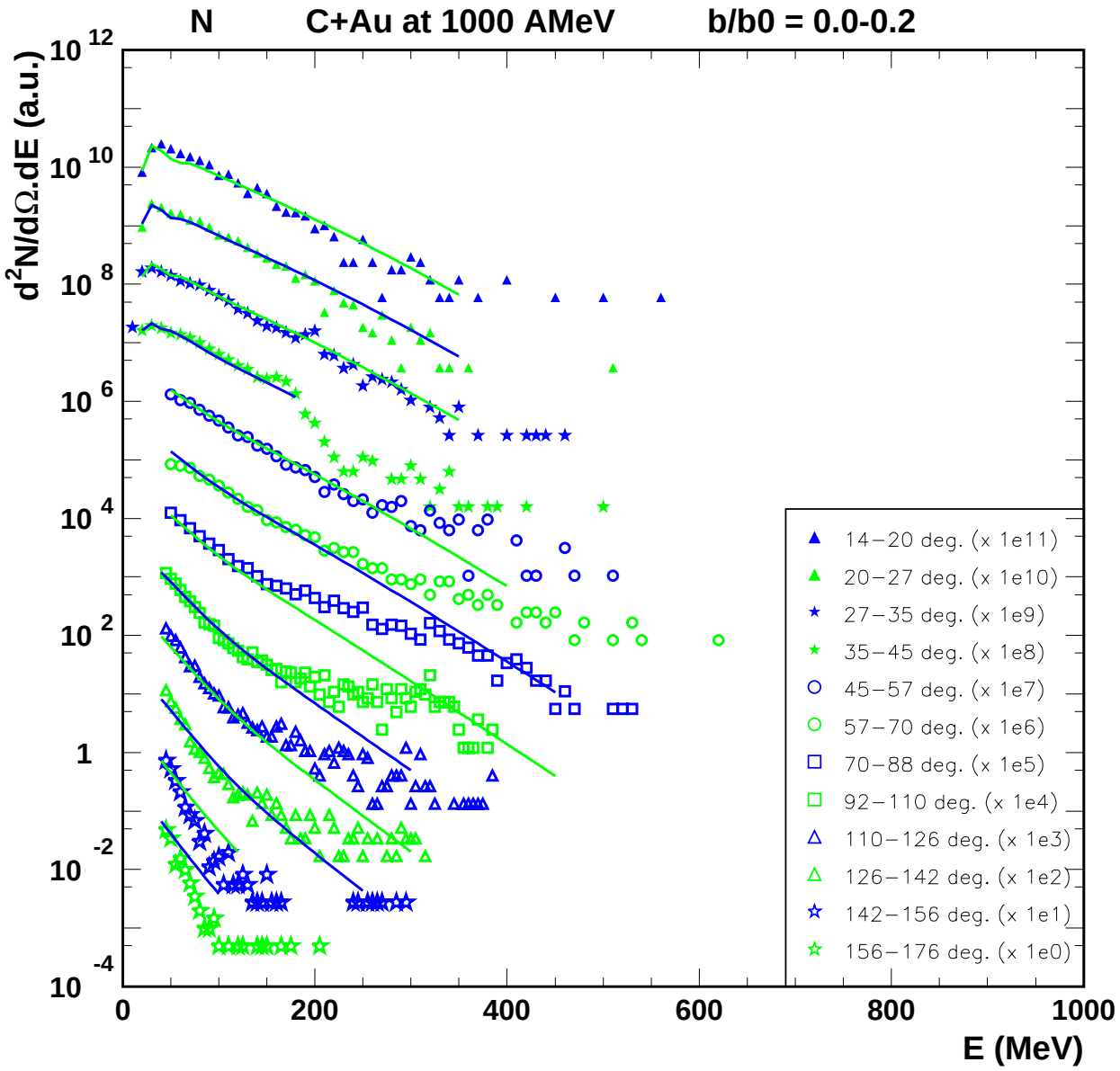

Figure 6.8: *Global fit (full lines) of nitrogen kinetic energy spectra (symbols) for the system C+Au at 1000 AMeV for central collisions (b/b0=0.0-0.2) at* $14 \leq \theta_{lab} \leq 176^{o}$.

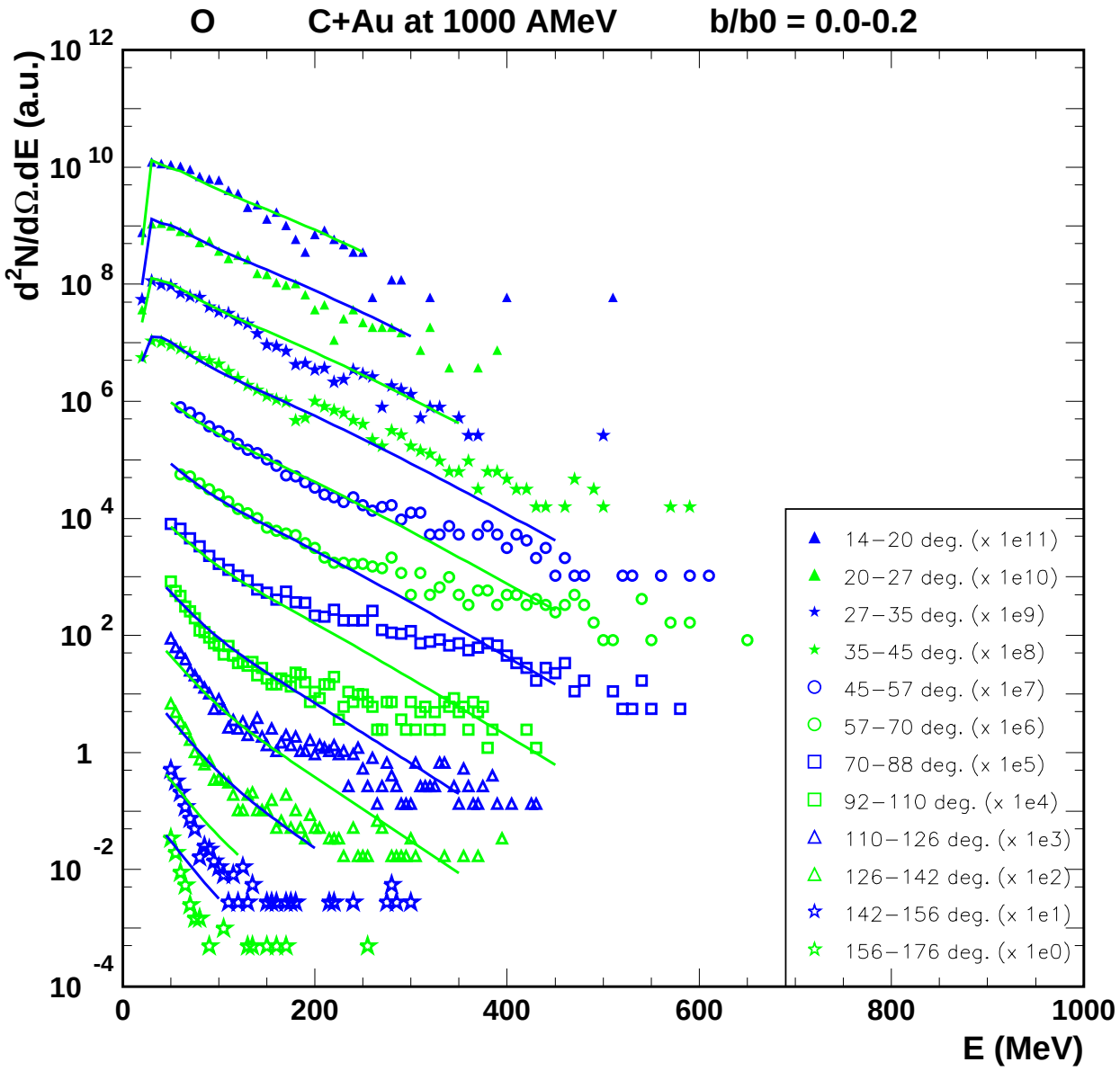

Figure 6.9: *Global fit (full lines) of oxygen kinetic energy spectra (symbols) for the system C+Au at 1000 AMeV for central collisions (b/b0=0.0-0.2) at* $14 \leq \theta_{lab} \leq 176^o$.

The target temperatures presented in the next sections are determined by the first fit at backward angles. On the other hand, the other target parameter, as the velocity, come from the two source fit. Four spectra are not enough to let converge a one source fit on stable values for these parameters. The fits of the non-linear beryllium and boron spectra take only into account the data coming from the ionisation chamber (E $\leq$ 120 MeV) and from the CsI (E $\geq$ 300 MeV). The spectra at backward angles ($45 \leq \theta_{lab} \leq 176^o$) are cut at low energy corresponding of the high identification thresholds in the ionisation chambers in this part of the INDRA multidetector. The stray particle effects for the peripheral collisions are avoided by stopping the fit at a kinetic energy corresponding to the lowest energy of these particles (see chapter 2.4).

Temperatures and velocities

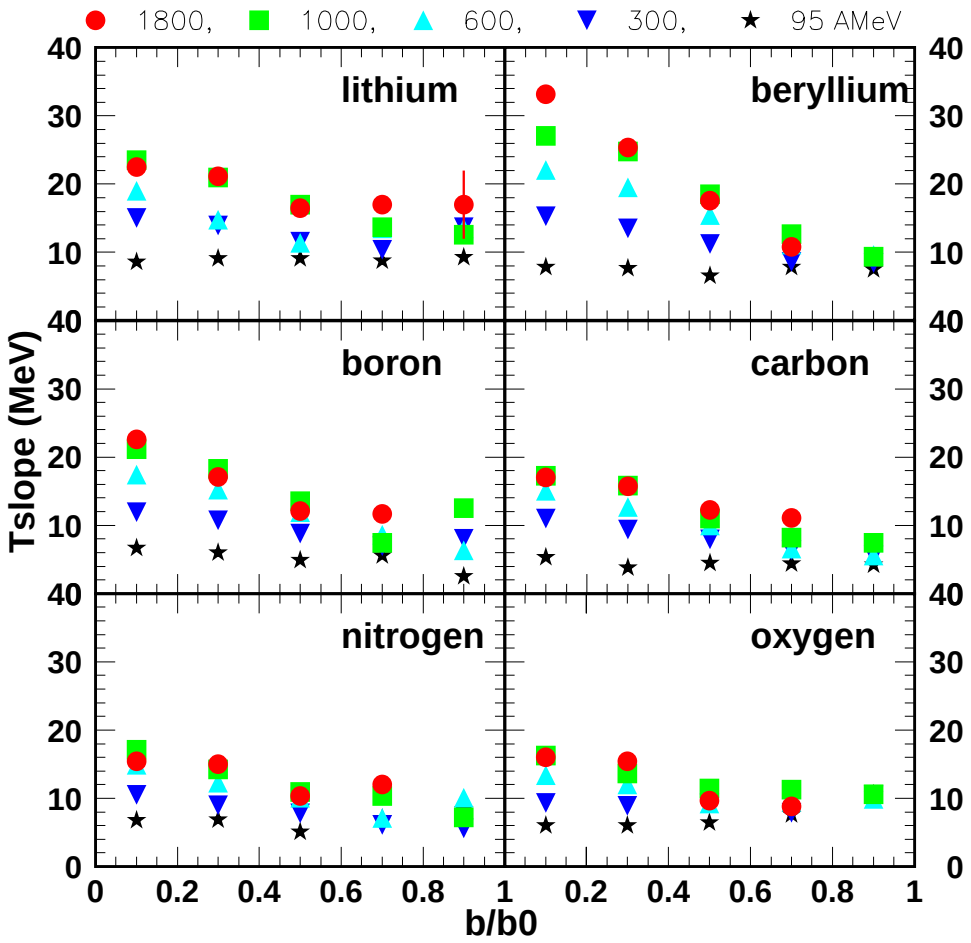

Figure 6.10: *Target slope temperature as a function of the reduced impact parameter b/b0 for the incident energies 95, 300, 600, 1000, and 1800 AMeV for the elements lithium, beryllium, boron, carbon, nitrogen, and oxygen. The very weak production of fragments of Z≥4 at 1800 AMeV for peripheral reactions does not always allow the determination of the slope temperature.*

The target temperatures are displayed in Fig. 6.10 as a function of the reduced impact parameter for the incident energies from 95 AMeV to 1800 AMeV for the light fragments lithium to oxygen. For each element, the slope temperature increases with centrality and beam energy. Nevertheless, the IMF multiplicity (see Fig. 6.2) show that at 1800 AMeV, for the highest charged particle multiplicity, the system reaches the vaporisation regime and produces more light particles and less fragments. This may explain the saturation visible in the fragment slope temperature at 1000 AMeV while this saturation does not appear in the case of the protons (see chapter 5.2).

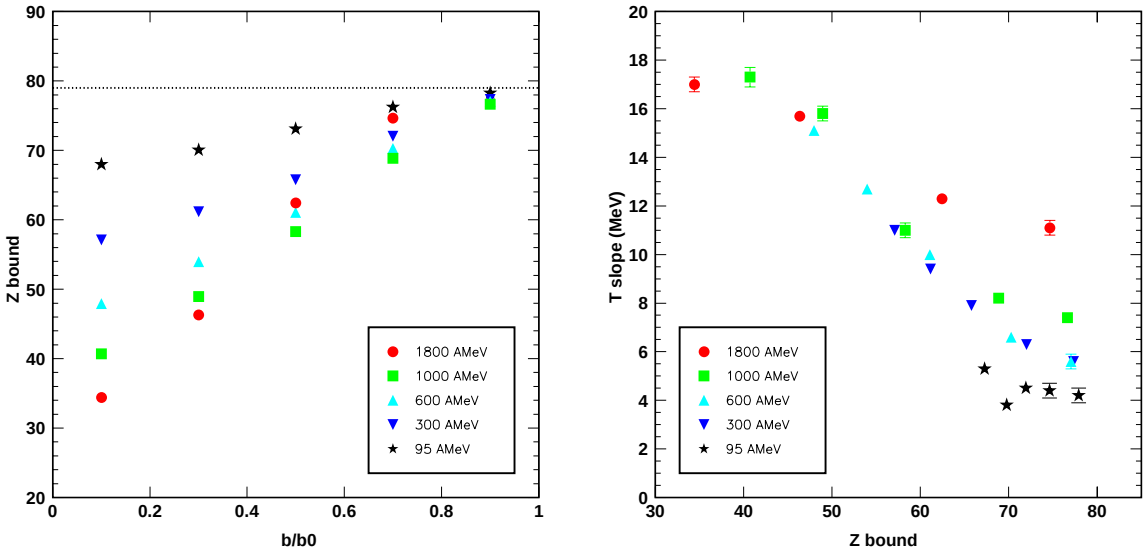

Figure 6.11: *Left panel: Z_{bound} (Z_{Au} - $M_h ydrogen$) at $45 \leq \theta_{lab} \leq 142^o$ and normalised over 4π as a function of the reduced impact parameter b/b0 for the system C+Au at the incident energies from 95 to 1800 AMeV. Right panel: Carbon slope temperature of the target source as a function of Z_{bound} for the system C+Au at the incident energies from 95 to 1800 AMeV.*

The increase of the kinetic temperature as a function of the incident energy until 1000 AMeV seems in contradiction with previous ALADIN results presenting an independence of the fragment emission with the beam energy according to the centrality determined by the variable Z_{bound} ($\sum_{Z\geq 2} Z$ or Z_{Au} - $M_{hydrogen}$ in our case) [Sch96, Ode99]. The left panel of Fig. 6.11 shows Z_{bound} as a function of the reduced impact parameter b/b0 for the system C+Au at the incident energies from 95 to 1800 AMeV. In fact, this is only an estimation of Z_{bound} because of the detector energy loss thresholds: we measure in this case the hydrogen multiplicity at $45 \leq \theta_{lab} \leq 142^o$ and we normalize over 4π. This is an approximation as in the previous chapter, we observed that none of proton source is isotropic. Moreover, in this angular region, the maximum proton energy detected by INDRA is E = 138 MeV. We then miss a part of the high energy protons, especially for central collisions. Here, we consider only the target emission but the perfect application of the formula should oblige us to take also in account the projectile emission. Nevertheless, this rough estimation of Z_{bound} gives values similar to ALADIN Z_{bound} and appears to be dependent on the reduced impact parameter and on the incident energy. This dependence is comparable to those remarked for the slope temperatures. Via the reduced impact parameter, the carbon slope

temperature of the target source is plotted as a function of Z_{bound} and exhibits for 300, 600, and 1000 AMeV an independence in beam energy. The weak production of carbons at 1800 AMeV for semi-peripheral peripheral reactions may explain the fluctuations of the slope temperature. By this way, we retrieve the universality observed in the ALADIN experiment. In fact, the variable Z_{bound} is related to the excitation of the source while the reduced impact parameter b/b0 coming from the charged particle multiplicity is connected to the geometry of the reaction. One can remark that the slope temperature of the target is very constant with the centrality of the reaction for 95 AMeV. The reactions at this energy lead only to an evaporation of the system. This effect is also visible in the IMF multiplicities in Fig. 6.2.

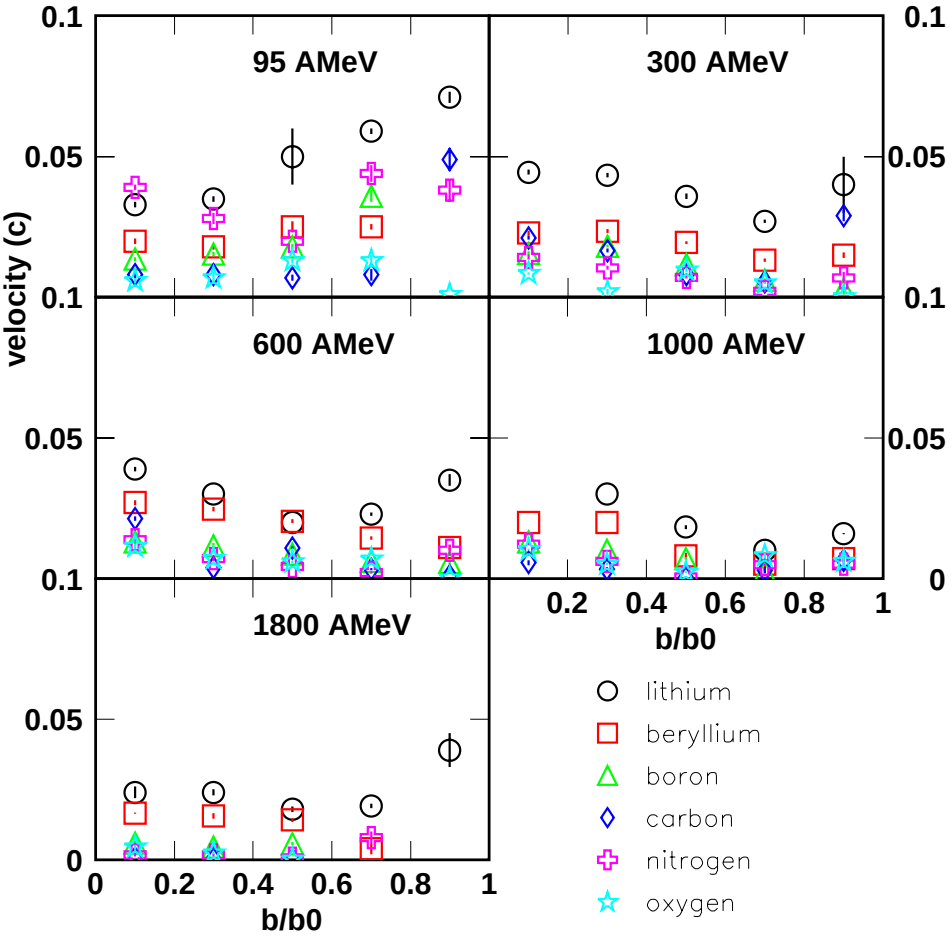

Figure 6.12: *Target velocity as a function of the reduced impact parameter b/b0 for the incident energies 95, 300, 600, 1000, and 1800 AMeV for the elements lithium, beryllium, boron, carbon, nitrogen, and oxygen. The very weak production of fragments of Z≥4 at 1800 AMeV for peripheral reactions does not always allow the determination of the slope temperature.*

The velocity of the target source, displayed in Fig. 6.12 as a function of the reduced impact parameter b/b0, present a decrease with decreasing centrality, with increasing incident energy, and with increasing charge of the fragment for the beam energy of 300 AMeV and above. The

velocity of the source at 95 AMeV, on the contrary, increases with b/b0 for the lithiums, this increase roughly diminishing for Z≥4. The fluctuations of these latter velocities are due to the very weak production of these fragments at 95 AMeV, especially for peripheral collisions. The same reason may explain the higher lithium velocities for $0.8 \leq b/b0 \leq 1.0$.

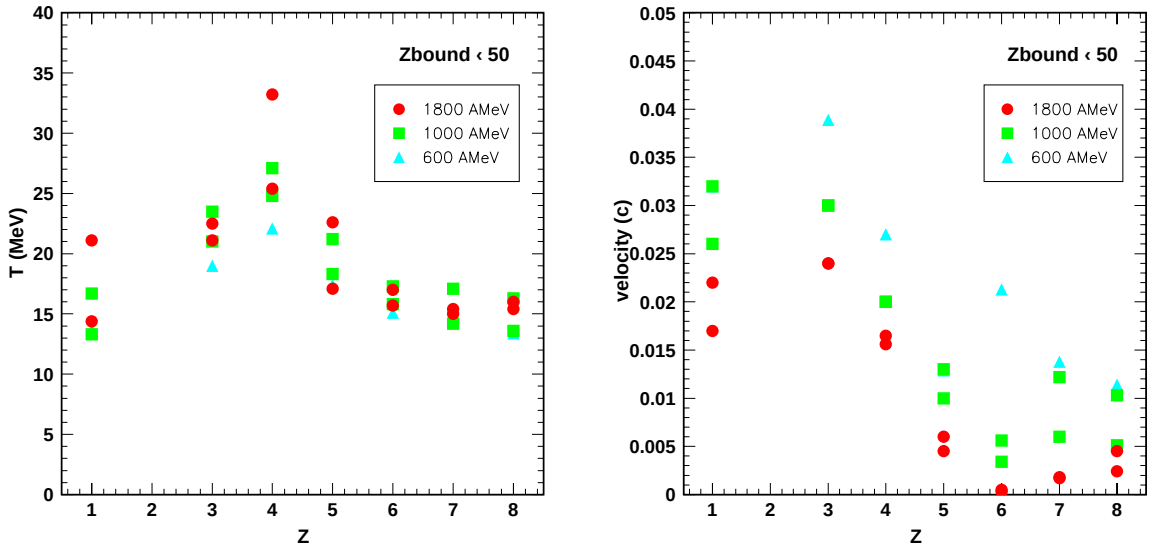

Figure 6.13: *Left panel: temperature of the target source as a function of the charge for $Z_{bound} < 50$. Right panel: velocity of the target source as a function of the charge for $Z_{bound} < 50$.*

By selecting a certain region in Z_{bound} ($Z_{bound} < 50$) corresponding to very energetic collisions, i.e. central collisions for a beam energy of 600, 1000, and 1800 AMeV, we observe in the left panel of Fig. 6.13 the distribution of the target source temperature from the protons to the oxygens. This figure shows an increase of the temperature from about 17 MeV for the protons to 27 MeV in mean value for the berylliums and a following decrease until 15 MeV for the oxygens. The higher temperature for the beryllium is not yet well understood but is suspected to be due to identification problems. The general decrease of fragment temperature as a function of the charge was already observed in Au+Au reactions at 600 and 800 AMeV in ALADIN experiments for the mean kinetic energies [Sch96, Sch96b]. The velocity distribution (right panel of Fig. 6.13 gives a maximum for the lithiums at around 0.03 c and decreases for higher Z until 0.006 c in mean value for the oxygens. One may remark that the proton temperatures and velocities are very close to the fragment ones. Nevertheless, an ideal multifragmentation source, i.e. an equilibrated source, would give the same temperature and velocity for all the light particles and fragments that it emits. The discrepancies observed here, especially the relatively high velocities of protons, lithiums and berylliums, can be due to particles coming from non-equilibrated sources. This effect shows us the limits of our experiment. In spite of these fluctuations, the low energy protons and fragments studied in this work appear as coming from the same target spectator source.

Comparison with SMM

The lithium kinetic energy spectra are compared to simulations coming from the Statistical Multifragmentation Model (SMM) (see appendix A.1) for the reaction C+Au at 1000 AMeV. The excitation energy, charge and mass input parameters are given by the combination of the Liège IntraNuclear Cascade and a percolation code, as in the previous chapter (see also appendix B.3). Fig. 6.14 shows these comparisons for the most central bin of reduced impact parameter b/b0.

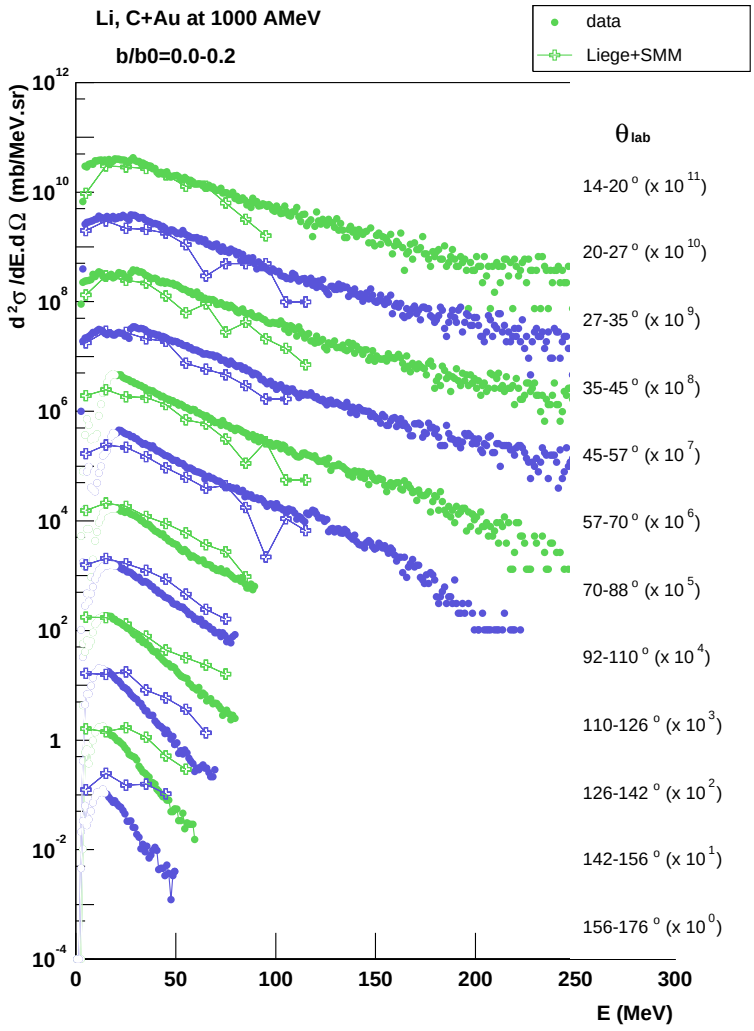

Figure 6.14: *Comparison between lithium kinetic energy spectra with the SMM multifragmentation model for b/b0=0.0-0.2 (central collisions) for the system C+Au at 1000 AMeV.*

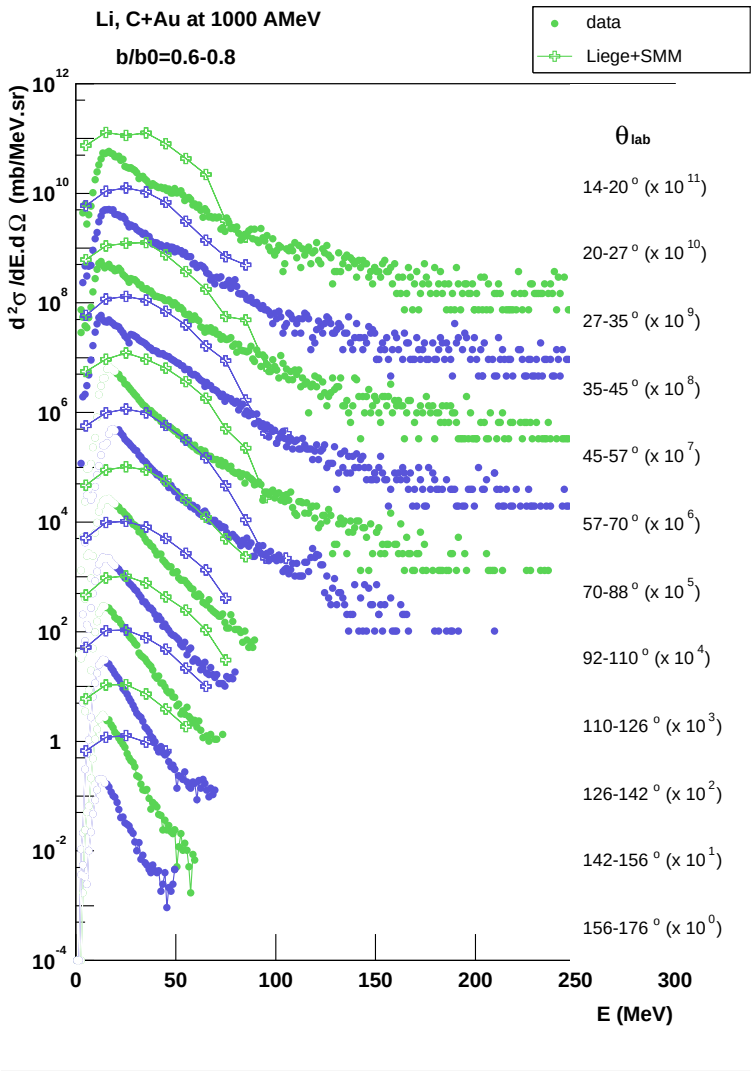

Figure 6.15: *Comparison between lithium kinetic energy spectra with the SMM multifragmentation model for b/b0=0.6-0.8 (almost peripheral collisions) for the system C+Au at 1000 AMeV.*

The model gives a globally good description of the experimental data for b/b0=0.0-0.2. Nevertheless, one may remark discrepancies already for these central collisions at backward angles, $\theta_{lab} \geq 110^o$. This high overestimation of the model increases and reaches all the angles for peripheral collisions as it is shown in Fig. 6.15. In this analysis, we used a combination of first stage models before starting the statistical model, in the contrary to previous ALADIN studies. This kind of combination give good results for protons, as shown in the previous chapter, but may give not well adapted input parameters to SMM in the frame of the fragment study. The cascade and the percolation code seem to produce a too high excitation energy for the peripheral collisions. Moreover, even if SMM reproduces well the target source in central collisions, the lithium spectra continue at large kinetic energy, coming from a second source that may be called non-statistical.

6.3 Second fragment source

In spite of the non-statistical feature of the second fragment source at high energies, we attempt to fit this source by the combination of Maxwellians previously used for the target source. In central collisions (see Fig. 6.4 to 6.9), one can observe some discrepancies between the fits and the experimental spectra for the heaviest ions at $45 \leq \theta_{lab} \leq 126^o$ from E > 200 MeV. The divergence of the fit increases with b/b0. The Fig. 6.16 shows the impossibility of the code to fit the lithium spectra at forward angles ($14 \leq \theta_{lab} \leq 57^o$) for peripheral C+Au reactions at 1000 AMeV for E > 100 MeV.

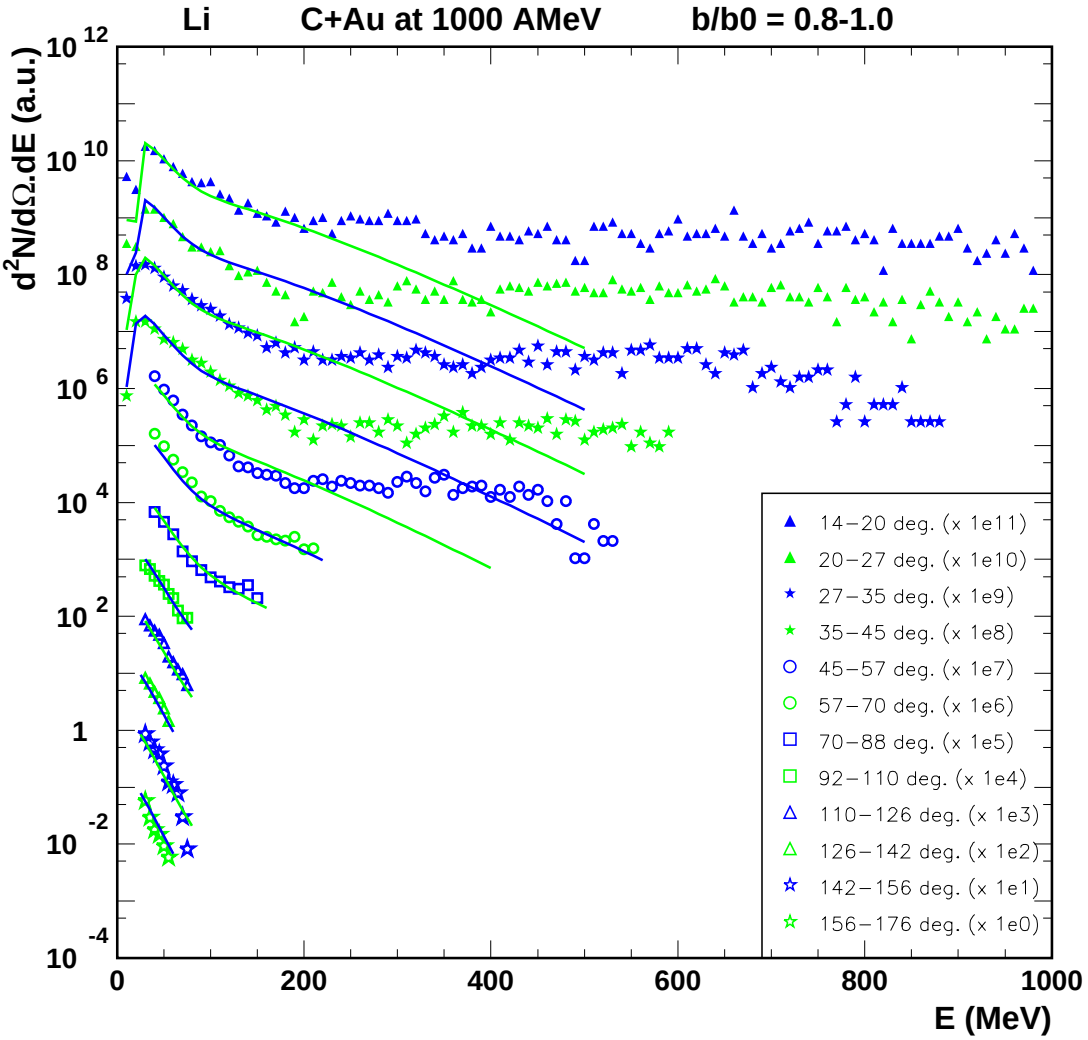

Figure 6.16: *Global fit (full lines) of lithium kinetic energy spectra (symbols) for the system C+Au at 1000 AMeV for peripheral collisions (b/b0=0.8-1.0) at* $14 \leq \theta_{lab} \leq 176^o$. *The non-linear of the spectra at backward angles* $70 \leq \theta_{lab} \leq 176^o$ *is due to the stray particle effects (see chapter 2.4), the high energy part of these spectra is not taken in account in the fit.*

The inability of the Moving Source Fit code to fit the second fragment source can be interpreted as a signal of the non-thermal feature of this source. Besides, it is interesting to remark that these high energy fragments are not coming from a mid-rapidity source ($y \simeq 0.7$), as observed for Xe+Sn reactions between 15 and 50 AMeV in INDRA experiments [Pla00, Luk97], but their rapidity is close to the rapidity of the center of mass (see chapter 2.4). The high energy fragment source would be then characterised as non-thermal and emitting in the center of mass of the C+Au reaction.

Chapter 7

Correlations Between Early Light Particles and Fragments

In this chapter, we study the correlations between the multiplicities of charged pions or energetic protons ($E_p \geq 150$ MeV) and the fragment multiplicities in reactions $^{12}C +^{197} Au$ at incident energies from 300 to 1800 AMeV. The pions and energetic protons are both produced in an early stage, just after the collision, while the fragmentation happens at the end of the reaction process. The analysis of the correlations between these two kinds of particles should allow a better understanding of the relation between these two stages of the nuclear reaction.

7.1 Pion cycle and decay modes

In reactions at relativistic incident energies, the excitation of Δ-resonances represents an important mechanism for the transfer of energy from the relative motion of the colliding nuclei into other degrees of freedom. This excitation is the first step of pion production, it is considered as important also for the heating of the spectator residues via reabsorption or multiple scattering of the pion from the Δ decay.

At beam energies above few hundred of AMeV, the nucleons can be excited into Δ-resonances. One of the potential signals for the presence of Δ-matter is the creation of pions as decay products of the Δ-resonance. Pions are mesons, exchange particles of the strong interaction between nucleons.

The Δ-resonances and pions are coming from inelastic nucleon-nucleon reactions:

$$\begin{aligned} NN \rightarrow \Delta N \quad & \text{(hard } \Delta \text{ production)} \\ \Delta \rightarrow N\pi \quad & (\Delta \text{ decay}) \\ \Delta N \rightarrow NN \quad & (\Delta \text{ absorption}) \\ N\pi \rightarrow \Delta \quad & \text{(soft } \Delta \text{ production)} \end{aligned}$$

The pion production cycle, as it is coded in the IQMD model, is illustrated in the Fig. 7.1. The IQMD model is a variation of the QMD model, briefly presented in Appendix A, explicitly incorporating isospin and pion production via the Δ resonance [Har89]. In this diagram, the main process for sustaining Δ-matter is the $\Delta \rightarrow N\pi \rightarrow \Delta$ loop, which, however, first has to be fueled by the $NN \rightarrow \Delta N$ process.

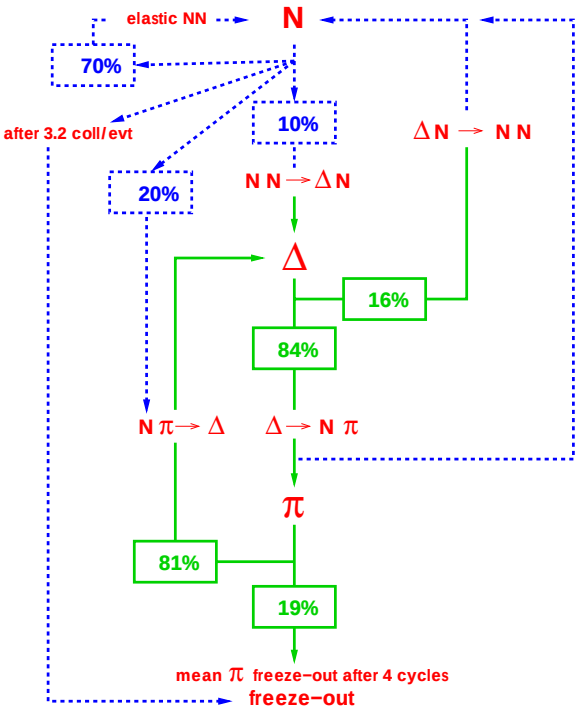

Figure 7.1: *Pion cycle in the IQMD model. The scheme describes (for $b \leq 5$ fm and time-averaged) all the model possible processes linked to the creation of Δ-matter. The probabilities in the boxes always refer to the vertices they are directly connected with. The main process for sustaining Δ-matter is the $\Delta \rightarrow N\pi \rightarrow \Delta$ loop, which, however, first has to be fueled by the $NN \rightarrow \Delta N$ process (from reference [Har89]).*

Different sorts of Δ's are produced and decay in their specific way:

$$\begin{aligned} \Delta^{++} &\rightarrow 1(p + \pi^+) \\ \Delta^{+} &\rightarrow \frac{2}{3}(p + \pi^0) + \frac{1}{3}(n + \pi^+) \\ \Delta^{0} &\rightarrow \frac{2}{3}(n + \pi^0) + \frac{1}{3}(p + \pi^-) \\ \Delta^{-} &\rightarrow 1(n + \pi^-) \end{aligned}$$

The decay of the Δ^{++} is visualized on the quark level as sketched in Fig. 7.2.

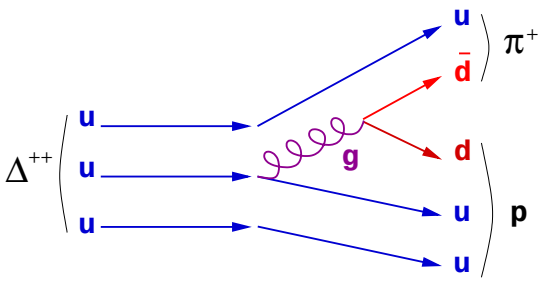

Figure 7.2: *Delta (Δ^{++}) decay. A pair quark-antiquark ($d - \overline{d}$) is created, allowing the formation of a pion (π^+) and a nucleon (p).*

The π^0 decays electromagnetically: $\pi^0 \rightarrow 2\gamma$ ($\tau_{\pi^0} = 8.4 \times 10^{-17} s$). The charged pions decay weakly in matter: $\pi^+ \rightarrow \mu^+ \nu_\mu$ and $\pi^- \rightarrow \mu^- \bar{\nu}$ ($\tau_{\pi^+,\pi^-} = 2.6 \times 10^{-8} s$). However, the negative pion π^- has a high probability to be absorbed.

7.2 Pions and fast protons in INDRA

Detection

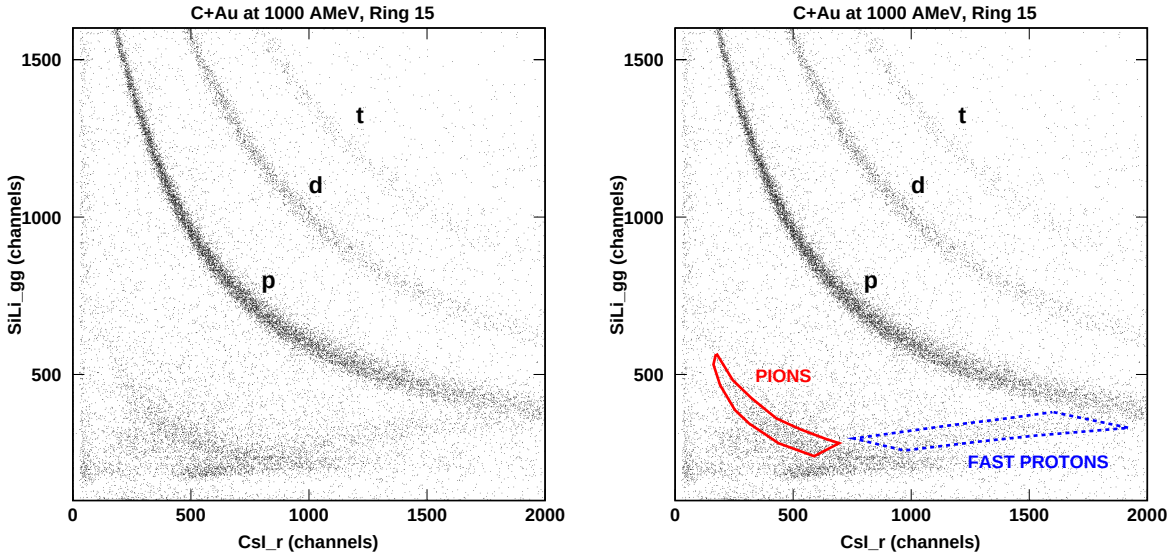

Figure 7.3: *Matrix SiLi versus CsI for the reaction C+Au at 1000 AMeV, for the ring 15 ($126^o \leq \theta_{lab} \leq 142^o$). In the left panel, the three main lines correspond to the protons, deuterons and tritons stopped in the CsI crystal. In the right panel, the area surrounded by a solid line corresponds to the π^+'s stopped in the CsI. The dashed line indicates the fast protons ($E_k \geq 150$ MeV) punching through the CsI.*

INDRA was not built for the study of pion physics. For instance, there is no magnetic field which could allow us to disentangle π^+'s and π^-'s. The 2 γ's from π^0 decay are drowned in the huge amount of neutral particles detected by the CsI's. However, as it is noticeable in the

two panels of Fig. 7.3 for the reaction C+Au at 1000 AMeV, the pions are well detected in the silicons and CsI's and specially in the calibration telescopes, also for C+Au at 300, 600, and 1800 AMeV. Pions having a mass around 140 MeV, are consequently very rare at 95 AMeV. According to the pion decay modes, we can say that the main part of the stopped pions in this spectra are π^+'s (right panel of Fig. 7.3). The π^-'s are captured and absorbed by the ions of the CsI. We expect a considerable energy deposition from the decay of the nucleus after π^- absorption which most likely moves the hit away from the pion line. The punch-through branch of the pion line, in the bottom of the two panels of Fig. 7.3, is made of the two charged pions, π^+ and π^-. Our interest is also attracted by the 'fast protons' ($E_k \geq 150$ AMeV), which are punching through the whole telescopes of INDRA. Only their energy losses are detected and they can be identified by a line below the stopped proton line, on the right part of the right panel of Fig. 7.3.

Due to this behaviour, we will not study pion energy spectra but pion yields as it will be exposed in the following of the chapter. In our study, the background is defined by a judicious shift of the gate corresponding to the wished particle, pion or fast proton, and substracted from the data.

Multiplicities

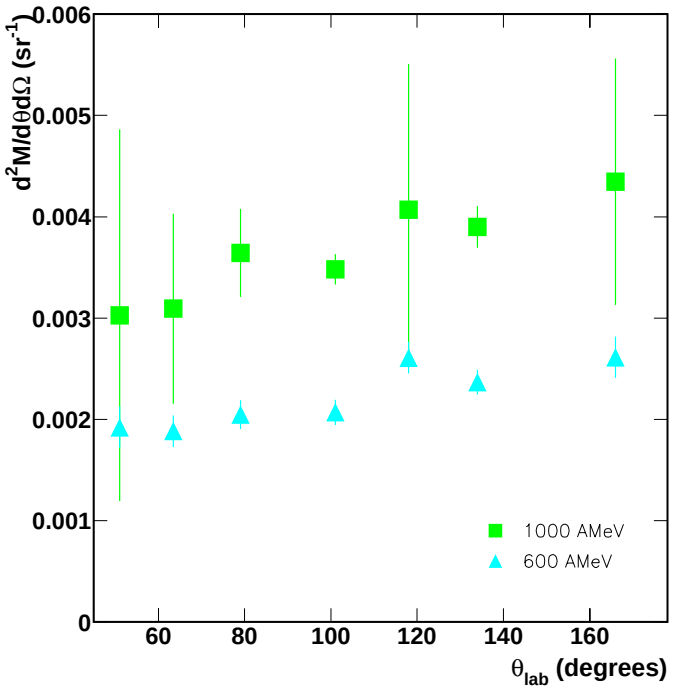

Figure 7.4: *Inclusive mean multiplicity of pions for 600 and 1000 AMeV as a function of θ_{lab}. The error bars correspond to the error due to background substraction or the statistical error, if larger.*

The pions stopped in the CsI have a very low kinetic energy (between 2 and 46 MeV) in the laboratory. The kinetic energy, E_μ=4 MeV, of the muons emitted in the pion decay is subtracted from the measured kinetic energy of the pions. Due to the technical characteristics of the calibration telescopes used for this analysis, the kinetic energy range changes according to the detector. For this reason, cuts applying the shortest energy range (E=2-23 MeV) were built to select pions in order to determine their angular distribution.

This distribution is visible in Fig. 7.4 for the reaction systems C+Au at 600 and 1000 AMeV. The error bars correspond to the errors due to the background or, if superior, to the statistical errors. For the incident energy of 1000 AMeV, the background in the calibration telescope is very heterogeneous due to stray particle effects. This gives large error bars while they are much smaller for the multiplicities at the energy of 600 AMeV. The stray particle effects decrease with the beam energy (see chapter 2.4). The pions at 1000 AMeV presents the same behaviour than at 600 AMeV with a multiplicity higher of a factor 1.7 than the multiplicity at 600 AMeV. This reflects the exponential incident energy dependence of the pion production [Sto86, App95]. The second remarkable point is that these two multiplicities reflect a slight anisotropy of the pion emission as they are increasing with the polar angle θ_{lab}. This anisotropic emission is known for higher energy pions [Sto86, Pel97]. Experiments performed at the Berkeley Laboratory and GSI with the systems Ar+KCl at 1.8 AGeV [Bro84] and Au+Au at 1.06 AGeV [Pel97] respectively show that the anisotropy of the pion emission increases with the pion energy until a maximum for a pion kinetic energy in the center of mass of about 0.3 GeV. The anisotropy decreases for higher energy pions.

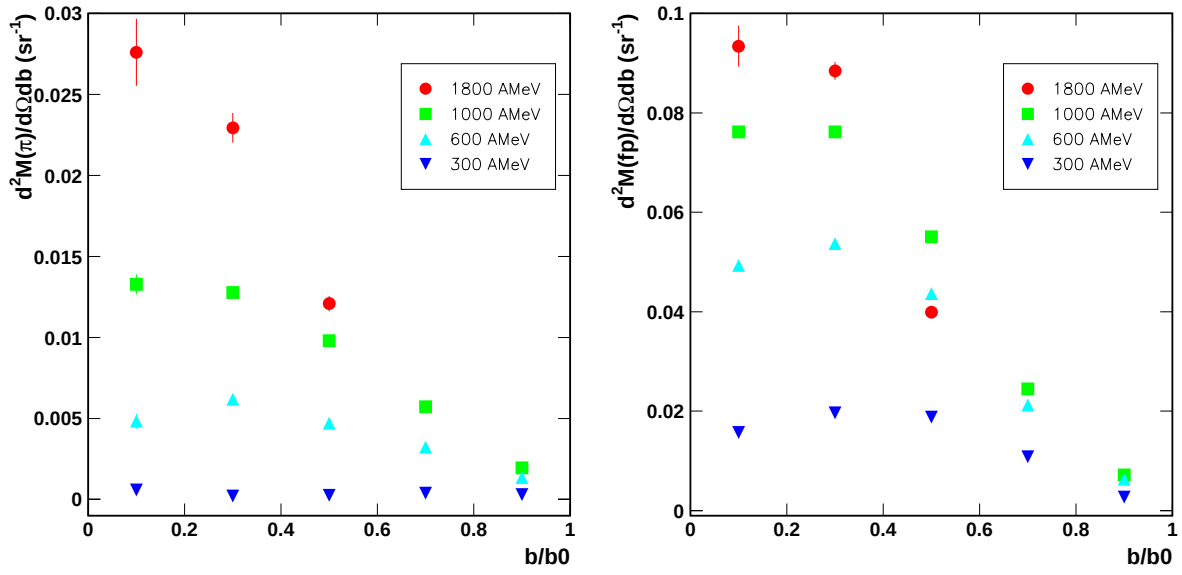

Figure 7.5: *Pion (left panel) and fast proton (right panel) multiplicities as a function of the reduced impact parameter b/b0 for C+Au at 300, 600, 1000, and 1800 AMeV.*

For the following of the chapter, all the identified stopped pions are taken into account despite the different energy ranges given by the detectors. We maintain the choice of the charged particle multiplicity as global variable for the determination of the relative impact parameter as this mul-

tiplicity is constitued, for the main part, of light particles (protons, alphas) so the fact that an autocorrelation exists between the IMF's and the charged particle multiplicity will very slightly affect the results. This autocorrelation is cancelled in the correlation functions presented further.

The incident energy dependence exhibited by the pion angular distribution (Fig. 7.4) is also visible with the mean multiplicty of pions as a function of the reduced impact parameter in the left panel of Fig. 7.5 for the beam energies from 300 to 1800 AMeV. From studies with the detectors Plastic Ball and FOPI [Wag96, Pel97], one knows that the pion multiplicity is a linear function of the number of participants which is a function of the impact parameter. This explains the increasing pion multiplicity with the increasing centrality that we observe also in this figure. The fast protons show a similar behaviour with a higher production rate (see right panel of Fig. 7.5).

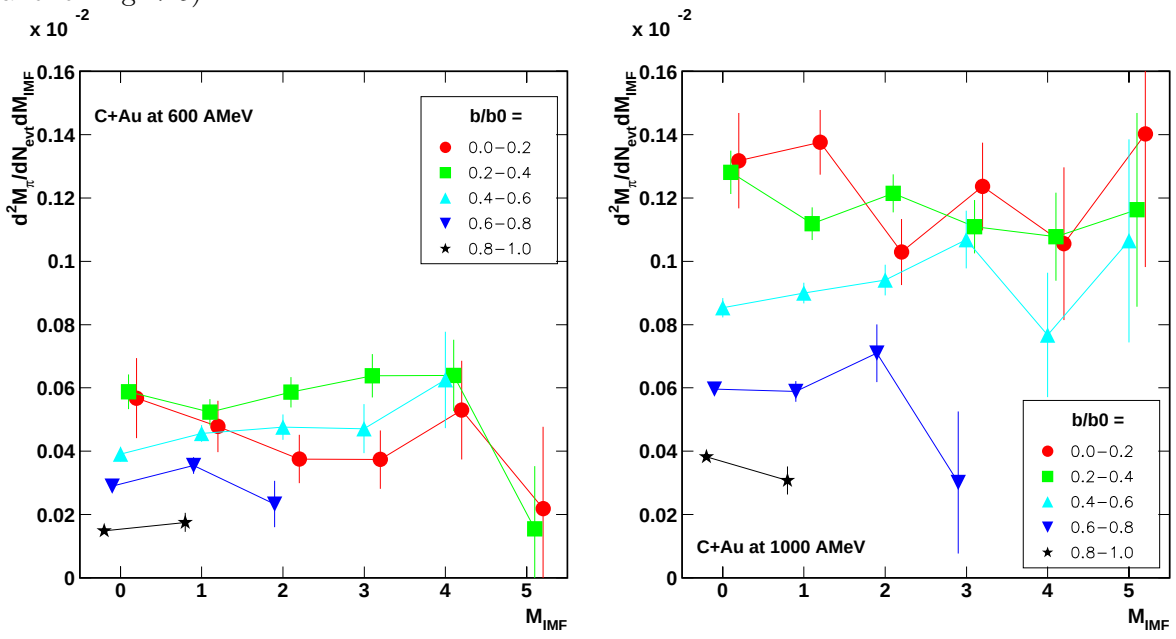

Figure 7.6: *Pion mean multiplicity as a function of IMF multiplicity for C+Au at 600 (left panel) and 1000 AMeV (right panel) for five bins in impact parameter from central collisions with b/b0=0.0 to peripheral reactions with b/b0=1.0.*

Fig. 7.6 presents, as a first look on early stage-fragmentation relations, the mean pion multiplicity as a function of IMF multiplicity for five cuts in relative impact parameter for the incident energy of 600 AMeV (left panel) and 1000 AMeV (right panel). The Intermediate Mass Fragments (IMF) are selected in a charge range from Z=3 to Z=30. The distributions show for 600 and 1000 AMeV a negative slope for the very central reactions (b/b0=0.0-0.2). This slope becomes more and more positive with decreasing centrality, with the exception of the multiplicities for the very peripheral collisions (b/b0=0.8-1.0) for 1000 AMeV that exhibits a negative slope. One observes an evolution of pion emission as a function of fragment production.

Correlation functions

The correlation function of two particles is the ratio of the production yield of two particles in coincidence over the production yields of each of these particles:

$$1 + R(\pi, IMF) = \frac{< M_\pi \times M_{IMF} >}{< M_\pi >< M_{IMF} >} \tag{7.1}$$

with the mean multiplicity product $< M_\pi \times M_{IMF} >$, the mean multiplicity of pions $< M_\pi >$, and the mean multiplicity of IMF's $< M_{IMF} >$.

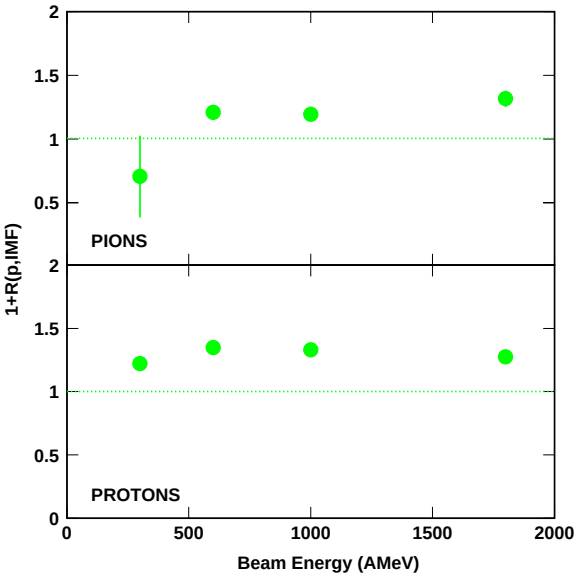

Figure 7.7: *Correlation functions pion-IMF (top panel) and fast proton-IMF (bottom panel) as a function of the incident energy for the system C+Au. Only the target IMF's are selected for these functions.*

The Fig. 7.7 presents the inclusive correlation functions of stopped $\pi+$ (top panel) and fast protons (bottom panel) with IMF's as a function of the incident energy. The target IMF's are selected for these correlation functions to be lower in rapidity than y=0.3 as displayed in Fig. 7.9. Due to the kinematics of the reaction, this selection is valid for all the incident energies. Both distributions show a positive correlation except for the pion-IMF correlation function for 300 AMeV. This may be explained by the very low pion production rate at this incident energy. The positive correlations indicate that the more high energetic particles are produced, the more IMF's are produced. Both types of particles are mainly produced in central collisions (see Fig. 7.7 and chapter 6) and we could easily guess that this positive correlation is due to the central collisions where both particles are produced and then highly correlated. The correlation functions displayed as functions of the reduced impact parameter b/b0 in Fig. 7.8 reveal in contrary an slight anticorrelation for pions or no correlation in the case of fast protons for the central collisions for the incident energies from 300 AMeV to 1800 AMeV. The correlation function increases with b/b0, becomes positive for b/b0=0.4-0.6 when there is not complete overlap of the carbon projectile and the gold target.

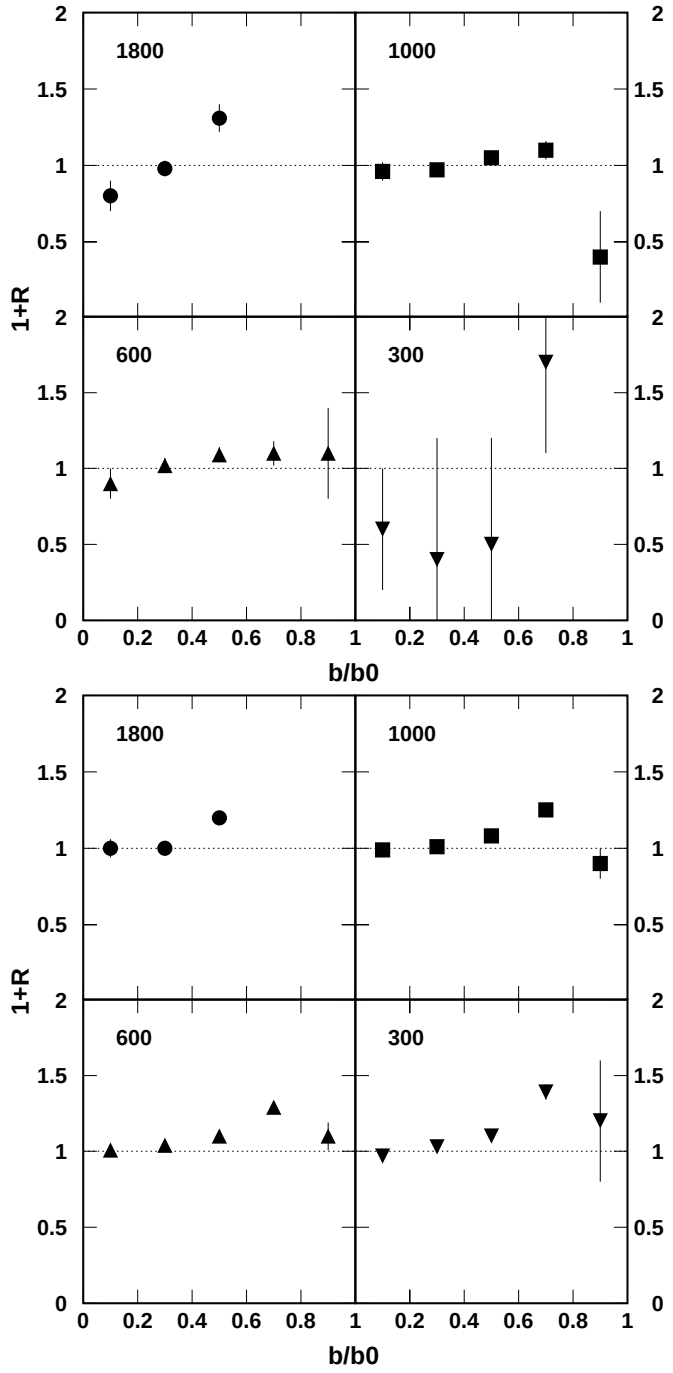

Figure 7.8: *Correlation functions of pion-IMF, in the top panel, and fast proton-IMF, in the bottom panel as functions of the relative impact parameter b/b0 for the system C+Au at 300, 600, 1000, and 1800 AMeV (down triangles, up triangles, squares, and circles, respectively). Only the target IMF's are selected for these functions.*

The fast proton distributions increase more than these ones of pions with b/b0 but they all decrease mor or less sharply for the very peripheral collisions. This part of the data is largely influenced by stray particle effects. The correlation functions presented here are corrected by subtraction from particle multiplicities coming from data without target. This correction gives for pions at 600 AMeV a positive correlation while it is below one for 1000 AMeV. The fast proton correlation functions show a correlation for 300 and 600 AMeV and an anticorrelation for 1000 AMeV. The most peripheral data are very uncertain due to the low statistics given by the small calibration telescopes (see chapter 2.2) and the stray particle correction. The data for the pions at 300 AMeV and the data missing in pion correlations for 300 and 1800 AMeV and in fast proton correlation at 1800 AMeV suffer from too low statistics.

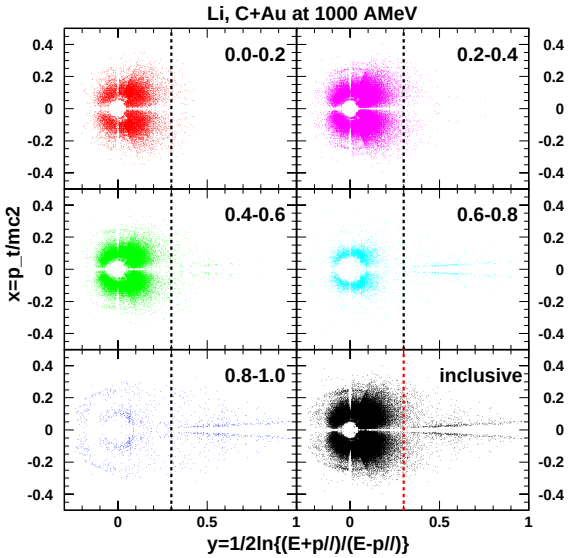

Figure 7.9: *Rapidity distribution of Lithium's for C+Au reactions at 1000 AMeV. Five cuts in relative impact parameter are represented as well as inclusive data. The large disk around y=0 corresponds to the gold target. In the very peripheral collisions (b/b0=0.8-1.0), the second circle is due to stray particle effects. In order to avoid projectile fragments, the data are selected with a rapidity* $y \leq 0.3$.

To compare our experimental results with theory, we choose the combination of cascade and statistical models already used in the proton case (see chapter 5). The correlation functions of $\pi+$ and fast protons with IMF's as functions of the reduced impact parameter b/b0 for the incident energy are compared in Fig. 7.10, pions in top panel and fast protons in bottom panel, to the corresponding correlation functions simulated by two IntraNuclear Cascade (INC) models: the Liège INC coupled with the statistical model SMM [Cug80, Cug89, Cug97, Cug97b, Dor01, Vol02, Bon95] and the Dubna INC also coupled with SMM [Ton83, Bon85, Bot02]. The cascade model is a dynamical model describing the preequilibrium emission of light particles, including pions. After the cascade, in the Liège case, the percolation provides the transition to the evaporation code that produces the fragments (see appendix B.3). In the Dubna case, at the end of the cascade, a residue with a certain mass, charge and excitation energy remains which then can be used as input for the statistical description of the fragment production (see appendices B.1 and A.1).

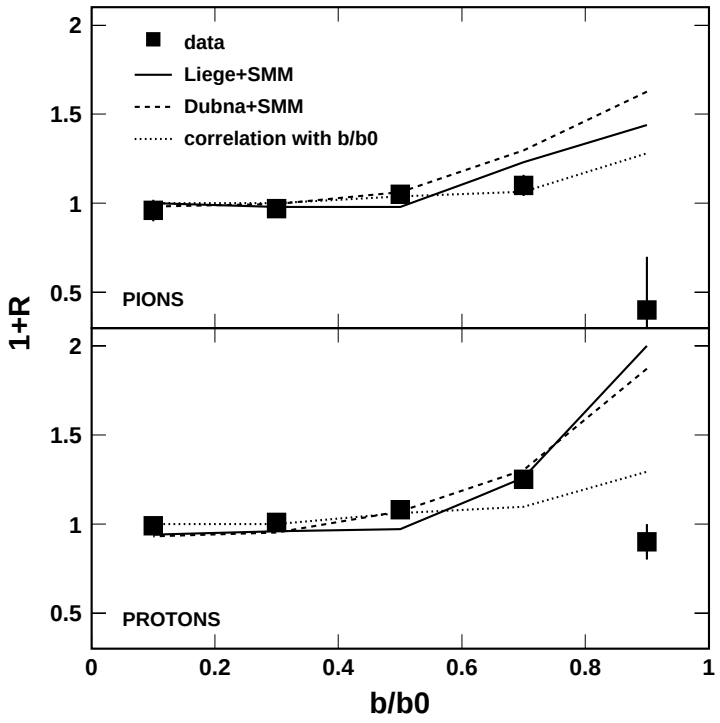

Figure 7.10: *Comparison of correlation functions of pions (top panel) or fast protons (bottom panel) with fragments for the C+Au reactions at 1000 AMeV coming from the experiment (full squares), the Liège Cascade model coupled to SMM (full line), the Gudima Cascade model also coupled to SMM (dashed line), and Monte-Carlo calculation corresponding to a correlation with the reduced impact parameter b/b0 (dotted line).*

It has also been tested whether the information contained in the deduced correlation functions significantly surpasses that contained in the dependences on the impact parameter exhibited by the particle and fragment multiplicities [Tra02]. For this purpose, correlation functions have been calculated by using a smoothed interpolation of the multiplicities as a function of the charged-particle multiplicity and the reaction cross-section as a function of the same quantity as an input. For the ranges of N_c corresponding to a given impact parameter bin, coincidence events have been generated by randomly choosing particle multiplicities from Poisson distributions with mean multiplicities that corresponded to the individual N_c values of this bin. In this model, the correlation functions will be one for infinitely narrow bins of N_c and it is only the correlated behaviour of the mean values as a function of N_c in finite bins that can produce values other than unity.

Fig. 7.10 shows good agreement between model and experimental data for both pion- and fast proton-IMF correlation functions, except for the bin of largest impact parameter where the pion and fast proton correlations are overestimated. These very peripheral data suffer a lack of statistics due to the small size of the detectors and the stray particle correction. Their analysis is then uncertain. Nevertheless, the consistence between the data, the models, and the calculations

from the mean multiplicities for central and semi-peripheral collisions ($0 \leq b/b0 \leq 0.8$) let us remark that the increasing correlation functions with the decreasing centrality are the fact of the correlation between the different multiplicities and the reduced impact parameter rather than between the multiplicities themselves. According to the study done in this section, the production of pions or fast protons in the early stage of the reaction does not seem to directly influence the emission of fragments during the multifragmentation stage.

Summary

The present thesis work reports on the study of mechanisms in the C+Au reaction at relativistic energies at the occasion of the INDRA@GSI experiment. This experiment was a unique opportunity to combine a technologically highly advanced detector usually working at non-relativistic energies at GANIL with the higher energy beams produced by the SIS facility at GSI. The aim of the Carbon beam part of the experiment is to study the reaction mechanisms in relativistic heavy ion collisions in order to disentangle early and multifragmentation emissions of light particles. This sorting should permit the determination of a more precise nuclear caloric curve T(E*) from the multifragmentation data, as previous works revealed a dependence of the excitation energy E* on the incident energy [Ode99].

C+Au is a system already studied in ALADIN and EOS experiments, but in inverse kinematics [Sch96, Hau98]. The INDRA@GSI experiment brings advantages including a large angular coverage (90% of 4π), a very good resolution for light particles, and, in direct kinematics, target emissions observed at the same rapidities from 95 AMeV to 1800 AMeV. On the other hand, this experiment suffers from low and high technical thresholds that do not allow the detection of all the reaction products. The particularity of the INDRA@GSI experiment led to additional experimental difficulties such as stray particles polluting the data at low multiplicities (see chapter 2). Nevertheless, the charged particle multiplicity is chosen in this study as a global variable to determine the reduced impact parameter of the reaction (see chapter 4).

The proton kinetic energy spectra were first studied via combinations of Maxwell-Boltzmann functions for two sources. These fits emphasize the anisotropy of the two proton sources. The results of these fits reveal the existence of a low energy source corresponding to the target emission with temperatures increasing with the beam energy as a function of the reduced impact parameter. The high energy proton source is also analysed using Maxwell-Boltzmann functions and allows a good convergence of the fits. This fact may be interpreted as a signal of the thermal feature of the source. On the other hand, the high energy protons are well reproduced by the Liège Intra Nuclear Cascade model, also called Cugnon cascade. This good agreement demonstrates that these high energy protons come from the early cascade source, emitting light particles just after the first impact. The low energy proton spectra are compared to two different statistical models, the Dresner evaporation code and the multifragmentation model SMM (see appendices A and B). Whereas the evaporation overestimates the data, SMM gives predictions in good agreement with the data because of a higher fragment production. According to these comparisons, the favoured scenario of proton production would be an intranuclear cascade followed by a statistical multifragmentation emission. The INDRA data are also compared to other cascade models as the Dubna and the Isabel codes. Theses two models overestimate the

experimental proton spectra. These spectra are nevertheless in very good agreement with EOS proton spectra for the reaction in inverse kinematics Au+C at 1000 AMeV. The proportions of early cascade and multifragmentation protons are determined from the combination Liège-SMM for C+Au at 1000 AMeV, but also for Au+Au at 600 AMeV giving a possibility to correct the ALADIN nuclear caloric curve (see chapter 5).

The low energy light fragments present similar temperature distributions as the protons. In this work, Z_{bound} is shown to be dependent on the beam energy as a function of the reduced impact parameter in particular conditions. The dependences of temperature and Z_{bound} as function of the impact parameter compensate each other and lead to the universality observed in the ALADIN experiments [Sch96, Ode99]. The reduced impact parameter b/b0 and Z_{bound} appear as complementary variables, as the reduced impact parameter is related to the geometry of the source while Z_{bound} is connected to the excitation of this source. The kinetic energy spectra of fragments are compared to the combination of the Liège cascade and the SMM model. A good agreement is observed for central collisions but not for peripheral collisions. The cascade and percolation codes seem here to bring a too high excitation energy into the SMM code for peripheral collisions. For the high energy fragments, the combination of Maxwell-Boltzmann functions used in this analysis do not converge. This fact may denote the non-thermal feature of these fragments. Their second remarkable characteristic is their rapidity close to the center of mass rapidity (see chapter 6).

The observation of pions, for the first time with the INDRA multidetector, gives us the occasion to study correlations between the early source and the multifragmentation source for incident energies $E_{inc} \geq 300$ AMeV. The pions were detected at backward angles $45 \leq \theta_{lab} \leq 176^o$ and present a mean multiplicity that increases slightly with the angle in the laboratory for the reactions C+Au at 600 AMeV and 1000 AMeV. The correlation functions of pions and fast protons (E > 150 MeV), both kinds of particles emitted at the beginning of the reaction, with intermediate mass fragments ($3 \leq Z \leq 30$) exhibit an increase from a small anticorrelation for central collisions to a positive correlation for peripheral collisions. The comparisons with combinations of cascade and statistical models, Liège and Dubna cascades, each coupled with SMM (see appendices A and B), show good agreement between the data and the models. Correlation functions calculated by using a smoothed interpolation of the multiplicities and the reaction cross-section are also in good agreement. This emphasizes the dominating dependence of the pion- and fast proton-fragment correlation functions on the reduced impact parameter. The production of pions or fast protons in the early stage of the reaction does not seem to directly influence the emission of fragments during the multifragmentation stage (see chapter 7).

The present work does not give a complete analysis of the data obtained with relativistic ^{12}C beams. Another part of the INDRA@GSI experiments was dedicated to various combinations of ^{12}C and Sn, and Xe and Sn isotopes as projectiles and targets respectively. These experiments are in the direction of isotopic studies [Sai02]. Concerning the ^{12}C+^{197}Au, the two proton sources determined in this work should allow us in the following to determine the excitation energy of the multifragmentation source and then a caloric curve of the C+Au reaction. During this work, we stumbled on some results which are not yet understood, such as the higher temperatures of beryllium in comparison to lithium and boron slope temperatures (see chapter 6.2). The anticorrelation of fast protons with fragments for the peripheral collisions at the in-

cident energy of 1000 AMeV (see chapter 7.2) will also need further checks in the following of this work. One of the most fascinating observations that one should follow more closely is the high energy source of framents with a velocity close to the center-of-mass velocity. This seems to indicate that the spectator picture is too simple. It will also be interesting to correct the high identification thresholds of the backward ionization chambers ($45 \leq \theta_{lab} \leq 176^o$) in order to obtain an IMF multiplicity comparable to the ALADIN and EOS results [Sch96, Hau98]. Furthermore, the calibration telescopes of the INDRA multidetector, i.e. the silicons and CsI detectors at forward angles, may allow the continuation of the temperature analysis by studying isotopic thermometers.

Appendix A

Statistical, Dynamical and Hybrid Models

A.1 Statistical models

Statistical models assume an equilibrated source emitting fragments in either microcanonical, canonical, or grand canonical ensembles. There are two major aspects that give rise to differences between models. The first concerns the assumption of the break-up process itself. Either it happens spontaneously, all fragments are emitted at the same time, or this process is slow, the fragments are emitted sequentially. The second aspect of physical relevance for model predictions is how individual nuclei are included.

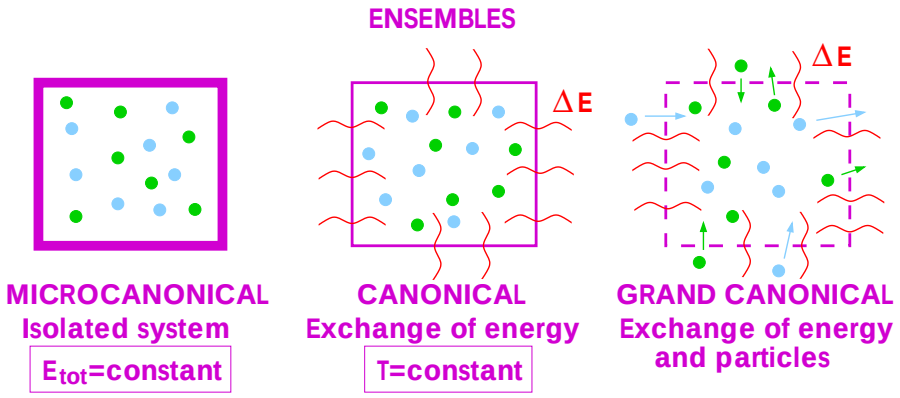

Figure A.1: *The three thermodynamical ensembles, microcanonical, canonical, and grand canonical (also called macrocanonical).*

Statistical Multifragmentation Model (SMM)

The Statistical Multifragmentation Model (SMM) [Bon85, Bon95] is used in several versions to predict the break-up partitions of fragments at freeze-out density. It is a mixed approach, based on the microcanonical assumption (conservation of the total energy) and using canonical prescriptions of partitions. It assumes that fragments are distributed in a certain available volume V (supposed to be the freeze-out volume) following Boltzmann statistics. The density of the freeze-out corresponds to the coexistence region of the phase diagram. The free volume V_f, which determines the translation entropy, is $V_f = \chi V_0$. The total freeze-out volume is $V_{tot} = (1+\chi)V_0$. This factor χ is in fact multiplicity dependent through

$$\chi = \left(1 + \frac{d_0.(M^{1/3} - 1)}{r_0.A_0^{1/3}}\right)^3 - 1 \tag{A.1}$$

therefore d_0 is the relevant model parameter rather than χ itself. For d_0, usually a value of 1.4 fm is chosen and $r_0 = 1.17$fm.

The internal structure of the extended fragments is described by means of the liquid drop model (see, for instance, the Ref. [Eva55]). Each single fragment contributes to the total free energy through its thermal motion, the volume, surface, Coulomb, and symmetry energy terms, in the following way:

$$F_{tot} = \sum_{(A,Z)} F(A,Z) = \sum_{(Z,A)} F_{therm}(Z,A) + F_{vol}(Z,A) + F_{surf}(Z,A) + F_{Coulomb}(Z,A) + F_{sym}(Z,A) \tag{A.2}$$

In particular, for a fragment of charge Z and mass A, these contributions are:

$$\begin{aligned}
F_{therm}(A,Z) &= -Tln\left(\frac{g(A,Z).V_f}{\lambda^3}\right) + T\frac{lnN(A,Z)}{N(A,Z)} \\
F_{vol}(A,Z) &= (-W_0 - T^2/\epsilon_0).A \\
F_{surf}(A,Z) &= \beta_0\left(\frac{T_c^2 - T^2}{T_c^2 + T^2}\right)^{5/4}.A^{2/3} \\
F_{Coulomb}(A,Z) &= \frac{3}{5}.\frac{Z^2e^2}{r_0A^{1/3}}\left(1 - \frac{1}{(1+\chi)^{-1/3}}\right) \\
F_{sym}(A,Z) &= \nu\frac{(A-2Z)^2}{A}
\end{aligned} \tag{A.3}$$

with the degeneracy factor g(A,Z), the thermal wavelength λ, the number N(A,Z) of fragments (A,Z) in the partition, the binding energy W_0 per nucleon of nuclear matter at the saturation density, the inverse level density parameter ϵ_0 originating from the Fermi gas model ($\epsilon_0 = 16$ MeV), the surface tension energy β_0 of a nucleus in its ground state ($\beta_0 = 18$ MeV), the critical temperature T_c as shown on Fig. A.2 ($T_c = 16$ MeV in the present case), and the symmetry energy ν corresponding to the Bethe-Weizsäcker mass formula ($\nu = 25$ MeV).

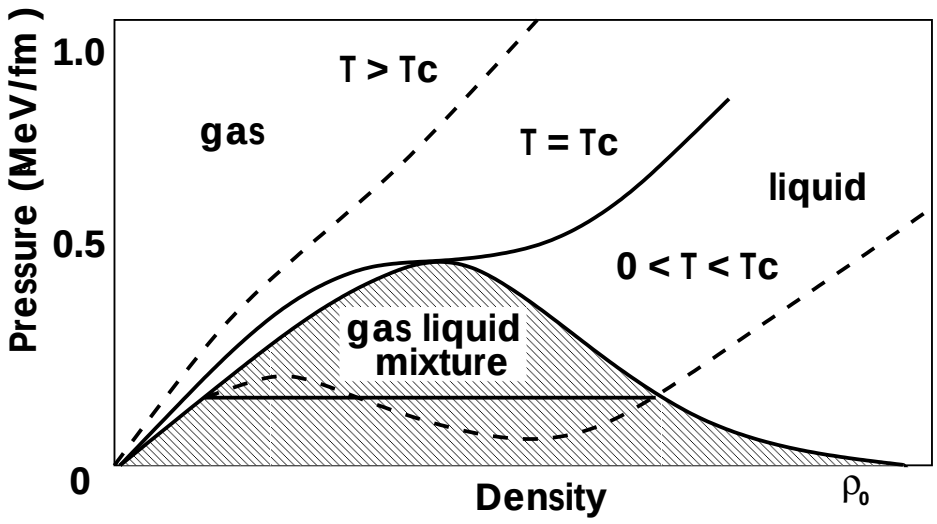

Figure A.2: *The qualitative behaviour of the equation of state of nuclear matter $P(\rho, t)$ in the region of the liquid-gas phase transition. The hatched area indicates the region where liquid and gaseous phases can coexist under the condition of thermodynamical equilibrium. ρ_0 corresponds to the density of stable nuclei [Cur83].*

In this approach, the temperature T is derived from utilising the conservation of the total energy, which is:

$$E_{tot} = E_0 + E_{g.s.} = \frac{3}{5}.\frac{Z^2e^2}{r_0A^{1/3}} + \sum_{all fragments} N(A,Z)\left(F(A,Z) - T\frac{\partial F(A,Z)}{\partial T}\right) \tag{A.4}$$

with the energy $E_{g.s.}$ of the ground state of the decaying initial nucleus with A_0 and Z_0.

In the canonical prescription, the probability distribution for all possible fragment partitions f.p. is

$$P(f.p.) = \frac{exp(-F_{f.p.}/T)}{\sum_{all f.p.} exp(-F_{f.p.}/T)} \tag{A.5}$$

where $F_{f.p.}$ is the total free energy of a given fragment partition.

Here the mass and charge are exactly conserved within every single partition, or in other words, within every single event. However, in the grand canonical mode of this model, the fragment numbers have to be replaced by their average values. The produced fragments (so-called 'primary' fragments) may be excited and may also undergo a secondary decay. The channel in which they will de-excite depends on their mass: fragments up to oxygen can deexcite by breaking into several single nucleons and light clusters. Heavier, excited fragments can evaporate light particles [Bot87].

Here, one follows the suggestion of Weisskopf and Ewing [Wei40] in a generalized form which allows also heavier clusters to be emitted. It used the level density in the Fermi gas model:

$$\rho(E^*) \propto exp\Big(2\sqrt{aA.E^*}\Big) \tag{A.6}$$

as an *ansatz* for the population of the highly bound nuclear states. The level density a is $a \simeq 0.12MeV^{-1}$.

Within this SMM approach, a drastic change in the decay pattern of an excited nucleus is found around temperatures of 6 MeV [Bot87]. At the lower part of the corresponding energy scale, evaporation from a compound nucleus is the most important process, whereas at the higher temperatures, the multifragment break-up dominates. It seems that this transition is a manifestation of the liquid-gas phase transition of finite nuclei.

A.2 Percolation model

The percolation model [Bau85, Cug89] has the basic advantage that it explicitly includes a phase transition and is therefore suited to analyse the evolution through the critical region. Percolation is based on a Monte Carlo technique. The sites of an infinite lattice are randomly occupied. Clusters are defined by a couple of sites which are connected through links between nearest neighbours. The probability of a link between lattice sites being broken is commonly assumed to increase monotically with the excitation energy brought into the system. The transition from an intranuclear cascade, the Liège code, to a percolation model is presented in the section B.3 of the appendix B.

A.3 Dynamical models

With the appearance of exclusive measurements, it was necessary to perform more elaborate calculations treating the dynamics of the collision. The dynamical models follow the time evolution of the system. There exist numerous models simulating the dynamics of two colliding nuclei. We will present the model based on molecular dynamics in this appendix. The appendix B is fully dedicated to the cascade models.

In molecular dynamics, the time evolution of the N-body phase space density f^N follows the Liouville equation:

$$\frac{df^N}{dt} = \{f^N, H^N\} + \frac{\partial f^N}{\partial t} = 0 \tag{A.7}$$

with $f^N(x_1, p_1, x_2, p_2, \ldots, x_N, p_N)$ and the classical Poisson brackets $\{.,.\}$ containing the initial conditions of the N-body hamiltonian H^N , i.e. different microscopic states of the system but having the same macroscopic properties.

For given initial conditions describing the system in a certain state at time t_0

$$r_i = r_i(t = t_0) \text{ and } p_i = p_i(t = t_0) \quad i = 1, \ldots, N. \tag{A.8}$$

with the position in normal space r_i and the momentum p_i in momentum space for the particle i, the propagation of nucleons in the system is reduced to the Hamilton equations of motion

$$\dot{r}_i = \frac{\partial H^N}{\partial p_i} \quad \dot{p}_i = -\frac{\partial H^N}{\partial r_i} \quad i = 1, \ldots, N. \tag{A.9}$$

In order to apply this formalism to heavy-ion collisions, it has been substantially extended to the quantum molecular dynamics model (QMD) [Aic88, Aic91, Pei89, Pei92] which incorporates the most important quantum features, such as the Fermi motion, the hard scattering and the Pauli blocking of the final states in the binary nucleon-nucleon collisions.

The basic idea of quantum molecular dynamics is to propagate nucleons, which are represented by Gaussian-shaped functions in configuration and momentum space,

$$f_i(x, p, t) = \frac{1}{(\pi\hbar^3)} exp\left\{ -\frac{(x - r_i(t))^2}{2L^2} - \frac{2L^2}{\hbar^2}(p - p_i(t))^2 \right\} \tag{A.10}$$

with respect to mutual two- and three-body forces, with the positions $x, r_i(t)$ in normal space, the positions $p, p_i(t)$ in phase space, and the theoretical 'width' of the wave packets L, a parameter that does not correspond to any physical observable and should therefore be determined by the condition that its actual value should not influence the results of the model [Gro90].

The QMD model does not proceed the mean field approximation but treats instead the two- and three-body interactions of nucleons. The nucleons evolve in a total interaction potential composed of a Coulomb term, a Yukawa term, a local term and an additional term taking into account the momentum dependence of the interactions. The local potential term is parametrized from Skyrme two- and three-body forces [Sky59] with a dependence on the density, which allows a direct link to the equation of state. The reaction is made of an ensemble of binary collisions between nucleons that are submitted to the Pauli principle in their final state. The fragments are formed at the end of the reaction with a coalescence criterium in the position space. This criterium consists in linking two nucleons (or more) if the centroids of their respective wave packets are distant of less than 3fm. The calculations are done event by event, which allows to simulate the bias of the detection setups for the comparison with experimental measurements.

Several extensions based on the QMD model have been developed:

-IQMD [Har89] distinguishes the protons and the neutrons and treats the production, the propagation and the absorption of the pions through the Δ resonances.

-BQMD [Boh91] is intended to the description of multifragmentation.

-QMD+SMM [Pei92] treats the deexcitation of fragments by association with a statistical multifragmentation model (see section A.1).

-PQMD [Kon95] utilises an 'auto-consistent' Pauli potential.

-GQMD [Jae92] uses the Brückner theory for the calculation of the nucleon-nucleon interaction potential.

-RQMD [Sor89] describes the dynamics of the reactions in a relativistic formalism.

A.4 Transport models

There are different approaches that differ in the techniques of numerical treatment of the Landau-Vlasov equation: Vlasov-Uehling-Uhlenbeck (VUU) [Kru85, Mol87], Boltzmann-Uehling-Uehlenbeck (BUU) [Ber84, Aic85], and Landau-Vlasov (LV) [Gre87]. These models are based on the assumption that the one-body phase-space distribution function of nucleons evolves under the influence of its own mean field and is only modified by binary collisions. The collision integral usually is of a Boltzmann-type with additional phase space density factors, which account for the possible Pauli blocking of the final states. The time derivative of the phase space density df/dt follows the Landau-Vlasov equation which is using the Vlasov equation accounting for the evolution of the f function in the mean field, added with extra gain and loss terms, on the right-hand side, which accounts for the hard scattering of the nucleons. This equation is the following:

$$\begin{aligned}\frac{\partial f}{\partial t} + v.\nabla_r f - \nabla_r U.\nabla_p f = -\int \frac{d^3p_2 d^3p_1' d^3p_2'}{(2\pi)^6}\sigma.v_{12} \\ \times(f_1 f_2(1-f_1')(1-f_2') - f_1' f_2'(1-f_1)(1-f_2)) \\ \times\delta(p+p_2-p_1'-p_2')\end{aligned} \tag{A.11}$$

with the phase space densities f_1, f_2, f_1', f_2' ($1, 2$= two scattering particles, $'$= final state), the velocities v, v_{12}, the momenta p, p_2, p_1', p_2', and the nucleon-nucleon cross-section σ. Note that the right-hand side differs from the classical collision integral by the Pauli-blocking factor.

In this approach, the mean field is sometimes approximated by the Skyrme parametrization [Sky59]:

$$U = \frac{E}{N} = \alpha\rho + \beta\rho^{\nu} \tag{A.12}$$

with $\alpha = \frac{t_1}{2}$, $\beta = \frac{t_2}{2}$, the density ρ, and the constant ν equal to 2 in the three-body interaction. The constants t_1, t_2 measure the mean central potential. Only the two-and three-body terms of the spatial part of the interaction are used without regarding the exchange terms, like in the local Skyrme interaction $V(r_1) = t_1\delta(r_1 - r_2) + t_e\delta(r_1 - r_2)\delta(r_1 - r_3)$, with the positions r_1, r_2, r_3 of three particles in normal space. Sometimes, this parametrization is extended to a momentum dependence of the force ('Gogny' force).

There are differences in the numerical realisation of the propagation. Numerically, the equation A.11 can be solved using a test particle method, where each physical nucleon is represented by a number of pointlike test particles. This is done in order to provide a smooth density profile. The nucleons are allowed to collide with the free nucleon-nucleon cross-section σ in BUU/VUU. VUU uses a phase space sphere around each nucleon, while BUU has a fixed grid, which can be interpreted as a Lagrangian or Eulerian system. Within these realisations, several events can be calculated in parallel, but without allowing two nucleons from different events to collide. In contrast, in Landau-Vlasov calculations, this is not the case: here nucleons from different events may collide. As a consequence, the corresponding LV cross-section has to be scaled down by the number of test particles

$$\sigma_{LV} = \frac{\sigma_{free}}{N_{testparticles}} \tag{A.13}$$

These approaches describe in a satisfactory way the raw features of the observed phenomenons, but they have as principal drawback the impossibility of natural formation of fragments as they describe the evolution of the one-body distribution function. A rather recent 'hybrid' version [Zha95], has been developed including the treatment of coulombian effects, of the momentum dependence of the interactions and of the fragment formation by a coalescence criterium. Methods based on the Boltzmann-Langevin equation have been developped that allow to simulate approximately the dynamical path followed by nuclear systems crossing the spinodal region. They consist of a 'Boltzmann evolution' starting from an inhomogeneous initial system complemented by a brownian force (Brownian One-Body Dynamics: BOB) [Cho94, Gua96, Fra01]. The amplitude of the initial density fluctuations or the magnitude of the stochastic force is chosen to reproduce the dynamics of the most unstable modes for infinite nuclear matter in the spinodal region.

A more complete presentation of multifragmentation models is given in references [Mor93] and [Poe96].

Appendix B

Intra-Nuclear Cascade Models

The Intra-Nuclear Cascade models (INC) are dynamical models dedicated to the description of the first step of the heavy-ion reaction, which means the evolution of this reaction from the beginning of the collision up to the onset of equilibration. In so-called hybrid models, the subsequent evolution of the reaction is generally treated in a statistical way (see appendix A.1).

Usually, the nucleon is described as a sphere of diluted gas, a Fermi gas of protons and neutrons, where the nucleons can hit each other. The nucleons are considered essentially as free particles, the principal effect of the medium is due to the Fermi degeneracy of the nuclear matter according to the Pauli principle. Fig. B.1 shows the scheme of a nucleon interaction in a reaction in the cascade stage.

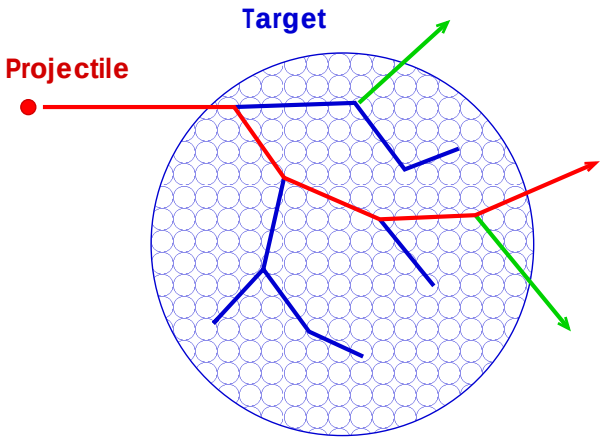

Figure B.1: *Cascade process.*

The motion and the history of each nucleon and product of the interactions is followed. The impact parameter determines the sequence of the events. For a peripheral collision, very few projectile nucleons make a collision, then little of energy is transferred to the target nucleus, if the colliding nucleons do not fly out of the target. In contrary, in central reactions, the projectile particles have to perform several collisions in the nuclear matter, giving up a lot of energy to

the target nucleons, until a possible capture. The secondary nucleons can escape or carry out other collisions themselves, dissipating in this way a bigger fraction of the initial energy. This process leads to the formation of a composite nucleus close to thermal equilibrium.

B.1 Dubna cascade

The INC model is based on a Monte-Carlo solution of the relativistic Boltzmann equation for a one-particle distribution function $f^A(x, p_A) \equiv f^A$ of a gas mixture:

$$p^{\mu}_{(A)} \partial_{\mu} f^A(x, p_{(A)}) = \sum_{A'} D_{coll}(f^A, f^{A'}) \tag{B.1}$$

with the collision term D_{coll}, the four-dimensional coordinate x^{μ} and the momentum p^{μ} of a particle.

In the case of a heavy-ion collision, an important simplification of the cascade equations comes from neglecting the interaction between particles of the same kind. Three kinds of particles are considered: projectile and target spectators, and the participants.

For the projectile spectator (proj), the Boltzmann equation becomes

$$p^{\mu}_{proj} \partial_{\mu} f^{proj}(x, p_{proj}) = -f^{proj} \sum_{J=target,part} \int f^J Q_{proj.J} . \sigma^{proj.J}_{tot} d\omega_J \tag{B.2}$$

for the target spectator (target),

$$p^{\mu}_{target} \partial_{\mu} f^{target}(x, p_{target}) = -f^{target} \sum_{J=proj,part} \int f^J Q_{target.J} . \sigma^{target.J}_{tot} d\omega_J \tag{B.3}$$

and for the participant part (part),

$$\begin{aligned} p^{\mu}_{part} \partial_{\mu} f^{part}(x, p_{part.}) = & -f^A \sum_{J=proj,target} \int f^J Q_{part.J} . \sigma^{part.J}_{tot} d\omega_J \\ & + \sum_{J=proj,target} \int \int f^{part'} f^J Q_{part'.J} \sum_{\nu=2}^{n_{part'.J}} \frac{d\sigma^{part.J}(\nu)}{d\omega_{part}} d\omega_{part'} d\omega_J \\ & + \int \int f^{proj} f^{target} Q_{proj.target} \sum_{\nu=2}^{n_{proj.target}} \frac{d\sigma^{proj.target}(\nu)}{d\omega} d\omega_{proj} d\omega_{target} \end{aligned} \tag{B.4}$$

with the relative momentum-energy tensor $Q_{IJ} = \sqrt{p_{\mu(I)} p_(J)^{\mu} - (c^2 m_I m_J)^2}$.

Properties of hadron-nucleon collisions enter into the equations B.2, B.3, and B.4, describing the two-nucleus interaction through the differential distributions $d\sigma(\nu)/d\omega$ and total cross section σ_{tot}, the latter being corrected for the Pauli exclusion principle.

In the limit of hadron reactions, when the projectile nucleus is replaced by a nucleon, the terms with a factor f^{proj} should be omitted (the equation B.2 is absent). Using conventional

three-dimensional variables $x, p \to \vec{r}, \vec{v}, t$, one may now rewrite the equations B.3 and B.4 as follows

$$\Big(\frac{\partial}{\partial t} + v_{\vec{target}}\vec{\nabla}\Big) f^{target} = -f^{target}\rho_{part}(\vec{r}, t) < \sigma v_{rel} > \tag{B.5}$$

$$\begin{aligned}\Big(\frac{\partial}{\partial t} + \vec{v}_{part}\vec{\nabla}\Big) f^{part} &= -f^{part}\rho_{target}(\vec{r}, t) < \sigma v'_{rel} > \\ &+ \int d\vec{v}_{part'} f^{part'} \rho_{target}(\vec{r}, t) < \sigma v''_{rel} >\end{aligned} \tag{B.6}$$

with $v_{rel} = cQ_{IJ}/(p_{0(I)}p_{0(J)})$.

The averages over the distribution functions are determined in the standard manner

$$< \sigma v_{rel} >= \frac{1}{\rho(\vec{r}, t)} \int d\vec{v} f(\vec{r}, \vec{v}, t) v_{rel} \sigma(v) \tag{B.7}$$

with the normalisation to the particle number density

$$\rho(\vec{r}, t) = \int d\vec{v} f(\vec{r}, \vec{v}, t) \tag{B.8}$$

The equation B.6 can be reduced to the integral equation

$$\begin{aligned}f^{part}(\vec{r}, \vec{v}, t) = \int_{-\infty}^{0} d\tau . exp\Big[- \int_{t}^{\tau} d\tau' < \sigma v'_{rel} > \rho_{target}(\vec{r} - \vec{v}(t - \tau'), \tau')\Big] \\ \times \int d\vec{v}_{part'} f^{part'}(\vec{r} - \vec{v}(t - \tau), \vec{v}_{part'}, \tau) \rho_{target}(\vec{r} - \vec{v}(t - \tau), \tau) < \sigma''_{rel} >\end{aligned} \tag{B.9}$$

In this integral form, the physical meaning of the cascade model is most clearly manifested: the probability to find a fast particle is governed by all the previous collisions taken with the exponential absorption factor of survival.

In a naive cascade approach, one neglects the time dependence of the nucleon number density of the target nucleus, i.e. $\rho_{target}(\vec{r}, t) \simeq \rho_0(\vec{r})$.

The joint solution of B.5 and B.6 takes into account the depletion of the nucleon density of the target nucleus in the course of the intranuclear cascade. As follows from B.5, the nucleon density decreases exponentially and this decrease may essentially influence the dynamics of subsequent collisions in the case of high density cascade particles (i.e. at high bombarding energies) or for targets with few nucleons. The depletion leads to the saturation of the beam energy dependence for the number of knocked-out nucleons, the excitation energy and the transfer momentum of the residual nucleus (the limitation of the fragmentation of the target nucleus). Physically, these phenomena result from the finite number of nucleons in an interacting nuclear system.

Coming to heavy-ion collisions, the solutions of the cascade equations B.2, B.3, and B.4 will result in limiting the fragmentation of both the target and the projectile. The density of cascade

particles increases and the assumption that after a certain time t_{casc}, the cascade particles do not interact is less justified. The final state interaction can give rise to the coalescence of nucleons into composites.

A more complete presentation of the Gudima-Toneev cascade and comparisons with experiments can be found in [Ton83].

B.2 Isabel cascade

The Isabel code [Yar79, Yar81] is a direct generalisation of the VEGAS calculations [Che69] which aims to treat fairly accurately the multiple collision processes in nuclei, but disregards the nucleon-nucleon correlations. It is based on concepts of relativistic classical mechanics, i.e. the momenta and coordinates (trajectories) of particles are treated classically. Both target and projectile are assumed initially to be cold Fermi gases in their respective potential wells. The nucleon-nucleon cross-sections in the calculations are free nucleon-nucleon cross-sections. The only quantum mechanical concept incorporated is the Pauli principle. The pions are produced and absorbed via Δ formation, decay, and capture $N+N \rightleftharpoons \Delta+N$ and $\Delta \rightleftharpoons \pi+N$ (see Chap. 7).

The simulation process uses a 'timelike basis' Monte Carlo procedure [Che69]. This procedure follows the states of all the cascade particles as a function of time. One advantage of using the timelike basis is the possibility of changing the global properties of the system as the nucleus-nucleus interaction proceeds. The nuclear density distributions in both the projectile and the target are approximated by a step-function distribution. The relative densities to the folded-Yukawa-sharp-cutoff density distribution with the sharp cutoff radius $R_s = 1.18A^{1/3}$ fm (half density radius $R_s = 1.18[1-0.85A^{-2/3}]A^{1/3}$), and $t = r_{0.1} - r_{0.9}$=2.4 fm, $r_{0.1}$ and $r_{0.9}$ being the radii at which the density drops to 0.1 and 0.9 times the central density (which is always 0.145 fm^{-3}), respectively. Both the target and projectile particles reside in potential wells. The momentum distribution of these nucleons is assumed to be that of a degenerate Fermi gas. The depth of the potential well for protons and neutrons is the sum of the corresponding Fermi energy and the separation energy.

All calculations are performed in the target frame. Effects of the Pauli principle are taken into account for both the projectile and target. Cascade particle energies are not allowed to fall below the Fermi energies in either the target or projectile systems. One considers interactions between the Fermi sea particles or the projectile and the Fermi sea particles of the target, or between the cascade particles (i.e. particles which have been lifted out of the Fermi sea) and Fermi sea particles of either projectile or target. Interactions between particles in the same Fermi sea are not allowed. In the present version of the program, one neglects the interaction between cascade particles. The cascade particles in the region of overlap between the projectile and target are followed until they leave the region (independent of their kinetic energy), whereas outside of the overlap region, they are followed until they either leave the projectile and target volume, or their energy falls below a given cutoff energy (the prescription of the cutoff energy is the same as in Ref. [Che69]).

As a cascade develops, the density in the participating Fermi seas is depleted. Since the detailed nature of the density rearrangement is unknown, one has applied two extreme prescriptions:

a. Fast rearrangement. After each collision with a target (projectile) partner, the density distribution ρ_i of the 'partner' type (i denotes proton or neutron) in the target (projectile) is instantaneously and uniformly reduced for the whole nucleus. In addition, any given particle is not allowed to interact within a distance smaller than $\rho_i^{-1/3}$ from its last interaction.
b. Slow rearrangement. After each collision, a 'hole' of volume $1/\rho_i$ is punched in the density distribution configuration space around the position of the interaction. No more interactions are allowed in this hole volume. The holes may depend or not of the isospin, i.e. one may apply them to protons and neutrons independently using their proper densities, or make holes for all nucleons with a radius based on the total nuclear density.

The residual excitation energies of the target and the projectile are the sums of the hole (in the particle-hole sense) energies and the energies of the particles which have fallen below the cutoff energy. The residual linear and angular momenta are calculated in a similar fashion. The projectile velocity is kept constant during the collision, the recoil being calculated at the end.

B.3 Liège cascade

The main difference between the Liège and Isabel cascades is that the Cugnon procedure does not follow the state of the ensemble of the cascade particles but the state of each cascade particle as a function of time, as it is done also in the Dubna cascade. This permits to take into account in a total explicit way the Fermi motion of the nucleons and the collisions that it generates. Most of the details on the Cugnon cascade, or Liège INC model, are given in Ref. [Cug80].

In this thesis, we have used the hybrid code INC+percolation of Ref. [Cug89] including also a recently improved parametrization of the nucleon-nucleon interaction cross-sections as described in Ref. [Cug97, Cug97b]. This code is followed by an evaporation calculation [Dre62]. The model includes pion and delta production as well as an isospin degree of freedom. This hybrid version is the newest of the three INC codes that we present in this work.

At the beginning, nucleons inside each nucleus are randomly positioned in a sphere of radius $1.12A^{1/3}$ fm (where A is the nucleus mass) and in a momentum sphere of radius $P_F = 235$ MeV/c. The Fermi motion of all nucleons is frozen up to its first collision. The impact parameter b of the collision is randomly chosen in a disk of radius equal to the sum of the radii of the two nucleii. The calculation uses relativistic kinematics. Particles move along straight line trajectories until two of them reach their minimum distance of approach, d_{min}. Wether they collide or not is governed by a comparison of the total collision cross section with πd_{min}^2. The Pauli principle is applied to forbid final states which are already occupied. The blocking factor relies on phase space occupation probabilities inside a reference volume centered around each particle in the final state. This reference volume is the direct product of a sphere in ordinary

space of 2 fm radius and a sphere in momentum space of 200 MeV/c radius. Soft collisions, i.e., with a c.m. energy smaller than 35 MeV, are suppressed. The potential energy of the nucleons in the nuclei is neglected. The absence of a potential, avoiding a treatment of collisions for off mass shell nucleons, is justified at high bombarding energies. At these high bombarding energies, the potential energy will be restored in an approximate manner, as explained in the following.

In order to partly restore the effect of the potential well felt by nucleons inside a nucleus, the procedure given by the Ref. [Mon93] is applied, a feature that can be of importance at the relatively low bombarding energy. It has proved to be quite successful for the analysis of a vast body of data in the 250-800 AMeV range. Since the origin of all colliding nucleons is known (target or projectile), their energy, relative to their emitter, can be determined after any nucleon-nucleon collision. It is compared to a value V. This 'potential' energy, 32 MeV, was determined in a somewhat *ad hoc* manner in Ref. [Mon93], but it is close to the average (over all the nucleons of a nucleus) energy needed for a nucleon to escape from the potential well. Nucleons more energetic than V can 'escape', with an energy of V substracted. Otherwise they 'reintegrate' into their parent nucleus waiting for a possible new collision.

This procedure satisfactorily describes the kinetic energy of the free nucleons. It however introduces a violation of energy conservation in the model calculation. This can be taken into account, considering that the energy lost in this procedure is mainly recovered under the form of the excitation energy of the clusters formed in the percolation. It is reasonable that this extra excitation energy can be attributed to the nucleons that have been hit but that did not have enough energy to escape their parent nucleus. The energy conservation is restored in the following way. Let ΔE be the energy not conserved in this procedure. One then corrects the excitation energy of a fragment f by a quantity δE given by $(Nin_f/Nin_{tot})\Delta E$ where Nin_{tot} is the total number of nucleons that are not able to escape in the whole system and Nin_f the number of nucleons that included in a fragment f which were not able to escape. This correction is applied to fragments of charge greater than 6. This procedure restores energy conservation in the model, it allows us to treat in a reasonable manner the potential energy effects while keeping the simplicity of the cascade approach. Correcting the excitation energy rather than the kinetic energy of the fragments is justified in some sense by the fact that the main momentum flow is governed by collisions, accurately described by the cascade model.

INC to percolation

All the particles are followed in time, up to a stopping time t_{stop}. Since colliding nuclei are treated as a cloud of nucleons, fragments are not naturally defined at the stoppping time. A percolation procedure is used to construct residual fragments.

In the version of Liège cascade for nucleon-nucleus collisions (where a static potential well is introduced), the stopping time has been parametrized [Cug97b] as a function of target mass, incident energy, and impact parameter using criteria based on the time evolution of various variables with time. Namely, the excitation energy of the remnant (naturally defined by the nucleons that are remaining in the volume of the potential well), the emission anisotropy, and the saturation of the cumulative numbers of collisions or escaping particles. Changes of behaviour

of these observables were observed at about the same time, so defining the stopping time t_{stop} rather consistently. In the nucleus-nucleus case, the stopping time is determined in a similar manner and has been set to 40 fm/c [Dor01].

In Ref. [Cug89], the percolation is applied to the configuration at the late collision just before the stopping time. The percolation distance d_{cut} is chosen to be 2 fm, a reasonable value as regard to the average distance between nucleons in ordinary nuclear matter. Moreover one considers the possibility of performing the percolation at a time t_{per} later than t_{last}, the time at which the latest collision occurs.

For small impact parameter, the configuration are rather homogeneous and close to a spherical geometry. The collision process is almost over. In such conditions, there is an approximate correlation between d_{cut} and t_{per} leading to roughly the same fragmentation pattern: an increase of t_{per} can be compensated by an increase of d_{cut}, as explained in Ref. [Cug89, Mon93]. This exactly holds for a self-similar radial flow, i.e., when the particles have a radial outward velocity proportional to their distance from the center of the system.

For the very peripheral collisions, t_{last} is rather small, and, at this time, the quasiprojectile and the quasitarget are almost touching each other, with perhaps one or two nucleons in between. A straight application of percolation on such a configuration leads to a spurious 'fusionlike' event. Since quasiprojectile, quasitarget, and nucleons in between have rather different velocities in the longitudinal direction, there are no $d_{cut} - t_{per}$ correlations for this case. Adopting a t_{per} larger than t_{last} propagates further the fragments and the nucleons and separates the two big fragments from each other. One has to remember that nucleons inside the quasiprojectile and the quasitarget have practically not interacted. The Fermi motion is thus frozen inside these objects and they move as a whole.

For not too large impact parameters (midperipheral collisions), the situation is a little bit different: there are still two large fragments, not too far away from each other, with nucleons and perhaps one or two light clusters in between. Increasing t_{per} to achieve a good separation of the big clusters may dissociate the light ones. This can be circumvented by increasing d_{cut}.

These considerations suggest that a compromise can be reached by an appropriate b-dependent choice of t_{per} and d_{cut}. Similar considerations and choices are made in Ref. [Mon93]. One has adopted $t_{per} = t_{last} + 0.75(t_{stop} - t_{last})$ and d_{cut}^2 varying linearly with the impact parameter from 9 fm^2 for central collisions to 18 fm^2 for peripheral ones for the system C+Au at 1000 AMeV studied in this work. These values are significantly larger than those used for the system Ar+Ni at 95 AMeV [Dor01]. The reason is that, st a time of 40 fm/c, the system at 1000 AMeV is more expanded and the percolation distances have to be increased. This distance has been phenomenologically adjusted to reproduce the measured ratio of the fast proton production measured in the present experiment [Vol02]. These adjustments allow to make vary slightly and monotically with the impact parameter the mean position of the noninteracting nucleons of the projectile, relative to the target position, at the percolation time. This permits to perform the percolation in homogeneous conditions. This procedure can be interpreted as a compensation required by percolation being performed in ordinary space only and not in phase space.

Percolation generates free nucleons, light composite particles and excited fragments. The excitation energy of the clusters can be evaluated by looking at the internal motion in their center of mass frame. It is defined as the difference between the total energy of the nucleons inside a cluster and the sum of the mass energy of the constituents. This excitation energy has to be released by means of an afterburner. The evaporation code of Dresner [Dre62] has been chosen for that purpose. It calculates the statistical decay of the fragments, following the Weisskopf theory [Wei37], through light particle (n, p, d, t, ^3He, ^4He) emission. Angular momentum is neglected. Level density parameters are taken from Ref. [Ign75]. For the deexcitation of light fragments with mass number between 5 and 21, instead of the standard evaporation formula, the code utilises the Fermi breakup [Fer50] model .

See Ref. [Dor01] for more complete informations on first tests of this new nucleus-nucleus version of Liège Intra-Nuclear Cascade.

Appendix C

Moving Source Fit

In a canonical ensemble, the probability to find a particle at a certain energy is determined by the state density, represented by the Boltzmann factor exp(-E/T) . Here, E is the kinetic energy of a particle and T the temperature of the system. The corresponding energy spectra show the classical Maxwell-Boltzmann distribution

$$f(E) = \frac{1}{C}\sqrt{E}\exp(-\frac{E}{T}) \tag{C.1}$$

where isotropic emission is assumed; C is a normalization factor.

Assuming, that a reaction system consists of one or several distinct sources, travelling with different velocities in the laboratory system, the moving-source formalism is appropriate to describe the energy spectra for a species of particles. For this reason, this appendix explains how to combine Maxwell-Boltzmann distributions, taking into account the Coulomb repulsion of the particles from the source, and later on generalizing this approach to a relativistic treatment. The inclusion of a radial flow profile is done for the sake of completeness and for documentation purposes, even if it is not part of this thesis.

C.1 Maxwell-Boltzmann distribution

In order to describe energy spectra of an experiment, we have to normalize Eq. C.1 in an appropriate way. This will be done first by the normalization of the probability distribution f(E)

$$\int f(E)dEd\Omega = 4\pi\int_0^\infty f(E)dE = 1$$

The integration of Eq. C.1 over all energies and over solid angle yields the normalization constant C.

$$\begin{aligned} C &= 4\pi\int_0^\infty \sqrt{E}\exp\left(-\tfrac{E}{T}\right)\,dE \\ &= 4\pi\,\left(\tfrac{1}{T}\right)^{-3/2}\Gamma(3/2) \\ &= 4\pi\,\tfrac{\sqrt{\pi}}{2}(T)^{3/2} \\ &= 2(\pi T)^{3/2} \end{aligned}$$

with the Gamma function $\Gamma(3/2) = \Gamma(1/2+1) = 1/2\Gamma(1/2) = 1/2\sqrt{\pi}$ [Rot60]

and hence

$$f(E) = \frac{1}{2(\pi T)^{3/2}} \sqrt{E} \exp\left(-\frac{E}{T}\right) \tag{C.2}$$

Expressed in terms of a double-differential cross-section, Eq. C.2 becomes

$$\frac{\partial^2\sigma}{\partial E\, \partial\Omega} = \sigma f(E) = \frac{\sigma\sqrt{E}}{2(\pi T)^{3/2}} \exp\left(-\frac{E}{T}\right)$$

C.2 Radial flow

As a Schmankerl[1], we extend the momentum spectra by the radial flow. For the sake of simplicity, we assume a constant radial flow p_F pointing away from the center of the source. It is straight forward to implement also flow profiles which need simply one integration more. The radial flow enters by substituting the momentum p by $\overrightarrow{p} - \overrightarrow{p}_F$.

Therefore, we have

$$\begin{aligned}
\frac{\partial^3\sigma}{\partial p^3} &= \sigma\, C \tfrac{3}{4\pi R^3} \int \exp\left(\frac{-\left(\overrightarrow{p}-\overrightarrow{p}_F\right)^2}{2mT}\right) r^2\, dr\, d\Omega \\
&= \sigma\, C\, \tfrac{1}{4\pi} \int_0^{2\pi}\int_0^{\pi} \exp\left(\frac{-p^2-p_F^2+2pp_F\cos(\vartheta)}{2mT}\right) \sin(\vartheta)\; d\vartheta\, d\phi \\
&= \sigma\, C\, \tfrac{1}{2}\, \exp\left(\frac{-p^2-p_F^2}{2mT}\right) \int_0^{\pi} \exp\left(\frac{2pp_F\cos(\vartheta)}{2mT}\right) \sin(\vartheta)\; d\vartheta \\
&= \sigma\, C\, \tfrac{1}{2} \exp\left(\frac{-p^2-p_F^2}{2mT}\right) \int_{-1}^{+1} \exp\left(\tfrac{pp_F z}{mT}\right)\; dz \\
&= \sigma\, C\, \tfrac{1}{2}\, \exp\left(\frac{-p^2-p_F^2}{2mT}\right) \tfrac{mT}{pp_F} \left[\exp\left(\tfrac{pp_F}{mT}\right) - \exp\left(\tfrac{-pp_F}{mT}\right)\right] \\
&= \sigma\, C\, \exp\left(\frac{-p^2-p_F^2}{2mT}\right) \tfrac{mT}{pp_F} \sinh\left(\tfrac{pp_F}{mT}\right).
\end{aligned}$$

The integration variable $d\Omega$ describes here the integration over the spherical source with radius R. The r integration is necessary in order to perform a volume integration (see below). Normalization is performed by looking up an integration table (see [Gra65], 3.562(4)) and yields $C = (2\pi mT)^{3/2}$. It is the same normalization constant as that for the thermal distribution. That is understandable, since the introduction of p_F did only change the shape of the momentum spectrum. In a Gedanken-experiment, we can imagine to sample a energy spectrum in a Monte-Carlo simulation. If we add to each sampled entry of the energy spectrum the radial flow, this entry is sorted into the spectrum at a different energy, but the integral of the spectrum does not change. The Maxwell-Boltzmann distribution with radial flow yields therefore

$$\frac{\partial^3\sigma}{\partial p^3} = \frac{\sigma}{(2\pi mT)^{3/2}}\; \exp(-\frac{p^2+p_F^2}{2mT})\; \frac{mT}{pp_F} \sinh(\frac{pp_F}{mT}).$$

[1] german or austrian for delicacy

C.3 Coulomb repulsion

Charged particles, emitted from a charged source, are objects of the mutual Coulomb repulsion. Therefore, a cross-section in the center of mass of the source at an energy E has to be calculated at the original energy $E - V_C$, with the Coulomb energy V_C , before the particle is accelerated by the source. This is the appropriate description for the emission of a particle from the surface, pushed by the charge within the source, or accelerated by the charge within a sphere around the center of the system. For a volume breakup of the source, however, this approach is too simple and a volume integration over all emission points of the source is needed. If we take as an approximation a mean momentum vector pointing away from the center, one ends again with the description of a thermal source with radial flow. To make it clear, the Coulomb repulsion of a volume breakup of an source can be described in first order by the formulae given in the radial flow section. In second order, it is exactly the formula for radial flow, if one incorporates instead of a mean constant flow a flow profile like the Hubble flow [Rei97b]. In case of an surface emission, we get

$$\frac{\partial^2\sigma}{\partial E\,\partial\Omega} = \sigma\frac{\sqrt{E-V_C}}{2(\pi T)^{3/2}}\exp\left(-\frac{E-V_C}{T}\right) \qquad (E \geq V_C)$$

C.4 A moving source in the laboratory

In a classical picture the (triple differential) cross section is Galilei invariant since $d^3p = d^3p'$, that is

$$\frac{\partial^3\sigma}{\partial p^3} = \frac{\partial^3\sigma'}{\partial p'^3}$$

where the primed quantities are in the center of mass system and the unprimed quantities in the laboratory system. The transition from momenta to energies is done by

$$\frac{\partial^3\sigma}{\partial p^3}\,p\,m = \frac{\partial^2\sigma}{\partial\Omega\,\partial E} \quad and \quad \frac{pm}{p'm} = \sqrt{\frac{E}{E'}}$$

and

$$\frac{\partial^2\sigma}{\partial\Omega\,\partial E} = \sigma\,\sqrt{\frac{E}{E'}}\,\frac{\sqrt{E'-V_C}}{2(\pi T)^{3/2}}\exp\left(-\frac{E'-V_C}{T}\right)$$

for a thermal source with Coulomb repulsion. The connection between the primed and unprimed quantities is given by a boost of the particle in the center of mass system into the laboratory by the (vector-)velocity of the source.

C.5 Relativistic energies

We set for the sake of simplicity $c = 1$ and start again from

$$\frac{d^3\sigma}{dp^3} = \sigma\, C\, \exp(-\frac{E}{T})$$

with $E = \sqrt{p^2 + m^2}$ beeing now the total energy of the particle.

With $dE/dp = p/E$, we get

$$\frac{d^3\sigma}{dp^3} = \frac{d^2\sigma}{p^2 dp\, d\Omega} = \frac{d^2\sigma}{p^2 \frac{E}{p} dE\, d\Omega} = \frac{1}{pE}\frac{d^2\sigma}{dE\, d\Omega}$$

The relativistic invariant Maxwell-Boltzmann spectrum is represented by

$$\frac{d^2\sigma}{dE\, d\Omega} = C\, \sigma\, pE\, \exp(-E/T),$$

with normalization C. It is defined as

$$\begin{aligned} C^{-1} &= 4\pi \int pE \exp(-E/T) dE \\ &= 4\pi \int_m^\infty \sqrt{E^2 - m^2} E \exp(-E/T) dE \end{aligned}$$

with 4π for the solid angle integration and with

$$\begin{aligned} \frac{d}{dE}\frac{1}{3}\left(E^2 - m^2\right)^{\frac{3}{2}} &= \frac{1}{3}\frac{3}{2}\left(E^2 - m^2\right)^{\frac{1}{2}} 2E \\ &= \sqrt{E^2 - m^2} E \quad , \end{aligned}$$

the partial integration yields

$$\begin{aligned} C^{-1} &= 4\pi \left[\frac{1}{3}\left(E^2 - m^2\right)^{\frac{3}{2}} \exp(-E/T)\right]_m^\infty - 4\pi \int_m^\infty \frac{1}{3}\left(E^2 - m^2\right)^{\frac{3}{2}} \frac{-1}{T} \exp(-E/T) dE \\ &= \frac{4\pi}{3T} \int_{mc^2}^\infty \left(E^2 - m^2\right)^{\frac{3}{2}} \exp(-E/T) dE. \end{aligned}$$

Using an integration table (see [Gra65], 3.387-6), it gives

$$\begin{aligned} C^{-1} &= \frac{4\pi}{3T}\frac{1}{\sqrt{\pi}} (2mT)^2 \Gamma\left(\frac{5}{2}\right) K_2\left(\frac{m}{T}\right) \\ &= \frac{4\pi}{3T}\frac{1}{\sqrt{\pi}} (2mT)^2 \sqrt{\pi}\frac{3}{4} K_2\left(\frac{m}{T}\right) \\ &= 4\pi\, T m^2 K_2\left(\frac{m}{T}\right). \end{aligned}$$

K_2 is a modified Bessel function (also called Macdonald functions) and can be expressed by (see [Gra65], 8.486-17)

$$K_2\left(\frac{m}{T}\right) = \frac{2T}{m}K_1\left(\frac{m}{T}\right) + K_0\left(\frac{m}{T}\right).$$

This yields finally

$$\begin{aligned} C^{-1} &= 4\pi\, Tm^2\left[\frac{2T}{m}K_1\left(\frac{m}{T}\right) + K_0\left(\frac{m}{T}\right)\right] \\ &= 4\pi\, 2T^2m^2K_1\left(\frac{m}{T}\right) + Tm^2K_0\left(\frac{m}{T}\right) \\ &= 4\pi\, m^3\left[2\left(\frac{T}{m}\right)^2 K_1\left(\frac{m}{T}\right) + \frac{T}{m}K_0\left(\frac{m}{T}\right)\right]. \end{aligned}$$

The $K_{0,1}$ are usually expressed by polynomials

$$P_{0,1} = \sqrt{\frac{m}{T}}\exp(\frac{m}{T})K_{0,1}(\frac{m}{T})$$

listed eg. in [Abr65], 9.8.6-8, which have a big numerical advantage. In the exponential of the Boltzmann factor, the total energy $E = E_{kin} + m$ is used. However, the large values of the particle masses cause problems to evaluate it numerically. If we take out the mass, it is canceled by the exponential in the normalization constant. Therefore, the final equation becomes

$$\frac{\partial\sigma^2}{\partial E\,\partial\Omega} = \sigma\,\frac{p\,(E_{kin}+m)\;\exp(-\frac{E_{kin}}{T})}{4\pi\;(T\,m)^{3/2}\;\left(2\frac{T}{m}P_1(\frac{m}{T}) + P_0(\frac{m}{T})\right)}.$$

C.6 A relativistic moving source

Since the equation of the total energy as function of the momentum is different to the classical case

$$\frac{d^3\sigma}{dp^3} = \frac{1}{pE}\frac{d^2\sigma}{dE\,d\Omega},$$

and the differential invariant cross section

$$E\frac{d^3\sigma}{dp^3} = E'\frac{d^3\sigma'}{dp'^3}$$

We get then

$$\frac{d^2\sigma}{dE\,d\Omega} = \frac{p}{p'}\frac{d^2\sigma'}{dE'\,d\Omega'}$$

and the moving source yields

$$\frac{\partial\sigma^2}{\partial E\,\partial\Omega} = \sigma\,\frac{p}{p'}\,\frac{p'\,(E'_{kin}+m)\;\exp(-\frac{E'_{kin}}{T})}{4\pi\;(T\,m)^{3/2}\;\left(2\frac{T}{m}P_1(\frac{m}{T}) + P_0(\frac{m}{T})\right)}$$

with the primed quantities in the center of mass of the source. We get the primed quantities by applying a Lorentz transformation, or Lorentz boost, into the rest frame of the source. For a boost in arbitrary direction, see [Loh92], A 1.3.

C.7 Relativistic radial flow

The relativistic radial flow is listed here only, since the original paper [Sie79] contains some errors, which are corrected in subsequent papers [Lis95, Rei97b] and yields

$$\frac{\partial\sigma^2}{\partial E\,\partial\Omega} = \sigma\,\frac{p}{p'}\,\frac{p'\,(E'_{kin}+m)\;\exp(-\frac{\gamma'_F E'_{kin}}{T})}{4\pi\;(T\,m)^{3/2}\;\left(2\frac{T}{m}P_1(\frac{m}{T})+P_0(\frac{m}{T})\right)}\;\left[(\frac{T}{E'}+\gamma'_F)\frac{\sinh\alpha'}{\alpha'}-\frac{T}{E'}\cosh\alpha'\right]$$

with $\gamma_F = 1/\sqrt{1-\beta_F^2}$, the average flow velocity β_F, and $\alpha{=}\gamma_F\beta_F p/T$. The primed quantities are in the center of mass system. The normalization factor is the same as for the relativistic case without radial flow for the same arguments given already in the classical case.

C.8 'Relativistic' Coulomb repulsion

The Coulomb repulsion is treated as in the classical case, reducing the total energy by the Coulomb repulsion and calculating momenta from this reduced quantity relativistically. Certainly, this is only a approximation and can be improved.

Appendix D

Proton kinetic energy spectra

The proton energy spectra for C+Au at 1000 AMeV are presented in this appendix for central collisions (b/b0=0.0-0.2) to peripheral collisions (b/b0=0.8-1.0). They are compared to the Liège cascade (see appendix B.3) coupled with two statistical models: the Dresner evaporation code and the multifragmentation model SMM (see appendix A.1). The most peripheral collision spectra are corrected from stray particle effects (see chapter 2). Some spectra exhibit non-exponential shapes as at $4.5^o < \theta_{lab} < 7^o$, $10^o < \theta_{lab} < 14^o$, and $27^o < \theta_{lab} < 45^o$ for peripheral collisions. This effect is due to identification problems not yet solved.

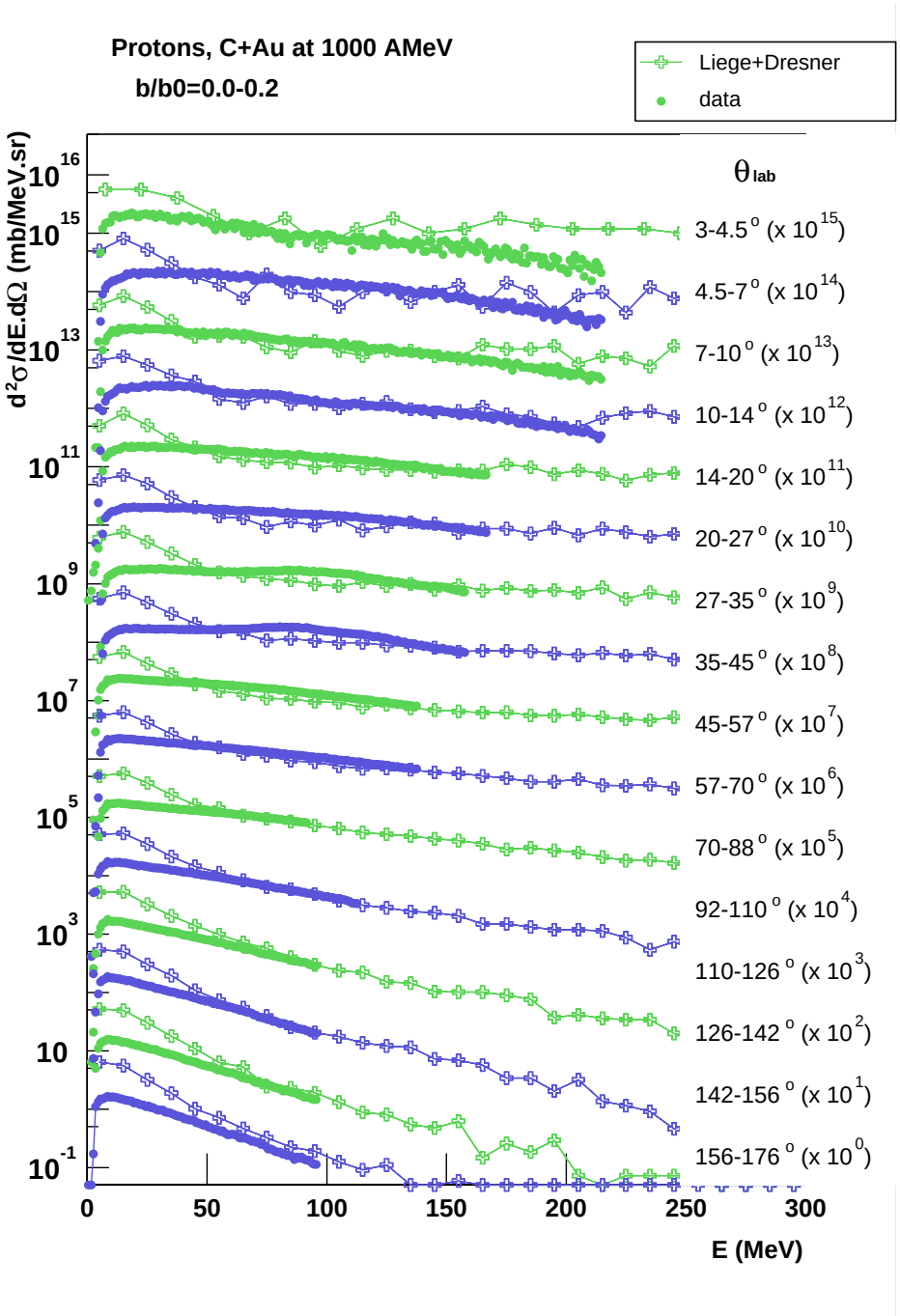

Figure D.1: *The proton kinetic energy spectra for C+Au at 1000 AMeV are compared to the Liège cascade model (high energies) coupled to the evaporation Dresner code (low energies) for b/b0=0.0-0.2 (central collisions).*

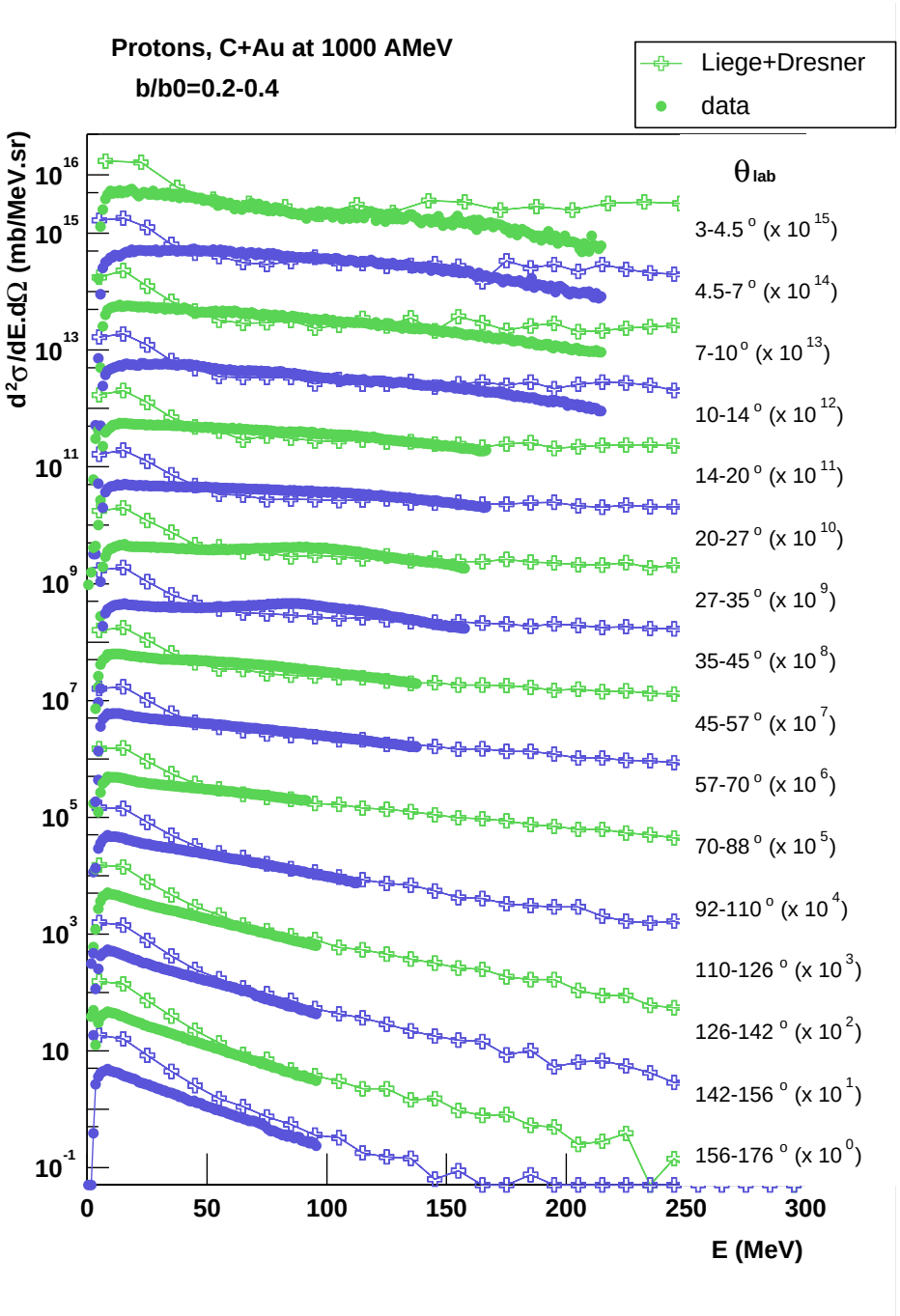

Figure D.2: *The proton kinetic energy spectra for C+Au at 1000 AMeV are compared to the Liège cascade model (high energies) coupled to the evaporation Dresner code (low energies) for b/b0=0.2-0.4 (almost central collisions).*

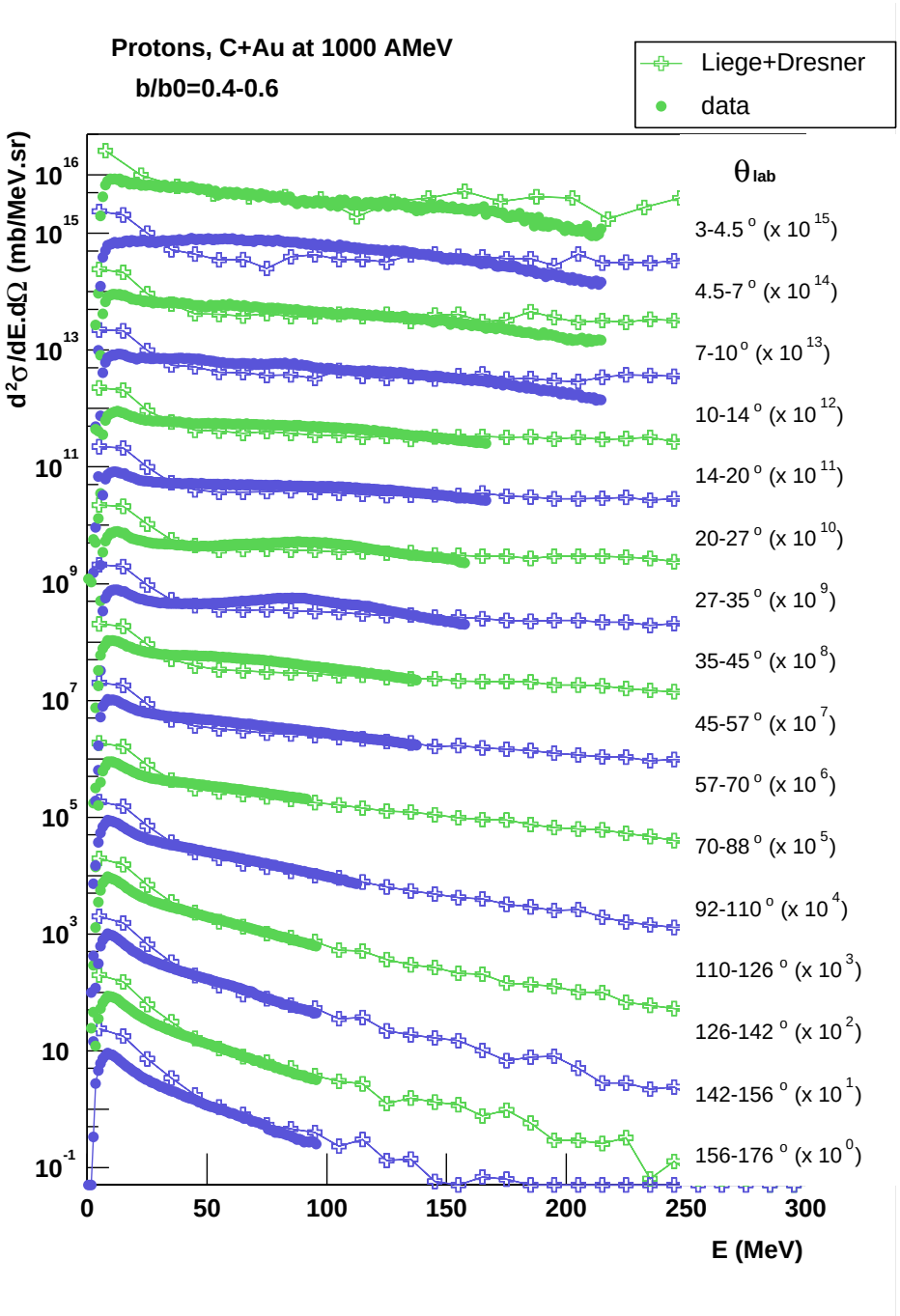

Figure D.3: *The proton kinetic energy spectra for C+Au at 1000 AMeV are compared to the Liège cascade model (high energies) coupled to the evaporation Dresner code (low energies) for b/b0=0.4-0.6 (semi-peripheral collisions).*

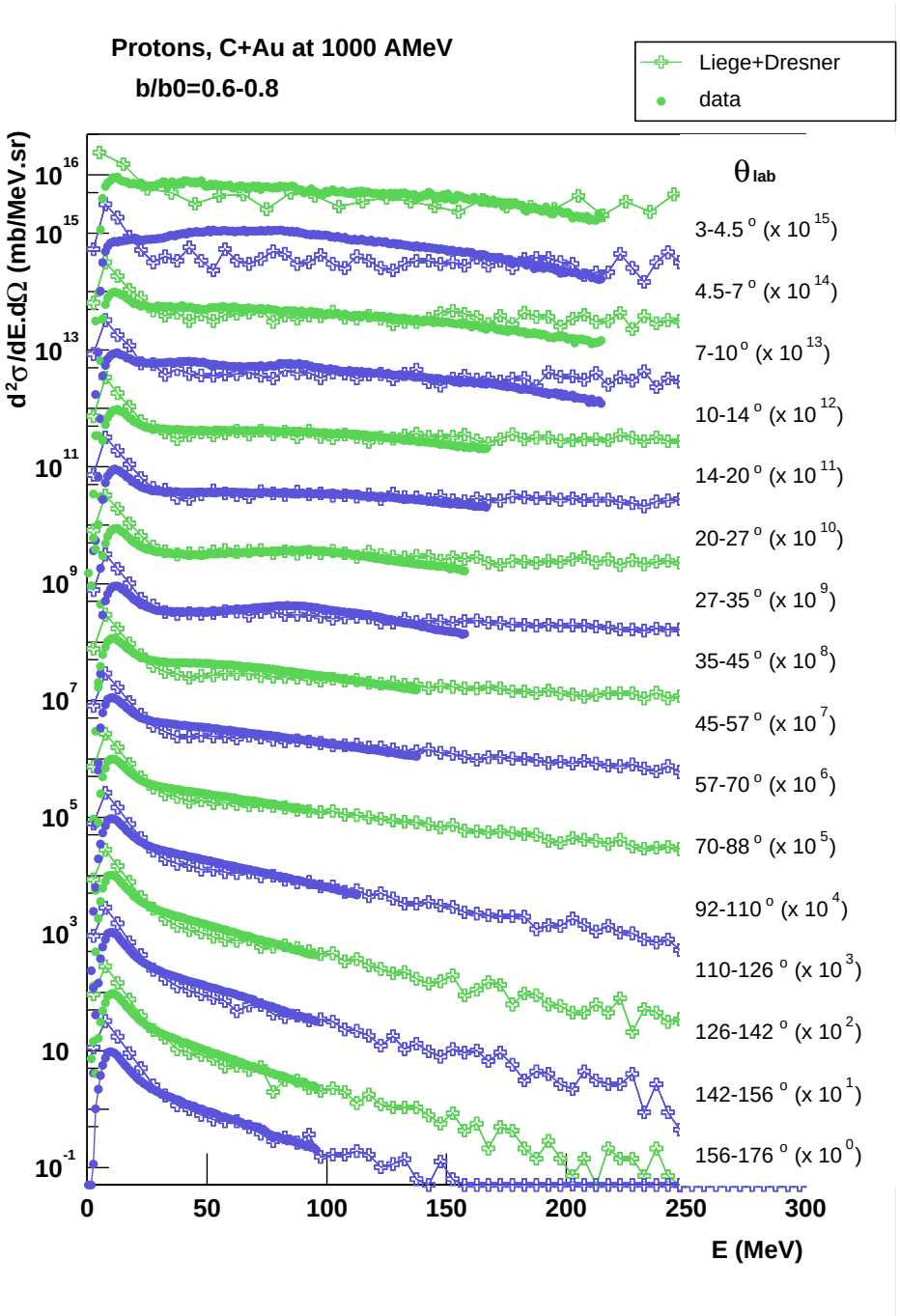

Figure D.4: *The proton kinetic energy spectra for C+Au at 1000 AMeV are compared to the Liège cascade model (high energies) coupled to the evaporation Dresner code (low energies) for b/b0=0.6-0.8 (almost peripheral collisions).*

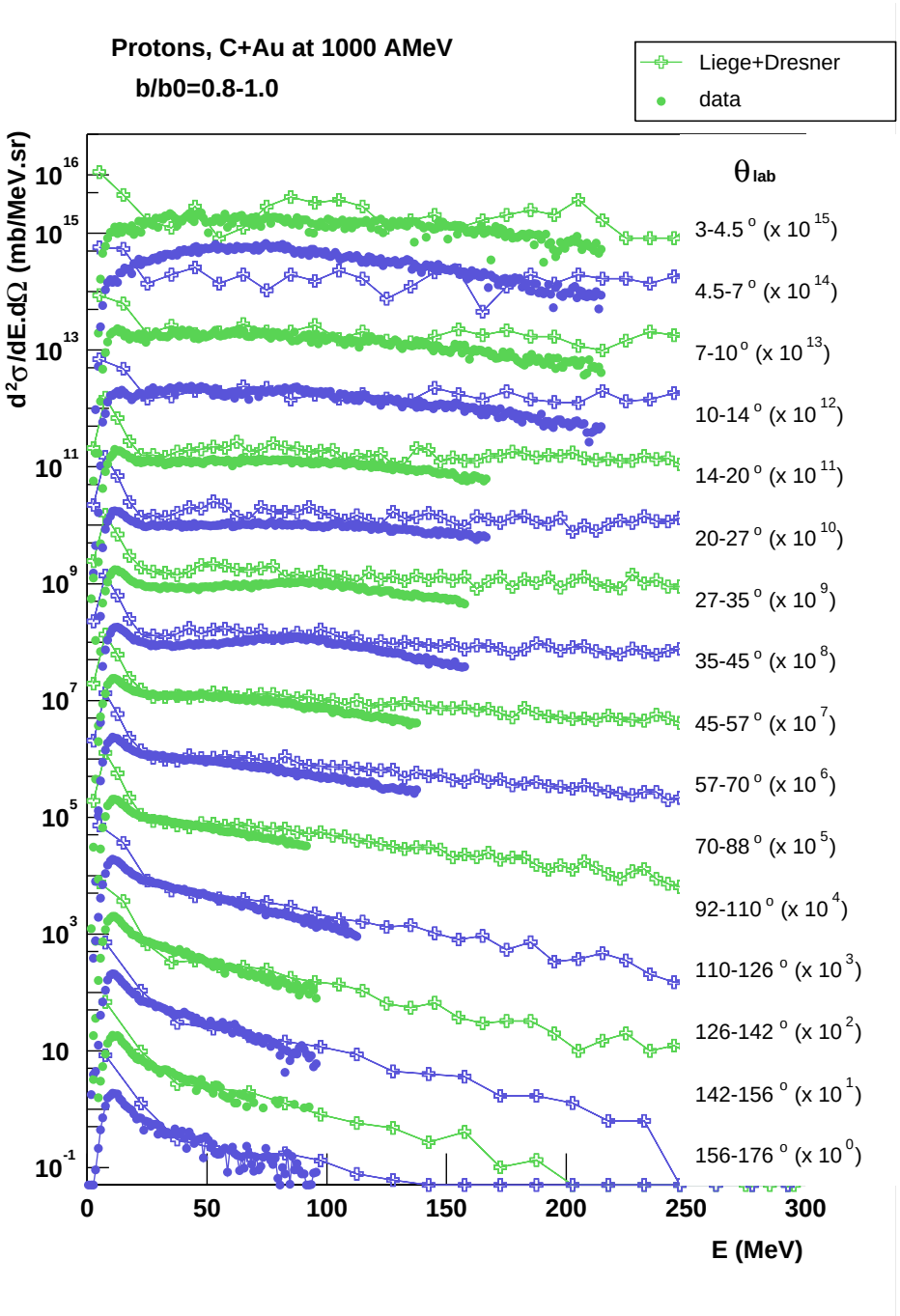

Figure D.5: *The proton kinetic energy spectra for C+Au at 1000 AMeV are compared to the Liège cascade model (high energies) coupled to the evaporation Dresner code (low energies) for b/b0=0.8-1.0 (peripheral collisions).*

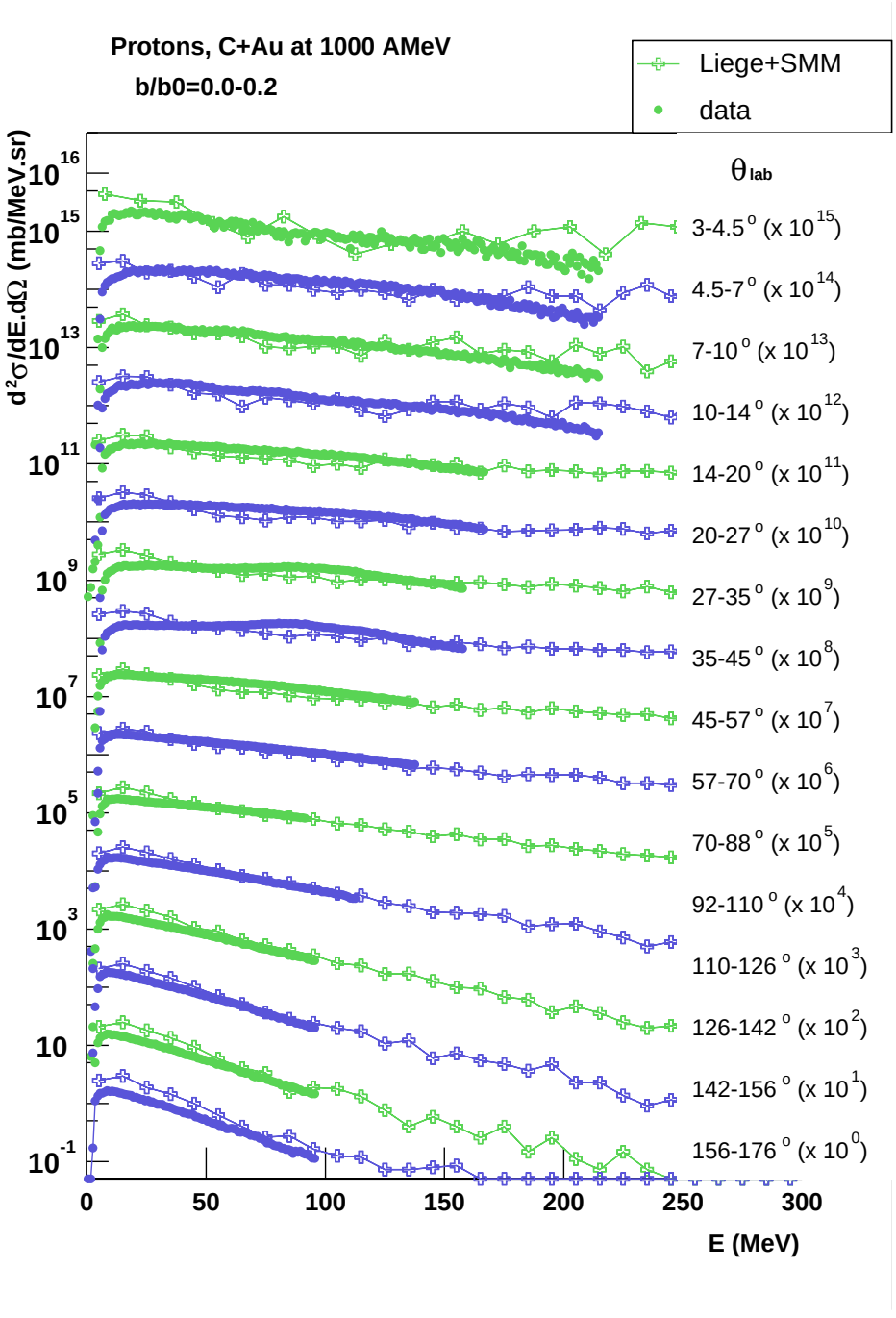

Figure D.6: *The proton kinetic energy spectra for C+Au at 1000 AMeV are compared to the Liège cascade model (high energies) coupled to SMM (low energies) for b/b0=0.0-0.2 (central collisions).*

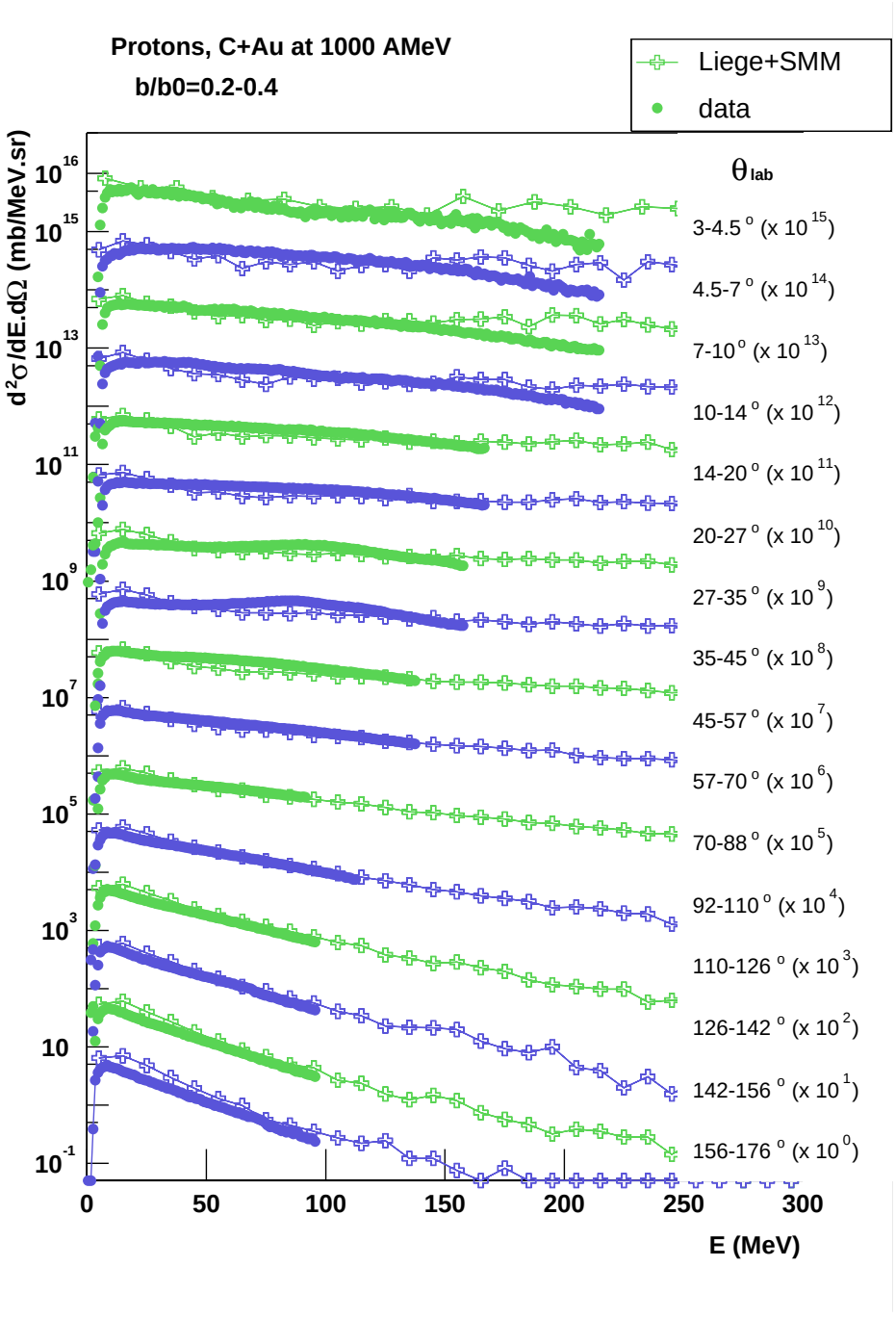

Figure D.7: *The proton kinetic energy spectra for C+Au at 1000 AMeV are compared to the Liège cascade model (high energies) coupled to SMM (low energies) for b/b0=0.2-0.4 (almost central collisions).*

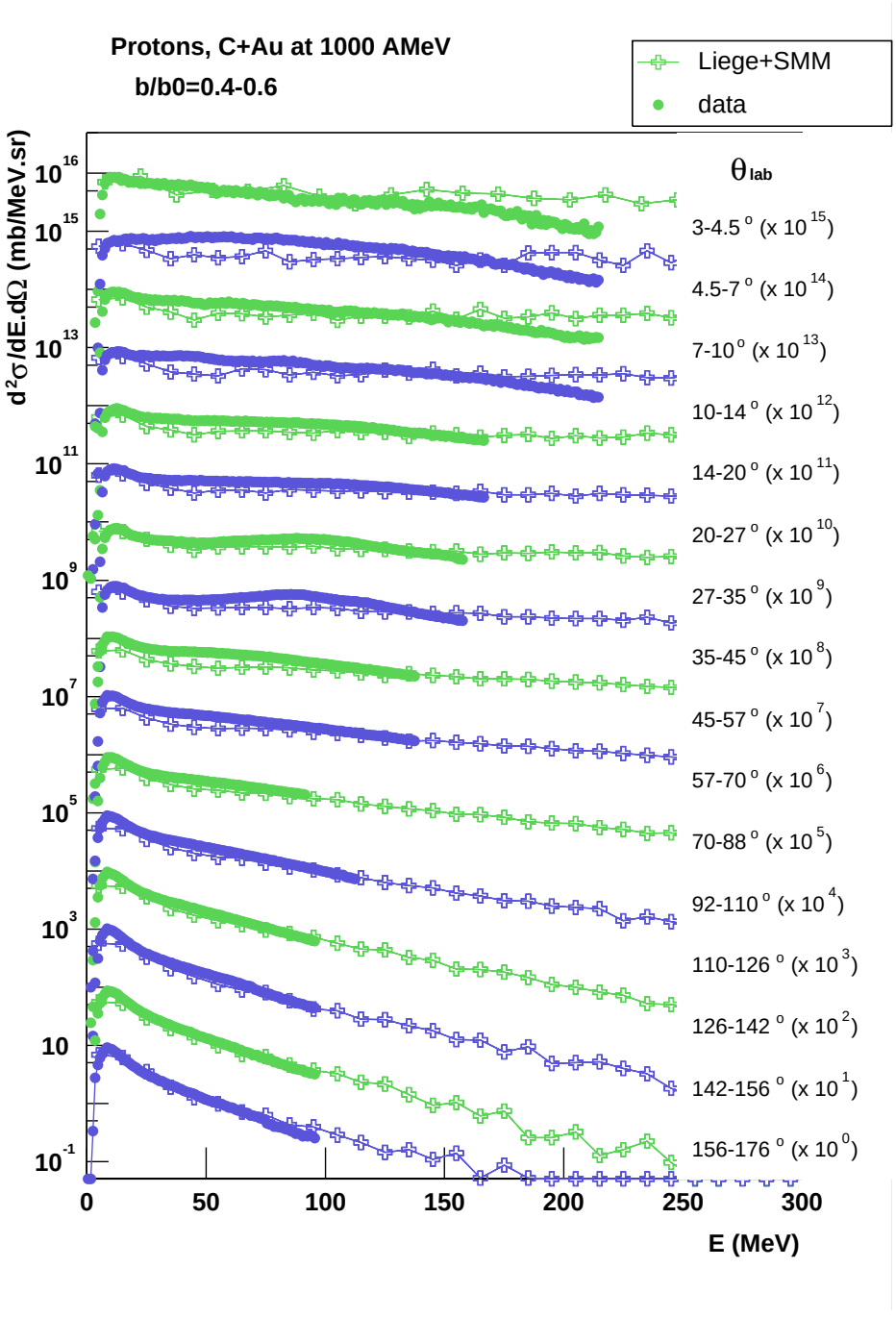

Figure D.8: *The proton kinetic energy spectra for C+Au at 1000 AMeV are compared to the Liège cascade model (high energies) coupled to SMM (low energies) for b/b0=0.4-0.6 (semi-peripheral collisions).*

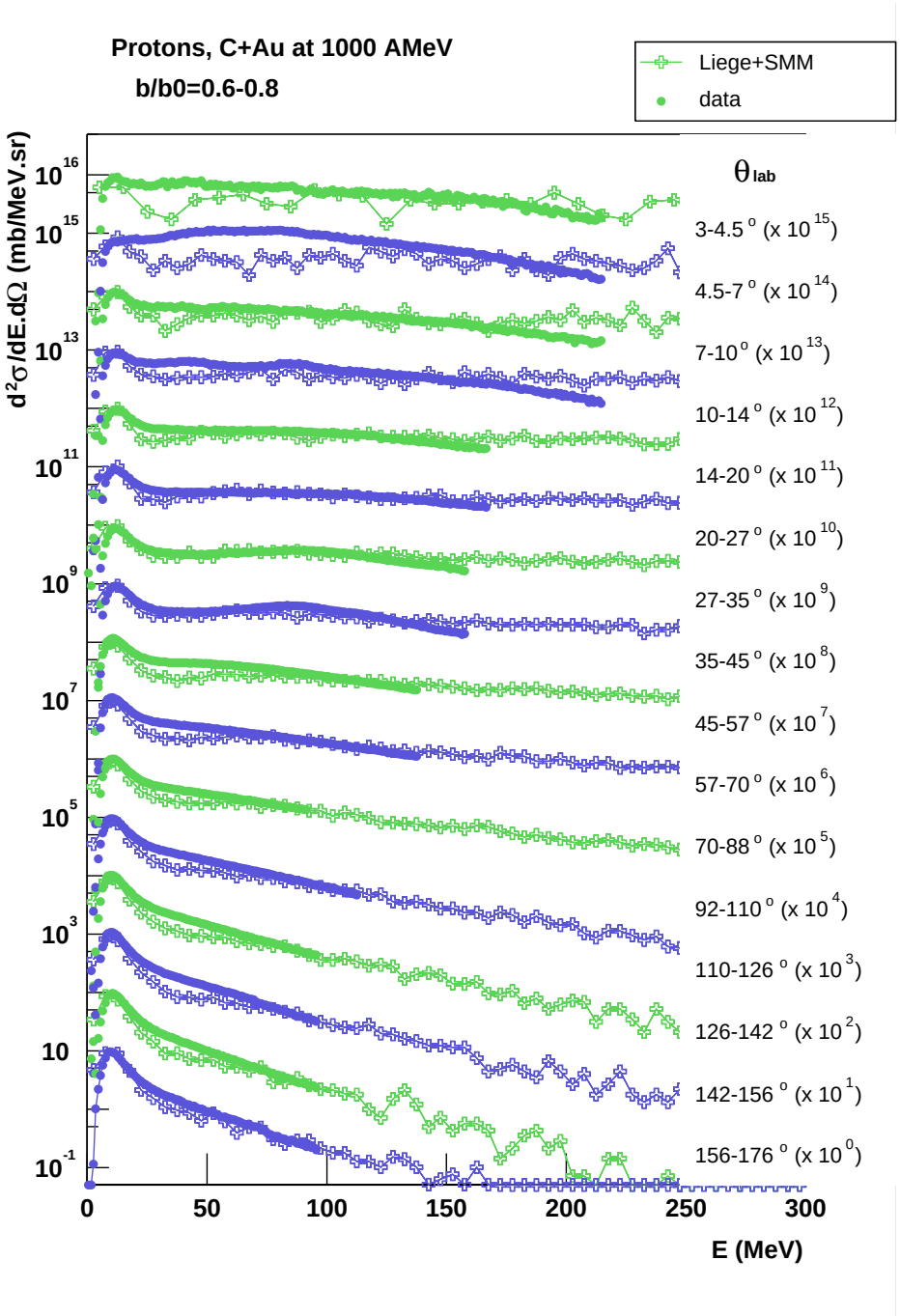

Figure D.9: *The proton kinetic energy spectra for C+Au at 1000 AMeV are compared to the Liège cascade model (high energies) coupled to SMM (low energies) for b/b0=0.6-0.8 (almost peripheral collisions).*

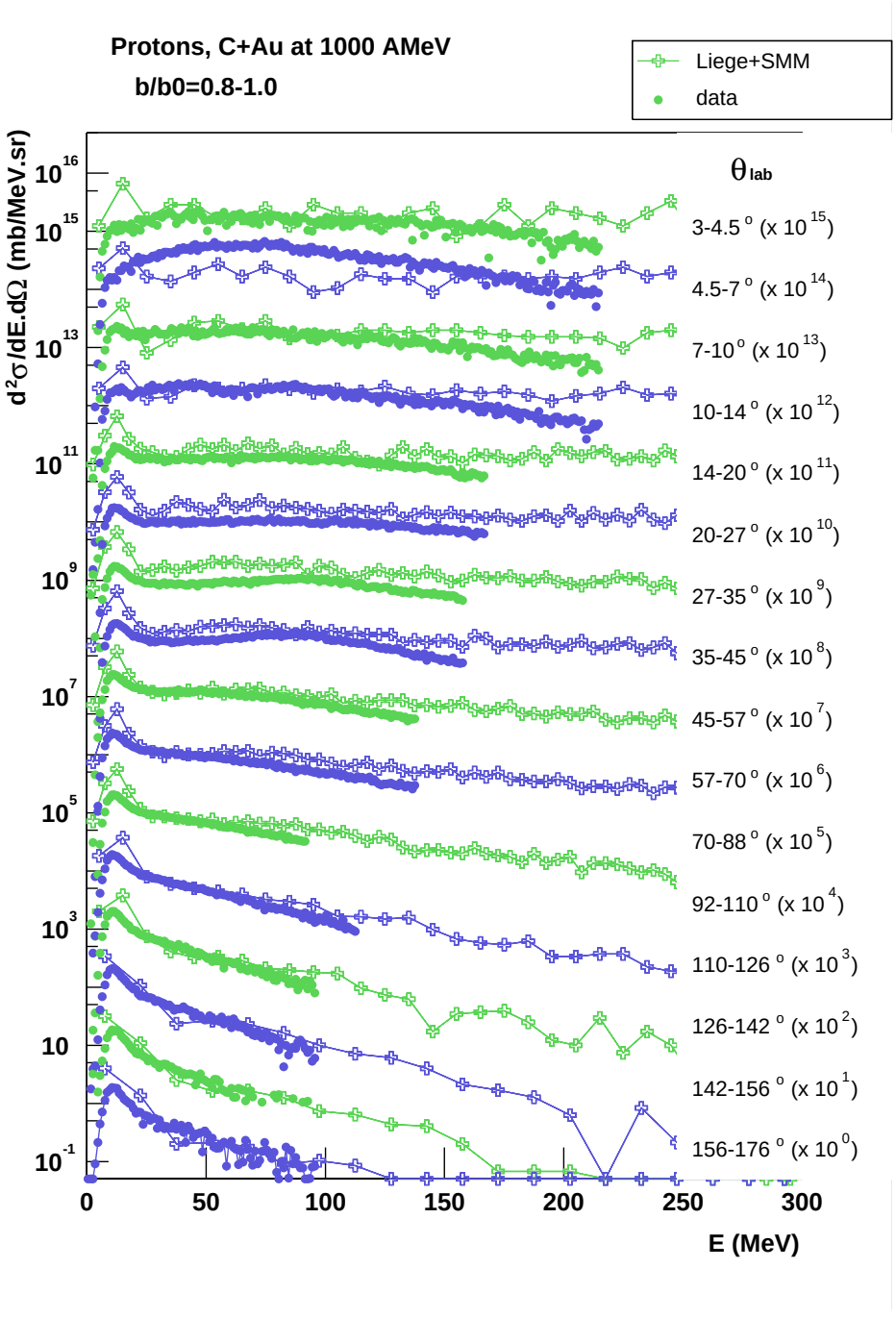

Figure D.10: *The proton kinetic energy spectra for C+Au at 1000 AMeV are compared to the Liège cascade model (high energies) coupled to SMM (low energies) for b/b0=0.8-1.0 (peripheral collisions).*

Bibliography

[Abr65] M. Abramowitz and I.A. Stengun, **Handbook of Mathematical Functions**, *Dover Publications*, INC., New-York, 1965

[Aic85] J. Aichelin and G.F. Bertsch, Phys. Rev. C 31(1985)1730

[Aic88] J. Aichelin et al., Phys. Rev. C 37(1988)2451

[Aic91] J. Aichelin et al., Phys. Rep. 202(1991)233

[Ala92] J.P. Alard et al., Phys. Rev. Lett. 69(1992)889

[Alb85] S. Albergo et al., Il Nuovo Cimento A 89(1985)1

[And99] A. Andronic and the FOPI Collaboration, Nucl. Phys. A 661(1999)333c

[And02] A. Andronic, private communication (2002)

[App95] M. Appenheimer et al., TAPS Collaboration, GSI Annual Report (1995)

[Aug96] G. Auger et al., Proposal of Experiment (1996)

[Avd98] S.P. Avdeyev et al., Eur. Phys. J. A 3(1998)75

[Avd99] V. Avdeyev et al., Nucl. Instr. and Meth. A 437(1999)424

[Bau85] W. Bauer et al., Phys. Lett. B 150(1985)53

[Bay71] G. Baym et al., Nucl. Phys. A 175(1971)225

[Bea99] L. Beaulieu et al., Phys. Lett. B 463(1999)159

[Bea00] L. Beaulieu et al., Phys. Rev. Lett. 84(2000)5971

[Bel00] N. Bellaize, PhD thesis, University of Caen, France (2000)

[Ber84] G.F. Bertsch et al., Phys. Rev. C 29(1984)673

[Bet30] H.A. Bethe, Annals of Physics 5 (1930) 325

[Bet90] H.A. Bethe, Rev. Mod. Phys. 62(1990)801

[Boc00] F. Bocage et al., Nucl. Phys. A 676(2000)391

[Boh91] A. Bohnet et al., Phys. Rev. C 44(1991)2111

[Bon85] J. Bondorf et al., Nucl. Phys. A 443(1985)321

[Bon95] J. Bondorf et al., Phys. Rep. 257(1995)133

[Bon95b] J. Bondorf et al., Phys. Lett. B 359(1995)261

[Bot87] A. Botvina et al., Nucl. Phys. A 475(1987)663

[Bot02] A. Botvina, private communication (2002)

[Bou01] B. Bouriquet, PhD thesis, University of Caen, France (2001)

[Bro60] I.N. Bronstein and K.A. Semendjajew, **Taschenbuch der Mathematik**, *Verlag Harri Deutsch*, Zürich und Frankfurt/Main, 1960

[Bro84] R. Brockmann et al., Phys. Rev. Lett. 53(1984)2012

[Bru54] K.A. Brückner, et al., Phys. Rev. 95(1954)217

[Bru55] K.A. Brückner and C.A. Levinson, Phys Rev. 97(1955)1344

[Bru55b] K.A. Brückner, Phys. Rev. 97(1955)1353

[Cam02] X. Campi et al., in Proceedings of the XL International Winter Meeting on Nuclear Physics, Bormio, Italy, edited by I.Iori (2002)

[Cav90] C. Cavata et al., Phys. Rev. C 42(1990)1760

[Chb01] A. Chbihi, private communication (2001)

[Che69] K. Chen et al., Phys. Rev. 166(1969)949

[Chi00] S. Chikazumi et al., Phys. Lett. B 476(2000)273

[Cho94] Ph. Chomaz et al., Phys. Rev. Lett. 73(1994)3512

[Col97] M. Colonna et al., Phys. Rev. C 55(1997)1404

[Cug80] J. Cugnon, Phys. Rev. C 22(1980)1885

[Cug89] J. Cugnon and C. Volant, Z. Phys. A 334(1989)435

[Cug97] J. Cugnon et al., Phys. Rev. C 56(1997)2431

[Cug97b] J. Cugnon et al., Nucl. Phys. A 620(1997)475

[Cur83] M.W. Curtin et al., Phys. Lett. B 123(1983)289

[Dag00] M. D'Agostino et al., Phys. Lett. B 473(2000)219

[Dan91] P. Danielewicz and G.F. Bertsch, Nucl. Phys. A 533(1991)712

[Des00] P. Désesquelles et al., Phys. Rev. C 62(2000)024614

[Dor01] D. Doré et al., Phys. Rev. C 63(2001)034612

[Dre62] L.W. Dresner, Oak Ridge Report No. ORNL-TM-196, 1962

[Eva55] R.D. Evans, **The atomic nucleus**, *Mac Graw-Hill*, Book company, Inc., N-Y., 1955

[Fel95] H. Feldmeier et al., Nucl. Phys. A 586(1995)493

[Fel99] H. Feldmeier, J. Knoll, W. Nörenberg, J. Wambach (Eds.), *Multifragmentation Proceedings of the International Workshop XXVII*, Hirschegg, Austria, Jan. 17-23, 1999; GSI, Darmstadt, Germany 1999, ISSN 0720-8715

[Fer50] E. Fermi, Prog. Theor. Phys. 5(1950)570

[Fra98] J.D. Frankland, PhD thesis, University of Paris XI, Orsay, France (1998)

[Fra01] J.D. Frankland et al., Nucl. Phys. A 689(2001)940

[Fri81] B. Friedmann and V.R. Pandharipande, Nucl. Phys. A 361(1981)502

[Fri99] S. Fritz et al., Phys. Lett. B 461(1999)315

[Fuc01] C. Fuchs et al., Phys. Rev. Lett. 86(2001)1974

[Gal86] J. Galin, Nucl. Phys. A 447(1986)519c

[Gen99] E. Genouin-Duhamel, PhD thesis, University of Caen, France (1999)

[Gle88] N.K. Glendenning, Phys. Rev. C, 37(1988)2733

[Gol78] A.S. Goldhaber and H. H. Heckman, Ann.

[Gra65] I.S. Gradshteyn and I.M. Ryzhik, **Tables of Integrals, Series, and Products**, *Academic Press*, 1965

[Gre87] C. Grégoire et al., Nucl. Phys. A 465(1987)317

[Gro98] C. Gross, PhD thesis, Universität Frankfurt (1998)

[Gro90] D.H.E. Gross, Rep. Prog. Phys. 53(1990)605

[Gro93] D.H.E. Gross, Prog. Part. Nucl. Phys. 30(1993)155

[Gua96] A. Guarnera et al., Phys. Lett. B 373(1996)267

[Gua97] A. Guarnera et al., Phys. Lett. B 403(1997)191

[Gus84] H.A. Gustafsson et al., Phys. Rev. Lett. 52(1984)1590

[Har89] C. Hartnack et al., Nucl. Phys. A 495(1989)303

[Hau98] J.A. Hauger et al., Phys. Rev. C 57(1998)764

[Hau00] J.A. Hauger et al., Phys. Rev. C 62(2000)024616

[Hub90] F. Hubert, R. Bimbot, and H. Gauvin, Atomic Data and Nuclear Data Tables, 46(1990)1

[Hub91] J. Hubele et al., Z. Phys. A 340(1991)263

[Hud01] S. Hudan, PhD thesis, University of Caen, France (2001)

[Ign75] A.V. Ignatyuk et al., Yad. Fiz. 21(1975)485 (Sov. J. Nucl. Phys. 21(1975)485)

[Kez00] K. Kezzar et al., Proposal of Experiment (2000)

[Jae92] J. Jaenicke et al., Nucl. Phys. A 536(1992)201

[Jak82] B. Jakobsson et al., Z. Phys. A 307(1982)293

[Jon01] K.L. Jones, PhD Thesis, University of Surrey, United Kingdom (2001)

[Jon02] K.L. Jones, private communication (2002)

[Kon95] J. Konopka et al., Nucl. Phys. A 583(1995)357

[Koo77] S.E. Koonin, Phys. Lett. 70B(1977)43

[Kru85] H. Kruse et al., Phys. Rev. Lett. 54(1985)289

[Kwi98] K. Kwiatkowski et al., Phys. Lett. B 423(1998)21

[Lau00] F. Laue et al., Eur. Phys. J. A 9(2000)397

[Lav01] F. Lavaud, PhD thesis, University of Strasbourg, France (2001)

[Lef97] A. Le Fèvre, PhD thesis, University of Caen, France (1997)

[Lef99] A. Le Fèvre et al., Phys. Rev. C 60(1999)051602

[Lef99b] T. Lefort et al., Phys Rev. Lett. 83(1999)4033

[Lef01] A. Le Fèvre et al., GSI Scientific Report 2001

[Len99] N. Le Neindre, PhD thesis, University of Caen, France (1999)

[Leo87] W.R. Leo, **Techniques for Nuclear and Particle Physics Experiments**, Springer-Verlag Berlin Heidelberg 1987

[Li93] Bao-An Li and D.H.E. Gross, Nucl. Phys. A 554(1993)257

[Li93b] Bao-An Li et al., Phys. Lett. B 303(1993)225

[Lis95] M.A. Lisa et al., Phys. Rev. Lett. 75(1995)2662

[Loh92] E. Lohrmann, **Hochenergiephysik**, *B.G. Teubner*, Stuttgart, 1992

[Luk97] J. Łukasik et al., Phys. Rev. C 55(1997)1906

[Luk02] J. Łukasik, private communication (2002)

[Mar95] N. Marie, PhD thesis, University of Caen, France (1995)

[Mas99] A.-M. Maskay-Wallez, PhD thesis, University of Lyon, France (1999)

[Met00] V. Métivier et al., Nucl. Phys. A 672(2000)357

[Met53] N. Metropolis et al., J. Chem. Phys. 21(1953)1087

[Mey80] W.G. Meyer et al., Phys. Rev. C 22(1980)179

[Mil91] U. Milkau, PhD Thesis, Universität Frankfurt (1991)

[Mol87] J.J. Molitoris et al., Phys. Rev. C 36(1987)220

[Mon93] G. Montarou et al., Phys. Rev. C 47(1993)2764

[Mor93] L.G. Moretto and G.J. Wozniak, Ann. Rev. Nucl. Part. Sc. 43(1993)379

[Mor94] D.J. Morrissey et al., Ann. Rev. Nucl. Part. Sc. 44(1994)27

[Mye66] W.D. Myers and W.J. Swiatecki, Nucl. Phys. 81(1966)1

[Nal97] L. Nalpas, PhD thesis, University of Paris XI, Orsay, France (1997)

[Ode99] T. Odeh, PhD Thesis, University Frankfurt, 1999; GSI Rep. Diss. 99-15, 1999

[Ode00] T. Odeh et al., Phys. Rev. Lett. 84(2000)4557

[Ogi89] C.A. Ogilvie et al., Phys. Rev. C 40(1989)654

[Par00] M. Pârlog et al., Preprint (2000)

[Pei89] G. Peilert et al., Phys. Rev. C 39(1989)1402

[Pei92] G. Peilert et al., Phys. Rev. C 46(1992)1457

[Pel97] D. Pelte et al. Z. Phys. A 357(1997)215

[Pha92] L. Phair et al., Nucl. Phys. A 548(1992)489

[Pla00] E. Plagnol et al., Phys. Rev. C 61(2000)014606

[Poc95] J. Pochodzalla et al., Phys. Rev. Lett. 75(1995)1040

[Poe96] D.N. Poenaru, **Nuclear Decay Modes**, J. Konopka and H. Stöcker, *Fundamental and applied nuclear physics series (R.R. Betts, W. Greiner and W.D. Hamilton)*, Institute of Physics Publishing, Bristol and Philadelphia, 1996

[Pou95] J. Pouthas et al., Nucl. Inst. and Meth. A 357(1995)418

[Ram00] F. Rami et al., Phys. Rev. Lett. 84(2000)1120

[Rei97] W. Reisdorf and H.G. Ritter, Ann. Rev. Nucl. Part. Sc. 47(1997)663

[Rei97b] W. Reisdorf et al., Nucl Phys. A 612(1997)493

[Rei00] W. Reisdorf, *Dynamics of Multifragmentation in heavy Ion Collisions*, Progress of Theoritical Physics, Supplement n^o 140 (2000) 111

[Rit88] H.G. Ritter, Nucl. Phys. A 488(1988)651c

[Riv98] M.F. Rivet et al., Phys. Lett. B 430(1998)217

[Rot60] K. Rottmann, **Mathematische Formelsammlung**, Bibliographisches Institut AG Mannheim 1960

[Sai02] A. Saija, PhD thesis, University of Catania, Italy (2002)

[Sau76] G. Sauer, Nucl. Phys. A 264(1976)221

[Sch78] W.U. Schröder et al., Phys. Rep. 45(1978)301

[Sch96] A. Schüttauf et al., Nucl. Phys. A 607(1996)457

[Sch96b] A. Schüttauf, PhD Thesis, University Frankfurt, 1996

[Sch94] O. Schwalb et al., Phys. lett. B 321(1994)20

[Sch93] C. Schwarz et al., Phys. Rev. C 48(1993)676

[Sch01] C. Schwarz et al., Nucl. Phys. A 681(2001)279c

[Sie79] P.J. Siemens and J.O. Rasmussen, Phys. Rev. Lett. 42(1979)880

[Sky59] T.H.R. Skyrme, Nucl. Phys. 9(1959)615

[Sor89] H. Sorge et al., Nucl. Phys. A 498(1989)567c

[Sri99] B.K. Srivastava et al., Phys. Rev. C 60(1999)064606

[Sto83] H. Stöcker, Nucl. Phys. A 400(1983)63c

[Sto86] R. Stock, Phys. Rep. 135(1986)259

[Stu01] C. Sturm et al., Phys. Rev. Lett. 86(2001)39

[Stu99] M. Stute and A. Teterev, Summer Student Program, private communication (1999)

[Ton83] V.D. Toneev and K.K. Gudima, Nucl. Phys. A 400(1983)173c

[Tra02] W. Trautmann, private communication (2002)

[Trz02] A. Trzciński, private communication (2002)

[Tsa89] M.B. Tsang et al., Phys. Lett. B 220(1989)492

[Tsa91] M.B. Tsang et al., Phys. Rev. C 44(1991)2065

[Tur98] K. Turzó, Dipl. thesis (1998), University of Strasbourg (France)

[Vau72] D. Vautherin and D.M. Brink, Phys. Rev. C 5(1972)626

[Vio98] V. Viola and K. Kwiatkowski, American Scientist, 86(1998)449

[Vol02] C. Volant, private communication (2002)

[Wag96] A. Wagner, PhD Thesis, University of Darmstadt, Germany (1996)

[Wei37] V.F. Weisskopf, Phys. Rev. 52(1937)295

[Wei40] V.F. Weisskopf and D.H. Hewing, Phys. Rev. 57(1940)472 and 935

[Xi97] H. Xi et al., Z. Phys. A 359(1997)397

[Yar79] Y. Yariv and Z. Fraenkel, Phys. Rev. C 20(1979)2227

[Yar81] Y. Yariv and Z. Fraenkel, Phys. Rev. C 24(1981)488

[Zha95] J. Zhang and C. Gale, Phys. Rev. C 51(1995)1425

Study of the $^{12}C+^{197}Au$ reaction at relativistic energies with the INDRA 4π multidetector.

ABSTRACT: The INDRA@GSI experiment permits to explore the mechanisms of the reaction $^{12}C+^{197}Au$ in normal kinematics by the use of the INDRA 4π multidetector and relativistic ^{12}C beams. The target spectator source is determined for protons and light fragments, separately from the early cascade source emitting light particles and a high energy source producing fragments approximately in the center of mass. The proton kinetic energy spectra are compared to combinations of the Liège IntraNuclear Cascade model and statistical models. The favoured scenario associates a cascade process with a statistical multifragmentation process. The fragment slope temperatures determined by a Maxwell-Boltzmann function combination emphasize a dependence on incident energy, with the reaction centrality given by the charged particle multiplicity. The pions, for the first time detected in INDRA, and the fast protons emitted in the early stage of the reaction present a correlation with the impact parameter but not with the fragment production.

DOMAIN: Nuclear Physics
KEY WORDS: heavy ion collisions, INDRA multidetector, reaction mechanisms, proton and fragment sources, pions, correlation fonctions

---

Etude de la réaction $^{12}C+^{197}Au$ aux énergies relativistes avec le multidétecteur 4π INDRA.

RESUME : L'expérience INDRA@GSI permet d'étudier les mécanismes de la réaction $^{12}C+^{197}Au$ en cinématique directe par l'utilisation du multidétecteur 4π INDRA et de faisceaux de ^{12}C aux énergies relativistes. La source du spectateur de la cible est déterminée pour les protons et les fragments légers, séparément de la source de cascade émettant des particules légères et d'une source de haute énergie émettant des fragments approximativement dans le centre de masse. Les spectres de protons en énergie cinétique sont comparés à des combinaisons du modèle de Cascade IntraNucléaire de Liège avec des modèles statistiques. Le scénario privilégié associe un processus de cascade avec une multifragmentation statistique. Les températures de pente des fragments déterminées par une combinaison de fonctions de Maxwell-Boltzmann mettent en évidence une dépendance en énergie de faisceau, la centralité de la réaction étant donnée par la multiplicité de particules chargées. Les pions, détectés pour la première fois avec INDRA, et les protons rapides présentent une corrélation avec le paramètre d'impact mais non avec la production de fragments.

DISCIPLINE : Physique Nucléaire
MOTS-CLES : collisions d'ions lourds, multidétecteur INDRA, mécanismes de réaction, sources de protons et de fragments, pions, fonctions de corrélations

---

Institut de Physique Nucléaire de Lyon
43, Bd du 11 Novembre 1918, F-69622 Villeurbanne Cedex, France